

Exploiting EPR to elucidate fine and hyperfine interactions in complex chemical and biological systems

by

Gabriel Moise

A thesis submitted in partial fulfilment of the requirements for the degree of Doctor of Philosophy

New College, University of Oxford
Michaelmas Term 2020

ABSTRACT

Exploiting EPR to elucidate fine and hyperfine interactions in complex chemical and biological systems

The research presented in this thesis is concerned with the applications of Electron Paramagnetic Resonance (EPR) spectroscopy to the study of porphyrin systems and cryptochrome proteins. In particular, the fine and hyperfine interactions measured using EPR are exploited to further our understanding of both the intricate electronic and spatial structure of these systems as well as their potential future applications.

In a first project, the ^{1}H and ^{14}N hyperfine couplings in the radical cations of oligoporphyrin molecular wires were determined using continuous-wave EPR (cwEPR) as well as pulsed Electron-Nuclear Double Resonance (ENDOR). The degree of spin delocalisation, which quantifies the viability of these systems as nano-wires, can be elucidated via these hyperfine couplings.

A comparison of a previously investigated *butadiyne-linked* oligoporphyrin series with a novel series of *ethyne-linked* analogues revealed that the trends in the cwEPR spectral envelopes of the latter deviate from the trends expected for complete spin delocalisation, in contrast to the former series which follows the theoretical trend neatly. The consequences of these cwEPR envelope trends to the spin delocalisation in both series is explored in detail from the perspective of Density Functional Theory (DFT) calculations, complementary ENDOR measurements, and a re-examination of the original theory behind the cwEPR envelope analysis method.

The applicability of trEPR and ENDOR to studying complex spin density trends was further exploited in the investigation of the photo-excited triplet states of palladium(II), zinc(II), free-base, and *meso*-perfluoro oligoporphyrin systems. For these triplet states, the information obtained from ENDOR about the hyperfine couplings is complemented by the fine-structure parameters, *i.e.* the **g**-tensor and zero-field splitting (ZFS) tensor, and the non-Boltzmann (spin polarised) populations of the triplet spin sublevels, all of which dominate their trEPR spectral signature.

In the palladium(II) systems, the spin-orbit interaction due to this heavy metal ion is shown to dominate all the fine-structure and spin polarisation parameters. However, ENDOR and electronic structure calculations reveal that the spin density in the Pd^{2+} systems is conserved relative to the Zn^{2+} and free-base porphyrins. This means that the Pd^{2+} ion could replace the Zn^{2+} in molecular wires when a particular type of spin polarisation pattern is desired without compromising on spin delocalisation.

In view of the potential to control spin delocalisation in nano-wires, the trends in the fine-structure parameters of *meso*-perfluoro/acceptor substituted porphyrin systems was also investigated. The σ-acceptor groups are shown to disturb the planarity of the porphyrin backbone, causing significant orthorhombic distortions in the symmetry of the spin density. The implications of these distortions on the future use of *meso*-perfluoro groups in molecular wires, as well as on the continuing role of EPR spectroscopy in their study, is reviewed in light of the experimental observations.

The last chapter continues the exploitation of light induced spin polarisation but turns its attention to spin-correlated radical pairs in a series of cryptochrome proteins, which could be responsible for the ability of songbirds to sense and exploit the Earth's magnetic field for navigation. The fine and hyperfine interactions obtained by new simulation methods will be linked to the all-essential spin-correlation and to the intimate spatial structure of the radical pairs.

ACKNOWLEDGEMENTS

First and foremost, I would like to thank my supervisor Prof. Christiane Timmel, who welcomed me into her group, allowed me to pursue my ambitions and ideas, gently guided me back when I went too far, and pushed me further when I was drawn too close to my comfort zone. Most of all, I have really enjoyed our earnest discussions about zero-field splittings, spin-orbit couplings, coherences, hats on operators, and life. These discussions never failed to inspire me throughout my DPhil, and I look forward to many more in the future.

I am very thankful to Prof. Harry Anderson and his group for synthesising all the strange and beautiful porphyrins and allowing me to study them with EPR. In particular, I am thankful to Dr. Lara Tejerina-Gonzales for so patiently preparing all those radical cations and generally, for becoming such a good friend and always cheering me up. I am also thankful to Prof. Michael Therien and his doctoral student Erin Viere for sending us their acceptor porphyrin systems. Furthermore, I would like to express my gratitude to the Quantum Birds team, particularly to Prof. Henrik Mouritsen and his group for their cryptochrome samples, and to Prof. Peter Hore for the helpful tips for simulating the cryptochrome spectra.

On the EPR front, over the past four years, I have worked closely with quite a few Part II students and have learnt a great deal from the postdocs in the group. I am thankful to all of you for bearing with me and the look of desperation on my face when the spectrometer was still at room temperature at midnight of the first measurement day. In particular, I would like to mention (in a randomly assigned order generated using the *rand* function in MATLAB): Charles Larminie, Tommy Pitcher, Rebecca Satchwell, Ashley Redman, Edmund Little and so many more. I am also greatly indebted to Dr. Alice Bowen, Dr. Sabine Richert, and Dr. William Myers for teaching me so much about EPR experiments and spectrometers (and how to 'prevent' all their unique ways of crashing).

I have also made a number of friends in the group who have supported me and kept me entertained at all times. I will be able to thank all of them in person in the next few days (Matt, you promised to organise?), and regardless, there are too many to mention here. However, I would like to thank past group members Lauren and Christian for their friendship and for all their amazing food and the best company.

Finally, I would like to thank my amazing parents and brother (Vă mulţumesc din suflet!), my wonderful Dougie, my always-friends from the good old Romanian days, and my 'adoptive' British family and friends for always being there for me.

Iar în lumea asta mare, noi copii ai lumii mici,
Facem pe pământul nostru muşuroaie de furnici...
*

And in this vast expanse, we, children of a world so small,
Raise upon our planet anthills to over-top them all...

Mihai Eminescu, *Scrisoarea I*

Contents

Abstract iii

Acknowledgements v

Contents ix

1 Foundations of EPR spectroscopy 1

1.1 Spin angular momentum . . . 1

1.1.1 Quantum mechanical angular momentum . . . 2

1.1.2 Spin: a new degree of freedom . . . 4

1.1.3 The Wigner-Eckart theorem . . . 5

1.2 The total Spin Hamiltonian . . . 6

1.2.1 The Zeeman interaction . . . 7

1.2.2 The zero-field splitting interaction . . . 9

1.2.3 The hyperfine interaction . . . 17

1.3 Continuous-wave EPR . . . 24

1.3.1 Acquisition and instrumentation . . . 25

1.3.2 Peak intensities, selection rules, and linewidths . . . 27

1.3.3 Spectral simulations . . . 31

1.4 Pulse EPR . . . 34

1.4.1 Acquisition and instrumentation . . . 35

1.4.2 The free induction decay experiment . . . 36

1.4.3 The Hahn echo sequence . . . 40

1.4.4 Electron-nuclear double resonance . . . 41

2 Spin delocalisation in the radical cations of porphyrin molecular wires 44

2.1 Oligoporphyrins as molecular wires . . . 44

2.2 Probing delocalisation: the Norris Equation . . . 45

2.2.1 The origin of the Norris equation . . . 46
2.2.2 First-order corrections due to non-uniformity . . . 51
2.3 The monomer system as a reference . . . 53
2.4 CwEPR of the oligomers . . . 56
2.4.1 Sample preparation and cwEPR acquisition . . . 56
2.4.2 Envelope linewidth analysis . . . 57
2.4.3 Spectral simulations . . . 59
2.5 The DFT computed spin densities . . . 61
2.5.1 Methodology . . . 61
2.5.2 ^{14}N spin densities and DFT predicted spectra . . . 62
2.5.3 Dihedral angle dependence of ^{14}N spin densities . . . 64
2.6 ^{1}H-ENDOR measurements . . . 66
2.6.1 Experimental method . . . 66
2.6.2 Summary of ^{1}H-ENDOR results . . . 66
2.6.3 ^{1}H spin densities and hyperfine tensors of ***l1*-P1**$^{+\cdot}$, ***l1*-P2**$^{+\cdot}$, and ***l2*-P2**$^{+\cdot}$ . . . 68
2.7 Concluding remarks . . . 69

3 EPR spectroscopy of photo-generated triplet states 71
3.1 The spin-orbit coupling interaction . . . 71
3.2 The origin of the **g**-tensor . . . 73
3.3 The origin of the **D**-tensor . . . 75
3.3.1 The SSC contribution to ZFS . . . 76
3.3.2 The relationship between $\mathbf{D}_{SSC}$ and molecular symmetry . . . 79
3.3.3 The sign of D and the spheroidal symmetry of the spin density . . . 80
3.3.4 The SOC contribution to ZFS . . . 83
3.3.5 Relationship between $\mathbf{D}_{SOC}$ and molecular symmetry . . . 86
3.3.6 Relationship between $\mathbf{D}_{SOC}$ and $\mathbf{D}_{SSC}$ . . . 87
3.3.7 Relationship between $\mathbf{D}_{SOC}$ and the **g**-tensor . . . 88
3.3.8 Summary of fine-structure interaction tensors . . . 88
3.4 Transient EPR on photoexcited triplet states . . . 90
3.4.1 Acquisition and instrumentation . . . 90
3.4.2 Triplet states in thermal equilibrium . . . 90
3.4.3 Spin polarised triplet states . . . 93
3.5 Spin-orbit driven intersystem crossing . . . 96
3.5.1 The Franck-Condon ISC mechanism . . . 98

3.5.2 The vibronic/ Herzberg-Teller ISC mechanism . . . 99
3.5.3 The emergence of spin polarisation . . . 99
3.5.4 Selection rules for ISC . . . 101
3.6 Determining the orientation of the ZFS tensor . . . 103
3.6.1 Low temperature cwEPR . . . 103
3.6.2 Principles of the magneto-photo-selection experiment . . . 106
3.6.3 Model simulations of the MPS experiment . . . 108
3.7 ENDOR spectroscopy of triplet states . . . 110
3.7.1 Model Mims ENDOR spectra . . . 110
3.7.2 The orientation of **D** from ENDOR . . . 112
3.8 Chapter summary . . . 114

4 Spin-orbit effects in the triplet states of porphyrins 115
4.1 Context and motivation . . . 115
4.2 Monomer systems . . . 117
4.2.1 TrEPR spectra . . . 117
4.2.2 Understanding the ^{3}**Fb** and ^{3}**Zn** systems . . . 118
4.2.3 Elucidation of the ^{3}**Pd** system . . . 126
4.3 Dimer systems . . . 135
4.3.1 TrEPR spectra of homodimer systems . . . 136
4.3.2 The orientation of the **D**-tensor in ^{3}**PdPd** . . . 138
4.3.3 The heterodimer systems . . . 140
4.4 Fine and hyperfine structure trends in linear palladium oligoporphyrins . . . 143
4.5 Concluding remarks . . . 145

5 The fine-structure of acceptor porphyrin systems 147
5.1 Context and motivation . . . 147
5.2 Experimental and computational methodology . . . 149
5.3 Results and discussion . . . 150
5.3.1 Transient EPR . . . 150
5.3.2 Magneto-photo-selection . . . 152
5.3.3 Mims ENDOR . . . 154
5.3.4 Electronic structure calculations . . . 156
5.4 Concluding remarks . . . 159

6 Applications of EPR to the study of cryptochrome proteins 161

6.1 Introduction . . . 162
6.1.1 Cryptochromes as compasses of night-migratory songbirds . . . 162
6.1.2 Principles of spin-correlated radical pairs . . . 163
6.1.3 The role of EPR spectroscopy . . . 166
6.2 Transient EPR of SCRPs . . . 167
6.2.1 The simplest SCRP spectrum . . . 167
6.2.2 Towards simulating complex SCRPs . . . 170
6.2.3 Applications to cryptochromes . . . 175
6.3 Out-of-phase ESEEM of SCRPs . . . 180
6.3.1 Introduction to oopESEEM . . . 180
6.3.2 Methodology . . . 183
6.3.3 Results and discussion . . . 185
6.4 Concluding remarks . . . 189

A General eigensolution of the Hamiltonian for triplet states 192

B The Breit-Rabi equation 193

C Adaptive computation of resonance fields 196

D The D_{2h} character table 204

E Selected ORCA input and output files 205
E.1 Chapter 2 . . . 205
E.2 Chapter 4 . . . 206

F Further experimental details and results 210
F.1 Chapter 2 . . . 210
F.2 Chapter 4 . . . 211
F.3 Chapter 5 . . . 213
F.4 Chapter 6 . . . 214

G TrEPR simulation scripts for SCRPs 216
G.1 The *cockatiel* script . . . 216
G.2 The *fawns* script . . . 220

Bibliography 228

Chapter 1

Foundations of EPR spectroscopy

Similarly to the many other types of spectroscopy employed by chemists, electron paramagnetic resonance (EPR) is rooted at the junction between physics and chemistry. Many aspects pertaining to EPR phenomena are only reconcilable by some of the most fundamental scientific theories, such as quantum mechanics, special relativity, and, at the highest of levels, quantum electrodynamics. A natural question thus arises: how can we employ such a remarkably complex technique without having to be fluent in the highest echelons of physics? Perhaps even more importantly: what pragmatic information can we learn about a molecule using a technique as sophisticated and seemingly as abstract as EPR?

The answer to the latter question is, at first sight, disheartening: EPR spectroscopy cannot be used to study all molecules, only those which have unpaired electrons (radicals, certain metal complexes, certain excited states). However, when such unpaired electrons *are* present, *i.e.* if the molecule has non-zero electronic spin, then EPR can reveal a wealth of crucial information about the system. EPR measures the interaction between the electronic spin and any externally applied magnetic fields (whether static or time-dependent), as well as interactions between electronic spins with each other and with nuclear spins (of which there are many types). As will be seen throughout this thesis, these interactions help to paint a detailed picture of the electronic structure of the molecule and, in certain instances, of the actual spatial structure of the molecule.

Answering the former question (regarding the complexity of the foundations of EPR) is the topic of this chapter. The theory of EPR spectroscopy is dramatically simplified by one of the most elegant models of molecular quantum mechanics, namely the phenomenological spin Hamiltonian. This mathematical construct condenses all the quantum chemical, relativistic, and magnetic interactions present in molecular systems into a set of pragmatic parameters which can easily be interpreted and employed throughout chemistry, physics, biology, and materials science. The spin Hamiltonian/EPR parameters, which are most relevant to this thesis, will be presented in this chapter followed by a brief overview of the key experimental EPR techniques.

1.1 Spin angular momentum

Consider the motion of a non-relativistic classical particle. In the absence of any net force (free particle), a complete description of the motion of this particle requires only a knowledge of its position vector, $\mathbf{r}$, and linear momentum vector, $\mathbf{p}$, at a single given point along its trajectory. This is made possible

by the fact that in the absence of a net force, the momentum of the particle is conserved (because $\mathbf{F} = \dot{\mathbf{p}} = 0$). Importantly for free particles, the conservation of momentum can be used as a physical law governing the dynamics. If the position and momentum at a given time is measured, the past and future trajectory of the particle can be determined exactly. In the context of this thesis, the investigated particles are (mainly) unpaired electrons within molecules. Such particles are generally subject to non-zero net forces, their linear momentum is not conserved, and furthermore classical mechanics is not suitable for describing their motion. However, before transitioning to quantum theory, the following vector quantity is of particular relevance to the dynamics of electrons in atoms and molecules:

$$\mathbf{l} = \mathbf{r} \times \mathbf{p} \tag{1.1}$$

The importance of $\mathbf{l}$, called the angular momentum vector, comes from the fact that it is conserved in cases where the net force is parallel to $\mathbf{r}$:

$$\dot{\mathbf{l}} = \dot{\mathbf{r}} \times \mathbf{p} + \mathbf{r} \times \dot{\mathbf{p}} = \mathbf{r} \times \mathbf{F} = 0 \tag{1.2}$$

Examples of such problems are one electron atoms where the electrostatic force between the electron and nucleus is parallel to the position vector of the electron relative to the nucleus. More generally, the angular momentum vector is conserved in spherically symmetric problems. Whilst molecules are not spherically symmetric, many have axes of rotational symmetry with respect to which angular momentum is conserved.

1.1.1 Quantum mechanical angular momentum

The classical angular momentum, $\mathbf{l}$, in equation 1.1 can be transcribed to the quantum mechanical angular momentum operator, $\hat{\mathbf{l}}$, by replacing the position and momentum with the corresponding operators:

$$\hat{\mathbf{l}} = \hat{\mathbf{r}} \times \hat{\mathbf{p}} \tag{1.3}$$

Whilst this seems to be merely a change of notation, the carets ($\hat{}$) above the symbols indicate operators which act on functions. In the position representation, the linear momentum operator corresponds to the gradient operator, $\hat{\mathbf{p}} = -i\hbar\hat{\nabla}$, whereas the position operator represents multiplication by the components of the position vector. In other words, the angular momentum vector operator can be written explicitly in the position representation as follows:

$$\hat{\mathbf{l}} = \hat{\mathbf{r}} \times \hat{\mathbf{p}} = -i\hbar\hat{\mathbf{r}} \times \hat{\nabla} = -i\hbar \begin{pmatrix} y\dfrac{\partial}{\partial z} - z\dfrac{\partial}{\partial y} \\ z\dfrac{\partial}{\partial x} - x\dfrac{\partial}{\partial z} \\ x\dfrac{\partial}{\partial y} - y\dfrac{\partial}{\partial x} \end{pmatrix} \tag{1.4}$$

where the components of the angular momentum vector are $\hat{l}_x$, $\hat{l}_y$, and $\hat{l}_z$, respectively. These are termed angular momentum projection operators, and they allow the square magnitude of the total angular momentum to be written as:

$$\hat{l}^2 = \hat{l}_x^2 + \hat{l}_y^2 + \hat{l}_z^2 \tag{1.5}$$

Generally, the quantum mechanical angular momentum problem is concerned with finding the eigenstates of all the operators specified in the two equations above. However, it is impossible to find a simultaneous eigenfunction of $\hat{l}_x$, $\hat{l}_y$, $\hat{l}_z$, and $\hat{l}^2$, because this set of operators do not mutually commute with one another. In other words, the following commutation relations:

$$\left[\hat{l}_p, \hat{l}_q\right] = i\hbar\epsilon_{pqr}\hat{l}_r \tag{1.6}$$

$$\left[\hat{l}^2, \hat{l}_p\right] = 0 \tag{1.7}$$

where $p, q, r \in \{x, y, z\}$ and ϵ_{pqr} is the Levi-Civita symbol, imply that a function can *at most* be a simultaneous eigenfunction of $\hat{l}^2$ and only one of the projection operators, $\hat{l}_p$. Whilst this seems to be an abstract conclusion arising from commutation relations, it does have real consequences for measurements of angular momenta. The formalisation of these consequences comes in the form of the Heisenberg Uncertainty Principle. According to this principle, the observables represented by two non-commuting operators cannot be measured simultaneously with arbitrary precision. In other words, the commutators in equation 1.6 restrict the number of eigenvalue equations that can be solved simultaneously which in turn restricts the amount of information that can be obtained simultaneously from measurements.

In the specific case of angular momentum, and without loss of generality, one typically chooses to find simultaneous eigenfunctions of $\hat{l}^2$ and $\hat{l}_z$, as defined in equations 1.4 and 1.5. Consequently, if a quantum system is prepared in such an eigenfunction then, the projections of angular momentum along x and y cannot be specified with arbitrary precision. The simultaneous eigensolution of $\hat{l}^2$ and $\hat{l}_z$ is the following:

$$\hat{l}^2 Y_l^m(\theta, \phi) = \hbar^2 l(l+1) Y_l^m(\theta, \phi) \tag{1.8}$$

$$\hat{l}_z Y_l^m(\theta, \phi) = m\hbar Y_l^m(\theta, \phi) \tag{1.9}$$

where $Y_l^m(\theta, \phi)$ are Laplace's spherical harmonics and are tabulated in textbooks [1–3]. The variables θ and ϕ are the polar and azimuthal angular components of the $\mathbf{r}$ vector in spherical polar coordinates. Importantly, the spherical harmonics are completely specified by two numbers, l and m, which can only take the following integer values:

$$l = 0, 1, 2, \ldots \tag{1.10}$$

$$m = -l, (-l+1), \ldots (l-1), l \tag{1.11}$$

These two numbers, called the total and projection/magnetic angular momentum quantum numbers encapsulate the quantization of angular momentum. Importantly, they are sufficient to quantify all the rotational dynamics of quantum systems with conserved angular momentum. For example, the spherical harmonics are the solutions to the particle on a sphere problem and the angular part of the wavefunction in hydrogenic atoms and ions.

1.1.2 Spin: a new degree of freedom

The above treatment of angular momentum seems to follow exactly from the postulates of nonrelativistic quantum mechanics. However, the quantum numbers l and m defined above are not sufficient to explain a number of experimental results such as: the observation of fine-structure in atomic spectra, the anomalous Zeeman effect, or the Stern-Gerlach experiment. All of these experiments seem to point to the fact that electrons have an additional degree of freedom, which manifests as a form of angular momentum with $l = 1/2$, which is not permitted according to equation 1.10.

Nowadays, we refer to this additional degree of freedom as spin angular momentum. The correct description of the properties of spin angular momentum had excited all the founders of quantum theory from the 1920s.[1] For example, Wolfgang Pauli wrote:

> It seems therefore plausible to set against these ideas that especially the doublet structure of the alkali spectra and their anomalous Zeeman effect are caused by a classically undescribable two-valuedness of the quantum theoretical properties of the optically active electron [4].

In other words, the existence and properties of spin angular momenta are not encapsulated by the original framework of non-relativistic quantum mechanics. Nonetheless, for simplicity, we will give here the modern day formulation of what is regarded as Pauli's 'ad-hoc' description of spin. Whilst this description is mathematically correct, it requires a redefinition of what constitutes an angular momentum operator. From this perspective, spin is merely an 'add-on' to quantum mechanics, albeit an indispensable add-on.

To make progress, we define a vector operator $\hat{\mathbf{j}}$ with Cartesian components $\hat{j}_x$, $\hat{j}_y$, $\hat{j}_z$, and squared magnitude $\hat{j}^2$. If the following commutation relations are satisfied:

$$\left[\hat{j}_p, \hat{j}_q\right] = i\hbar\epsilon_{pqr}\hat{j}_r \tag{1.12}$$

$$\left[\hat{j}^2, \hat{j}_p\right] = 0 \tag{1.13}$$

then $\hat{\mathbf{j}}$ is an angular momentum. This generalised definition of angular momentum is consistent but, crucially, not limited to the position representation explicitly shown in equation 1.4. As a result, when we find the simultaneous eigenstates of $\hat{j}^2$ and $\hat{j}_z$, we are not restricted only to functions of the spatial coordinates. It can be shown using only equations 1.12 and 1.13 that the two quantum numbers, j and m, associated with the two operators, $\hat{j}^2$ and $\hat{j}_z$, can take half-integer values [2]. The general angular momentum solutions are written as:

$$\hat{j}^2|jm\rangle = \hbar^2 j(j+1)|jm\rangle \tag{1.14}$$

$$\hat{j}_z|jm\rangle = m\hbar|jm\rangle \tag{1.15}$$

where the angular momentum and projection quantum numbers can be integers or half-integers:

$$j = 0, \frac{1}{2}, 1, \frac{3}{2} \ldots \tag{1.16}$$

$$m = -j, (-j+1), \ldots (j-1), j \tag{1.17}$$

[1] And whilst the properties of spin are understood better now, it remains as exciting and as profound as it has always been.

Whilst equations 1.14-1.17 are in keeping with the existence of half-integer angular momenta and thus, the spin of electrons, they do not offer a general and explicit form of the angular momentum eigenstates, $|jm\rangle$. In fact, for half-integer values of j, there is no function of x, y, and z which simultaneously satisfies 1.14 and 1.15. This means that the wavefunction of an electron, which has spin 1/2, cannot be represented as purely a function of position *i.e.* a new degree of freedom is required.

Although the spin of the electron seems to manifest itself in a dimension which is distinct from space, it does not mean that it has no connection to space. As shown in equations 1.12 and 1.13, the components of spin angular momentum are defined and measurable (within the limits of the uncertainty principle) in a Cartesian coordinate system. This is to say that the spin degree of freedom has a well defined projection onto the spatial degrees of freedom, and these Cartesian projections are components of a vector, just like position, linear momentum, or orbital angular momentum.

1.1.3 The Wigner-Eckart theorem

Before we continue with a survey of the interactions involving spin, it is necessary to introduce (without derivation) one of the most important theorems regarding the algebra of spin operators, which will become invaluable later. Firstly, consider a set of operators labelled by two indexes, $\hat{T}_q^{(k)}$, where k is any positive integer (including zero) and $q = -k, -k+1, \ldots, k-1, k$. We can define an abstract object which represents this entire set of operators. This object will be denoted by $\hat{\mathbf{T}}^{(k)}$ and will be referred to as *a tensor operator of rank k*.[2] For example, the angular momentum vector operator, $\hat{\mathbf{j}}$, is a tensor operator of rank 1, where we could assign $\hat{T}_{-1}^{(k)} = \hat{j}_x$, $\hat{T}_0^{(k)} = \hat{j}_z$, and $\hat{T}_{+1}^{(k)} = \hat{j}_y$ (as well as any other permutation). It is clear that (in this broad definition) not all tensor operators are relevant or have any meaning. However, it is possible to formulate a tensor operator whose components satisfy the following commutation relations with the angular momentum operators:

$$\left[\hat{j}_z, \hat{T}_q^{(k)}\right] = q\hbar \hat{T}_q^{(k)} \tag{1.18}$$

$$\left[\hat{j}_\pm, \hat{T}_q^{(k)}\right] = \hbar\sqrt{k(k+1) - q(q\pm 1)}\,\hat{T}_{q\pm 1}^{(k)} \tag{1.19}$$

where we have also introduced the *raising* and *lowering* angular momentum operators:

$$\hat{j}_\pm = \hat{j}_x \pm i\hat{j}_y. \tag{1.20}$$

If the components of $\hat{\mathbf{T}}^{(k)}$ satisfy both equation 1.18 and equation 1.19, then we say that $\hat{\mathbf{T}}^{(k)}$ is a spherical tensor operator[3] of rank k with respect to $\hat{\mathbf{j}}$. We will encounter a few examples of spherical tensor operators throughout this thesis.

The usefulness of spherical tensor operators is a result of the Wigner-Eckart theorem: if $\hat{\mathbf{T}}^{(k)}$ is a spherical tensor operator with respect to an angular momentum operator $\hat{\mathbf{j}}$, then:

$$\langle jm|\hat{T}_q^{(k)}|j'm'\rangle = \langle j'm'kq|jm\rangle\langle j||\hat{\mathbf{T}}^{(k)}||j'\rangle \tag{1.21}$$

[2] This is *not* the usual definition of a tensor operator, as found in textbooks. This particular definition is invented by the author to simplify the discussion and facilitate a intuitive understanding of the Wigner-Eckart theorem. All the points that follow are, however, uninfluenced by this definition. By contrast, the definition of spherical tensor operators given in this section is entirely consistent with the definition used in the literature.

[3] Also known as an irreducible tensor operator.

where $\langle j' m' kq|jm\rangle$ is a Clebsch-Gordan coefficient and $\langle j||\hat{\mathbf{T}}^{(k)}||j'\rangle$ is a reduced matrix element. The Clebsch-Gordan coefficients are a set of real numbers which can be found tabulated in many books on quantum mechanics [2]; they relate to the transformation which takes kets from the uncoupled basis of j' and k to the coupled basis of j. The important consequence of expression 1.21 is that the dependence of the matrix elements of $\hat{T}_q^{(k)}$ on the magnetic quantum numbers m and m' is entirely specified by the Clebsch-Gordan coefficients. This means that $\langle j||\hat{\mathbf{T}}^{(k)}||j'\rangle$ is a common factor, independent of m and q, which links all the matrix elements of the components of $\hat{\mathbf{T}}^{(k)}$.

The Wigner-Eckart theorem will be instrumental in deriving the spin Hamiltonian for the interactions relevant to this work. Generally, the theorem tells us that if we can find one matrix element of any operator within the set represented by $\hat{\mathbf{T}}^{(k)}$, then all the other matrix elements can be obtained by equation 1.21 (it is simply a matter of computing Clebsch-Gordan coefficients, which are known analytically). Furthermore, the Clebsch-Gordan coefficients have a number of symmetry properties, which facilitate qualitative discussions about the influence of spherical tensor operators on energies and states. For instance, one of the symmetry properties is that $\langle j' m' kq|jm\rangle = 0$ if $m' - m \neq q$, which is the origin of all the spectroscopic selection rules involving transitions $m \leftrightarrow m'$ driven by $\hat{T}_q^{(k)}$.[4]

1.2 The total Spin Hamiltonian

In an EPR experiment, microwave radiation (either continuous or pulsed) is used to induce transitions between the spin energy levels of systems containing unpaired electrons. These transitions can be characterised with high precision by the eigenstates and eigenvalues of the spin Hamiltonian. For a system quantified by n effective electron spin operators, $\hat{\mathbf{S}}_i$,[5] and m nuclear spin operators, $\hat{\mathbf{I}}_j$, all the possible interactions are included in the following spin Hamiltonian:

$$\hat{H}_{\text{spin}} = \sum_{i=1}^{n}\left[\hat{H}_{\text{EZ}}\left(\mathbf{B},\hat{\mathbf{S}}_i\right) + \hat{H}_{\text{ZFS}}\left(\hat{\mathbf{S}}_i\right)\right] + \sum_{i=1}^{m}\left[\hat{H}_{\text{NZ}}\left(\mathbf{B},\hat{\mathbf{I}}_i\right) + \hat{H}_{\text{NQ}}\left(\hat{\mathbf{I}}_i\right)\right] + \\ + \sum_{i=1}^{n}\sum_{j\neq i}\hat{H}_{\text{EE}}\left(\hat{\mathbf{S}}_i,\hat{\mathbf{S}}_j\right) + \sum_{i=1}^{n}\sum_{j=1}^{m}\hat{H}_{\text{HF}}\left(\hat{\mathbf{S}}_i,\hat{\mathbf{I}}_j\right) + \sum_{i=1}^{m}\sum_{j\neq i}\hat{H}_{\text{NN}}\left(\hat{\mathbf{I}}_i,\hat{\mathbf{I}}_j\right) \quad (1.22)$$

For brevity, the acronyms EZ, ZFS, NZ, NQ, EE, HF, and NN which label the different types of interactions contained in $\hat{H}_{\text{spin}}$ are expanded in the caption of figure 1.1. All of these interactions play a role in the wide field of EPR spectroscopy, however, they rarely need to be considered all at once: either because they are absent, or because they are small in magnitude. The most relevant interactions for the work described in this thesis are the EZ, ZFS, and HF interactions, and thus the remaining sections will focus solely on these. The EZ and ZFS interactions are often referred to as fine-structure interactions, because in many instances, they are larger in magnitude compared with the electron-nuclear hyperfine interactions.

[4] These are called 'specific selection rules'. The 'gross selection rules' are a result of the requirement that $\langle j||\hat{\mathbf{T}}^{(k)}||j'\rangle \neq 0$.
[5] Either single electrons with $s = 1/2$ or coupled spin-spin or spin-orbit states with $S > 1/2$.

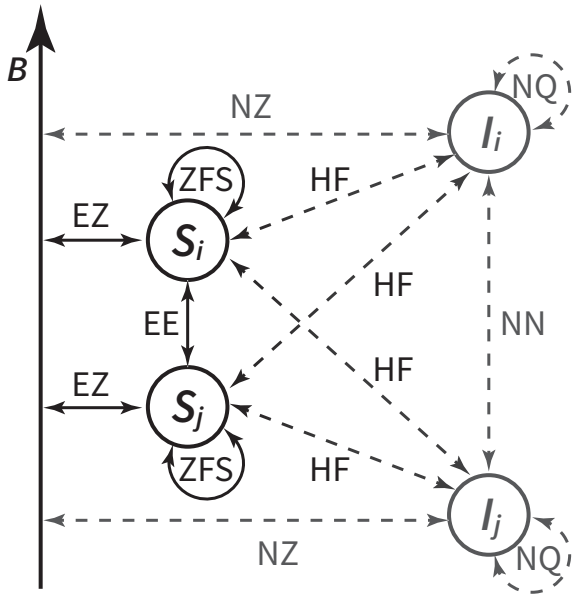


Figure 1.1: Pictorial representation of the spin Hamiltonian interactions. The acronyms for the interactions have the following meaning: electron Zeeman (EZ), nuclear Zeeman (NZ), electron-nuclear hyperfine couplings (HF), electron-electron couplings (EE), nuclear-nuclear couplings (NN), nuclear quadrupole (NQ), and zero-field splitting (ZFS). The solid arrows represent fine-structure interactions, whereas the dashed arrows indicate hyperfine interactions and inter-nuclear spin interactions. The symbols $\mathbf{S}_i/\mathbf{S}_j$ represent electron spins i and j, whereas $\mathbf{I}_i/\mathbf{I}_j$ are nuclear spins i and j.

1.2.1 The Zeeman interaction

The explicit and most general form of the EZ interaction for an effective spin, $\hat{\mathbf{S}}$, in an external magnetic field, $\mathbf{B}$, is given by the following equation:

$$\hat{H}_{EZ}\left(\mathbf{B},\hat{\mathbf{S}}\right) = \frac{\mu_B}{\hbar}\mathbf{B}^{\dagger}\cdot\mathbf{g}\cdot\hat{\mathbf{S}} \tag{1.23}$$

where $\mathbf{g}$ is a real-valued and symmetric (3×3) matrix acting on the Cartesian components of the spin vector operator.[6] This quantity is referred to as the $\mathbf{g}$-tensor, and it is the only variable needed to fully quantify the Zeeman interaction in the framework of the spin Hamiltonian. In Chapter 3, the origin of the elements of the $\mathbf{g}$-tensor will be illustrated briefly. In this section, however, the properties of the $\mathbf{g}$-tensor and the EZ interaction will be analysed from a more abstract perspective.[7]

The fact that $\mathbf{g}$ is real-valued and symmetric implies that there exists a unitary matrix, $\mathbf{U}_g^{\dagger} = \mathbf{U}_g^{-1}$, which diagonalises it:

$$\mathbf{g} = \mathbf{U}_g^{\dagger}\cdot\boldsymbol{g}\cdot\mathbf{U}_g \tag{1.24}$$

The unitary transformation, $\mathbf{U}_g$, is a Cartesian rotation matrix which transforms the $\mathbf{g}$-tensor into its diagonal form, $\boldsymbol{g}$, given by:

$$\boldsymbol{g} = \begin{pmatrix} g_1 & 0 & 0 \\ 0 & g_2 & 0 \\ 0 & 0 & g_3 \end{pmatrix} \tag{1.25}$$

[6] The 'dagger' superscript attached to the field vector, $\mathbf{B}^{\dagger}$, represents a row vector *i.e.* the transpose of a column vector.
[7] *i.e.* without delving into details pertaining to the physical origin of the $\mathbf{g}$-tensor.

Substituting equation 1.24 into the EZ Hamiltonian in 1.23 results in:

$$\hat{H}_{EZ}\left(\mathbf{B},\hat{\mathbf{S}}\right) = \frac{\mu_B}{\hbar}\mathbf{B}^{\dagger}\cdot\mathbf{g}\cdot\hat{\mathbf{S}} = \frac{\mu_B}{\hbar}\mathbf{B}^{\dagger}\cdot\mathbf{U}_g^{\dagger}\cdot\boldsymbol{g}\cdot\mathbf{U}_g\cdot\hat{\mathbf{S}} = \frac{\mu_B}{\hbar}\mathcal{B}^{\dagger}\cdot\boldsymbol{g}\cdot\hat{\mathcal{S}} \tag{1.26}$$

whereby the field vector and spin operator is now written in the eigenframe of the **g**-tensor:

$$\hat{\mathcal{S}} = \mathbf{U}_g\cdot\hat{\mathbf{S}}$$
$$\mathcal{B} = \mathbf{U}_g\cdot\mathbf{B}$$

This transformation of the EZ interaction into the eigenframe of **g** is completely general, and, in the absence of any other interactions, it shows that the effect of the six (apparently) unique elements of the **g**-tensor is reduced to only three g-values as shown in 1.25. If other interactions are present, the transformation $\mathbf{U}_g$ can still be used, however, it could lead to more complicated expressions for the other interactions in the spin Hamiltonian. Often, this transformation to the g-eigenframe is the convention of choice for analysing EPR spectra of disordered samples.[8]

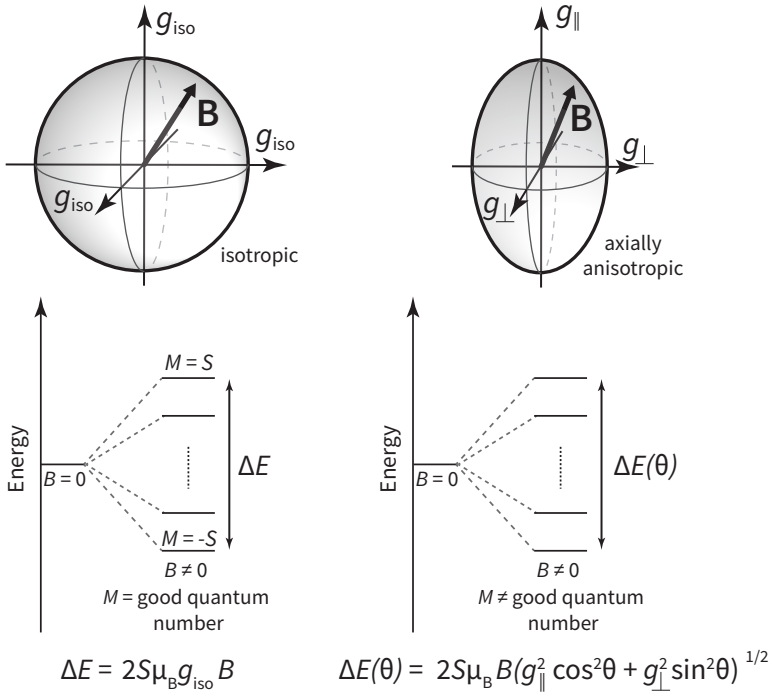


Figure 1.2: (Left) Isotropic or spherically symmetric **g**-tensor with $g_1 = g_2 = g_3 = g_{iso}$. The energy splitting of the spin sub-levels is independent of θ and ϕ, the polar and azimuthal angles of the field vector. Furthermore, the states can always be labelled by M, which is the angular momentum projection quantum number quantifying the eigenvalues of $\hat{S}_z$. Note that S is the total spin angular momentum quantum number. (Right) Axially anisotropic **g**-tensor with two axes given by $g_\perp$ and one axis given by $g_\parallel$. The energy separation of the spin sub-levels is shown to depend on θ (due to the axial symmetry, ΔE does not depend on ϕ). The magnetic quantum number M is not generally a good quantum number, except for particular orientations (such as $\theta = 0$).

If $g_1 = g_2 = g_3 = g_{iso}$, the Zeeman interaction becomes:

$$\hat{H}_{EZ}\left(\mathbf{B},\hat{\mathbf{S}}\right) = \frac{\mu_B}{\hbar}g_{iso}\mathcal{B}^{\dagger}\cdot\hat{\mathcal{S}} \tag{1.27}$$

[8] referred to as 'working in the g-frame'.

and thus, the eigenvalues of the EZ Hamiltonian are independent of the orientation of the magnetic field vector.[9] This case is often referred to as the *isotropic* or *spherically symmetric* **g**-tensor. It simply means that the splitting in energy between the $(2S + 1)$ spin sub-levels is independent of the orientation of the magnetic field relative to the spin system (figure 1.2). For a free electron *i.e.* an electron not bound by any potential, the isotropic Zeeman interaction is characterised by a g-value of approximately 2.002319. The origin of the free-electron g-value is linked both to the quantum-relativistic Dirac equation which predicts a value of exactly 2, and the remaining significant figures represent fine-structure corrections obtained using quantum electrodynamics.

By contrast, if at least two of the diagonal elements in equation 1.25 are distinct, the **g**-tensor is said to be *anisotropic*. If exactly two values are identical, the system is *axially symmetric* and if the values are pairwise distinct, the symmetry is classed as being *orthorhombic*. In both of the latter cases, the splitting of the spin sub-levels is dependent on the orientation of the magnetic field vector relative to the eigenvectors of the **g**-tensor. Due to these symmetry classifications, the **g**-tensor can be represented as an ellipsoid with characteristic radii proportional to the three g-values, as shown in figure 1.2. This ellipsoid has a fixed orientation relative to the molecular framework, and thus, as will be shown in a later section, the EPR spectra of frozen solutions are a sum of sub-spectra corresponding to all the possible orientations of the molecule relative to the external field.

1.2.2 The zero-field splitting interaction

In molecules with more than one unpaired electron, the effective spin quantum number of interest is often greater than 1/2. For example, two unpaired electrons, may exist in an electronic triplet state. This is observed for instance in molecular oxygen or when a triplet state is generated after photo-excitation of an aromatic organic molecule.

In such systems, with $S \geq 1$, the $(2S + 1)$ spin sub-levels are often non-degenerate even in the absence of a magnetic field *i.e.* there exists a zero-field splitting (ZFS). In certain systems, such as the photoexcited triplet states investigated in this thesis, the ZFS interaction is the largest component of the spin Hamiltonian apart from the EZ interaction.[10] However, the ZFS is rarely larger than the energy splitting of the Born-Oppenheimer eigenstates. Therefore, whilst ZFS is fundamental for the EPR spectra of high-spin systems, it is only a small perturbation on the scale of the complete electronic structure (hence, its effects are not typically detectable in optical spectroscopy). This is one of the reasons why it is often very challenging to model this interaction accurately (and many other EPR interactions) because most electronic structure methods are not designed to capture such minute energy differences (*e.g.* the ZFS parameters reported in this work are all less than $0.1\,\mathrm{cm}^{-1}$). Therefore, the ZFS remains one of the most elusive interactions in the spin Hamiltonian, and it is also fundamental to the research presented in this thesis. In Chapter 3, the origin of the ZFS interaction together with a number of experimental techniques used to characterise it will be presented in significantly more detail.

The spin Hamiltonian for the ZFS interactions relevant to this work takes the following form:

$$\hat{H}_{ZFS}\left(\hat{\mathbf{S}}\right) = \hat{\mathbf{S}}^{\dagger} \cdot \mathbf{D} \cdot \hat{\mathbf{S}} \tag{1.28}$$

[9] Because the dot product of two vectors is conserved by unitary coordinate transformations.
[10] Albeit the effects of ZFS are frequently larger than the effects of g-anisotropy.

where **D** is a symmetric, real-valued (3 × 3) Cartesian matrix which will hereby be referred to as the **D**-tensor. Generally, the ZFS interaction is not necessarily quadratic in the spin operators, as discussed for example in reference [5]. However, the Hamiltonian in equation 1.28 suffices for the modelling of all the experiments in this thesis, and we will thus restrict our attention only to this type of ZFS.

The remainder of this section will start by defining and justifying one of the most popular conventions employed in the EPR literature for ZFS parameters. Afterwards, the consequences of $\hat{H}_{ZFS}\left(\hat{\mathbf{S}}\right)$ on the eigenstates of the spin Hamiltonian in the absence and the presence of an external magnetic field will be explored.

The convention for ZFS parameters

First of all, because the expression for the ZFS interaction does not involve the magnetic field, only the relative energies of the spin sub-levels are important (for EPR experiments), not the absolute energies. Therefore, the **D**-tensor may be assumed to be traceless.[11] Furthermore, in the absence of any other interactions, the eigenframe of **D** is the natural choice as a reference frame, and it is defined by the following unitary transformation:

$$\mathbf{D} = \mathbf{U}_D^{\dagger} \cdot \mathcal{D} \cdot \mathbf{U}_D \tag{1.29}$$

$$\hat{\mathcal{S}} = \mathbf{U}_D \cdot \hat{\mathbf{S}} \tag{1.30}$$

In this frame, if the eigenvalues of **D** are denoted by D_x, D_y, and D_z, the ZFS Hamiltonian can be expanded as follows:

$$\hat{H}_{ZFS} = \hat{\mathcal{S}}^{\dagger} \cdot \overbrace{\begin{pmatrix} D_x & 0 & 0 \\ 0 & D_y & 0 \\ 0 & 0 & D_z \end{pmatrix}}^{\mathcal{D}} \cdot \hat{\mathcal{S}} = D_x \hat{\mathcal{S}}_x^2 + D_y \hat{\mathcal{S}}_y^2 + D_z \hat{\mathcal{S}}_z^2 \tag{1.31}$$

And thus, it would seem that three parameters (D_x, D_y, and D_z) are required to completely quantify the ZFS interaction. However, because $D_x + D_y + D_z = 0$, the eigenvalues of **D** are not independent of each other. Thus, the additional constraint of a traceless **D**-tensor, implies that the ZFS interaction can be fully specified by only two parameters instead of three.

Throughout the EPR literature, these two unique ZFS parameters are frequently denoted by D and E, and they are defined such that:

$$\begin{cases} D_x = -\frac{1}{3}D + E \\ D_y = -\frac{1}{3}D - E \\ D_z = \frac{2}{3}D \end{cases} \quad \Longleftrightarrow \quad \begin{cases} D = \frac{3}{2}D_z = -\frac{3}{2}\left(D_x + D_y\right) \\ E = \frac{D_x - D_y}{2} \end{cases} \tag{1.32}$$

[11] This merely means that a third of the trace of the ZFS Hamiltonian, $\mathrm{tr}\left[\hat{H}_{ZFS}\left(\hat{\mathbf{S}}\right)\right]$ is subtracted from all of its diagonal entries.

The above definition allows the expression for the ZFS Hamiltonian to be written in the following form:

$$\hat{H}_{ZFS} = D\left(\hat{S}_z^2 - \frac{1}{3}\hat{S}^2\right) + E\left(\hat{S}_x^2 - \hat{S}_y^2\right). \tag{1.33}$$

This last equation for the ZFS Hamiltonian is exactly analogous to equation 1.28, if the convention in equation 1.32 is employed. However, this unusual convention requires some justification as to its origin and usefulness for both EPR in general, as well as the present work in particular.

Firstly, the definitions in equation 1.32 are important for the very reason that they allow the expression of the ZFS Hamiltonian in the form given by equation 1.33. More precisely, the two spin operators enclosed by the brackets in equation 1.33 are components of Steven's spin operators of rank 2. The symmetry properties of such operators imply that the D and E parameters can easily be mapped[12] to the crystal field parameters in transition metal complexes. This is, in fact, the basis of the original derivation of the spin Hamiltonian as outlined in the textbook by Abragam and Bleaney [5].

However, in the cases investigated in this thesis, crystal field theory is inapplicable because we are not concerned with unpaired electrons located (almost exclusively) on transition metal ions. Nonetheless, for the purpose of consistency, this convention for the definitions of D and E is unanimously adopted by the EPR research community. Thus, throughout this thesis, this convention will also be adopted when reporting ZFS parameters. However, as will be seen shortly, this convention also has a profound effect on the way in which the ZFS is interpreted and extracted from EPR spectra.

Another aspect concerning the convention in equation 1.32 is regarding the labelling of the eigenvalues D_x, D_y, and D_z. From this point on, the following inequality:

$$|D_x| \leq |D_y| \leq |D_z| \tag{1.34}$$

will be satisfied regardless of the signs of D and E. This means that, as written, the labelling in equation 1.32 also assumes that D and E have the same sign. Furthermore, in later discussions, the Cartesian x, y, and z subscripts will be replaced by the capitalised versions X, Y, and Z subscripts to indicate that these are the eigenvalues of **D** which satisfy convention 1.34.

The signs and magnitudes of D and E dictate the shape of the ellipsoidal representation of the **D**-tensor which in turn can be related to the symmetry of the electronic wavefunction (as will be discussed further when we derive the formulas for D and E for triplet states). The conventions represented by equations 1.32 and 1.34 also provide a useful criterion for quantifying the symmetry of the **D**-tensor. More precisely, note that from equation 1.32, the **D**-tensor cannot be spherically symmetric unless both D and E are exactly zero. Thus, in its most symmetric manifestation, the ZFS interaction is axial.[13]

Also from equation 1.32, we might be tempted to say that the **D**-tensor should be perfectly axial if either $D = 0$ or $E = 0$. However, the convention in equation 1.34 does not allow $D = 0$ and $E \neq 0$ simultaneously because it would require swapping the labels such that eventually E becomes D. Therefore, an axial **D**-tensor is obtained if and only if E is zero. Due to this line of reasoning, D is known as the axial ZFS parameter and E is the orthorhombic ZFS parameter.

A much simpler way to asses the non-axiality of the **D**-tensor is via the so-called orthorhombicity

[12] Using the Wigner-Eckart theorem.

[13] By contrast, the **g**-tensor can be isotropic/spherically symmetric, and it will still contribute to the spin Hamiltonian.

parameter, λ, defined as:

$$\lambda = \frac{|E|}{|D|} = \frac{1}{3}\frac{|D_x - D_y|}{|D_z|} \tag{1.35}$$

This parameter is invaluable for the interpretation of the ZFS splitting, and it constitutes the most compelling reason for adopting the above convention despite not investigating transition metal complexes. The reason why λ is so important can be seen by looking at the range of values it can adopt. There is a clear and rigid lower limit for λ:

$$\lambda \geq 0 \tag{1.36}$$

where equality is obtained if $D_x = D_y$ *i.e.* if the tensor is perfectly axial. Thus, λ is clearly a direct measure of the orthorhombicity of the **D**-tensor.

However, the most important property of λ is that, within this convention, it has an upper limit of exactly 1/3, beyond which the eigenvalues of **D** can always be relabelled to give $\lambda < 1/3$. In other words, values of λ *outside* of the following range:

$$0 \leq \lambda \leq \frac{1}{3} \tag{1.37}$$

have no physical meaning because one can always define an equivalent set of ZFS parameters, D' and E' such that the new ratio λ' is *inside* the range.

To prove this fact, let us assume we perform some arbitrary experiment from which E and D are obtained by least-squares fitting of the Hamiltonian in equation 1.33 to a particular data set. If the fitting algorithm is not constrained to search for values in the range of equation 1.37 then it is perfectly possible to obtain a value of λ greater than 1/3. When this occurs, it is possible to define a strictly positive number, $\mathcal{K} > 0$, such that:

$$\lambda > \frac{1}{3} \iff E = \pm\frac{1}{3}|D| \pm \mathcal{K}, \quad \mathcal{K} > 0 \tag{1.38}$$

By application of 1.32, the eigenvalues of the **D**-tensor are then given by the following three expressions:

$$\pm\mathcal{K}, \quad \left(\mp\frac{2}{3}|D| \mp \mathcal{K}\right), \quad \pm\frac{2}{3}|D| \tag{1.39}$$

And now, we have to assign a new set of labels, D'_x, D'_y, and D'_z , to these eigenvalues, such that the convention in equation 1.34 is satisfied. It is important to stress that this relabelling procedure employed in the assignment of the new D'- and E'-values is not problematic. This is because it corresponds to a unitary transformation (*i.e.* rotation) of the **D**-tensor which, by definition, leaves the eigenvalues of the ZFS Hamiltonian invariant. Clearly, the middle value has to be D'_z because it has the largest absolute magnitude. Therefore, the absolute value of the new D'-value is:

$$|D'| = |D| + \frac{3}{2}\mathcal{K} \tag{1.40}$$

The first and last expression in 1.39, can then be used to construct the absolute value of the new E'-value:

$$|E'| = \frac{1}{2}\left|\pm\frac{2}{3}|D| \mp \mathcal{K}\right| = \frac{1}{3}\left|\pm|D| \mp \frac{3}{2}\mathcal{K}\right| \tag{1.41}$$

By combining equations 1.40 and 1.41, the new orthorhombicity parameter is obtained as:

$$\lambda' = \frac{1}{3}\frac{\left|\pm|D| \mp \frac{3}{2}\mathcal{K}\right|}{|D| + \frac{3}{2}\mathcal{K}} < \frac{1}{3} \tag{1.42}$$

which proves the original statement about λ. As such, whether one simulates the experimental data with the old D- and E-values (for which $\lambda > \frac{1}{3}$) or with the newly defined D'- and E'-values (for which $\lambda' < \frac{1}{3}$) is a matter of choice. The convention employed here will be to restrict the values of λ to lie between zero and 1/3. This convention offers a very useful restriction which can be employed in extracting the D- and E-values from experimental data: for a given D value, the fitting algorithm only has to search over a small interval for the best fit E-value.

The eigensolution of the ZFS Hamiltonian

In light of the previous section, the discussion that follows will revolve around the effect of the D- and E- values on the eigenvalues and eigenstates of the ZFS Hamiltonian in equation 1.33. The discussion will be restricted to the ZFS of triplet states, since these are directly relevant to this work. Thus, the matrix representation[14,15] in the $\{|1,+1\rangle, |1,0\rangle, |1,-1\rangle\}$ basis of the ZFS Hamiltonian is:

$$\mathcal{H}_{ZFS} = \begin{pmatrix} D/3 & 0 & E \\ 0 & -2D/3 & 0 \\ E & 0 & D/3 \end{pmatrix} \tag{1.43}$$

And therefore, the eigenvalues are:

$$\begin{cases} E_X = -D_x = +\frac{1}{3}D - E \\ E_Y = -D_y = +\frac{1}{3}D + E \\ E_Z = -D_z = -\frac{2}{3}D \end{cases} \tag{1.44}$$

and the orthonormal eigenvectors are:

$$\begin{cases} |X\rangle = \frac{1}{\sqrt{2}}\left(|1,+1\rangle - |1,-1\rangle\right) \\ |Z\rangle = |1,0\rangle \\ |Y\rangle = \frac{1}{\sqrt{2}}\left(|1,+1\rangle + |1,-1\rangle\right) \end{cases} \tag{1.45}$$

[14] We will denote the matrix representation of an operator $\hat{A}$ by the corresponding calligraphic symbol $\mathcal{A}$. Furthermore, when we say that the matrix is in the $\{|n_1\rangle, |n_2\rangle, \dots\}$ basis, this refers to the ordering of the entries of the matrix *e.g.* the second entry of the first row is $(\mathcal{A})_{12} = \langle n_1|\hat{A}|n_2\rangle$.

[15] Also, note that within this section the D and E values are in energy units. In the previous section these parameters were in units of Joules$\times\hbar^{-2}$.

In other words, we can define the following unitary transformation:

$$\mathcal{T} = \frac{1}{\sqrt{2}}\begin{pmatrix} +1 & 0 & +1 \\ 0 & \sqrt{2} & 0 \\ -1 & 0 & +1 \end{pmatrix} \tag{1.46}$$

which converts the ZFS matrix from the $\{|1,+1\rangle, |1,0\rangle, |1,-1\rangle\}$ basis to the $\{|X\rangle, |Z\rangle, |Y\rangle\}$ basis (*i.e.* the ZFS eigenbasis):

$$\mathcal{H}_{ZFS}^{eig} = \mathcal{T}^{\dagger} \cdot \mathcal{H}_{ZFS} \cdot \mathcal{T} = \begin{pmatrix} -D_x & 0 & 0 \\ 0 & -D_z & 0 \\ 0 & 0 & -D_y \end{pmatrix} \tag{1.47}$$

Equation 1.44 shows that the eigenvalues of the ZFS Hamiltonian have the same magnitude as the eigenvalues of the **D**-tensor. Moreover, inspection of equation 1.45 reveals that the ZFS eigenstates cannot be represented by the eigenstates of $\hat{\mathcal{S}}_z$ *i.e.* M is not generally a good quantum number. The only exception is if the **D**-tensor is axial ($E = 0$), then $|X\rangle$ and $|Y\rangle$ become degenerate. In turn, this means that any linear combination of $|X\rangle$ and $|Y\rangle$ is also an eigenstate of the ZFS Hamiltonian and thus, M is a good quantum number.

We now turn our attention to the eigenstates resulting from the sum of the EZ and ZFS interactions. In doing so, two choices have to be made: one regarding the basis for the matrix representations and another choice between the eigenframe of the **g**-tensor or the **D**-tensor. The results are the same regardless of the choices of basis and eigenframe, and for simplicity, both the ZFS eigenbasis and eigenframe are chosen here.[16] The total spin Hamiltonian (in the $\{|X\rangle, |Z\rangle, |Y\rangle\}$ basis) will thus be given by:

$$\mathcal{H} = \mathcal{T}^{\dagger} \cdot (\mathcal{H}_{EZ} + \mathcal{H}_{ZFS}) \cdot \mathcal{T} = \mathcal{T}^{\dagger} \cdot \mathcal{H}_{EZ} \cdot \mathcal{T} + \mathcal{H}_{ZFS}^{eig} \tag{1.48}$$

The transformation to the ZFS eigenbasis of the EZ interaction can be performed easily if the EZ Hamiltonian is written as follows:

$$\mathcal{H}_{EZ} = \frac{\mu_B}{\hbar}\mathbf{B} \cdot \mathbf{g} \cdot \mathcal{S} = \gamma_x \mathcal{S}_x + \gamma_y \mathcal{S}_y + \gamma_z \mathcal{S}_z \tag{1.49}$$

where γ_q is the projection of the magnetic field onto the eigenvectors of the **g**-tensor,[17] and is easily computed according to:

$$\gamma_q = \frac{\mu_B}{\hbar} \sum_p g_{qp} B_p, \quad \forall p, q \in \{x, y, z\} \tag{1.50}$$

Therefore, by combining equations 1.48-1.50 together with the formula of the transformation in 1.46, the total spin Hamiltonian in the $\{|X\rangle, |Z\rangle, |Y\rangle\}$ basis becomes:

$$\mathcal{H} = \begin{pmatrix} -D_x & -i\hbar\gamma_y & \hbar\gamma_z \\ +i\hbar\gamma_y & -D_z & \hbar\gamma_x \\ \hbar\gamma_z & \hbar\gamma_x & -D_y \end{pmatrix} \tag{1.51}$$

[16] This means that the **g**-tensor and the magnetic field vector in $\mathcal{H}_{EZ}$ are both defined with respect to the axes of the **D**-tensor. Note also that the unitary transformation $\mathcal{T}$ can only convert the *matrix representation* of an *operator* from the eigenbasis of $\mathcal{S}_z$ to the ZFS eigenbasis. The transformation $\mathbf{U}_D$ from the previous section (equation 1.30) converts interaction tensors to the eigenframe of **D** *and* it changes the Cartesian frame of the components of vectors and vector operators to the ZFS frame.

[17] This quantity is independent of the choice of frame, because projections are conserved by unitary transformations.

The full analytical eigensolution of $\mathcal{H}$ is not a trivial problem. However, analytical solutions are rarely required, since there are numerous efficient numerical simulation methods which can be used to characterise the EPR spectra of triplet states. Nonetheless, as shown in Appendix A, by solving the secular determinant of equation 1.51, it is possible to obtain an analytical expression for the three eigenvalues E_0, E_1, and E_2 of the total spin Hamiltonian, $\mathcal{H}$:

$$E_k = 2\sqrt{-\frac{\mathrm{tr}\left(\mathrm{adj}\left(\mathcal{H}\right)\right)}{3}}\cos\left(\frac{1}{3}\arccos\left(-\frac{3\det\left(\mathcal{H}\right)}{2\,\mathrm{tr}\left(\mathrm{adj}\left(\mathcal{H}\right)\right)}\sqrt{-\frac{3}{\mathrm{tr}\left(\mathrm{adj}\left(\mathcal{H}\right)\right)}}-k\frac{2\pi}{3}\right)\right), \quad \text{for } k\in\{0,1,2\} \tag{1.52}$$

where 'tr', 'adj', and 'det' represent the trace, classical adjoint, and determinant of a square matrix, respectively. These energies can then be substituted into the eigenvalue equation of $\mathcal{H}$ and the normalised eigenvectors in the $\{|X\rangle, |Z\rangle, |Y\rangle\}$ basis can be obtained (although the expressions will be complicated).

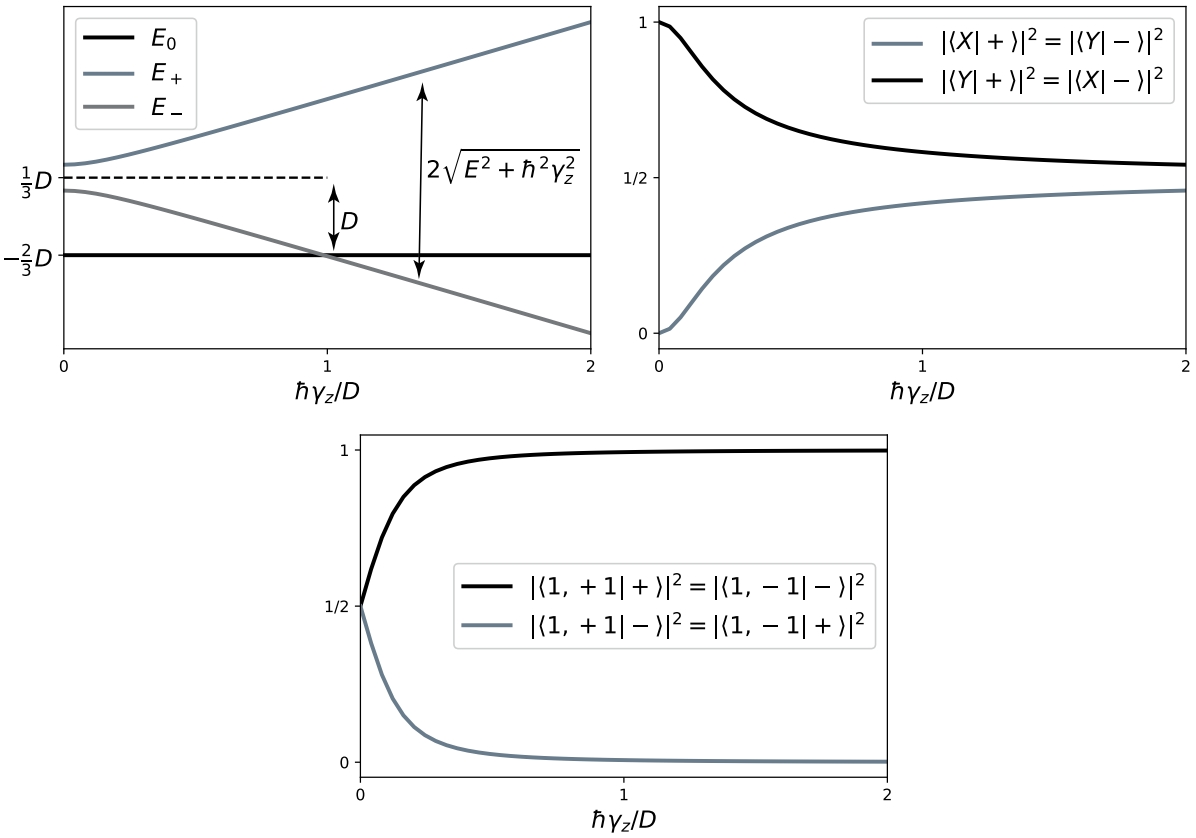


Figure 1.3: (Top left) The eigenvalues of the ZFS Hamiltonian with the field along the z-axis of the **g**-tensor as a function of $\hbar\gamma_z/D$ (equation 1.53). (Top right) The coefficients of the ZFS eigenstates $|X\rangle$ and $|Y\rangle$ in the true $|\pm\rangle$ eigenstates of the total Hamiltonian as a function of $\hbar\gamma_z/D$. (Bottom) The coefficients of the $\mathcal{S}_z$ eigenstates $|1,\pm1\rangle$ in the true $|\pm\rangle$ eigenstates of the total Hamiltonian as a function of $\hbar\gamma_z/D$. Note, in all three cases: $D > 0$, $E > 0$, and $\lambda = 1/6$.

Whilst equation 1.52 is exact and completely general, more insight can be gained by considering the eigenvalues of $\mathcal{H}$ for particular orientations of the magnetic field. For example, if the magnetic field is

along the z-axis of the **g**-tensor, *i.e.* if $\gamma_x = \gamma_y = 0$, the eigenvalues are given by:

$$\begin{cases} E_0 = -\frac{2}{3}D \\ E_\pm = +\frac{1}{3}D \pm \sqrt{E^2 + \hbar^2\gamma_z^2} \end{cases} \tag{1.53}$$

and the eigenvectors are given by:

$$\begin{cases} |0\rangle = |Z\rangle \\ |\pm\rangle = \pm\frac{1}{\sqrt{2}}\sqrt{1 \mp \frac{E}{\sqrt{E^2 + \hbar^2\gamma_z^2}}}|X\rangle \\ \qquad\qquad + \frac{1}{\sqrt{2}}\sqrt{1 \pm \frac{E}{\sqrt{E^2 + \hbar^2\gamma_z^2}}}|Y\rangle \end{cases} \tag{1.54}$$

Figure 1.3 summarises the behaviour of the eigenvalues and coefficients of the eigenstates as a function of magnetic field as resulting from equations 1.53 and 1.54. Of particular interest is the behaviour of the eigenvalues and eigenstates in certain limiting situations. Clearly, in the zero-field limit, the ZFS eigenvalues and eigenstates in equations 1.44 and 1.45 are recovered:

$$\lim_{\gamma_z \to 0} E_\pm = \begin{cases} E_Y \\ E_X \end{cases} \quad , \quad \lim_{\gamma_z \to 0} |\pm\rangle = \begin{cases} |Y\rangle \\ |X\rangle \end{cases} \tag{1.55}$$

In the limit of an axially symmetric **D**-tensor, we also recover the eigenstates of $\mathcal{S}_z$ (M becomes a good quantum number) and the energies of the $|1, \pm1\rangle$ states become linear in the magnetic field:

$$\lim_{E \to 0} E_\pm = \frac{1}{3}D \pm \hbar\gamma_z \quad , \quad \lim_{E \to 0} |\pm\rangle = |1, \pm1\rangle \tag{1.56}$$

Interestingly, M also becomes a good quantum number in the high-field limit, regardless of the value of E:

$$\lim_{\gamma_z \to \infty} |\pm\rangle = \frac{1}{\sqrt{2}}|Y\rangle \pm \frac{1}{\sqrt{2}}|X\rangle = |1, \pm1\rangle \tag{1.57}$$

whilst the energies also scale linearly with the magnetic field if $\hbar\gamma_z \gg E$.

The above discussion will become invaluable in the description of the EPR spectra of photoexcited triplet states. Particularly, the high-field limit is often approached in EPR experiments and thus, the analysis of spectra is simplified significantly. Furthermore, as will become apparent, a knowledge of the coefficients of the eigenstates is also critical in calculating the intensity of EPR transitions for cases in which the triplet sub-levels are not populated according to the Boltzmann distribution (spin polarisation).

1.2.3 The hyperfine interaction

Within the framework of the phenomenological spin Hamiltonian, the hyperfine coupling between a total electronic spin, $\hat{\mathbf{S}}$, and a nuclear spin, $\hat{\mathbf{I}}$, is quantified by the following equation:

$$\hat{H}_{HF} = \hat{\mathbf{S}} \cdot \mathbf{A} \cdot \hat{\mathbf{I}} \tag{1.58}$$

where $\mathbf{A}$ is a real-valued, symmetric (3×3) matrix known as the hyperfine coupling tensor. The existence of this interaction can be justified from a classical picture: both the electron and the nucleus have a magnetic dipole moment associated with their spin, hence, we expect an interaction between them. The quantum mechanical origin of this interaction is, however, more subtle. There are many terms in the true electronic Hamiltonian which can contribute to a spin Hamiltonian of the form in equation 1.58.[18] In this section, only the following interaction between an electron and a nucleus will be considered:

$$\hat{V} = \underbrace{-\frac{8\pi}{3}\mathcal{C}\hat{\mathbf{s}}_i \cdot \hat{\mathbf{I}}\delta^3(\mathbf{r}_i)}_{\hat{V}_{FCI}} + \underbrace{\mathcal{C}\left\{\frac{\hat{\mathbf{s}}_i \cdot \hat{\mathbf{I}}}{\hat{r}_i^3} - 3\frac{\left(\hat{\mathbf{r}}_i \cdot \hat{\mathbf{s}}_i\right)\left(\hat{\mathbf{r}}_i \cdot \hat{\mathbf{I}}\right)}{\hat{r}_i^5}\right\}}_{\hat{V}_{dip}} \tag{1.59}$$

where there is an implicit summation over all the electrons indexed by i with spin operators $\hat{\mathbf{s}}_i$, and the dipolar constant is given by $\mathcal{C} = \frac{\mu_0}{4\pi} g_e \gamma_e \gamma_n$.[19] This interaction is one of the many terms in the more general Breit-Pauli Hamiltonian [6]. As indicated, the total interaction in equation 1.59 can be thought of as having two components quantified by: the Fermi contact interaction term, $\hat{V}_{FCI}$, and the 'dipolar-like' interaction term, $\hat{V}_{dip}$. We say that $\hat{V}_{dip}$ is 'dipolar-like' because it has the same mathematical form as the *classical* dipolar interaction between two point magnetic dipoles. However, $\hat{V}_{dip}$ is not classical. In fact, it can be derived directly from the relativistic quantum mechanical Breit equation for an electron-nucleus system without ever having to resort to any classical arguments [6].

The Fermi contact interaction

The hyperfine coupling in equation 1.58 is linear in both $\hat{\mathbf{S}}$ and $\hat{\mathbf{I}}$. Therefore, only first-order perturbations to the states of interest need to be considered. However, in order to be able to write the equation for the perturbation, the states of interest have to be defined such that they include both the electronic and nuclear spin degrees of freedom. It is no longer sufficient to refer to the unperturbed states as $|SM\rangle$, but rather:

$$\hat{H}_0|nSM, IM_I\rangle = E^{(0)}|nSM, IM_I\rangle \tag{1.60}$$

where n labels the spatial part of the electronic wavefunction, S and M are the quantum numbers corresponding to the total electronic spin, and I and M_I to the nuclear spin. Hence, the first-order correction due to the Fermi contact interaction to the electron-nuclear manifold is:

$$\mathcal{V}_{MM',M_IM_I'} = -\frac{8\pi}{3}\mathcal{C}\langle nSM, IM_I| \sum_i \hat{\mathbf{s}}_i \cdot \hat{\mathbf{I}}\delta^3(\mathbf{r}_i)|nSM', IM_I'\rangle \tag{1.61}$$

[18] For example, the interaction between the nuclear spin and the electronic orbit will be neglected.

[19] The total spin operator in 1.58 is defined with respect to the spin of the individual electrons as $\hat{\mathbf{S}} = \sum_i \hat{\mathbf{s}}_i$.

and thus, $\mathcal{V}$ is a square matrix of dimension $(2S+1)(2I+1)$. The expectation value in the equation above can be evaluated by separating the integration over the space and spin degrees of freedom:

$$\mathcal{V}_{MM',M_IM_I'} = -\frac{8\pi}{3}\mathcal{C}\sum_i \langle n|\delta^3(\mathbf{r}_i)|n\rangle\langle SM, IM_I|\hat{\mathbf{s}}_i\cdot\hat{\mathbf{I}}|SM', IM_I'\rangle \tag{1.62}$$

The spatial integral can be evaluated as follows:

$$\langle n|\delta^3(\mathbf{r}_i)|n\rangle = \int\cdots\int \psi_n^*\delta^3(\mathbf{r}_i)\psi_n\, d\tau = \int\cdots\int |\psi_n(\mathbf{r}_i=0)|^2\; d\tau' = \rho(0) \tag{1.63}$$

where, by definition, $\rho(0)$ is the probability density of finding an electron at the position of the nucleus in question.[20] Since electrons are indistinguishable, $\rho(0)$ is independent of the index i of the electron, and thus, the perturbation can be rewritten:

$$\mathcal{V}_{MM',M_IM_I'} = -\frac{8\pi}{3}\mathcal{C}\rho(0)\sum_i\langle SM, IM_I|\hat{\mathbf{s}}_i\cdot\hat{\mathbf{I}}|SM', IM_I'\rangle = -\frac{8\pi}{3}\mathcal{C}\rho(0)\langle SM, IM_I|\hat{\mathbf{S}}\cdot\hat{\mathbf{I}}|SM', IM_I'\rangle \tag{1.64}$$

A comparison of the above result with the spin Hamiltonian formulation of the HF interaction in equation 1.58, implies that the hyperfine coupling tensor arising from the Fermi contact interaction has the following form:

$$\mathbf{A}_{FCI} = -\frac{8\pi}{3}\mathcal{C}\rho(0)\mathbf{1}_3 = a_{iso}\mathbf{1}_3 \tag{1.65}$$

Furthermore, it can be seen that this contribution to the HF interaction is isotropic and therefore, the hyperfine interaction tensor is not generally traceless. The probability density of finding an electron at the position of the nucleus vanishes unless the electronic wavefunction has *s*-character (because *p*, *d*, *f* ... orbitals are zero at the origin). As shown in reference [1], it is relatively straightforward to evaluate the electron density at the nucleus for an electron in a 1*s*-orbital on a hydrogen atom:

$$\rho_{1s}(0) = \frac{1}{\pi a_0^3} \Longrightarrow a_{iso,1s} = 1423\,\text{MHz} \tag{1.66}$$

The relationship between equation 1.65 and the spin density can be established if the electron density is decomposed into the probabilities of finding an α versus a β electron at the nucleus:

$$\mathbf{A}_{FCI} = -\frac{8\pi}{3}\mathcal{C}\rho(0)\mathbf{1}_3 = -\frac{8\pi}{3}\mathcal{C}\left(\rho^\alpha(0)+\rho^\beta(0)\right)\mathbf{1}_3 \tag{1.67}$$

Frequently, the β electron density, ρ^β, is defined as being the negative of the β spin density, *i.e.* $\sigma^\beta = -\rho^\beta$, whereas the α spin density is defined as $\sigma^\alpha = \rho^\alpha$. By adopting this convention, equation 1.67 becomes:

$$\mathbf{A}_{FCI} = -\frac{8\pi}{3}\mathcal{C}\left(\sigma^\alpha(0)-\sigma^\beta(0)\right)\mathbf{1}_3 = -\frac{8\pi}{3}\mathcal{C}\Delta\sigma(0)\mathbf{1}_3 \tag{1.68}$$

and therefore, the isotropic hyperfine coupling is proportional to the difference between the α and β spin density at the nucleus of interest. It is customary to define the difference between the α and β spin density, $\Delta\sigma$, as being the 'net unpaired electron density' often abbreviated simply as the 'spin density'. Within this convention, an excess of α electrons at the nucleus results in a positive value for a_{iso}, whilst an excess of β electrons leads to $a_{iso} < 0$. In other words, the hyperfine couplings obtained from EPR

[20] In equation 1.63, $d\tau$ refers to the position variables of all the electrons, whereas $d\tau'$ refers to all electrons except one.

spectra are a direct measure of the distribution of the spin density of the molecule.

In 1956, McConnell established an approximate and extremely useful form of equation 1.68 as applicable to the hyperfine couplings of protons, a_j^{H}, in the radicals of aromatic molecules (such as benzene) [7]:

$$a_j^{\mathrm{H}} \propto \rho_j^{\mathrm{C}} \tag{1.69}$$

where ρ_j^{C} is the net unpaired electron density at carbon atom j. Whilst formally the unpaired electron resides in a π-orbital, McConnell showed that the interaction between the $2p_z$ orbital on carbon and the $1s$ orbital on hydrogen (mediated by the inter-electron repulsion operator) leads to a hyperfine coupling between the electron and the proton. This mixing between the π and σ frameworks which leads to s-character in what is formally classed as a p-orbital is often referred to as 'spin polarisation'. However, this terminology will be avoided in this thesis because 'spin polarisation' will be used later in a different context. The McConnell relation will be at the heart of the discussion in Chapter 2 of this thesis.

The dipolar hyperfine interaction

In order to find the dipolar contribution to the hyperfine tensor, the expression in equation 1.59 will be rewritten as follows:

$$\hat{V}_{\mathrm{dip}} = \mathcal{C} \sum_i \left\{ \frac{\hat{\mathbf{s}}_i \cdot \hat{\mathbf{I}}}{\hat{r}_i^3} - 3\frac{\left(\hat{\boldsymbol{\epsilon}}_i \cdot \hat{\mathbf{s}}_i\right)\left(\hat{\boldsymbol{\epsilon}}_i \cdot \hat{\mathbf{I}}\right)}{\hat{r}_i^3} \right\} = \mathcal{C} \sum_{p,q} \sum_i \left\{ \frac{\delta_{pq} - 3\hat{\epsilon}_{iq}\hat{\epsilon}_{ip}}{r_i^3} \hat{s}_{iq}\hat{I}_p \right\} \tag{1.70}$$

where $p, q \in \{x, y, z\}$, $\hat{\boldsymbol{\epsilon}}_i = \hat{\mathbf{r}}_i/|\hat{\mathbf{r}}_i|$ is the position unit vector for electron i, and δ_{pq} is the Kronecker delta (the elements of the Cartesian unit matrix). Hence, the first-order correction to the manifold represented by the $|nSM, IM_I\rangle$ states is given by:

$$\mathcal{V}_{\mathrm{dip}}^{MM',M_I,M_I'} = \mathcal{C} \sum_{p,q} \sum_i \left\langle \frac{\delta_{pq} - 3\hat{\epsilon}_{iq}\hat{\epsilon}_{ip}}{r_i^3} \right\rangle \langle SM, IM_I|\hat{s}_{iq}\hat{I}_p|SM', IM_I'\rangle \tag{1.71}$$

where the spatial and spin integrals have been separated. This equation leads directly to the expression for the dipolar contribution to the hyperfine coupling tensor:

$$\mathbf{A}_{\mathrm{dip}} = \mathcal{C} \left\langle \frac{\mathbf{1}_3 - 3\hat{\boldsymbol{\epsilon}} \otimes \hat{\boldsymbol{\epsilon}}}{r^3} \right\rangle \tag{1.72}$$

The expectation value in equation 1.72 is taken over the spatial part of the wavefunction. This expression implies that the dipolar hyperfine tensor is anisotropic and traceless.

Before proceeding to an analysis of the effects of the Fermi-Contact and dipolar couplings on the eigenstates and energies of spin systems, it is useful to look at a particular example where $\mathbf{A}_{dip}$ can be evaluated explicitly. In the previous section, it was determined that for an electron in the $1s$ orbital of hydrogen, there is an isotropic hyperfine coupling of 1423 MHz due to the Fermi-Contact term. For this system, the dipolar interaction clearly vanishes because the integrals in equation 1.72 are zero over a spherically symmetric wavefunction.

However, in the $2p_z$ state of the hydrogen atom, the Fermi-Contact interaction vanishes, whereas the

anisotropic dipolar interaction is expected to be non-zero. Following the discussion in reference [1], the dipolar hypefine tensor for this electronic state can be evaluated by first defining the $2p_z$ orbital of hydrogen:[21]

$$|^1\mathrm{H}2p_z\rangle = \sqrt{\frac{1}{32\pi a_0^5}} r\cos\theta e^{-r/2a_0} \tag{1.73}$$

which can be substituted into equation 1.72 to yield the following formula:

$$\mathbf{A}_{\mathrm{dip}}(^1\mathrm{H}2p_z) = \frac{\mathcal{C}}{32\pi a_0^3}\int_0^{2\pi}\int_0^{\pi}(\mathbf{1}_3 - 3\hat{\boldsymbol{\epsilon}}\otimes\hat{\boldsymbol{\epsilon}})\cos^2\theta\sin\theta d\,\theta d\,\phi \tag{1.74}$$

We thus obtain the dipolar hyperfine tensor by evaluating the six possible angular integrals. The final result is:

$$\mathbf{A}_{\mathrm{dip}}(^1\mathrm{H}2p_z) = \frac{C}{8a_0^3}\begin{pmatrix}\frac{2}{15} & 0 & 0\\ 0 & \frac{2}{15} & 0\\ 0 & 0 & -\frac{4}{15}\end{pmatrix} \tag{1.75}$$

Using the numerical value for the dipolar constant between a proton and electron, $\mathcal{C} = -78.5\times10^{-3}$ MHz nm^3, and the Bohr radius, $a_0 = 0.0529$ nm, we obtain the following result:

$$\mathbf{A}_{\mathrm{dip}}(^1\mathrm{H}2p_z) \approx \begin{pmatrix}-8.85 & 0 & 0\\ 0 & -8.85 & 0\\ 0 & 0 & 17.7\end{pmatrix}\mathrm{MHz} \tag{1.76}$$

The final results shown analytically in equation 1.75 and numerically in equation 1.76 have a number of consequences. The fact that the dipolar HF interaction is perfectly axial and traceless is entirely reflective of the symmetry of the $2p_z$ wavefunction. Another noteworthy point is that all three of the couplings in equation 1.76 are significantly smaller than the Fermi-Contact interaction. From a purely classical perspective, this result is reflective of the fact that in a $1s$ orbital, the electron is permitted to approach the proton infinitely closely, and thus it will experience a much larger hyperfine field compared to the electron in the $2p_z$ orbital.

Despite the fact that the above discussion was restricted to proton hyperfine couplings (in the hydrogen atom), the results are in fact useful for predicting the relative strength of hyperfine couplings expected in molecules with other nuclei. As an approximation, the result in equation 1.76 can be generalized to a $2p_z$ orbital on a different atom, X, by simply scaling the hyperfine tensor as follows:

$$\mathbf{A}_{\mathrm{dip}}(\mathrm{X}2p_z) = Z_{\mathrm{eff}}^3\frac{\gamma_X}{\gamma_{^1\mathrm{H}}}\mathbf{A}_{\mathrm{dip}}(^1\mathrm{H}2p_z) \tag{1.77}$$

where Z_{eff}^3 is the (cube of the) effective nuclear charge experienced by the electron in a $2p_z$ orbital on atom X, and $\gamma_X/\ \gamma_{^1H}$ is the ratio of gyromagnetic ratios of the nucleus X and the proton. This relation leads to the relative magnitudes of the dipolar hyperfine coupling for the most common nuclei of organic radicals shown in table 1.1.

[21] This expression for the $2p_z$ orbital is in SI units *i.e.* m$^{-3/2}$.

	^{17}O	^{2}H	^{1}H	^{14}N	^{13}C	^{19}F
Z_{eff}	4.4532	1	1	3.8340	3.1358	5.1000
$\gamma_X/\gamma_{^1\text{H}}$	−0.1356	0.1535	1	0.0723	0.2515	0.9411
$\mathbf{A}_{\text{dip}}(\text{X}2p_z)/\mathbf{A}_{\text{dip}}(^1\text{H}2p_z)$	−11.97	0.15	1	4.07	7.75	124.84

Table 1.1: Relative magnitudes of the dipolar contribution to the HF tensor for an electron in a $2p_z$ orbital centred on various atoms (X). Note: the values for Z_{eff} were taken from [1].

Whilst this table does not accurately reflect the complicated electronic structure of real molecules, it provides a useful guide for the trends expected in the hyperfine couplings of organic radicals. For example, we expect that a $2p_z$ orbital on a carbon atom in a molecule will give rise to a slightly larger hyperfine coupling than an equivalent orbital on nitrogen.[22] Similarly, we also expect a reduction in hyperfine couplings by substituting a proton with a deuteron. The relative magnitude for ^{19}F is expected to be the largest despite the fact that the gyromagnetic ratio of ^{19}F is very similar to ^{1}H. This is due to the dependence on the cube of the effective nuclear charge (which is larger for ^{19}F). However, fluorine does not tend to form a π-bond in an organic molecule (the above trend refers only to $2p_z$ orbitals), and so, very large hyperfine couplings to ^{19}F are unlikely to be observed in typical radicals.

The HF eigensolutions for $S = 1/2$ and $I = 1/2$

Consider an electronic doublet, with effective spin quantum number $S = 1/2$, coupled to a nucleus with spin quantum number $I = 1/2$. The total spin Hamiltonian is given by:

$$\hat{H} = \underbrace{\frac{\mu_B}{\hbar}\mathbf{B}\cdot\mathbf{g}\cdot\hat{\mathbf{S}}}_{\text{electron Zeeman}} + \underbrace{\frac{\gamma_I}{\hbar}\mathbf{B}\cdot\hat{\mathbf{I}}}_{\text{nuclear Zeeman}} + \underbrace{\hat{\mathbf{S}}\cdot\mathbf{A}\cdot\hat{\mathbf{I}}}_{\text{hyperfine}} \tag{1.78}$$

In this work, all the measured hyperfine interactions are significantly smaller than the electronic Zeeman energy, hence, the high-field limit (to be defined below) will be assumed throughout. Nonetheless, a general analysis is still relevant to this work. As will be seen in the discussion of spin-correlated radical pairs, much of the behaviour of two electron states is analogous to the behaviour of the electron-nuclear spin system introduced here.

The general eigensolution of the Hamiltonian in equation 1.78 for arbitrarily orientated **g**- and **A**-tensors relative to each other and relative to the external magnetic field, **B**, is difficult to interpret analytically. However, many of the properties of this complicated spin system can be deduced by analysing the solution to a much simpler system. Let us consider the situation in which the **g**- and **A**-tensors are aligned with each other. Furthermore, the magnetic field will be taken to be aligned with the z-axis of the **g**-tensor (and **A**-tensor, implicitly). The matrix representation of $\hat{H}$ in the uncoupled basis $|M_S, M_I\rangle = \{|1/2, 1/2\rangle, |1/2, -1/2\rangle, |-1/2, 1/2\rangle, |-1/2, -1/2\rangle\} = \{|\alpha\alpha\rangle, |\alpha\beta\rangle, |\beta\alpha\rangle, |\beta\beta\rangle\}$ can now be

[22] Of course, the magnitudes would then also have to be scaled by the coefficient of the $2p_z$ atomic orbital. This comparison therefore assumes that we are comparing a carbon and nitrogen center with the same $2p_z$ orbital coefficient. In spite of this, carbon hyperfine couplings are not easily detectable given the low natural abundance of ^{13}C.

written as follows:

$$\mathcal{H} = \begin{pmatrix} \frac{a}{4} - \frac{t}{2} + \frac{1}{2}(\gamma_z + \beta_z) & 0 & 0 & 0 \\ 0 & -\frac{a}{4} + \frac{t}{2} + \frac{1}{2}(\gamma_z - \beta_z) & \frac{1}{2}(a+t) & 0 \\ 0 & \frac{1}{2}(a+t) & -\frac{a}{4} + \frac{t}{2} - \frac{1}{2}(\gamma_z - \beta_z) & 0 \\ 0 & 0 & 0 & \frac{a}{4} - \frac{t}{2} - \frac{1}{2}(\gamma_z + \beta_z) \end{pmatrix} \tag{1.79}$$

where the symbols have the following meaning:

- $\gamma_z = \mu_B g_z B$ corresponds to the electron Zeeman energy with the field along the z-axis of the **g**-tensor (which is diagonal with entries g_x, g_y, and g_z, because we are working in its eigenframe),
- $\beta_z = \gamma_I B$ is the nuclear Zeeman interaction (the 'z' subscript is superfluous because the interaction is considered isotropic here),
- a is the isotropic Fermi-Contact interaction,
- t is related to the dipolar hyperfine interaction tensor as follows:

$$\mathbf{A}_{dip} = \begin{pmatrix} t & & \\ & t & \\ & & -2t \end{pmatrix} \hbar^{-2} \tag{1.80}$$

  which is clearly aligned with the **g**-tensor axes.

The eigenvalues and eigenvectors of this spin system are therefore given by:

$$\begin{aligned} |1\rangle &= |\beta\beta\rangle & E_1 &= \frac{a}{4} - \frac{t}{2} - \frac{1}{2}(\gamma_z + \beta_z) \\ |2\rangle &= \sin\xi|\alpha\beta\rangle + \cos\xi|\beta\alpha\rangle & E_2 &= -\frac{a}{4} + \frac{t}{2} - \frac{1}{2}\sqrt{(a+t)^2 + (\gamma_z - \beta_z)^2} \\ |3\rangle &= \cos\xi|\alpha\beta\rangle - \sin\xi|\beta\alpha\rangle & E_3 &= -\frac{a}{4} + \frac{t}{2} + \frac{1}{2}\sqrt{(a+t)^2 + (\gamma_z - \beta_z)^2} \\ |4\rangle &= |\alpha\alpha\rangle & E_4 &= \frac{a}{4} - \frac{t}{2} + \frac{1}{2}(\gamma_z + \beta_z) \end{aligned}$$

where the variable ξ is defined according to:

$$\tan\xi = \frac{\gamma_z - \beta_z}{a+t} - \sqrt{1 + \left(\frac{\gamma_z - \beta_z}{a+t}\right)^2} \tag{1.81}$$

The energies as well as the $\sin\xi$ and $\cos\xi$ coefficients are plotted in figure 1.4. The behaviour of the eigenstates and energies of this spin system can now be analysed by considering the following limiting situations:

$$\underbrace{\frac{\gamma_z - \beta_z}{a+t} \to 0}_{\text{zero-field/ strong coupling}} \quad , \quad \underbrace{\frac{\gamma_z - \beta_z}{a+t} \to \infty}_{\text{high-field/weak coupling}} \tag{1.82}$$

As indicated, these two limits can be approached either by an increase/decrease of the net Fermi-Contact and dipolar hyperfine coupling, $(a + t)$, or of the difference between the electron and nuclear Zeeman interactions. [23]

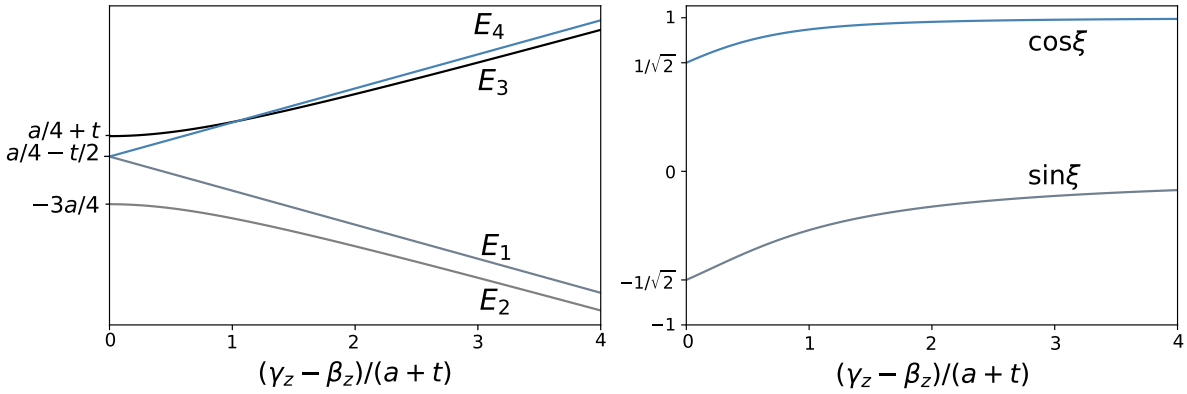


Figure 1.4: (Left) The energy levels as a function of magnetic field strength for a spin system comprised of an electron and a nucleus with spin 1/2. The field axis is scaled by the net hyperfine interaction $(a+t)$ in order to emphasize the emergence of the low-field/strong coupling and high-field/weak coupling limits. (Right) The coefficients of the $|\alpha\beta\rangle$ and $|\beta\alpha\rangle$ states within the true eigenstates $|2\rangle$ and $|3\rangle$ of the system. Note the collapse of these states to the coupled and uncoupled representations in the strong and weak coupling limits, respectively.

By consulting the left panel of figure 1.4 and the equations above, we note that in the zero-field/ strong coupling limit, states $|1\rangle$ and $|4\rangle$ are degenerate. As the magnetic field increases, the degeneracy is lifted and the energy difference between them is a linear function of the field strength. Furthermore, states $|1\rangle$ and $|4\rangle$ remain equal to $|\beta\beta\rangle$ and $|\alpha\alpha\rangle$, respectively, throughout the entire range (including in the high-field/weak coupling limit). These states can also be labelled $|T_-\rangle$ and $|T_+\rangle$, which correspond to the electron-nuclear triplet sub-levels. It is therefore clear that the behaviour of these two states is well defined and easily characterised regardless of the strength of the hyperfine coupling or magnetic field.

By contrast, the behaviour of states $|2\rangle$ and $|3\rangle$ is more complicated. In the zero-field/strong coupling limit they are not degenerate, they have an energy splitting of $(a + t)$, which corresponds to the net Fermi-Contact and dipolar hyperfine coupling. Furthermore, the coefficients of the eigenstates in the zero-field limit imply that states $|2\rangle$ and $|3\rangle$ are equivalent to the coupled electron-nuclear singlet and triplet states:

$$|2\rangle \xrightarrow{\frac{\gamma_z - \beta_z}{a+t} \to 0} \frac{1}{\sqrt{2}}(|\beta\alpha\rangle - |\alpha\beta\rangle) \equiv |S\rangle$$

$$|3\rangle \xrightarrow{\frac{\gamma_z - \beta_z}{a+t} \to 0} \frac{1}{\sqrt{2}}(|\beta\alpha\rangle + |\alpha\beta\rangle) \equiv |T_0\rangle$$

As the field increases and the high-field limit is approached, the energies of the states become linear with field strength. Furthermore, in the high-field/weak coupling limit, states $|2\rangle$ and $|3\rangle$ collapse to

[23] Since, the gyromagnetic ratio of electrons is much larger than for nuclei, $(\gamma_z - \beta_z)$ is often approximated to γ_z.

the uncoupled representation:

$$|2\rangle \xrightarrow{\frac{\gamma_z - \beta_z}{a + t} \to \infty} |\beta\alpha\rangle$$

$$|3\rangle \xrightarrow{\frac{\gamma_z - \beta_z}{a + t} \to \infty} |\alpha\beta\rangle$$

This analysis has important consequences for our understanding of the electron-nuclear spin system. In the zero-field/strong coupling limit, it is not suitable to consider the electron and nucleus as two separate entities with separate spin, but rather a coherent superposition of the $|\beta\alpha\rangle/|\alpha\beta\rangle$ electron-nuclear spin states. In the high-field/weak coupling limit, the Zeeman interaction dominates and both spins are quantized along the field axis, whilst the hyperfine field provides only a minor perturbation to the net magnetic field experienced by the spins. As can be seen in figure 1.4, this perturbation leads to a constant energy difference between the $|1\rangle/|2\rangle$ and $|3\rangle/|4\rangle$ pairs of states.

Finally, it is worth mentioning that between these two limits, the behaviour of the spin system is ever-changing and difficult to describe. More precisely, the energies of $|2\rangle$ and $|3\rangle$ are non-linear functions of the magnetic field, and the states themselves cannot be identified with either the coupled or uncoupled representation. In this intermediate regime, the states can cross in energy (*e.g.* in figure 1.4, states $|3\rangle$ and $|4\rangle$ cross each other near the point where $\gamma_z - \beta_z \approx a + t$) and as a result, there can be accidental degeneracy (*i.e.* a true crossing rather than an avoided crossing caused by symmetry). Whilst not encountered in the present work, all of these effects have the potential to complicate the assignment and interpretation of EPR data.

1.3 Continuous-wave EPR

Consider a general spin system whose energy levels and quantum states are dictated by a spin Hamiltonian, $\hat{H}$, of the type shown in equation 1.22. Usually, the strongest of the many possible interactions in $\hat{H}$ is the EZ interaction, which by definition is linearly dependent on the strength of the applied magnetic field. In EPR, the magnetic fields typically employed are of the order of 10^{-3}–1 T and thus, the energy separations of the electron spin states are covered by the microwave region of the electromagnetic spectrum (1 – 100 GHz).

Many schemes can be conceptualised for the detection of transitions between the eigenstates of $\hat{H}$. By far the most popular and easily implemented continuous-wave EPR (cwEPR) detection scheme involves using a fixed microwave frequency and a variable magnetic field strength. As the field is swept, the energy differences between certain pairs of states will match the input microwave energy, and hence, a transition will be observed between these states *i.e.* resonance occurs. The resulting spectrum will consist of peaks centred at *resonance fields* which depend on the microwave frequency and the spin Hamiltonian parameters.

1.3.1 Acquisition and instrumentation

Reference [8] contains a detailed survey of the aspects of cwEPR instrumentation which are most pertinent to this thesis, and it forms the basis for this section. The discussion will proceed with a description of the simplified diagram for a cwEPR spectrometer, depicted in figure 1.5.

Many complications related to the delivery of microwaves and the detection of signals are resolved by inserting the paramagnetic sample into a resonator. The microwaves are directed from the source (*e.g.* a Gunn diode with a slightly variable frequency and fixed power) to the resonator *via* a power attenuator and a waveguide. The microwaves entering the resonator are then reflected back into the waveguide, they pass through a circulator which directs the output to a detector diode (the circulator also prevents the microwaves returning to the source). At the detector diode, the incoming signal from the resonator is compared with the microwave radiation from the source (which arrives at the diode *via* the so-called 'reference arm').[24] This acquisition method is in many ways akin to the usual scheme employed in routine UV-vis measurements *except* for the presence of the resonator.

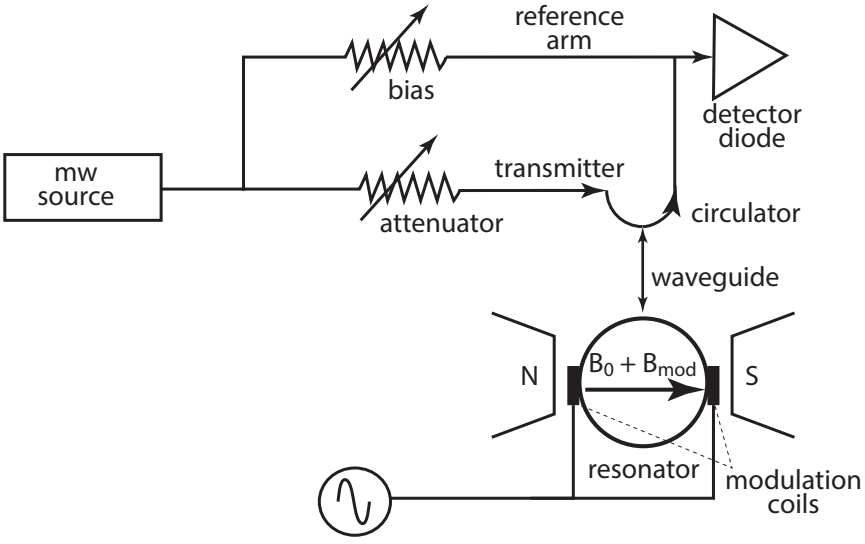


Figure 1.5: Simplified scheme of a continuous-wave EPR spectrometer. The sample is placed inside a resonator cavity which is coupled to the transmitter arm of the mw source by means of a circulator and waveguide. After being reflected from the resonator, the microwaves are directed by the circulator to the detector diode. The sample experiences both a static magnetic field, $\mathbf{B}_0$, as well as a modulated magnetic field, $\mathbf{B}_{\text{mod}} = B_{\text{mod}} \sin \omega_{\text{mod}} t$, which is parallel to $\mathbf{B}_0$. The magnetic component of the microwave radiation (not shown) is perpendicular to the external magnetic field ($\mathbf{B}_0 + \mathbf{B}_{\text{mod}}$). The microwaves from the source are also passed to the detector diode where they are used as a reference signal.

In one of its simplest implementations, the resonator is simply a metallic cavity. The shape of the cavity is designed to perform the following tasks: ensure maximum microwave power delivery to the sample, minimise the electric component and maximise the magnetic component of the microwaves at the center of the sample, and minimise the effects of small fluctuations in the incident microwave frequency. However, the mere presence of a resonator is not sufficient for a successful EPR measurement. Before

[24] The reference arm is also necessary to ensure that the detector diode is operating at its optimal current level both in the presence and absence of signals from the resonator. The spectrometer user can adjust both the phase and power (bias) of the reference arm in order to match it with the power and phase of the microwaves leaving the resonator.

a spectrum can be acquired, a careful tuning procedure is performed which ensures the microwave source, the resonator, and the detector diode are all working together optimally. Many of the concepts and intricacies involved in the spectrometer tuning procedure can be understood by analogy with the physics of two inductively coupled resonant circuits, as explained in reference [8]. In short, one of the primary aims of the tuning procedure is to optimise the quality factor, Q, of the cavity, which determines the efficiency with which microwave power can be delivered to the sample. In essence, as the Q-value becomes larger, the sensitivity of the spectrometer increases.

In spite of the efforts to optimise the delivery and detection of microwaves by using resonators, sources of noise are unavoidable in the laboratory. Hence, there is another essential set of components in the cwEPR detection scheme illustrated in figure 1.5, namely the field modulation coils. These modulation coils dramatically increase the sensitivity of the spectrometer by a process called *phase-sensitive detection*. In essence, rather than simply sweeping the external magnetic field linearly over the course of a scan, the field strength is also modulated sinusoidally at a fixed frequency[25] and user-defined amplitude.[26] As a resonance is passed, and provided that the modulation amplitude was suitably chosen, the EPR signal intensity will also oscillate at the modulation frequency. Therefore, by mixing the incoming modulated signals with a reference, noise which oscillates at a different frequency to the signal is filtered out of the final spectrum. In principle, the phase of the field modulation also needs to be optimised, however, in most cases, it can be calibrated with a standard EPR sample and kept the same for other samples.

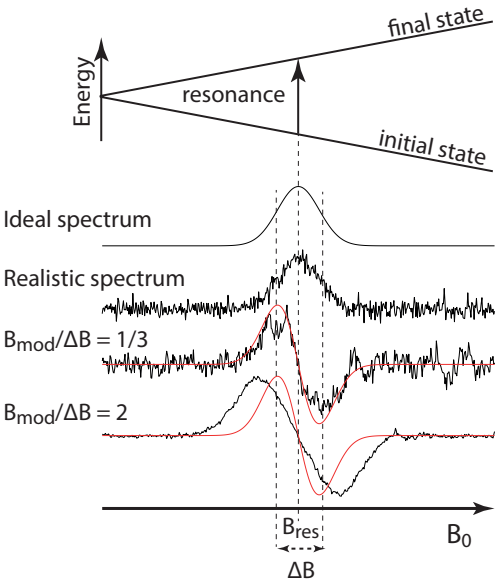


Figure 1.6: The field dependence of the energy levels for a pair of states undergoing a transition is shown in the top diagram. An ideal EPR spectrum for this resonance is shown below as a Gaussian centred at B_{res} with a width ΔB. The realistic spectrum is obtained by adding artificial noise (using the *rand* function in MATLAB) to the ideal spectrum. The remaining two spectra show the effects of modulation at two different values of B_{mod} relative to the linewidth ΔB (obtained using the *fieldmod* function of the EasySpin package [9]). However, when the modulation amplitude is greater than the width of the spectrum, significant deviations from the true derivative line-shape (shown in red) are expected. Generally, the noise level is reduced by field modulation (albeit, it is still rather significant if the modulation amplitude is small).

[25] In this thesis, a modulation frequency of exclusively 100 kHz is used.
[26] Of the order of a few millitesla or tenths of millitesla.

Another important aspect of phase-sensitive detection is that, if the modulation amplitude is sufficiently small, the intensity of the modulated signal at a particular field point will be a very good approximation of the derivative of the EPR signal at that field point. This all-essential field modulation is hence the reason why cwEPR spectra are measured in 'derivative mode'. On the other hand, if the modulation amplitude is too large, it leads to significant distortions from the exact derivative line-shape, and the interpretation of the cwEPR spectra will be compromised. As a rule-of-thumb, figure 1.6 shows that a good starting point for the modulation amplitude is 1/3 of the width of the narrowest feature in the spectrum. Of course, this information about the narrowest feature is typically unavailable before an initial 'rough' spectrum is acquired. After such a spectrum is available, the modulation amplitude can be adjusted until the widths of the narrowest features remain constant. Often, a compromise has to be made because lower modulation amplitudes lead to noisier spectra (and thus, more scans have to be accumulated). Apart from the Q-factor of the resonator which needs to be optimised for maximum sensitivity, the optimisation of the modulation amplitude is critical in cases where the line-shape/line-width of EPR spectra needs to be interpreted. Such considerations have proven to be paramount for the acquisition and analysis of the data presented in Chapter 2 of this thesis.

Finally, it is important to mention at this stage that (apart from a number of modifications) a typical cwEPR spectrometer can also be used to detect short lived signals, such as the transient triplet states formed by photo-excitation of organic chromophores. Since it is at the heart of the majority of projects in this thesis, the transient EPR technique will be presented in greater detail in Chapter 3.

1.3.2 Peak intensities, selection rules, and linewidths

Up to this point, it has been established that an EPR transition can occur when the resonance condition is satisfied, and a summary of the sort of equipment required to detect this phenomenon was also given. The field positions at which the energy differences between the eigenstates of the system match the microwave frequency are dictated exclusively by the spin Hamiltonian. However, the resonance condition is not sufficient to completely understand the resulting cwEPR spectra. In short, transitions do not all have the same probability of occurring. As is customary in spectroscopy, some transitions are said to be *allowed* and some transitions are *forbidden* as dictated by a set of *selection rules*.

Even more generally, each transition, or peak in an EPR spectrum, has an intensity which is dictated by many factors. These factors are at play both within the microscopic world governed by the quantum mechanical spin Hamiltonian, but also in the macroscopic world governed by the thermodynamic properties of the sample. A discussion of these two aspects is the focus of this section.

The quantum origin of peak intensities. Almost always, before microwave radiation is applied, the quantum system will be found in one of the eigenstates of the spin Hamiltonian:[27]

$$\hat{H}(\mathbf{B}_0)|n\rangle = E_n|n\rangle \tag{1.83}$$

We are only considering a single total electronic spin, with quantum numbers S and M, in a magnetic

[27] As for the entire ensemble consisting of *many* spin systems, each of them will be found in a different one of these eigenstates with an overall distribution dictated by statistical thermodynamics.

field, written as $\mathbf{B}_0$. Before radiation is applied, the time-dependence of the states is governed by:

$$|n\rangle(t) = e^{-iE_M t/\hbar}|n\rangle(t=0) \tag{1.84}$$

i.e. the system is in a stationary state. When microwave radiation is applied, the above Hamiltonian will be supplemented by the time-dependent interaction between the magnetic component of the radiation, $\mathbf{B}_1(t)$, and the electronic spin:

$$\hat{V}(t) = \frac{\mu_B}{\hbar}\mathbf{B}_1(t)\cdot\mathbf{g}\cdot\hat{\mathbf{S}} = \frac{\mu_B}{\hbar}\mathbf{B}_1\cdot\mathbf{g}\cdot\hat{\mathbf{S}}\cos(\omega t) = \hat{V}\cos(\omega t) \tag{1.85}$$

By design, for most cwEPR resonators, and certainly for the ones used in this work, the $\mathbf{B}_1(t)$ field is linearly polarised, perpendicular to $\mathbf{B}_0$ at all times, and oscillating at frequency ω. Under these conditions, and assuming that $|\mathbf{B}_1(t)| \ll |\mathbf{B}_0|$, the probability of a transition from an initial state, $|i\rangle$, to a final state, $|f\rangle$, can be calculated using Fermi's Golden rule according to:

$$\tilde{P}_{i\to f} \sim |\langle f|\hat{V}|i\rangle|^2 \mathcal{L}_\lambda(\Omega) \tag{1.86}$$

where $\Omega = \omega_0 - \omega$ is the offset frequency *i.e.* the difference between the spectrometer frequency and the frequency corresponding to the energy gap between the initial and final states, $E_f - E_i = \hbar\omega_0$ (the resonant frequency). The function $\mathcal{L}_\lambda(\Omega)$ can be either a Gaussian or Lorentzian function centred at $\Omega = 0$ with a width λ:[28]

$$\mathcal{L}_\lambda(\Omega) = \begin{cases} \sqrt{\frac{2}{\pi}}\frac{1}{\lambda}\exp\left[-2\left(\frac{\Omega}{\lambda}\right)^2\right] \\ \frac{2}{\pi\sqrt{3}}\frac{1}{\lambda}\left[1+\frac{4}{3}\left(\frac{\Omega}{\lambda}\right)^2\right]^{-1} \end{cases} \tag{1.87}$$

Equation 1.86 implies, first of all, that the maximum transition probability occurs when the resonance condition is satisfied, as mentioned before. However, it shows that this maximum in intensity will also depend on the nature of the initial and final states due the coupling matrix element of the $\hat{V}$ operator. Finally, the presence of a Lorentzian or Gaussian broadening rather than Dirac's delta function (which would be expected for an infinitely long perturbation) is a result of factors such as spin-spin and spin-lattice relaxation as well as small unresolved hyperfine couplings. Reference [10] contains a comprehensive overview into the origins of the inherent linewidth.

Selection rules. Whilst the $\mathcal{L}_\lambda(\Omega)$ part of equation 1.86 is responsible for the broadening of the peaks in the EPR spectrum, the matrix element $\langle f|\hat{V}|i\rangle$ is responsible for the intensity of the peaks. In this subsection, the most general possible statement of the EPR selection rules for systems with a single total electron spin, S, will be derived. If more than one electron spin is present in the total spin system, selection rules can still be derived, but the expression for $\hat{V}$ would have to be adapted to include all the relevant interactions with the microwave field.[29]

The derivation starts by expanding the dot product of the perturbation matrix element in the spherical

[28] Taken between the inflection points

[29] Also note that throughout this section, we have neglected completely the interactions between the nuclear spins and the $\mathbf{B}_1$ field. This is not problematic; nuclear spins interact very weakly with microwaves. In other words, nuclear transitions cannot be induced with the same radiation frequencies as used for electrons.

basis, $q = -1, 0, +1$:

$$\langle f|\hat{V}|i\rangle = \frac{\mu_B}{\hbar}\sum_q B_{1,-q} g_q \langle f|\hat{S}_q|i\rangle \tag{1.88}$$

The reference frame for this expansion is chosen to be the eigenframe of the **g**-tensor. This choice of eigenframe has no consequence for the statement of the selection rules, these are independent of the frames of the tensors and orientation of the spin system.

Now, the final and initial states, $|f\rangle$ and $|i\rangle$ are expanded into their corresponding linear superpositions of the $|SM\rangle$ basis:

$$\langle f|\hat{V}|i\rangle = \frac{\mu_B}{\hbar}\sum_q \sum_{M,M'} c^*_{fM'} c_{iM} B_{1,-q} g_q \langle SM'|\hat{S}_q|SM\rangle \tag{1.89}$$

This particular choice of basis is due to the fact that selection rules are typically stated with regards to the M quantum number. The final step in the derivation is the application of the Wigner-Eckart theorem:

$$\langle f|\hat{V}|i\rangle = \frac{\mu_B}{\hbar}\sum_q \sum_{M,M'} c^*_{fM'} c_{iM} B_{1,-q} g_q \langle SM1q|SM'\rangle\langle S||\hat{\mathbf{S}}||S\rangle \tag{1.90}$$

By evaluation of the reduced matrix element (using a retro-active application of the Wigner-Eckart theorem) the result is:

$$\langle f|\hat{V}|i\rangle = \mu_B\sqrt{S(S+1)}\sum_q \sum_{M,M'} c^*_{fM'} c_{iM} B_{1,-q} g_q \langle SM1q|SM'\rangle \tag{1.91}$$

And hence, the most general statement of the EPR selection rules for spin systems with a single total electronic spin is:

$$c^*_{fM'} c_{iM} B_{1,-q} \neq 0 \tag{1.92}$$

$$\Delta M = M' - M = q \tag{1.93}$$

In other words, if the microwave field is non-zero, the initial and final states must have at least one common pair of non-zero coefficients corresponding to magnetic quantum numbers which are either the same or different by at least one unit. The fact that, in certain situations, ΔM can be equal to zero is not usually recognized in many introductory EPR textbooks. The reason for neglecting this selection rule is because, in most cases, the states can usually be approximated by the eigenstates of $\hat{S}_z$. For example, in the high-field limit for a triplet state with non-zero D and E, or for the electron-nucleus system described in the previous sections, the initial and final states have a well defined magnetic quantum number (M and M'). Since transitions occur between different states, M must be different to M', and thus, only the $\Delta M = \pm 1$ selection rule is necessary. The selection rules in 1.92 and 1.93 are completely general: they apply to any single spin system, with any orientation with respect the microwave field, and even if M is not a good quantum number *i.e.* if the eigenstates are some linear superposition of $|SM\rangle$ basis states.

To see the emergence of the more usual selection rule, some approximations need to be applied to equation 1.89. Consider the case where the static external magnetic field is defined as the z-axis *i.e.* the Zeeman interaction is a term of the form $\hat{H}_{EZ} = \frac{\mu_B}{\hbar} g_z B \hat{S}_z$. If the high-field limit is also assumed, *i.e.* $\hat{H}_{EZ}$ is larger than all other interactions in the spin Hamiltonian, then the initial and final states in equation 1.89 are eigenstates of $\hat{S}_z$ and hence, M and M' are good quantum numbers. Furthermore, in this case,

the microwave B_1 field is perpendicular to the external magnetic field (suppose it is along the x-axis) and hence, equation 1.89 reduces to:

$$\langle M'|\hat{V}|M\rangle = \frac{\mu_B}{\hbar} B_{1,x} g_x \langle SM'|\hat{S}_x|SM\rangle = \frac{\mu_B}{\hbar} B_{1,x} g_x \frac{1}{2} \langle SM'|\hat{S}_+ + \hat{S}_-|SM\rangle \tag{1.94}$$

and hence, in this drastically simplified spin system, the well-known $\Delta M = \pm 1$ selection rule is fully applicable.[30]

The macroscopic origin of peak intensities. Apart from the requirements imposed by quantum mechanics on the feasibility of a transition (via equation 1.86), there are also thermodynamic requirements. The most important of these is that, within a macroscopic ensemble, the number of quantum systems in the initial state is different to the number of systems in the final state *i.e.* a population difference is required. Furthermore, the microwave power delivered to the resonator containing the sample must be carefully adjusted to avoid the saturation of the population difference in the time taken to observe the transition. All of these factors can be summarised in the following expression:

$$I \propto \Delta N_{if} P_{i \rightarrow f} \sqrt{P_{mw}} \tag{1.95}$$

which is the familiar result that, under non-saturating conditions, the EPR signal is (tri-)linear in the population difference, ΔN_{if}, quantum intensity, $P_{i \rightarrow f}$, and square root of the microwave power, $\sqrt{P_{mw}}$. For a sample in thermal equilibrium with the surroundings, the population difference can be calculated from the Boltzmann distribution:

$$\Delta N_{if} = (N_i - N_f) \propto \exp\left(-\frac{E_i}{kT}\right) - \exp\left(-\frac{E_f}{kT}\right) \tag{1.96}$$

Strictly speaking, the dependence on $\sqrt{P_{mw}}$ is already encapsulated by the formula for the quantum intensity by means of the dependence on B_1. Due to this fact, the $P_{i \rightarrow f}$ term in equation should be considered as being normalised by the magnitude of the microwave magnetic field strength.

Linewidths in field domain and the '$1/g$ factor'. It was noted in a previous section that the average quantum intensity is given by equation 1.86. Based on this expression one can write the formula for the EPR spectrum of a particular pair of states as:

$$S_{fi}(\Omega) = |\langle f|\hat{V}|i\rangle|^2 \mathcal{L}_\lambda(\Omega) \tag{1.97}$$

However, this equation for $S_{fi}(\Omega)$ is only applicable in the frequency domain *i.e.* it is applicable to frequency-swept cwEPR spectra. Since in this thesis (and in the great majority of EPR research), cwEPR spectra are acquired in field domain, the above formulation of the inherent line-widths needs to be

[30] Note that the famous $\Delta M = \pm 1$ selection rule is not in contradiction with the general selection rules in equations 1.92 and 1.93. The latter two become equivalent to $\Delta M = \pm 1$, if we assume that: $c^*_{fM'} c_{iM} \neq 0$ if and only if $M' \neq M$ *i.e.* if we assume that transitions always occur between pure states (eigenstates of $\hat{S}_z$).

adapted. After performing the conversion to field domain, the EPR spectrum will be given by [11, 12]:

$$S_{fi}(B) = \underbrace{\left[\left(\frac{\partial\omega_0}{\partial B}\right)_{\text{res}}\right]^{-1}}_{\gamma_0} |\langle f|\hat{V}|i\rangle|^2 \mathcal{L}_{\lambda'}(B) \tag{1.98}$$

where the so-called 'generalised $1/g$ factor' has been defined as γ_0 and the inherent linewidth in field domain is given by:

$$\lambda' = \left[\left(\frac{\partial\omega_{fi}}{\partial B}\right)_{\text{res}}\right]^{-1} \lambda \tag{1.99}$$

First of all, it can be seen that the linewidth in field domain is different to the linewidth in frequency domain. Of course, if EPR spectra are only acquired and analysed in field domain, this effect is irrelevant because the field domain linewidth can be used directly (by least-squares fitting for example). However, if the spectra need to be converted to frequency domain (say, for analysis purposes), then care needs to be taken to adapt the linewidth correctly.

Secondly, and more importantly, the intensity of an EPR transition also contains an additional factor, namely γ_0. The reason it is called 'the $1/g$ factor' is because, the derivatives of energy differences (recall that $\omega_0 = \frac{E_f - E_i}{\hbar}$) with respect to the magnetic field are proportional to the $\mathbf{g}$-tensor. This means that the $1/g$ contribution to the peak intensity is, generally speaking, anisotropic. In simple spin systems, with isotropic g-values, the term is given by:

$$\gamma_0 = \frac{\hbar}{\mu_B g_{\text{iso}}} \tag{1.100}$$

And therefore, this term becomes a constant multiplicative factor, and in these particular instances, can be neglected.

1.3.3 Spectral simulations

Nowadays, EPR spectroscopists have at their disposal a myriad of computational techniques to aid both with data analysis and parameter interpretation/quantification. Since a significant part of the present work has been to further the development of some of these techniques, a brief survey of some of the simulation methods employed in EPR spectroscopy is required. The focus will be on those aspects which are most applicable to this thesis. In particular, many of the simulations in the next chapters have been facilitated by the EasySpin package, a MATLAB toolbox for simulating EPR spectra [9]. Therefore, an outline of the relevant EasySpin functions will be given at various points throughout the following sections. A detailed description of the inner workings of this toolbox, can be found in the main EasySpin package reference [9] and references therein.

Isotropic EPR spectra. The first types of EPR spectra which will be discussed in detail in this thesis are those of spin 1/2 radicals in liquid solution (Chapter 2). If the tumbling motion of the radicals in solution is faster than the EPR time-scale (*e.g.* 1 ns) then it is said that the system is in the *isotropic regime*. This means that the EPR spectrum of a $S = 1/2$ radical coupled to a nucleus with spin quantum number I will be parametrised by the following spin Hamiltonian:

$$\hat{H} = \gamma_S B\hat{S}_z - \gamma_I B\hat{I}_z + a\hat{\mathbf{S}} \cdot \hat{\mathbf{I}} \tag{1.101}$$

where $\gamma_S = \frac{\mu_B g}{\hbar}$ and γ_I are the gyromagnetic ratios of the electron and nucleus, respectively.[31] As sketched in Appendix B, the eigenvalues of equation 1.101 can be shown to be given by the so-called Breit-Rabi equation:

$$E(\pm, m_F) = -\frac{a\hbar^2}{4} - \gamma_I B\hbar m_F \pm (I + 1/2)\frac{a\hbar^2}{2}\sqrt{1 + \frac{2m_F}{I + 1/2}\kappa + \kappa^2} \tag{1.102}$$

The corresponding eigenvectors are:

$$|+, m_F\rangle = \sin\theta|-\frac{1}{2}, m_F + \frac{1}{2}\rangle + \cos\theta|+\frac{1}{2}, m_F - \frac{1}{2}\rangle \tag{1.103}$$

$$|-, m_F\rangle = \cos\theta|-\frac{1}{2}, m_F + \frac{1}{2}\rangle - \sin\theta|+\frac{1}{2}, m_F - \frac{1}{2}\rangle \tag{1.104}$$

In equations 1.102 to 1.104 the following quantities have also been defined:

$$m_F = m_I + m_S \tag{1.105}$$

$$\kappa = \frac{\gamma_S B + \gamma_I B}{a\hbar} \tag{1.106}$$

$$\tan 2\theta = \frac{\kappa + \dfrac{m_F}{I + 1/2}}{\sqrt{1 - \left(\dfrac{m_F}{I + 1/2}\right)^2}} \tag{1.107}$$

The Breit-Rabi equation is exact and, in principle, it can be used directly in numerical simulations to obtain the resonance fields for a given spectrometer frequency, ν. In practice, however, the Breit-Rabi equation is rarely used in its exact form (1.102), because it only applies to the coupling between a single electron and a single nucleus. The approach taken in the EasySpin toolbox is to apply a fixed-point iteration to find the exact resonance fields predicted by the Breit-Rabi equation (see references [9, 13] and Appendix B). The starting point for the iteration is set equal to the solution of the Breit-Rabi resonance field by neglecting the nuclear Zeeman interaction. This iteration scheme is employed in the function *garlic* in EasySpin which will be used in Chapter 3 of this thesis. It is a valid approach to finding the resonance fields if the hyperfine couplings are significantly smaller than the microwave frequency (which is the equivalent of the high-field limit in frequency swept spectra).

Whilst the fixed-point iteration is invaluable in numerical simulations, there are some approximations which can significantly simplify the interpretation and analysis of cwEPR spectra. Consider again the same spin system as equation 1.101. If the nuclear Zeeman interaction is neglected[32], and if it is assumed that the hyperfine coupling is much smaller than the electron Zeeman interaction, then first-order perturbation theory can be used. In this case, the zero-order unperturbed states are given by the uncoupled $|m_S, m_I\rangle$ basis with the following energy:

$$\hat{H}^{(0)}|m_S, m_I\rangle = \gamma_S B\hat{S}_z|m_S, m_I\rangle = E^{(0)}_{m_S,m_I}|m_S, m_I\rangle = m_S\gamma_S\hbar B|m_S, m_I\rangle \tag{1.108}$$

If these states are then perturbed with the hyperfine coupling, the first-order correction to the energies

[31] In units of $\mathrm{J{\cdot}T^{-1}}/\hbar$ because all the spin operators in this thesis are in SI units. Also, the hyperfine coupling in this equation is in units of $\mathrm{J{\cdot}}\hbar^{-2}$.

[32] For example, the gyromagnetic ratio of a proton is three orders of magnitude smaller than for an electron.

is obtained as:

$$E^{(1)}_{m_S,m_I} = m_S\gamma_S\hbar B + a\hbar^2 m_S m_I \tag{1.109}$$

And hence, to this order in perturbation theory, the effect of the hyperfine coupling is to lift the m_I degeneracy of a given m_S state. Since EPR transitions are driven mainly by the interaction between the electronic spin and the B_1 field, the $\Delta m_S = \pm 1$ and $\Delta m_I = 0$ selection rule is valid to this order in perturbation theory. Hence, the EPR spectrum will consist of $(2I + 1)$ lines (one for each allowed value of m_I) of equal intensity. In field domain, the lines will be centred at $\nu/2\pi\gamma_S$ and neighbouring lines will be separated by $\hbar a/\gamma_S$.

It can also be shown relatively easily that: if there are n nuclei with spin I, then the spectrum will consist of $(2nI + 1)$ equally spaced lines (separated by $\hbar a/\gamma_S$) with intensities given by the $(2I + 1)$ multinomial coefficient. For example, if $I = 1/2$ and $n = 2$, there are 3 lines with binomial intensities $(1 : 2 : 1)$. Some of the properties of multinomial spectra will be explored in more detail in Chapter 2.

Solid state EPR spectra. The second category of EPR spectra relevant to this work are those of paramagnetic molecules in a frozen solution. In this case, the anisotropy of all the parameters in the spin Hamiltonian will be resolved and there is almost no method by which one can avoid directly diagonalising the spin Hamiltonian. Anisotropy is resolved due to the fact that every orientation of the paramagnetic center relative to the applied magnetic field will give rise to a different EPR sub-spectrum; the final EPR spectrum is a sum of these sub-spectra. As an example, figure 1.7 shows the solid state cwEPR spectra of a fictitious spin system with an anisotropic **g**-tensor. In this thesis, we will consider the frozen solution cwEPR spectra of photogenerated triplet states and spin-correlated radical pairs. The particulars pertaining to these specific spin systems will be discussed at the appropriate point.

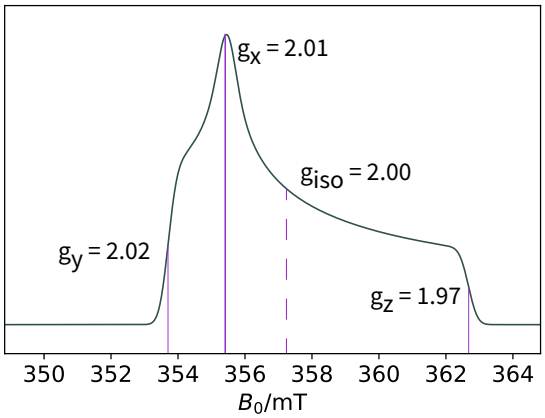


Figure 1.7: Example simulation of a spin system with an anisotropic **g**-tensor. The simulation was obtained using the function *pepper* for a microwave frequency of 10 GHz. The vertical lines show the positions corresponding to the three eigenvalues of the g-tensor as well as the isotropic value of $g_{iso} = (g_x + g_y + g_z)/3$.

Generally, the energies and eigenstates of a spin system depend on the magnitude of the magnetic field B, and its orientation (with respect to some reference frame) defined by the polar angles θ and ϕ. More formally:

$$\hat{H}(B,\theta,\phi)|n\rangle = E_n(B,\theta,\phi)|n\rangle \quad \text{where} \quad |n\rangle = \sum c_{nu}(B,\theta,\phi)|u\rangle \tag{1.110}$$

where the expansion of the eigenstates can be in performed in whichever basis is most convenient; most commonly, the completely uncoupled basis is chosen ($|u\rangle$ will be labelled by all the magnetic quantum numbers of all the electron and nuclear spins).

Conceptually, the simplest approach to solid state simulations would be to diagonalise the Hamiltonian on a three dimensional grid, (B, θ, ϕ), find pairs of states which satisfy the resonance condition, and calculate the intensity of the transition to obtain a complete set of sub-spectra. Despite the fact that such an algorithm is accurate in principle, it is rarely implemented. The reason for this is that it suffers from a dramatic computational 'bottleneck': the spin Hamiltonian is diagonalized for every magnitude and orientation of the magnetic field vector on a pre-defined grid. Not only would a sufficiently fine grid be required to obtain reliable results, for most combinations (B, θ, ϕ) the spin system is not on-resonance *i.e.* this algorithm performs many unnecessary (and slow) steps.

For standard frozen solution cwEPR spectra, the shortcomings of the above simple algorithm are circumvented in the function *pepper* of the EasySpin package. In many instances throughout this thesis, *pepper* will be used to extract the spin Hamiltonian parameters. However, as will be seen, in certain applications, such as magneto-photo-selection or spin-correlated radical pairs, the function *pepper* cannot be used to simulate the cwEPR spectra. For such cases, the development of simulation scripts has been an integral part of the research carried out in this thesis. Nonetheless, the algorithms developed in this work are either inspired by or directly employ some of the sub-routines of *pepper*. The original work of Stoll and Schweiger in reference [9] provides a detailed description of this function.

One of the central sub-routines within *pepper*, which is also invaluable for the present work, is the function *resfields*. In this function, for a given orientation of the magnetic field, the resonance fields are extracted from the spin system using the smallest possible number of diagonalisation steps. This is achieved using an adaptive searching algorithm [14].

To illustrate more clearly the methodology behind *resfields*, a vastly simplified but functional version of the original algorithm presented in reference [14] is provided in Appendix C as a Python script. The programs contained in Appendix C show how the resonance fields for an $S = 1$ spin system can be calculated using the adaptive procedure employed by EasySpin and the scripts can readily be extended to any arbitrary spin system. Whilst the programs in Appendix C are useful as an introduction to the principles of EPR simulations, they are not as general or optimised as the *resfields* function in EasySpin. However, these programs do encapsulate the fundamental building blocks of *resfields* and therefore can be used either for didactic purposes, or as a starting point for non-MATLAB based simulation scripts.[33]

1.4 Pulse EPR

The terminology 'pulse EPR' refers to a large number of specialised techniques aimed at disentangling the many possible interactions encompassed by the spin Hamiltonian as well as the interactions between the spin system and the environment. The building blocks of a pulse EPR experiment are microwave pulses which are applied in a well defined order and at precisely specified times. The resulting pulse sequences are most often designed with the aim of isolating a particular type of interaction (*e.g.* small unresolved hyperfine couplings). By contrast, in a cwEPR spectrum, all the possible interactions

[33] For instance, by universities around the world where, for various reasons, a MATLAB licence is not available.

are measured at once, and disentangled by simulation (which is not always trivial or even possible).[34]

Two types of pulse EPR experiments are directly relevant for this thesis: Electron Nuclear Double Resonance (ENDOR) and out-of-phase Electron Spin Echo Envelope Modulation (oopESEEM). The later will be described in detail in the final chapter, when the topic of spin-correlated radical pairs is considered in earnest. Since the former is necessary throughout the entire thesis, it will be presented at the end of this section. Before, however, a brief overview of pulse EPR instrumentation will be given, based on reference [15], together with the description of the effects of microwave pulses on spin systems.

1.4.1 Acquisition and instrumentation

There are a number of modifications to the spectrometer scheme depicted in figure 1.3 which allow pulse EPR experiments to be carried out. In the first instance, the microwave radiation from the source is directed to a pulse forming unit (PFU). The PFU is interfaced with the control computer and allows the design of pulse sequences composed of user specified pulse durations, pulse phases and powers, as well as inter-pulse delays.

Microwave pulse lengths can range from a few nanoseconds to a few microseconds. The duration of a pulse is chosen with two criteria in mind: to achieve a desired flip angle within the limitations of the available microwave powers, and to excite a specific range of spin packets;[35] shorter pulses can excite more spin packets, however, the microwave power might be insufficient to achieve the desired flip angles.

Because the bandwidth (excitation range) of microwave pulses is critical in most pulse EPR experiments, this also imposes restriction on the coupling of the resonator to the transmitter arm. Resonators will distort the frequency profile of the pulse due to their inherent bandwidth. For example, a critically coupled resonator (used in cwEPR) can have a bandwidth as small as 1–2 MHz, and all other frequency components of the incoming pulses will be reflected. This reflection of the frequency components outside of a sharp resonator bandwidth typically results in a distorted and significantly elongated pulse in time-domain (compared with the input waveform generated by the PFU; the elongation in time domain is often referred to as 'ringing'). To minimise these effects, the resonator is often over-coupled *i.e.* the quality factor is lowered, in order to achieve a uniform and sufficiently large resonator bandwidth. The over-coupling of the resonator not only helps to preserve the bandwidth and shape of the incoming pulses, but also prevents damaging the detection circuits by the ringing of the high-power microwave pulses.

Since the resonator quality factor in pulse experiments is significantly lower (*cf.* cwEPR), the microwave power delivered to the sample is drastically reduced compared with the source power. Therefore, it is necessary to pass the pulse sequence through a high-power amplifier which is typically a travelling wave tube (TWT) amplifier.

On the detection side of the pulse EPR spectrometer, both the in-phase (real) and out-of-phase (imaginary) components of the EPR signal are recorded. This so-called quadrature detection scheme allows the acquisition of the two orthogonal projections of the magnetisation vector in the plane perpendicular to the external magnetic field. In some applications, only one of these components contains the

[34] This is not to say that the equivalent of a cwEPR spectrum cannot be obtained using pulse EPR, for example by performing an echo field sweep. Most often, such experiments are indeed required to aid the 'set-up' of more specialised experiments.

[35] A spin packet is an ensemble of spins, all of which have the same resonance frequency.

desired information; *e.g.* in the oopESEEM experiment, only the imaginary component is necessary. Finally, there is one limitation in the detection capability of a typical spectrometer: the signals cannot be detected during or shortly after a microwave pulse. This is because the detector diode is designed to be highly sensitive to the relatively minute powers of the EPR signals and the ringing of the high power microwave pulses can damage it.[36]

1.4.2 The free induction decay experiment

The effects of microwave pulses on a spin system are most generally and accurately described using the density matrix formalism. Whilst the usual time-dependent Schrödinger equation is easily manipulated and solved even for complicated spin systems, it is not easily extended to macroscopic ensembles of spin systems (with their own inherent interactions and interactions with the surroundings). Therefore, the Schrödinger equation is typically re-written into the so-called Liouville von Neumann equation, which can readily be generalised to macroscopic ensembles. The description of pulse magnetic resonance via the density matrix formalism is described well in many textbooks, *e.g.* [16–18].

There exist two major simplifications to the density matrix formalism which can guide an understanding of pulse experiments. The more accurate of the simplifications is the product operator method in which a set of analytical rules is derived from the Liouville van Neumann equation. These rules greatly facilitate the description of the changes occurring in the density matrix during various stages of a pulse sequence. The analytical description of a large number of EPR experiments can be carried out using this formalism, despite being approximate.

The vector model constitutes the second and significantly less accurate simplification of the density matrix formalism. Much like the product operator formulation, the vector model is also comprised of a set of rules governing the motion of the magnetisation vectors during the pulse sequence. However, these rules are qualitative and they fail at the description of many spin systems (*e.g.* the vector model fails to describe the behaviour of two strongly coupled electrons). Nonetheless, the vector model suffices for the purpose of the following sections, where only a spin system comprised of a single unpaired electron is considered. In particular, this section will focus on the vector model description of the simplest pulse EPR experiment, namely, the free induction decay (FID) signal obtained by the application of a single microwave pulse. This benchmark experiment of pulse magnetic resonance was originally proposed theoretically by Felix Bloch and later measured experimentally by Erwin L. Hahn [19, 20].[37]

The net magnetisation vector. For a single electron spin in a static external magnetic field, $\mathbf{B}_0$ (chosen to be along the z-axis of the laboratory frame), we can define the net magnetisation vector, $\mathbf{M} = \left(\mathcal{M}_x, \mathcal{M}_y, \mathcal{M}_z\right)$, as the sum of the magnetic moments of all the electronic spins in the ensemble. Since the magnetic moment vector is proportional to the spin vector, the magnitude of the magnetisation along the q-axis is proportional to the expectation value of the $\hat{S}_q$ operator:

$$\mathcal{M}_q \propto \left\langle \hat{S}_q \right\rangle_e \tag{1.111}$$

[36] An electronic switch is often implemented during a pulse, in order to protect the detector diode (referred to as a 'protection pulse', 'defence pulse', or 'protection gate').

[37] This comment and these two references relate only to FIDs, not to the general field of magnetic resonance which was pioneered by many more theoreticians and experimentalists alike.

where the 'e' subscript indicates that the expectation value is averaged over the macroscopic ensemble.

At thermal equilibrium, it can be shown that the net magnetisation vector is exclusively along the z-axis and static in time. This does not mean that the spin vector of each individual electron is aligned with z. In fact, due to the uncertainty principle, the spin vector can never be perfectly aligned with the magnetic field because its components, $\hat{S}_q$, do not mutually commute. However, once the average is taken over the entire ensemble, the net in-plane components vanish.

Conversion to the rotating frame. The effects of microwave pulses are to rotate the equilibrium magnetisation away from the z-axis. As soon as **M** becomes tilted from the z-axis, it will be driven by the static magnetic field to precess around the z-axis at the Larmor frequency:

$$\omega_0 = \frac{\mu_B}{\hbar}\tilde{g}B_0 \tag{1.112}$$

where $\tilde{g}$ is the effective g-value in the direction of the magnetic field. However, a microwave pulse is also present at this stage (this is why **M** became tilted away from z in the first instance). Additionally, the oscillating magnetic component, $\mathbf{B}_1(t)$, of the microwave pulse is causing a Larmor precession (of **M**) around itself. In summary, within the laboratory frame, **M** will follow a complicated oscillatory path around the net magnetic field, $\mathbf{B}_0 + \mathbf{B}_1(t)$.

The motion of the magnetisation vector during a pulse sequence is greatly simplified by conversion to the rotating frame. By definition, the rotating frame is a coordinate system which rotates around the z-axis at the microwave frequency, ω_{mw}.

The first consequence of the conversion into the rotating frame is that the component of the precession around the static field will have a greatly reduced frequency. This is defined as the offset frequency:

$$\Omega = \omega_0 - \omega_{mw} \tag{1.113}$$

Hence, on resonance ($\omega_0 = \omega_{mw}$) spin packets will not oscillate around the z-axis. On the other hand, off-resonant spins can precess around z either in a clockwise or anti-clockwise direction depending on the sign of Ω.

The second consequence of converting to the rotating frame concerns the $\mathbf{B}_1(t)$ vector. A linearly polarised pulse along the x-axis of the laboratory frame:

$$\mathbf{B}_1(t) = B_1\left(\sin\omega_{mw}t, 0, 0\right) = \frac{1}{2}B_1\left(\sin\omega_{mw}t, \cos\omega_{mw}t, 0\right) + \frac{1}{2}B_1\left(\sin\omega_{mw}t, -\cos\omega_{mw}t, 0\right) \tag{1.114}$$

becomes the following in the rotating frame:

$$\mathbf{B}_1(t) = \frac{1}{2}B_1\left(1, 0, 0\right) + \frac{1}{2}B_1\left(\sin 2\omega_{mw}t, -\cos 2\omega_{mw}t, 0\right) \tag{1.115}$$

i.e. in the rotating frame the microwave magnetic field will have a static component along x (indicated as the red vector in figure 1.8), and an oscillating component with frequency $2\omega_{mw}$. Since in the rotating frame the resonance condition is $\Omega = 0$, the oscillating component of the radiation can be safely neglected since $2\omega_{mw} \gg \Omega$, by design.[38]

[38] Because the spectrometer frequency is chosen, on purpose, to be very near the Larmor/resonance frequency.

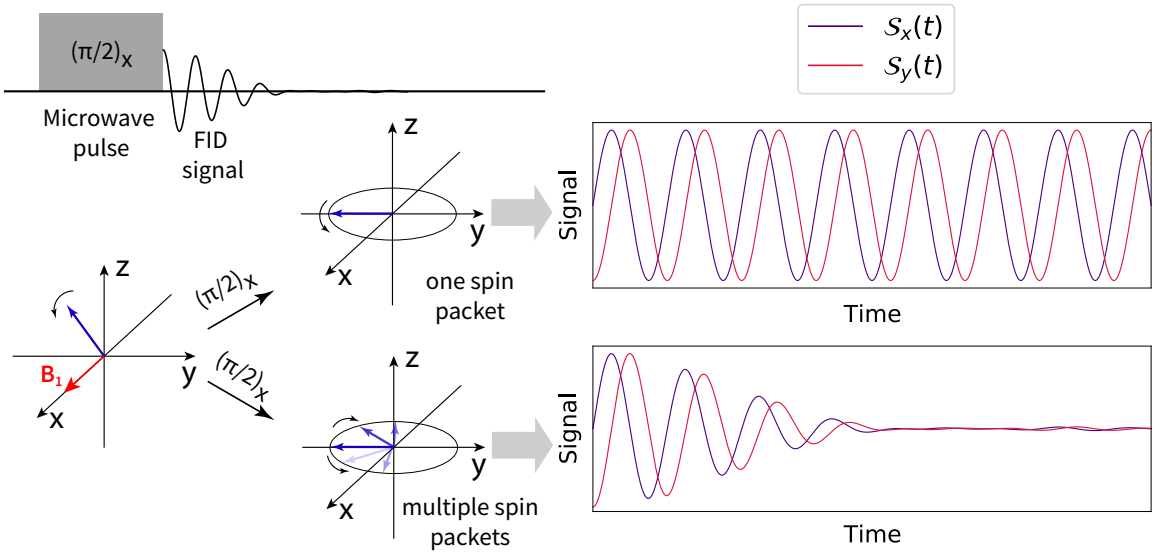


Figure 1.8: The top left diagram is a typical representation of an EPR pulse sequence; in this case it is shown for the FID experiment with a $\pi/2$ pulse along the x-axis, as discussed in the main text. The vector model description of the FID detection scheme is illustrated below the pulse sequence for a single spin packet (top) as well as for multiple spin packets (bottom). The spin packets are represented as blue vectors whereas the red vector is the $\mathbf{B}_1$ magnetic field. These diagrams are illustrating the situation in the rotating frame. The resulting real and imaginary FID signals, $\mathcal{S}_x$ and $\mathcal{S}_y$, for one and multiple spin packets are plotted in the two panels on the right. It is important to note that the these diagrams are approximate. In reality, the spin packets with $\Omega \neq 0$ will not experience a $\pi/2$ pulse and will not be precessing within the xy-plane immediately after the pulse. However, as will be mentioned in the main text, when $\omega_1 \gg \Omega$, *i.e.* an idealised $\pi/2$ pulse, then it can be assumed that all spin packets will experience the same $\pi/2$ flip angle (as the resonant spin packets). Such assumptions are rarely made in advanced pulse EPR work, however, they are sufficient for the purposes of this introduction. Also, note that the decay of the signal in the bottom graph (multiple spin packets) is due to the dephasing of the magnetisation vectors in the xy-plane (relaxation processes are not considered in this discussion). The precise interpretation of the idealised signals depicted here will become clearer towards the end of this section.

Evolution during a microwave pulse. During the pulse, on resonance spin packets will precess exclusively around the $\mathbf{B}_1$ vector. As shown in figure 1.8, if the pulse is phased such that $\mathbf{B}_1 \parallel x$, then the magnetisation will precess anti-clockwise exclusively in the yz plane. The precession frequency is:

$$\omega_1 = \frac{\mu_B}{\hbar} g_{\text{eff}} B_1 \tag{1.116}$$

and thus the flip angle will be equal to $\omega_1 t_p$ where t_p is the duration of the pulse. In an FID experiment, the desired flip angle is $\pi/2$ and the on-resonance spin packets will have a magnetisation exclusively along the $-y$ axis at the end of the pulse (figure 1.8). In a real experiment, one can tune the flip angle by both adjusting the pulse length and the pulse power (which is related to B_1).

As mentioned before, a microwave pulse can excite spin packets which deviate slightly from the resonance condition $\Omega = 0$. The excitation of near resonant spin packets is a consequence of the Heisenberg uncertainty principle according to which a time-limited pulse will have a correlated frequency distribution. The range of Ω values excited by the pulse can be approximated by Fourier transformation of the pulse waveform. The pulses considered here are rectangular in time domain, and hence, a sinc

function, $|\sin(\Omega t_p/2)/(\Omega/2)|$, is the corresponding frequency profile. The full-width at half maximum of this frequency distribution is approximately $1.207/t_p$ whereas the first zero-crossings occur at $\pm 1/t_p$. In other words, the shorter the pulse, the more off-resonant/near resonant spin packets are excited.

Near resonant spin packets will precess both around the $\mathbf{B}_1$ vector and around the z-axis. The net axis of precession will form an angle, ξ, with the z-axis, given by:

$$\xi = \arctan\left(\frac{\omega_1}{\Omega}\right) \tag{1.117}$$

and the net precession frequency around this axis is given by:

$$\omega_{\text{eff}} = \sqrt{\Omega^2 + \omega_1^2} \tag{1.118}$$

These two equations imply that near resonant spin packets, unlike on-resonance ones, will not be exactly aligned with the $-y$ axis at the end of the formal $\pi/2$ pulse. In the remaining discussion we will assume for simplicity that $\omega_1 \gg \Omega$, and hence that all spin packets experience the same flip angle (as shown in figure 1.8 in the multiple spin packet vector diagram). This is the reason why the one/multiple spin packet diagrams in figure 1.8 depict the magnetisation vectors precessing within the xy-plane.

The free induction decay. At the end of this idealised $\pi/2$ pulse for which $\omega_1 \gg \Omega$, the magnetisation vectors of all spin packets (resonant or near-resonant) within the range of the pulse profile will be aligned with the $-y$ axis. The on-resonance packets will remain along the $-y$-axis. As illustrated in the top graph of figure 1.8, all other spin packets will precess in the xy plane (at frequency Ω).[39] This motion of the magnetisation vectors in the xy plane constitutes the FID signal and it is often termed coherence or transverse magnetisation. In quadrature detection, both the components of the magnetisation along the x-axis ('real channel') and along the y-axis ('imaginary channel') are recorded as a function of time. The total signal can be thought of as a complex function of time, $\mathcal{S}(t) = \mathcal{S}_x(t) + i\mathcal{S}_y(t)$, with the components oscillating as depicted in the graphs in figure 1.8. In principle, the EPR spectrum can be recovered from $\mathcal{S}(t)$ by Fourier transformation.

In the absence of relaxation, the precession of an *individual* spin packet will be perpetual with a never changing frequency (top graph in figure 1.8). When the individual signals from the many spin packets is summed over the range of offset frequencies excited by the pulse, the net signal will show a dephasing effect[40] as illustrated in the bottom graph of figure 1.8. In essence, the FID signal decays with a specific time constant which can be approximated as the duration of the pulse, t_p, which initially induced the signal. Hence, the longer the pulse, the longer the FID signal. This criterion is often used in the detection of FID detected field-swept EPR spectra whereby a long microwave pulse is followed by a slowly decaying FID signal. Within this experiment, the signal decays slowly enough that it can be detected outside the range of the spectrometer dead-time.[41]

Since the precession of the transverse magnetization is perpetual, the FID signal is expected to refocus periodically after sufficiently long times following the initial dampening. This periodic refocusing is,

[39] In reality, the off-resonant spin packets will still precess around z but will not be in the xy-plane.

[40] This term means that there is an initial signal decay as a function of time caused by the fact that the overlap of many oscillations which are initially (approximately) in-phase will periodically become completely out-of-phase and perfectly in-phase (spontaneous refocussing).

[41] The dead-time is a period of time immediately after a pulse when it is not possible to detect the signal.

however, never/rarely detectable in real pulse EPR experiments. The presence of spin relaxation means that the precession in the xy plane cannot last indefinitely. The intricacies relating to the theory of spin relaxation are beyond the scope of this thesis and will only be considered briefly.

The return to equilibrium. First of all, the fact that the magnetisation vectors are in the xy plane immediately after the $\pi/2$ pulse means that the populations of the spin energy levels have been equalised. Hence, the environment/lattice will strive to return the spin system to thermal equilibrium in a process called *spin-lattice relaxation*. This process is characterised by a time-constant, conventionally denoted T_1, which quantifies the growth of the z component of the magnetisation back to its original value.

Secondly, there are other (typically, much faster) processes which lead to signal decay but do not involve energy exchange with the environment. All such processes are grouped together under the term *spin-spin relaxation*, quantified by the time-constant T_2. Spin-spin relaxation processes are varied, however, in a simple picture they can be considered as a perpetual drift of the frequency of an individual spin packet above and below its resonance frequency, caused by the fluctuating fields induced by the other spins. This causes the spin packets in the bottom left diagram in figure 1.8 to constantly swap their frequencies, such that the initial dephasing period in the xy plane is accelerated and also, spontaneous refocusing of the FID at a later time is no longer possible. Also, it should be noted that processes which lead to spin-lattice relaxation can also be responsible for the loss of xy coherence.

1.4.3 The Hahn echo sequence

One of the main disadvantages of the single pulse FID scheme in the previous sections is the fact that signal detection is limited by the spectrometer dead-time. Because the dead-time is often longer than the dephasing time of the FID, a different detection scheme is required. The most important of these detection schemes, which is a fundamental building block for numerous other pulse sequences, is the Hahn echo sequence illustrated in the top panel of figure 1.9. This sequence implements a second microwave pulse which refocuses the magnetisation into a signal called an electron spin echo. The first observation of an echo signal was reported (on the protons of glycerol) in 1950 by Erwin L. Hahn [21].

Immediately after the first $\pi/2$ pulse of the echo sequence, the magnetisation vectors will precess in the xy plane, giving rise to an (often undetectable) FID:

$$\mathbf{M} = \mathcal{M}\,(\sin\Omega t, -\cos\Omega t, 0) \tag{1.119}$$

which corresponds to the blue vectors in diagram (a) of figure 1.9. A time τ after the $\pi/2$ pulse, the magnetisation vectors are rotated by an angle π around the x-axis by using a second pulse. The result immediately after the π pulse is the following:

$$\mathbf{M} = \mathcal{M}\,(\sin\Omega\tau, \cos\Omega\tau, 0) \tag{1.120}$$

where the time variable, t, was replaced by τ to indicate the time at which the π pulse occurred. Afterwards, the magnetisation vectors will continue to precess around the z-axis. Provided that the τ interval was not too long compared with the phase memory time, $\mathbf{M}$ will precess in the same anti-clockwise direction, at the same frequency as before. During this free evolution period, the magnetisation is given

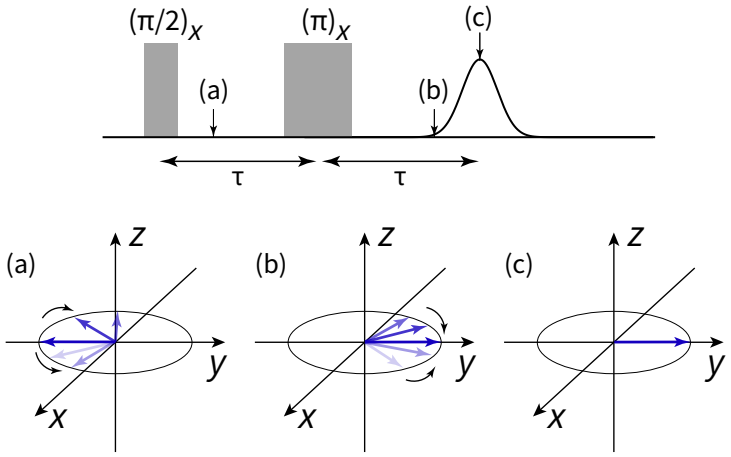


Figure 1.9: (Top) The Hahn echo pulse sequence. (Bottom) Evolution of the magnetisation vectors (blue arrows) in the rotating frame at various stages of free evolution during the Hahn echo sequence: (a) the inter-pulse delay, (b) some time after the refocusing pulse, and (c) at the time corresponding to the maximum of the echo signal.

by:

$$\mathbf{M} = \mathcal{M}\left(\sin\Omega(\tau - t), \cos\Omega(\tau - t), 0\right) \tag{1.121}$$

and it corresponds to the vectors in panel (b) of figure 1.9. In other words, during the second free evolution period the magnetisation acquires a phase Ωt which is in addition to the phase $\Omega\tau$ acquired during the initial evolution. Importantly, when $t = \tau$ in the second evolution period, the phase acquired by the magnetisation vector is the same regardless of the offset frequency, Ω. This means that as t approaches τ, all spin packets with any Ω will gradually become in-phase and refocus into an electron spin echo.

There are a few noteworthy points regarding the two pulse echo sequence. First, the inter-pulse delay, τ, can be chosen so as to allow the detection of the echo well-beyond the spectrometer dead-time. Also, the $\pi/2$ and π flip angles can be achieved either by keeping the B_1 field strength the same and adjusting the duration of the pulses, or by keeping the pulse lengths equal and doubling the B_1 of the second pulse. The latter scheme ensures the same bandwidth for both pulses, and can lead to more intense echoes. Secondly, the two-pulse echo sequence is not the only method to generate a detectable EPR signal. For instance, in the ENDOR experiment of the next section, three $\pi/2$ microwave pulses generate a stimulated echo. In other applications, this primary Hahn echo is refocused into a secondary Hahn echo by the application of another π pulse.

The vector model manipulations presented in equations 1.119 to 1.121 are, only in this simple case, analogous to the product operator formalism (although the notation is different). More information about spin echo pulse sequences and the product operator formalism can be found in reference [16].

1.4.4 Electron-nuclear double resonance

The two, FID and echo, detection schemes introduced above are often used to obtain the pulse EPR equivalent of the cwEPR spectrum. However, as mentioned previously, the true advantage of pulse EPR methodology lies in the fact that the interaction parameters can be addressed individually using

specialised experiments. For this thesis, particularly interesting are pulse techniques capable of providing a detailed picture of the small hyperfine couplings which are not typically resolved in conventional cwEPR spectra. The technique of choice is the electron nuclear double resonance (ENDOR) pulse sequence formulated by William B. Mims in a seminal publication in 1965 [22]. Whilst the Mims ENDOR technique is not the only type of pulse hyperfine spectroscopy, it is well-suited for the detection of small couplings. A general review of various types of ENDOR experiments as well as the basis of the following description can be found in reference [23].

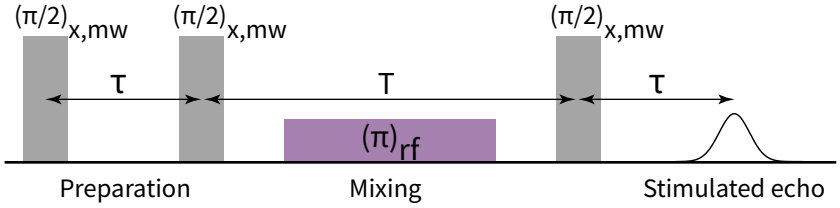


Figure 1.10: The Mims ENDOR pulse sequence. Microwave pulses are shown in grey and the rf pulse is shown in purple. The mixing time, T, is set to be longer than the phase memory time of the electron, and the preparation and detection delays, τ, are equal.

As shown in figure 1.10, the Mims ENDOR pulse sequence is a stimulated electron spin echo sequence (three pulse echo sequence) with a radiofrequency (rf) pulse applied between the second and third microwave pulses. Similarly to all ENDOR experiments, the first two pulses comprise what is referred to as the preparation period. Within this period, spin polarisation is transferred from the electron to the nucleus. Afterwards, an rf pulse is placed in the mixing period, in order to induce a nuclear transition. A final microwave pulse is applied for the detection of the stimulated echo. Whilst it is possible to describe the evolution of the spin system in the vector model formulation, the arguments do involve a number of unjustified leaps. In order to avoid such problems, the analysis of the Mims ENDOR sequence below will be from the perspective of the more accurate product operator formalism given in references [16] and [23].

The starting point is the product operator representing the electron spin in thermal equilibrium, namely $\hat{S}_z$. After the first two $\pi/2$ microwave pulses and after a mixing time, T, much greater than the spin-spin relaxation time, the following is obtained:

$$\hat{S}_z \xrightarrow{\frac{\pi}{2}\hat{S}_x} \xrightarrow{\tau} \xrightarrow{\frac{\pi}{2}\hat{S}_x} \xrightarrow{T \gg T_2} -\cos\left(\frac{a\tau}{2}\right)\cos(\Omega\tau)\,\hat{S}_z + \sin\left(\frac{a\tau}{2}\right)\sin(\Omega\tau)\,2\hat{S}_z\hat{I}_z \tag{1.122}$$

where a is the hyperfine coupling constant (taken as approximately equal to the projection of the hyperfine tensor axes in the direction of the external magnetic field). Both $\pi/2$ pulses induce coherences in the system. However, because the mixing time is much greater than T_2, all the transverse product operators decay in this time. The result shown in equation 1.122 is called a *polarisation grating*, because it corresponds to a redistribution of the spin polarisation into a sinusoidal pattern which depends on the offset frequency Ω. Within the resultant polarisation grating, the most important term is the one containing the two-spin order product operator, $2\hat{S}_z\hat{I}_z$. This component is a result of the presence of the hyperfine interaction and it corresponds to a population pattern in which the (relatively large) electron spin polarisation is transferred to the nuclear spin levels.

We now apply the product operator formulas to evaluate the effects of both the final pulse and the evolution during the detection period. At time τ after the last pulse, we obtain:

$$(1.122) \quad \xrightarrow{\frac{\pi}{2}\hat{S}_x} \quad \xrightarrow{\tau} \left\{ \sin^2\left(\frac{a\tau}{2}\right) \sin^2(\Omega\tau) + \cos^2\left(\frac{a\tau}{2}\right) \cos^2(\Omega\tau) \right\} \hat{S}_y =$$

$$= \frac{1}{2} \{1 + \cos(a\tau) \cos(2\Omega\tau)\} \hat{S}_y \quad (1.123)$$

which manifests itself as the stimulated echo depicted in figure 1.10 (because it contains an Ω- independent component). When the effect of an rf π pulse on resonance with a nuclear transition is included in the analysis, we obtain:

$$(1.122) \quad \xrightarrow{(\pi)_{rf}} \quad \xrightarrow{\frac{\pi}{2}\hat{S}_x} \quad \xrightarrow{\tau} \cos^2\left(\frac{a\tau}{2}\right) \cos^2(\Omega\tau) \hat{S}_y \quad (1.124)$$

i.e. the stimulated echo vanishes when the rf pulse successfully induces a nuclear transition (this is referred to as the 'ENDOR effect'). By recording the intensity of the stimulated echo as a function of radiofrequency, the spectrum of nuclear transitions can be obtained, and the hyperfine couplings can be extracted. The appearance of the final ENDOR spectrum will depend both on which hyperfine coupling regime (as discussed in section 1.2.3) is applicable and on the electronic and nuclear spin quantum numbers. All ENDOR spectra reported in this thesis can be understood in the weak hyperfine coupling limit.

The final point to clarify is that the product operator description above is only applicable to a single spin packet with offset frequency Ω. By averaging the ENDOR effect over the range of offset frequencies excited by the microwave pulses in a real experiment, one can derive a formula for the ENDOR efficiency:

$$F = \frac{1}{2} \sin^2\left(\frac{a\tau}{2}\right) \quad (1.125)$$

which quantifies the maximum relative change in the stimulated echo intensity induced by a resonant rf pulse. The fact that F oscillates as function of τ and a is one of the disadvantages of the Mims ENDOR experiment. If the preparation delay is chosen to be exactly $\tau = 2n\pi/a$ then there will be no ENDOR effect *i.e.* the ENDOR spectrum will contain blind spots at the corresponding hyperfine coupling values. Generally, the blind-spots in the ENDOR spectrum prevent any conclusions to be drawn from the lineshapes of complicated spectra. One of the key methods to minimise the impact of blind spots on the information content of ENDOR spectra is to acquire the data with multiple τ values. This τ-averaging method was implemented in all the ENDOR spectra in this thesis, and further details will be provided at the appropriate point.

Chapter 2

Spin delocalisation in the radical cations of porphyrin molecular wires

EPR is the key spectroscopic technique used to determine the extent of spin delocalisation in organic radicals. When the spin quantum number is 1/2, most of the information regarding the spatial distribution of the spin density can be deduced from the magnitudes of the hyperfine couplings to the nuclei in the system. The results presented in this chapter exploit both cwEPR and Mims ENDOR experiments to characterise the hyperfine couplings in a series of radical cations of oligoporhyrin molecules. The primary motivation for this project is to probe the viability of oligopoprhyins as building blocks for molecular wires. Furthermore, not only will the spin density distribution be elucidated, the continuing role of EPR based methodologies in the exploration of spin delocalisation in porphyrins and similar radicals will be reconsidered from the vantage point of the new results.

This work is part of a long-standing collaboration between our group and the synthetic organic chemistry group of Prof. Harry L. Anderson. A similar EPR driven study of porphyrin radical cations was carried out previously by Dr. Claudia Tait on a different series of oligoporphyrins, and some of those results will be shown and re-analysed here since they are crucial for comparison purposes. References to the original work will be provided at appropriate points in the discussion. Finally, note that some passages in this chapter have been quoted verbatim from the publication which resulted from this work [24].

2.1 Oligoporphyrins as molecular wires

Porphyrins are a class of π-conjugated macrocyclic molecules which play a central role in many fundamental biological processes such as photosynthesis and oxygen transport [25, 26]. This is a result of both their remarkable charge transport ability and diverse redox chemistry, as well as their varied photophysical and magnetic properties. These properties have inspired a wide range of studies aimed at using porphyrin molecules as building blocks for molecular wires in nano-scale electronic devices, spintronics and photovoltaic cells [27–36]. Despite the extensive research dedicated to the understanding of their ground and excited-state properties and their potential applications, porphyrin systems remain an elusive class of organic compounds. As a result, they also represent an ideal playground for numerous computational and quantum chemical studies in conjunction with various spectroscopic

techniques [37–40].

The design of porphyrin molecular devices also requires the ability to control the spatial distribution of the spin density within a multi-porphyrin array. Throughout this thesis, a number of the factors which can influence the spin delocalisation in oligoporphyrins in both ground and excited states will be investigated. Particularly in this chapter, the influence of the inter-porphyrin linker on the spin density of the radical cations of the systems shown in figure 2.1 will be addressed.

The neutral (and spinless) states of the linear and cyclic ethyne-linked zinc(II) oligoporphyrin series, ***l1*-PN** and ***c*-P6** in figure 2.1, were synthesised in the group of Prof. Harry L. Anderson primarily by Dr. Lara Tejerina-Gonzales in collaboration with Dr. Michel Rickhaus. The complete synthetic methodology is outlined in the publication resulting from the work presented in this chapter and references therein [24]. The chemical conversion to the radical (mono-)cation states, denoted ***l1*-PN$^{+\cdot}$**, was conducted by Dr. Lara Tejerina-Gonzales.

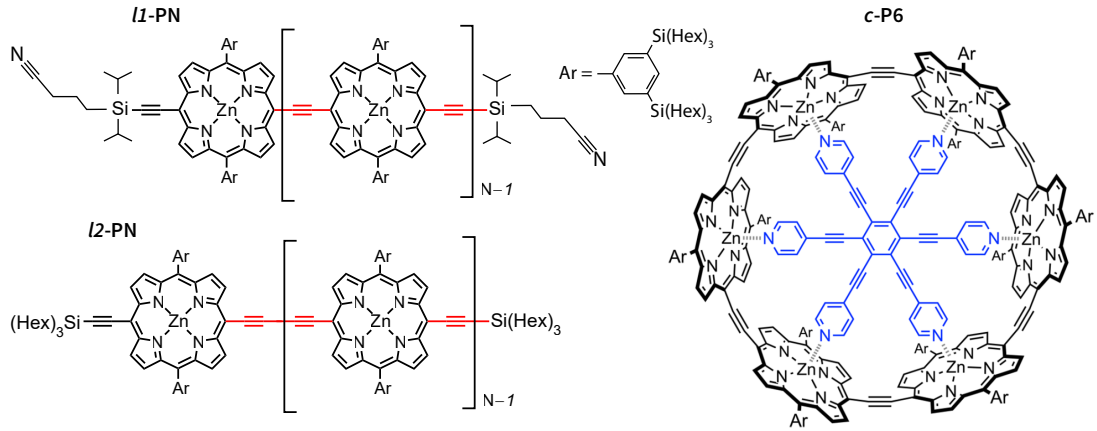


Figure 2.1: Skeletal structures of the oligoporphyrin systems investigated in this chapter. The two linear oligomer series are shown on the left. Throughout this chapter, the linear oligomers will be denoted as ***l1*-PN$^{+\cdot}$** and ***l2*-PN$^{+\cdot}$** where **N** represents the oligomer chain length. The key difference between the ***l1*-PN$^{+\cdot}$** and ***l2*-PN$^{+\cdot}$** series is the inter-porphyrin linker which consists of ethyne and butadiyne groups, respectively. The two series have the same aryl group substituents, however, they have different terminal protecting groups. The precise identity of these protecting groups has not been reported to have any discernible influence on the spin density. The cyclic templated oligomer, labelled ***c*-P6$^{+\cdot}$**, is shown in the right panel (the template is marked in blue).

The butadiyne-linked oligomer series, which will be denoted as ***l2*-PN$^{+\cdot}$**, was synthesised by Dr. Georg Fisher and Dr. Patrick Neuhaus from the Anderson group. As mentioned before, the original EPR study on the ***l2*-PN$^{+\cdot}$** series was conducted by Dr. Claudia Tait [41]. However, in light of the new work presented here for the ***l1*-PN$^{+\cdot}$** series, it is paramount for the proceeding discussion to include the results of the previous study on the butadiyne series.

2.2 Probing delocalisation: the Norris Equation

Previous studies of the radical cation states with $S = 1/2$ of ethyne-linked porphyrin oligomers indicated spin density delocalization lengths spanning up to seven porphyrin units (i.e., >7.5 nm) [42]. Similar results were also obtained for the butadiyne series reported in reference [41], as well as for porphyrin

radical anion systems [43]. Following methodology originally introduced by Norris et al. [44], these conclusions were based on the narrowing of the envelope linewidth of the room temperature cwEPR signature of the radical cations with increasing oligomer length. This analysis method, aimed at probing the extent of spin delocalisation, is encompassed by the following equation:

$$\Delta B_N = \frac{\Delta B_1}{\sqrt{N}} \tag{2.1}$$

which will be referred to as 'the Norris equation' throughout this chapter. According to the Norris equation, if the spin density is completely and uniformly delocalised,[1] the envelope linewidth/second moment of the EPR spectrum, ΔB_N, is inversely proportional to the square root of the number of units which comprise the N-th oligomer.

This analysis method is invaluable for assessing the viability of oligoporphyrins as molecular wires, since it constitutes an easily implemented criterion for the extent of spin delocalisation. According to 2.1, measurements of ΔB_N by progressively increasing the oligomer chain length should be sufficient to establish whether the spin density is fully delocalised across a molecular framework, and hence, whether the system is suitable as a molecular wire.

As with many equations, however, it is crucial to demonstrate that the assumptions behind the Norris equation are fully applicable to the system at hand. Particularly, if a system is found to deviate from the Norris equation, can it be stated that the spin density is not fully delocalised over all N units of an oligomer? Or alternatively, is the spin density fully delocalised, yet the Norris equation breaks down due to some perturbation which was neglected in its derivation? Such questions and considerations will form the topic of this section. The main conclusion which will resonate throughout the remaining sections is that, whilst valuable, the Norris equation is neither a necessary nor a sufficient condition for complete and uniform spin delocalisation over all the units of an oligomeric system, a fact which has hitherto not been addressed in the literature.

A note on terminology. It will become clear in the remaining sections that, from a purely mathematical perspective, the Norris equation is merely a restatement of the central limit theorem of statistics (as per the original derivation in [44]). However, equation 2.1 will not be referred to as 'the central limit theorem' because at the end of the next section, we will show that equation 2.1 can break down. Of course, it is not the central limit theorem that breaks down, it is the validity of the treatment proposed by Norris that becomes questionable when applied to some of the systems at hand. Finally, we emphasise that the work and conclusions of Norris in reference [44], regarding the mechanism of photosynthesis, are not under scrutiny. It is the use of the methodology proposed by Norris for the description of delocalisation in molecular wires, without additional experimental and computational evidence, which is reconsidered.

2.2.1 The origin of the Norris equation

Although not explicitly demonstrated by Norris et al. [44], the origin of equation 2.1 can be traced back to the properties of multinomial coefficients. This section is concerned with the derivation of the Norris

[1] The meaning of this phrase will be defined more formally in the next section. For the moment, it is used merely as an adjective.

equation for stick spectra and a discussion of the potential pitfalls of using arguments based solely on linewidth considerations. Whilst the original derivation is sketched briefly in [44], the discussion that follows will be slightly more detailed, so as to highlight both the advantages and disadvantages of this treatment.

N spin-1/2 nuclei. The derivation starts by writing the idealised EPR spectrum of an electron spin coupled to N equivalent spin-1/2 nuclei in analytical form as:

$$S_N(B) = \frac{1}{2^N} \sum_{k=-N/2}^{N/2} C^N_{k+\frac{N}{2}} \, \delta\left(B + 2kA_N\right) \tag{2.2}$$

The above expression describes an EPR spectrum (figure 2.2) in field domain, $S_N(B)$, comprised of $(N+1)$ equidistant infinitesimally thin lines separated by the hyperfine coupling constant, $2A_N$ (hence the use of the Dirac delta function).[2] The intensity of each line is given by the binomial coefficient, $C^N_{k+\frac{N}{2}}$, and the factor of $\frac{1}{2^N}$ ensures that the spectrum is normalized to a unit integral:

$$\int_{-\infty}^{+\infty} S_N(B)\, dB = \frac{1}{2^N} \sum_{k=-N/2}^{N/2} C^N_{k+\frac{N}{2}} = 1 \tag{2.3}$$

Note also that, as written, this spectrum has a centre field of zero, which means that the real field axis is obtained by shifting to an appropriate centre field ($B_{\text{real}} = B + B_{\text{centre}}$).

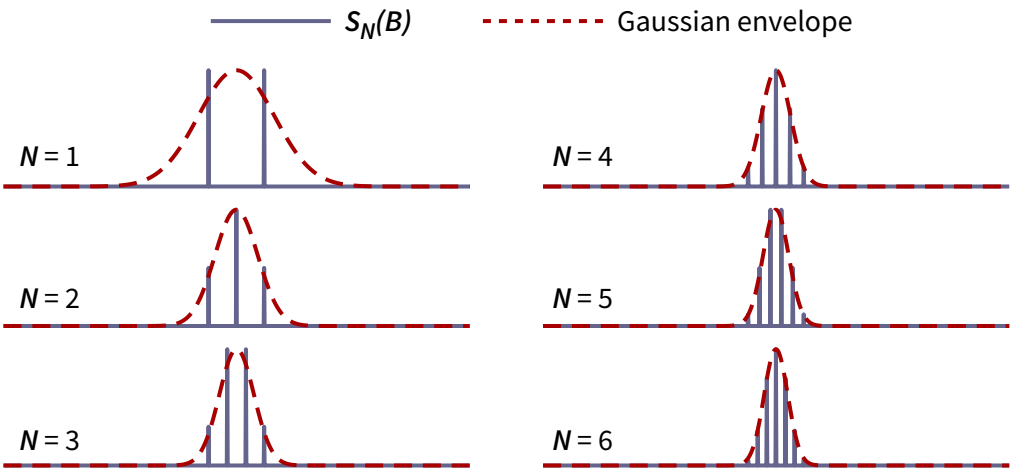


Figure 2.2: Stick spectra for an electron spin coupled to $N = 1$–6 equivalent spin-1/2 nuclei with a hyperfine coupling constant which is inversely proportional the number of nuclei ($A_N = A_1/N$, where A_1 is the hyperfine coupling in the $N = 1$ case). The red dashed line shows the Gaussian envelope of the spectra obtained from least-squares fitting to the stick spectra. As N becomes larger, the Gaussian scaling of the spectra becomes clearer.

The variance of the spectrum (relative to the centre field at $B = 0$) is defined as:

$$\Delta B_N^2 = \int_{-\infty}^{+\infty} B^2 S_N(B)\, dB = \frac{1}{2^N} \sum_{k=-N/2}^{N/2} C^N_{k+\frac{N}{2}} \left(2kA_N\right)^2 \tag{2.4}$$

[2] The factor of 2 in the hypefine coupling is present only for convenience, and has no special meaning.

If we now assume that the hyperfine coupling to each one of the N nuclei is given by $A_N = A_1/N$, *i.e.* the spin density is completely and uniformly delocalised over all the nuclei and the McConnell relation (equation 1.69) holds, then the equation for ΔB_N^2 becomes:

$$\Delta B_N^2 = \frac{A_1^2}{N^2 2^{N-2}} \sum_{k=-N/2}^{N/2} k^2 C_{k+\frac{N}{2}}^N \tag{2.5}$$

This particular sum of binomial coefficients can be trivially evaluated either by using the factorization properties of the binomial coefficients or by twice differentiating $(1+x)^N$ with respect to x and setting $x = 1$, to yield:

$$\sum_{k=-N/2}^{N/2} k^2 C_{k+\frac{N}{2}}^N = N 2^{N-2} \tag{2.6}$$

By substituting the above relation into 2.5, we obtain:

$$\Delta B_N^2 = \frac{A_1^2}{N} \tag{2.7}$$

and because $\Delta B_1^2 = A_1^2$, this is simply the square of the Norris equation (2.1).

N spin-1 nuclei. Since porphyrin molecules also contain ^{14}N nuclei, it is necessary to consider the second moment of the EPR spectra resulting from a coupling to N spin-1 nuclei, *i.e.*:

$$S_N(B) = \frac{1}{3^N} \sum_{k=-N}^{+N} T_k^N \delta\left(B + kA_N\right) \tag{2.8}$$

where T_k^N is a trinomial coefficient contained in the expansion of $(1 + x + x^2)^N$. The spectrum consists of $(2N+1)$ infinitesimally thin lines centered around zero and separated by A_N with an intensity given by T_k^N. Once again, the factor of $\frac{1}{3^N}$ ensures the spectrum is normalized to a unit integral.

The second moment of this spectrum can be written similarly to the spin-1/2 case as:

$$\Delta B_N^2 = \frac{A_1^2}{N^2 3^N} \sum_{k=-N}^{+N} k^2 T_k^N \tag{2.9}$$

The summation over the trinomial coefficients can be evaluated separately:[3]

$$\sum_{k=-N}^{+N} k^2 T_k^N = 2N 3^{N-1} \tag{2.10}$$

Thus, we obtain the second moment as:

$$\Delta B_N^2 = \frac{2A_1^2}{3N} \tag{2.11}$$

which is the Norris equation applied to spin-1 nuclei.

N spin-1 nuclei and M spin-1/2 nuclei. Having derived the second-moment for two separate cases, the derivation can now be generalised to a more realistic porphyrin cwEPR spectrum consisting of N

[3] By twice differentiating $(1 + x + x^2)^N$ at $x = 1$.

equivalent spin-1 nuclei (^{14}N), and M equivalent spin-1/2 nuclei (^{1}H):

$$S_{NM}(B) = \frac{1}{3^N}\sum_{k=-N}^{+N} T_k^N \mathcal{S}\left(B + kA_N\right) = \frac{1}{3^N}\frac{1}{2^M}\sum_{k=-N}^{+N} T_k^N \sum_{j=-M/2}^{M/2} C^N_{j+\frac{M}{2}}\,\delta\left(B + kA_N + 2j\mathcal{A}_M\right) \tag{2.12}$$

where $A_N = A_1/N$ and $\mathcal{A}_M = \mathcal{A}_1/M$ are the hyperfine couplings to the spin-1 and spin-1/2 nuclei, respectively. By contrast to the previous two subsections, in this case, the total spectrum $S_{NM}(B)$ is comprised of sub-spectra $\mathcal{S}\left(B + kA_N\right)$ centred at kA_N rather than infinitely sharp lines (previously denoted by the Dirac delta functions centred at kA_N). Each sub-spectrum $\mathcal{S}\left(B + kA_N\right)$ is split into $(M + 1)$ lines only by the hyperfine coupling to the spin-1/2 nuclei, and its centre is shifted by the coupling, kA_N, to the spin-1 nuclei. Each sub-spectrum is then weighted by the corresponding trinomial coefficient and normalised accordingly.

The second moment of $S_{NM}(B)$ is obtained from:

$$\Delta B^2_{NM} = \int_{-\infty}^{+\infty} B^2 S_{NM}(B)\,dB = \frac{1}{3^N}\sum_{k=-N}^{+N} T_k^N \int_{-\infty}^{+\infty} B^2 \mathcal{S}_M(B + kA_N)\,dB \tag{2.13}$$

The integral inside the summation can be evaluated by first changing variables and expanding the square:

$$\int_{-\infty}^{+\infty} B^2 \mathcal{S}_M(B + kA_N)\,dB = \int_{-\infty}^{+\infty} (B - kA_N)^2 \mathcal{S}_M(B)\,dB = \tag{2.14}$$

$$= \int_{-\infty}^{+\infty} B^2 \mathcal{S}_M(B)\,dB - 2kA_N \int_{-\infty}^{+\infty} B\mathcal{S}_M(B)\,dB + k^2A_N^2 \int_{-\infty}^{+\infty} \mathcal{S}_M(B)\,dB = \tag{2.15}$$

$$= \frac{\mathcal{A}_1^2}{M} + \frac{k^2A_1^2}{N^2} \tag{2.16}$$

Substituting equation 2.16 into 2.13 and evaluating the two resulting sub-summations as per the previous section gives :

$$\Delta B^2_{NM} = \frac{1}{3^N}\sum_{k=-N}^{+N} T_k^N \left(\frac{\mathcal{A}_1^2}{M} + \frac{k^2A_1^2}{N^2}\right) = \frac{\mathcal{A}_1^2}{M} + \frac{2A_1^2}{3N} \tag{2.17}$$

which is simply the sum of equations 2.7 and 2.11.

If we consider $\Delta B^2_{NM} \equiv \Delta B^2_1$ to be the second moment of a monomer system, then the corresponding n-th oligomer will have the following second moment:

$$\Delta B^2_{(nN)(nM)} = \Delta B^2_n = \frac{1}{n}\left(\frac{\mathcal{A}_1^2}{M} + \frac{2A_1^2}{3N}\right) = \frac{\Delta B^2_1}{n} \tag{2.18}$$

After adjusting the notation such that $n \equiv N$, and taking the square root, we obtain the Norris equation, which is now applicable to oligomers stemmed from monomers with a set of equivalent spin-1 nuclei and another set of equivalent spin-1/2 nuclei.

Limit of large numbers of nuclei. The problem with evaluating the second-moment of real cwEPR spectra is that they are not formed of infinitely thin lines; the peaks have an inherent linewidth. This means that the expressions for ΔB^2_N in the above derivations do not simplify to finite sums, and the integral in equation 2.4 has to be evaluated numerically. This numerical integral evaluation together

with the fact that the EPR spectra are recorded as the first derivative of $S_N(B)$ and that there is an uncertainty in determining the centre field of the integration range means that a direct evaluation of the second-moment from the integral is prone to many sources of error.

However, the stick spectra discussed above have a Gaussian scaling property (in the limit of large numbers of nuclei; see figure 2.2) which enables a different, and much more accurate, approach to be taken in evaluating the second-moment. We will illustrate the Gaussian scaling property for the case of many equivalent spin-1/2 nuclei starting from the general expression for the spectrum, as written before in equation 2.2.

We make use of the following two scaling relationships:[4]

$$\lim_{N\to\infty} \sum_{k=-N/2}^{N/2} f(k) \sim \int_{-\infty}^{+\infty} f(k)\, dk \tag{2.19}$$

$$\lim_{N\to\infty} \frac{1}{2^N} C^N_{k+\frac{N}{2}} \sim \frac{2}{\sqrt{2\pi N}} \exp\left(-\frac{2k^2}{N}\right) \tag{2.20}$$

to re-write the equation for the EPR spectrum as a 'sifter' integral which yields:

$$S_N(B) \sim \int_{-\infty}^{+\infty} \frac{2}{\sqrt{2\pi N}} \exp\left(-\frac{2k^2}{N}\right) \delta\left(B + 2kA_N\right)\, dk = \frac{2}{\sqrt{2\pi N (2A_N)^2}} \exp\left(-\frac{2B^2}{4NA_N^2}\right) \tag{2.21}$$

This equation implies that a Gaussian function becomes an ever better approximation of the envelope of the EPR spectrum. The corresponding variance of the Gaussian in equation 2.21 is $\Delta B_N^2 = NA_N^2$ which reduces to the Norris equation if we set $A_N = A_1/N$.

The analytical derivation of the equivalent scaling relation for spin-1 nuclei can be achieved by using the central limit theorem of statistics. According to this theorem, the envelope of the discreet multinomial distribution (which is the EPR spectrum in this case) will approach a Gaussian function as the number of 'trials', *i.e.* nuclei, increases.

The caveats of the Norris equation. In light of the above, fitting a Gaussian to the experimental spectra is a valid method for obtaining the second moment of the spectrum. The width of the Gaussian envelope can then be used to analyse the spectra of the oligomers using the Norris equation. However, there are a few relevant caveats which follow from the above derivations:

- If the number of nuclei is not large enough, then the envelope of the spectrum will deviate more significantly from a Gaussian function. This is, in fact, observed in the spectrum of ***l1*-P1**$^{+\cdot}$ which will be shown later. The best fit Gaussian envelope of the cwEPR spectrum of ***l1*-P1**$^{+\cdot}$ has a significantly larger uncertainty.
- If the peaks comprising the spectra have a finite, but small inherent Lorentzian linewidth then, we expect the total spectrum for the larger oligomers to scale more as a Lorentzian rather than a Gaussian. This is because it is essentially only a superposition of Lorentzians with small separations between the centers. As a result, we do not expect the Norris equation to be applicable if the largest hyperfine coupling in the oligomer is smaller than the inherent Lorentzian

[4]The second of which is derived by employing the exponentiated form of Stirling's approximation. Alternatively, one can simply employ the central limit theorem.

linewidth. There is thus an upper limit on the oligomer chain lengths which can be interpreted using this spectral envelope method. The upper limit will depend on the magnitude of the inherent Lorentzian linewidth.

- If the assumption of complete and uniform delocalisation is not entirely followed, i.e. if $A_N \neq A_1/N$, then the critical last step in all the derivations above is invalid, and the Norris equation will not be obeyed. However, we can show that the Gaussian scaling remains valid. Some particular aspects of this caveat are considered in more detail in the next section.

2.2.2 First-order corrections due to non-uniformity

In this section, it will be proven that even if the spin density is delocalised completely over all the units of an oligomer, it is still possible to observe deviations from the Norris equation. Particularly, the Norris equation breaks down if the spin density is non-uniform (to be defined below) across an individual unit of the oligomer. To begin, consider a fictitious monomer spectrum with N equivalent spin-1 nuclei:

$$S_1(B) = \frac{1}{3^N} \sum_{k=-N}^{+N} T_k^N \delta\left(B + ka\right) \tag{2.22}$$

where a is the hyperfine coupling constant. The second moment of $S_1(B)$ is:

$$\Delta B_1^2 = \frac{2Na^2}{3} \tag{2.23}$$

Now, a dimer spectrum can be constructed starting from this monomer spectrum. The first option is to double the number of nuclei, and divide the hyperfine couplings by two. As shown in figure 2.3, this would correspond to complete and uniform delocalisation of the spin density. Alternatively, a *non-uniformity parameter*, $q \in \left[0, \frac{1}{2}\right]$, could also be defined such that N nuclei have an enhanced hyperfine coupling $\left(\frac{a}{2} + qa\right)$ and the remaining N nuclei have a reduced hyperfine coupling $\left(\frac{a}{2} - qa\right)$.[5]
It is clear that $q = 0$ corresponds to complete and uniform delocalization. Moreover, the sum of the hyperfine couplings on all the nuclei is equal to the sum of the hyperfine couplings in the monomer, i.e. the spin density is normalized to the monomer. If $q \neq 0$ then figure 2.3 shows that there are different indistinguishable patterns for distributing the spin density relative to the structure of the dimer (some of which are more realistic than others). The corresponding dimer spectrum can be written regardless of the spin density pattern as:

$$S_2(B) = \frac{1}{3^N} \sum_{k=-N}^{+N} T_k^N \mathcal{S}\left(B + k\left(\frac{a}{2} + qa\right)\right) = \\ = \frac{1}{3^{2N}} \sum_{k=-N}^{+N} T_k^N \sum_{j=-N}^{+N} T_j^N \delta\left(B + k\left(\frac{a}{2} + qa\right) + j\left(\frac{a}{2} - qa\right)\right) \tag{2.24}$$

And it can be shown that if $q = 0$, the expression reduces to the usual dimer spectrum. In the case of a general oligomer with a chain length p we can also define, by analogy with the dimer, a non-uniformity

[5]The non-uniformity parameter is, strictly speaking, not restricted to values between zero and 1/2. The equations that follow are valid regardless of the value of q, however, the interpretation of q as a measure of non-uniformity is compromised if $q > 1/2$.

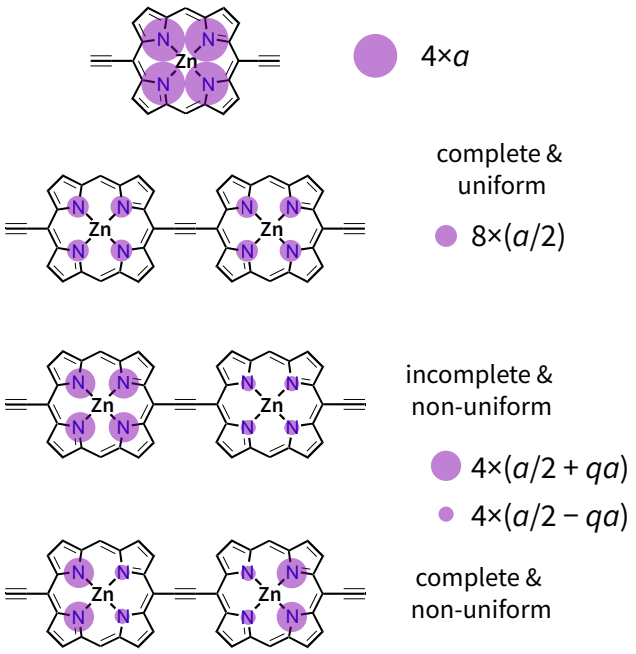


Figure 2.3: Illustration of the non-uniformity parameter, q, as applicable to the nitrogen hyperfine couplings within the series of linear porphyrin oligomers relevant for this work. In the case of the dimer, $q = 0$ corresponds to 8 equivalent ^{14}N hyperfine couplings of magnitude $a/2$ i.e. complete and uniform delocalization of the spin density. When $q \neq 0$, we can distinguish multiple possibilities for distributing the spin density, two of which are illustrated here. The middle dimer diagram is the incomplete and non-uniform pattern, whereas the bottom diagram is the case of complete and non-uniform delocalisation.

parameter, q, such that $pN/2$ nuclei have enhanced and reduced couplings $\left(\frac{a}{p} \pm qa\right)$.[6] At this stage, it is clear that treating the non-uniformity of oligomers beyond dimers using a single q-value is not entirely accurate. The non-uniformity across each unit of the oligomer could be different. However, this single non-uniformity parameter can be used to quantify the average non-uniformity across all units of an oligomer. In this sense, q is a mean-field/first order correction factor which avoids more than one degree of freedom being added to the final result. Thus, the general EPR spectrum for the p-th oligomer is:

$$S_p(B) = \frac{1}{3^{pN/2}} \sum_{k=-pN/2}^{+pN/2} T_k^{pN/2} \mathcal{S}\left(B + k\left(\frac{a}{p} + qa\right)\right) = \\ = \frac{1}{3^{pN}} \sum_{k=-pN/2}^{+pN/2} T_k^{pN/2} \sum_{j=-pN/2}^{+pN/2} T_j^{pN/2} \delta\left(B + k\left(\frac{a}{p} + qa\right) + j\left(\frac{a}{p} - qa\right)\right) \quad (2.25)$$

As before, we now evaluate the second moment of $S_p(B)$:

$$\Delta B_p^2 = \frac{1}{3^{pN/2}} \sum_{k=-pN/2}^{+pN/2} T_k^{pN/2} \int_{-\infty}^{+\infty} B^2 \mathcal{S}\left(B + k\left(\frac{a}{p} + qa\right)\right) dB \quad (2.26)$$

[6] Note that the allowed values of pN are restricted to even integers. This is sufficient for porphyrins.

The integral is evaluated by changing variables and expanding the square:

$$\int_{-\infty}^{+\infty} B^2 \mathcal{S}\left(B + k\left(\frac{a}{p} + qa\right)\right)\, dB = \int_{-\infty}^{+\infty} \left(B - k\left(\frac{a}{p} + qa\right)\right)^2 \mathcal{S}(B)\, dB = \tag{2.27}$$

$$= \int_{-\infty}^{+\infty} B^2 \mathcal{S}(B)\, dB - 2k\left(\frac{a}{p} + qa\right) \int_{-\infty}^{+\infty} B\mathcal{S}(B)\, dB + k^2 \left(\frac{a}{p} + qa\right)^2 \int_{-\infty}^{+\infty} \mathcal{S}(B)\, dB = \tag{2.28}$$

$$= \frac{pN}{3}\left(\frac{a}{p} - qa\right)^2 + k^2\left(\frac{a}{p} + qa\right)^2 \tag{2.29}$$

Therefore, we now have the second moment of the p-th oligomer as:

$$\Delta B_p^2 = \frac{pN}{3}\left(\frac{a}{p} - qa\right)^2 + \frac{pN}{3}\left(\frac{a}{p} + qa\right)^2 \tag{2.30}$$

and after taking the square root and simplifying we obtain:

$$\Delta B_p = \sqrt{1 + p^2 q^2}\frac{\Delta B_1}{\sqrt{p}}; \forall p > 1. \tag{2.31}$$

This final analytical result is a first-order generalisation of the Norris equation which allows for an average non-uniformity in the spin density, as quantified by the q-value. It can be seen that equation 2.1 is fully recovered when $q = 0$, and that if $q \neq 0$, the envelope linewidth of the p-th oligomer spectrum will be larger than the envelope predicted by the Norris equation. Importantly, when $q \neq 0$, the spin density can still be distributed such that each unit of the oligomer has the same overall spin density, however, the density within a unit is non-uniform. In other words, if the original Norris equation is not followed, then it does not mean that the spin density is incompletely delocalised across the units, it is merely non-uniform. In essence, equation 2.31 shows that the Norris equation is not a necessary criterion for spin delocalisation.

Finally, the Norris equation is also not a sufficient criterion for delocalisation. This is because in deriving the first-order generalisation in 2.31, we have neglected the inherent linewidth of the EPR peaks. If the inherent Lorentzian linewidth is of the order of qa, then it is possible for a series of oligomers to follow the Norris equation, despite the fact that $q \neq 0$ (as will be shown to be the case for the ***l2*-PN**$^{+\cdot}$ series).

2.3 The monomer system as a reference

In order to study the degree of delocalisation of the spin density in a series of oligomers by means of the Norris equation, a suitable reference system should be chosen (in order to obtain ΔB_1). Since the natural reference choice for the oligoporphyrins in figure 2.1 is the monomer system, ***l1*-P1**$^{+\cdot}$, its room temperature cwEPR spectrum will be discussed in this section. Without such a discussion, the spectra of the longer oligomers cannot be interpreted. The precise details regarding the experimental and computational work in this section will be deferred to the next section, whereby the discussion of the entire series is resumed in earnest.

Figure 2.4 shows the liquid solution cwEPR spectra of ***l1*-P1**$^{+\cdot}$ acquired at room temperature with two different modulation amplitudes, B_{mod} = 1 and 0.1 G. Both spectra are centred around a field value of ca. 347.85 mT which, at 9.75 GHz, corresponds to an isotropic g-value of ca. 2.00263. This g-value is

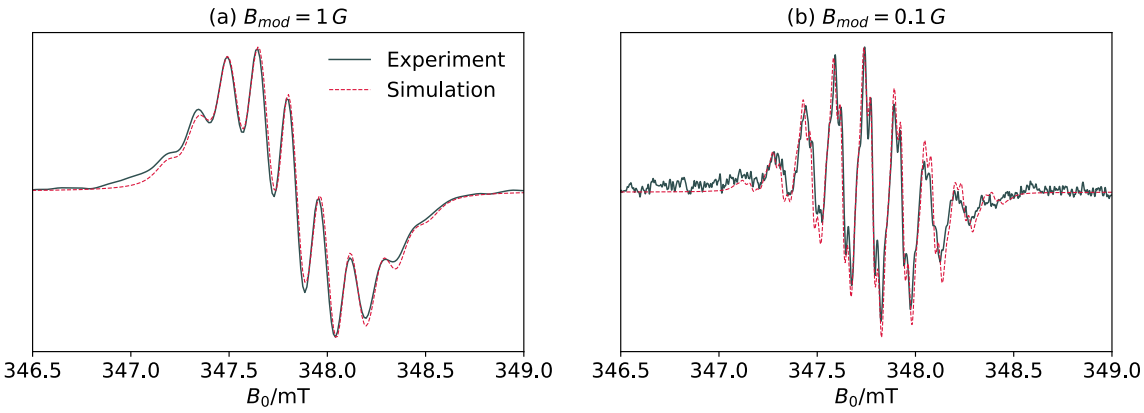


Figure 2.4: Room temperature X-band (9.75 GHz) cwEPR spectra of ***l1*-P1**$^{+\cdot}$ (solid grey line) and simulated spectra (dashed red line). The spectra in panels (a) and (b) were acquired with a modulation amplitude of 1 G and 0.1 G, respectively. The simulation parameters are as follows: (a) g_{iso} = 2.0027, 4 equivalent ^{14}N hyperfine couplings of 4.202 MHz, 4 equivalent ^{1}H hyperfine couplings of 1.04 MHz, and an inherent Lorentzian linewidth of 0.339 mT, (b) g_{iso} = 2.0030, 4 equivalent ^{14}N hyperfine couplings of 4.32 MHz, 4 equivalent ^{1}H hyperfine couplings of 0.97 MHz, and an inherent Lorentzian linewidth of 0.0597 mT. The effect of field modulation was explicitly taken into account in the simulations, both of which were carried out using the function *garlic* in EasySpin [9].

close to the free-electron g-value, thus indicating that the unpaired electron experiences only a minor perturbation due to spin-orbit coupling.

Secondly, and more importantly, both spectra contain clearly resolved hyperfine structure consisting primarily of the larger peak-to-peak separation of ~ 0.1 mT. Furthermore, the spectrum in panel (b) also displays a smaller peak-to-peak separation of ~0.025 mT. Despite the fact that the spectrum acquired with B_{mod} = 0.1 G has a lower signal-to-noise ratio (as expected), it clearly contains more information than the spectrum with B_{mod} = 1 G. This indicates that there is a small degree of over-modulation in the spectrum in panel (a).

Given that the discussion in this chapter is reliant on an accurate modelling of the hyperfine structure in the spectra of oligoporphyrin radical cations, it is clear that the modulation amplitude must be set to the lowest possible value, in line with the discussion in the previous chapter. This is important not only for the information content of the cwEPR spectra, but also for the general appearance of the spectral envelope from which ΔB_1 is extracted. More precisely, over-modulation not only reduces the information content, it also causes an artificial broadening of the overall spectral envelope.

The next point is concerned with the identity of the nuclei responsible for the hyperfine structure in figure 2.4. A cursory glance at the skeletal structure in figure 2.1 provides an initial guess: the unpaired electron is likely to reside in a π orbital primarily centred on the porphyrin core. Hence, a non-zero hyperfine coupling between the electron and the ^{14}N nuclei is expected. Hyperfine coupling to the pyrole ^{1}H nuclei is also feasible, however, these couplings should be weaker than the ^{14}N couplings because the Fermi-Contact interaction is attenuated when passing through the σ-bond framework (as described by McConnell in reference [7]). Furthermore, the spin density is likely to delocalise partially onto the aryl side chains. Hence, a non-zero hyperfine interaction with the protons attached to the aryl groups is also a sensible prediction. Of course, such arguments are not entirely reliable, but they help to paint a qualitative picture of the electronic structure.

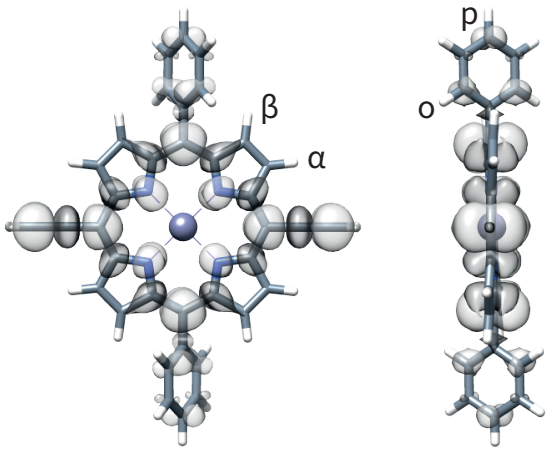


Figure 2.5: DFT predicted spin density of ***l1*-P1**$^{+\cdot}$ shown from two perspectives: top view on the left and side view on the right. For computational ease, the side-groups of the real system have been replaced by protons. The ORCA input file used in the calculation is provided in Appendix E.

Nucleus	$\tilde{\rho}/10^{-4}\mathrm{e}^{-}$	a_{iso}/MHz
^{14}N	861.4	+7.82
$^{1}\mathrm{H}_{\alpha}$	2.17	+0.35
$^{1}\mathrm{H}_{\beta}$	0.92	+0.03
$^{1}\mathrm{H}_{o}$	-9.76	-1.54
$^{1}\mathrm{H}_{p}$	-12.1	-1.60

Table 2.1: The Mulliken spin density, $\tilde{\rho}$, and DFT predicted isotropic hyperfine coupling constants, a_{iso}, corresponding to the four equivalent ^{14}N nuclei as well as the protons marked in figure 2.5. All other protons are not present in the real system, and are thus neglected.

A more quantitative description of the hyperfine couplings can be gained by calculating the spin density of ***l1*-P1**$^{+\cdot}$ using an appropriate electronic structure method. Figure 2.5 shows the spin density of ***l1*-P1**$^{+\cdot}$ obtained from a Density Functional Theory (DFT) calculation carried out using the ORCA software [45]. It is immediately obvious that the qualitative arguments of the previous paragraph are vindicated by the actual spin density depicted in figure 2.5. This can also be seen clearly in Table 2.1 which shows the net unpaired electron densities (quantified by the Mulliken spin populations)[7] of the nitrogens and protons as well as the predicted hyperfine coupling constants corresponding to these nuclei.

Although the DFT results displayed in figure 2.5 and table 2.1 are informative, there is a slight discrepancy between the theoretical hyperfine couplings and the experimental values obtained from the spectral simulations in figure 2.4. For instance, the experimental data shows that the hyperfine coupling to the ^{14}N nuclei is 45% smaller than the one predicted from the DFT spin density (see the caption of figure 2.4 and table 2.1).

One could hypothesize a number of reasons for this mismatch between experiment and theory. For example, the true electronic wavefunction could be an admixture (linear combination) between the lowest energy wavefunction predicted by DFT and an accessible excited state. Indeed, there is a low lying excited state at an energy of ca. 3200 cm^{-1} above the ground state corresponding to the unpaired

[7]The Mulliken spin population is shown in units of 'unpaired electron number' *i.e.* the sum of the spin populations on all the atoms will be equal to the number of unpaired electrons.

electron being promoted to the lowest unoccupied molecular orbital.[8] However, when the hyperfine coupling to the nitrogen nuclei is calculated for this excited state, the result is surprisingly similar, namely 7.83 MHz (*cf.* 7.82 MHz in the ground state). Hence, it is likely that different factors are at play.

Another potential explanation for the discrepancy between experiment and theory could be the accuracy of the basis set employed in the DFT calculation. The results in table 2.1 were obtained using the def2-SVP basis set for all atoms. It is possible that this basis set does not perfectly capture the so-called 'cusp' of the atomic orbitals at the position of the nucleus *i.e.* def2-SVP is inaccurate near the nucleus. Since the Fermi-Contact interaction exists only at the nucleus, this could be the reason behind the discrepancy. Indeed, by repeating the DFT calculation with the EPR-II basis set (which is specifically designed for more accurate EPR parameter calculations, see reference [46]), the resulting nitrogen hyperfine coupling is 3.13 MHz which is in much better agreement with the experimental value of 4.32 MHz.

As far as the ^{1}H hyperfine couplings are concerned, the DFT calculation correctly predicts their smaller magnitude compared to nitrogen. However, the experimental cwEPR spectra in figure 2.4 are dominated by the ^{14}N couplings, hence why, simulations with only four equivalent ^{1}H couplings are sufficient to reproduce the data. This is in spite of the fact that DFT predicts that more than four protons will have a hyperfine coupling of ~1.5 MHz. Furthermore, at room temperature, the aryl protons (particularly the ortho protons–$^{1}H_{o}$) are highly likely to be rotating very rapidly, and thus, their hyperfine coupling is likely to be very different (and smaller) to the static value in table 2.1. As a result of this, the simulations of all oligomers will only assume four equivalent ^{1}H hyperfine couplings per porphyrin macrocycle.

2.4 CwEPR of the oligomers

Having described the cwEPR spectrum of the monomer in detail, it is now possible to proceed to the discussion of the remaining oligoporphyrins. The experimental cwEPR spectra will be interpreted both from the perspective of the Norris equation as well as by spectral simulations.

2.4.1 Sample preparation and cwEPR acquisition

Chemical oxidation. Samples for the cwEPR measurements were prepared in a fully deuterated solvent mixture of toluene, THF, and DCM in a 1:1:1 volume ratio and de-oxygentaed using several freeze-pump-thaw cycles. For chemical oxidation, 0.5 equivalents of tris(4-bromophenyl)- amonium hexachloroantimonate (1.0 mM in DCM) were added to a solution of porphyrin oligomer (0.1 mM) under argon just before the EPR measurements. The samples were prepared in X-band tubes (3.8 mm outer diameter).

Spectrum acquisition. The cwEPR spectra were acquired at X-band microwave frequencies at room temperature on a Bruker EMX Micro spectrometer equipped with a high sensitivity Bruker probe head. The microwave frequency of operation was ca. 9.40 GHz and the spectra were acquired with a modulation amplitude of 0.01 mT and a modulation frequency of 100 kHz. This chosen modulation amplitude offered a compromise between the signal-to-noise ratio and the potential distortions caused by larger

[8] As predicted by a time-dependent DFT calculation, for example.

modulation amplitudes, as shown in the previous section. The quality factor of the cavity was similar between all the measurements ($Q \approx 1000$). The microwave power was scanned to rule out linewidth distortions due to saturation effects. The optimal microwave power used in all the cwEPR spectra was 2 mW corresponding to an attenuation of 20 dB on our spectrometer. The average spectra were obtained by combining individually recorded scans in order to ensure that the signal intensity and line-shape remained constant in time. The field axis of the reported spectra was adjusted using a frequency correction factor to a common value of 9.75 GHz, in order to minimise the effects of slight shifts in the centre fields of the experimental data (due to slight differences in the actual acquisition frequencies).

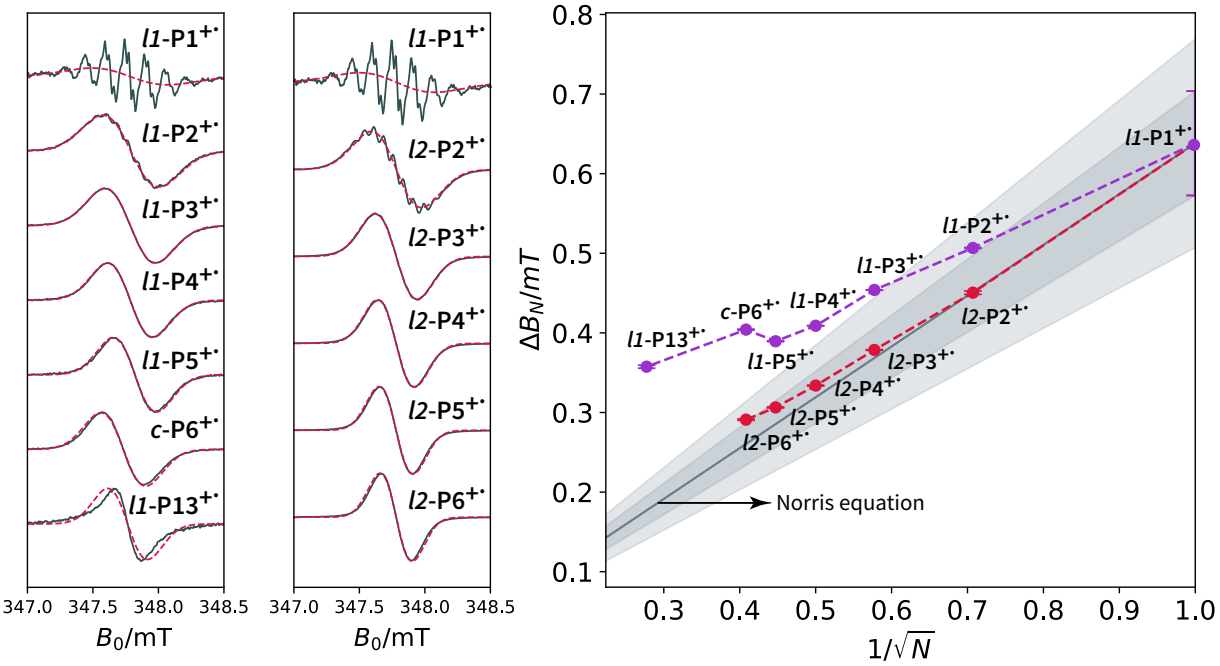


Figure 2.6: Linewidth analysis of the room temperature X-band cwEPR spectra (black lines in the left and central panel) of the radical cations of the linear porphyrin oligomers using a derivative Gaussian function as a model for the spectral envelope (dashed red lines). The linewidth of the best fit Gaussian envelope is plotted against $1/\sqrt{N}$ in the right panel for the two oligomer series. The dark grey shaded area represents the 95% confidence interval of the linewidth of the monomer spectrum, whereas the light grey shaded area shows an exaggerated uncertainty of ±0.1 mT. This exaggerated uncertainty illustrates the fact that the deviation from the Norris equation found for the ***l1*-PN**$^{+\cdot}$ series is significant.

2.4.2 Envelope linewidth analysis

The experimental cwEPR spectra of the ***l1*-PN**$^{+\cdot}$ and ***l2*-PN**$^{+\cdot}$ series of oligomers are shown in the left and central panels of figure 2.6. The second moments of these spectra were extracted by fitting to the normalised [9] data the following Gaussian function:

$$G_N(B_0) = \sqrt{\frac{2}{\pi}}\frac{1}{\Delta B_N}\exp\left[-2\left(\frac{B_0 - B_c}{\Delta B_N}\right)^2\right] \tag{2.32}$$

where B_0, B_c, and ΔB_N represent magnetic field, centre field, and second moment, respectively. The fitting was performed using the inbuilt MATLAB function *lsqnonlin* and the resulting values of ΔB_N

[9] To a unit double integral.

were plotted against $1/\sqrt{N}$ in order to compare the results with the Norris equation, as shown in the right panel of figure 2.6. The corresponding envelope functions, $dG_N(B)/dB$, are also shown as the red lines overlaid on the experimental data. The fact that the envelopes of (almost) all spectra are well reproduced by Gaussian functions is in line with the derivation in the previous section.

The 95% confidence interval relating to the envelope of the monomer spectrum (evaluated from the Jacobian matrix and residuals, as implemented in the *nlparci* function) is plotted as the dark grey shaded area in figure 2.6. As expected, there is a larger uncertainty associated with the monomer linewidth, ΔB_1. The gradient of the best-fit values of $\Delta B_{N\geq 2}$ was found to deviate significantly from the gradient predicted by the Norris equation even when an exaggerated error of ±0.1 mT is considered on the monomer envelope (light and dark grey shaded regions). The envelope of the ***l1*-P13**$^{+\cdot}$ spectrum deviates significantly from a Gaussian function (in fact, it becomes a Lorentzian) as per the discussion in the previous section. This linewidth behaviour for porphyrin oligomers with $N \geq 7$ was also observed in the work of Susumu et al. in reference [42].

If the entire discussion in section 2.2.1 were to be ignored, the overriding conclusion from figure 2.6 would be that the spin density in the ***l1*-PN**$^{+\cdot}$ series is less delocalised compared to the ***l2*-PN**$^{+\cdot}$ series. In other words, one might conclude that the butadiyne linker facilitates spin delocalisation, and hence, improves the viability of this series of oligoporphyrins as molecular wires. As will be detailed in the remaining sections, the origin of the deviations from the $1/\sqrt{N}$ trend are more subtle and require significantly more analysis, as well as further experimental evidence.

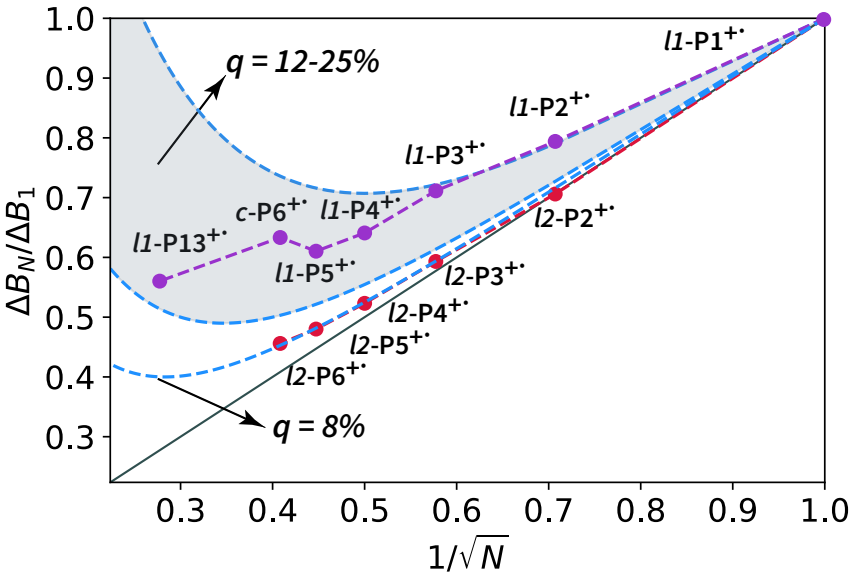


Figure 2.7: Analysis of the experimental Gaussian envelope linewidths of the porphyrin radical cations using equation 2.31. The shaded area corresponds to a non-uniformity parameter, q, in the range 12-25%. The butadiyne series, ***l2*-PN**$^{+\cdot}$, follows the 8% non-uniformity line, whereas the ethyne series, ***l1*-PN**$^{+\cdot}$, appears to be more non-uniform according to this first-order approximation.

Before however, some further information can be gleaned from the second moments of the ***l1*-PN**$^{+\cdot}$ series by comparison with the predictions from the first-order generalisation of the Norris equation. The experimental results as well as the theoretical plots for non-uniformity parameters of 8%, 12%, and 25% (equation 2.31) are shown in figure 2.7. Whilst it is not sufficient proof, this figure suggests that the data is consistent with a more uniform spin density in the butadiyne series compared with the ethyne

series. As will be seen in the next sections, DFT calculations enable the spin densities of the individual ^{14}N nuclei to be determined and the EPR spectra can be simulated directly. Nonetheless, from DFT we can still estimate an average non-uniformity parameter of ~7.5% for the ***l1*-PN$^{+\cdot}$** series which is less than half the one predicted in figure 2.7. This is, however, an acceptable discrepancy given that equation 2.31 assumes the existence of one clearly defined non-uniformity parameter, which is identical for all the porphyrin units of a given oligomer and also, it neglects the influence of the inherent linewidth of the transitions.

2.4.3 Spectral simulations

The deviations from the Norris equation described in the previous subsection are bound to be due to a failure of at least one of the assumptions which underpin this treatment. One of these essential assumptions is that the inherent linewidth of the EPR transitions is much smaller than the hyperfine coupling interaction (*i.e.* the spectral envelope is hyperfine dominated and the individual peaks are separated by more than the width of the lines) or that this inherent linewidth remains constant (and small) for all the oligomers.

In order to assess the possible breakdown of this assumption, the EPR spectra were simulated using the function *garlic* implemented in EasySpin. In the first instance, the best fit to the EPR spectrum of the porphyrin monomer was found by means of a least-squares fitting algorithm (in this case the Nedler-Mead simplex algorithm of the *esfit* function in EasySpin was used).

The parameters optimized in this fitting are an isotropic hyperfine coupling to 4 equivalent ^{14}N nuclei, an isotropic hyperfine coupling to 4 equivalent ^{1}H nuclei, an isotropic g-value, and a Lorentzian linewidth.[10] This particular choice of fitting parameters as well as the best fit values were shown and interpreted in section 2.3. The resulting parameters are consistent with the values reported in the literature [41].

After a suitable fit to the monomer spectrum was found, the spectra of the longer oligomers were obtained by dividing the values of the hyperfine couplings by the chain length, increasing the number of equivalent nuclei accordingly, and only allowing the inherent linewidth to be varied by the fitting algorithm. The results of these simulations are displayed in Figure 2.8.

These simulations indicate that if complete and uniform spin delocalisation is imposed on both series of oligomers (top and middle right panels of figure 2.8), then the data for the ***l1*-PN$^{+\cdot}$** series can only be simulated accurately by employing a significant change in the inherent linewidth. As can be seen in the bottom right panel of figure 2.8, the λ-value for the ethyne series rises by ca. 30% from ***l1*-P1$^{+\cdot}$** to ***l1*-P3$^{+\cdot}$**, whereas for the butadiyne series it remains small and constant.[11]

Initially, it might seem that there is a myriad of potential reasons for a change in λ with increasing N. In particular, this could be caused by changes in the rotational correlation times, τ_c, and/or relaxation rates. However, if the increase in λ between ***l1*-P1$^{+\cdot}$** and ***l1*-P3$^{+\cdot}$** were, for example, due to a change in τ_c as a function of molecular size, then we would expect the increase in λ to continue beyond ***l1*-P3$^{+\cdot}$**. Moreover, considering the structural similarity between the ethyne-linked oligomers and the

[10] Simulations with a Gaussian and Voigtian linewidth were also performed, however, the result of the optimization converged very closely to a predominant Lorentzian contribution

[11] The slightly larger change in λ between ***l2*-P1$^{+\cdot}$** and ***l2*-P2$^{+\cdot}$** is within the confidence interval of the best fit values for both.

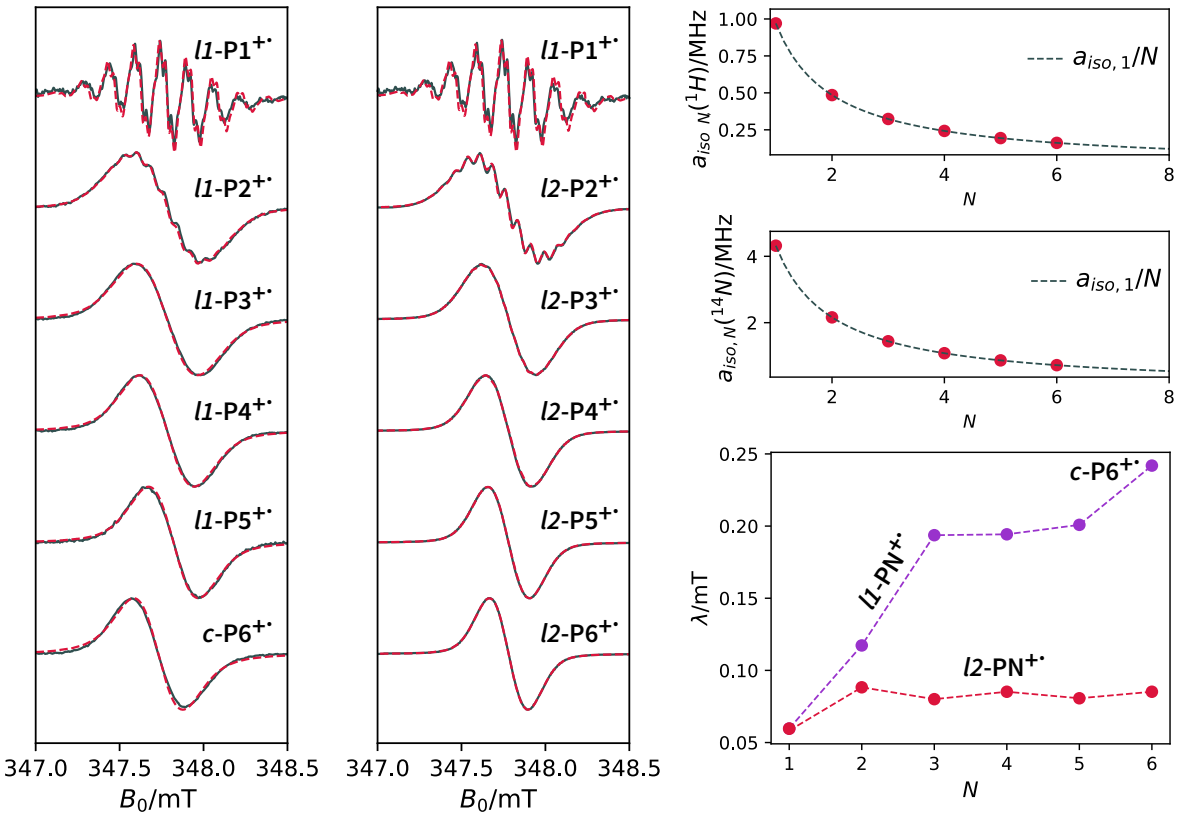


Figure 2.8: Numerical spectral simulations of the room temperature X-band cwEPR spectra of the radical cations of the linear and cyclic oligoporphyrins (except ***l1*-P13**$^{+\cdot}$ which contains too many nuclei to be handled correctly by *garlic*). The best fit to the monomer spectrum was found using a three-parameter fitting of the nitrogen hyperfines proton hyperfines, and an inherent Lorentzian linewidth, λ. The simulations for the longer oligomers were obtained from a one-parameter fitting of the inherent linewidth, whilst the hyperfine couplings were divided by the oligomer chain length (i.e. complete and uniform delocalization) and kept constant.

butadiyne-linked counterparts for which λ remains constant within error and approximately equal to the value obtained for ***l1*-P1**$^{+\cdot}$, the trends in λ depicted in figure 2.8 are unlikely to be caused by changes in τ_c.

Another potential cause for the differing trends in λ between the ***l1*-PN**$^{+\cdot}$ and ***l2*-PN**$^{+\cdot}$ series could be a difference in the time scales associated with dihedral angle distortions. When adjacent porphyrin units are bridged by ethyne groups, the steric hindrance of the α-pyrolle protons (figure 2.5) causes the porphyrins to adopt an angle of ca. 20° with respect to their molecular planes [47]. This might lead to different hyperfine couplings to the protons and nitrogen nuclei, which means that the spin density could be non-uniform in the ***l1*-PN**$^{+\cdot}$ series *e.g.* the eight nitrogen nuclei in the dimer could become significantly non-equivalent. Since the simulations in figure 2.8 impose equivalence of all the nuclei, the fitting algorithm compensates for the non-uniformity in spin density by increasing λ in an erratic manner.

It will be shown at the end of the next section, using DFT calculations, that the dihedral angle between adjacent units does indeed have an influence on the spin density. However, it will also be shown that the spin density in the ***l1*-PN**$^{+\cdot}$ series is generally more non-uniform regardless of dihedral angle. Thus, the significant deviation in ΔB_N from the Norris equation for the ***l1*-PN**$^{+\cdot}$ oligomers will be shown to

be caused by non-uniformity, as suggested by the analysis in figure 2.7.

2.5 The DFT computed spin densities

2.5.1 Methodology

The Gaussian16 software (reference [48]) was used for optimizing the geometries of the radical cations of the linear and cyclic oligoporphyrins as well as for computing the Mulliken spin densities necessary for simulating the EPR spectra. The basis set was def2-SVP for the H, C, and N centres, whereas def2-TZVP was used for Zn. The functional was B3LYP in all calculations. The THS substituents on the aryl groups and the protecting groups on the terminal ethynes were replaced with protons to increase the speed of the geometry optimization. The resulting structures are consistent with previous DFT optimizations and, as shown in figure 2.9, the linear ethyne-linked oligomers, ***l1*-PN**$^{+\cdot}$ have a dihedral angle of ~20° between adjacent porphyrin units, whilst the ***l2*-PN**$^{+\cdot}$ oligomers are flat [47].

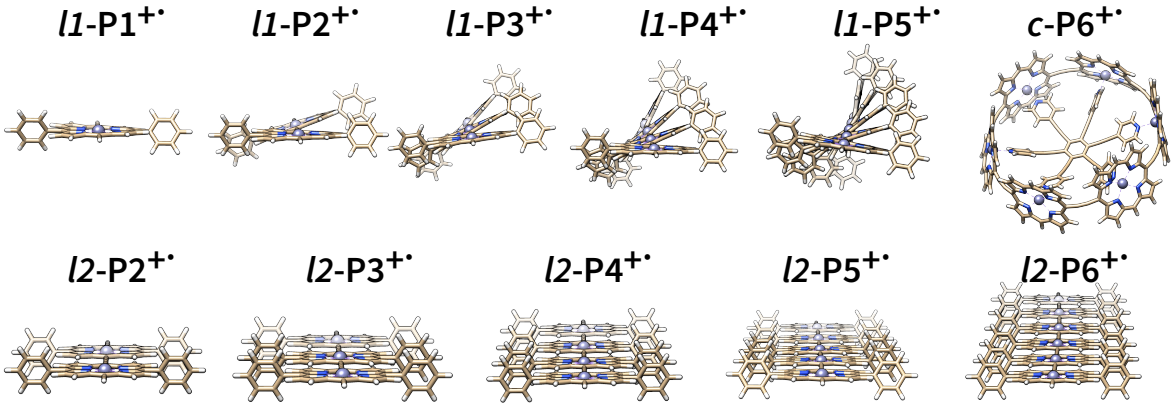


Figure 2.9: DFT optimised geometries of the linear and cyclic oligoporphyrin radical cations. The perspective was chosen in order to emphasize the dihedral angle differences between the two oligoporphyrin series.

The cw-EPR spectra presented in this work have a hyperfine structure which is attributed mainly to the nitrogen nuclei of the porphyrin units. Since the cwEPR spectra were acquired at room temperature, the observed couplings can be treated as isotropic with a magnitude proportional to the Mulliken spin density on the nitrogen atoms:

$$A_i = c\rho_i \tag{2.33}$$

The equation above is the McConnell relationship which states that the hyperfine coupling to a particular nucleus, A_i, is related to the spin density on that nucleus, ρ_i, via a proportionality constant, c, referred to as the McConnell constant. By using this equation, we can obtain a set of DFT predicted cwEPR spectra.

In order to generate DFT predicted spectra, the McConnell constant was determined from the EPR spectrum of the monomer. More precisely, the monomer spectrum was fitted using *garlic* in EasySpin to obtain the hyperfine coupling to the four equivalent ^{14}N nuclei as well as the inherent linewidth. By contrast with the simulations presented in the previous section, in this case, the proton couplings were treated as being part of the inherent Lorentzian linewidth and they were not explicitly included

in the simulations. The proton couplings were neglected in order to ease the computational cost of simulating using the large numbers of small DFT spin densities on all the protons (at least 14 non-equivalent protons need to be included just for the monomer). However, neglecting the protons only has an influence on the super-hyperfine structure of the monomer spectrum, but it does not change the overall linewidth of the Gaussian envelope, and it is insignificant for the larger oligomers.

The McConnell constant was then determined by dividing this hyperfine coupling by the ^{14}N Mulliken spin density determined from the DFT calculation of the monomer. As such, c was determined to be 51.25 MHz and the inherent Lorentzian linewidth is 0.12 mT. These values were then used together with the ^{14}N Mulliken spin densities obtained from DFT to obtain the DFT predicted spectra in figure 2.11. These spectra were then analysed in the same manner as the experimental spectra to yield the trend in the linewidth of the spectral envelope. The Mulliken spin densities of the ^{14}N nuclei are plotted in figure 2.10.

2.5.2 ^{14}N spin densities and DFT predicted spectra

The first observation from the top four panels in figure 2.10 is that, qualitatively, the ***l1*-PN**$^{+\cdot}$ and ***l2*-PN**$^{+\cdot}$ oligoporphyrin series have very similar ^{14}N spin densities. For both series, the two terminal porphyrin units beyond $N = 3$ have a smaller spin density compared with the central porphyrin units. By contrast, the spin densities in the dimers (shown in the top left panel) imply that the two peripheral ^{14}N nuclei have an enhanced spin density compared to the two central ^{14}N nuclei.

The second observation is that the average spin density of all the ^{14}N nuclei is approximately inversely proportional to N, as depicted in the bottom left panel of 2.10. In other words, as far as the nitrogen nuclei are concerned, the spin density is completely delocalised over the entire length of the oligomer. However, in the bottom right panel we see that the standard deviation from the mean, *i.e.* the non-uniformity of the spin density,[12] is consistently larger in the ***l1*-PN**$^{+\cdot}$ series compared with the ***l2*-PN**$^{+\cdot}$ series. In summary, the bottom two panels in figure 2.10 show that whilst the spin density is completely delocalised in both series, it is slightly more non-uniformly delocalised in the ***l1*-PN**$^{+\cdot}$ series.

In light of these observations, the natural question is whether the slightly enhanced non-uniformity (by ~2%) in the ***l1*-PN**$^{+\cdot}$ series is sufficient to cause a 25% deviation from the Norris equation. Purely from the theoretical result in equation 2.31 and the DFT spin densities in figure 2.10, the discrepancy between the two series should be significantly less pronounced.

However, the first-order generalisation in equation 2.31 is only valid in the limit of infinitely sharp peaks in the cwEPR spectrum. Once the inherent linewidth of the transitions is taken into account, the difference in non-uniformity predicted by DFT in figure 2.10 is sufficient to account for the deviation from the Norris equation of the ***l1*-PN**$^{+\cdot}$ series. This is illustrated in figure 2.11 whereby the DFT predicted spectra obtained directly from the Mulliken spin densities[13] follow an envelope trend which very closely resembles the experimental trend.

In summary, the good agreement between experiment and DFT in figure 2.11 is confirmation of the fact that the spin density in the ethyne bridged oligomers is approximately just as delocalised as in the

[12] The non-uniformity was calculated as the ratio between the standard deviation of the spin densities and the average spin density.

[13] For the linear oligomers, these are plotted in figure 2.10. For the monomer, the spin density is shown in table 2.1. There is also an additional DFT predicted EPR spectrum in figure 2.11 for the ***c*-P6**$^{+\cdot}$ system.

butadiyne-bridged series. However, the more pronounced non-equivalence between the ^{14}N nuclei in every non-central porphyrin unit depicted in the top four panels of figure 2.10 is responsible for the deviations from the Norris equation. This finding illustrates clearly that, whilst important, the trends in ΔB_N must not be interpreted in isolation in order to avoid erroneous conclusions.

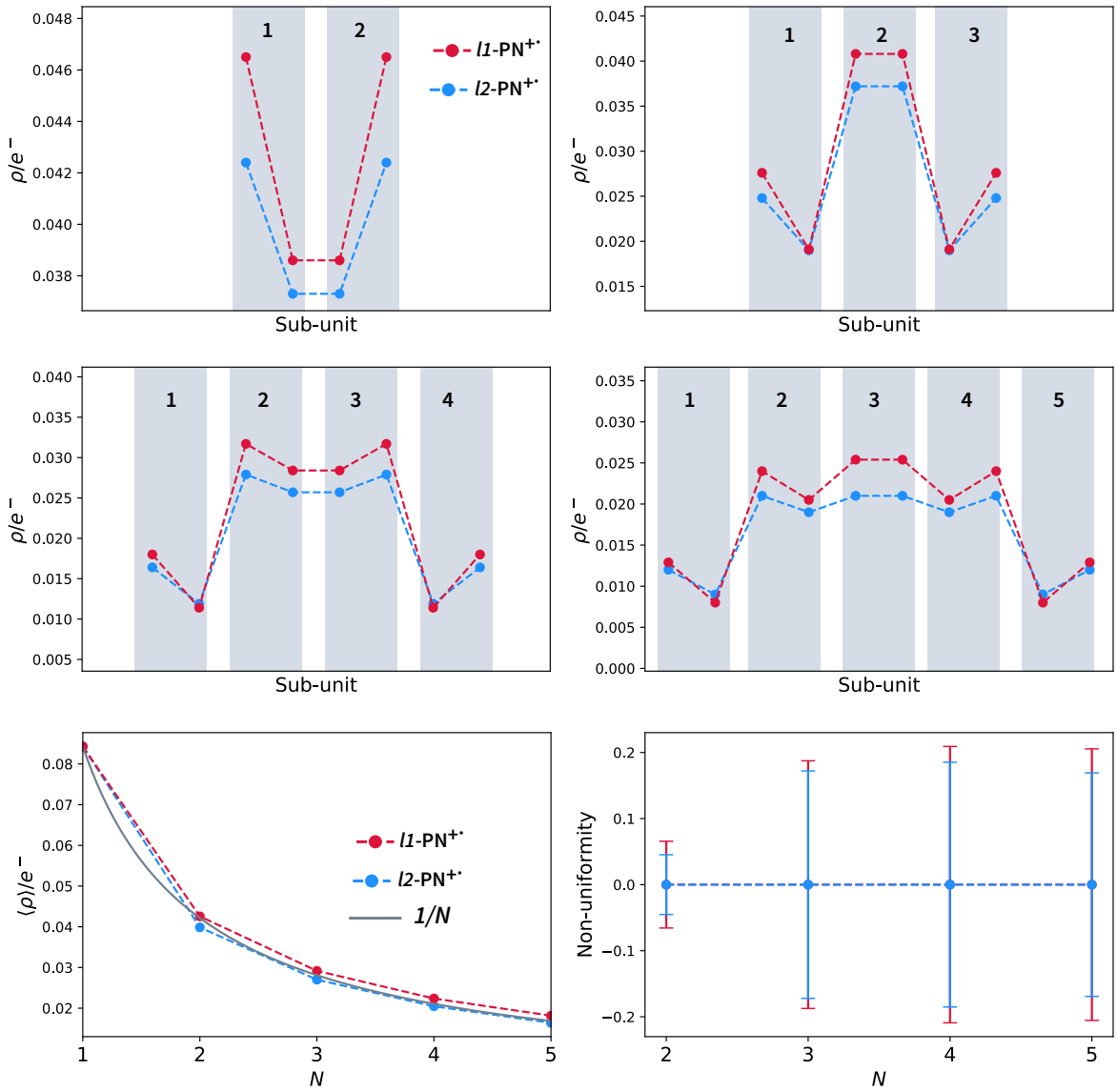


Figure 2.10: The top four panels represent the Mulliken spin densities of the ^{14}N nuclei for all the linear oligomers (except the monomer). The shaded area denotes each individual sub-unit. Within a sub-unit there are two data points, each of them corresponding to a set of two equivalent ^{14}N nuclei. The bottom left panel depicts the trend in the average ^{14}N spin density across both oligoporphyrin series. The non-uniformity in these spin densities is shown in the bottom right panel for all the linear oligomers except the monomer (which is perfectly uniform). In all panels, blue lines and markers refer to the ***l2*-PN$^{+\cdot}$** series, and red lines and markers refer to the ***l1*-PN$^{+\cdot}$** series.

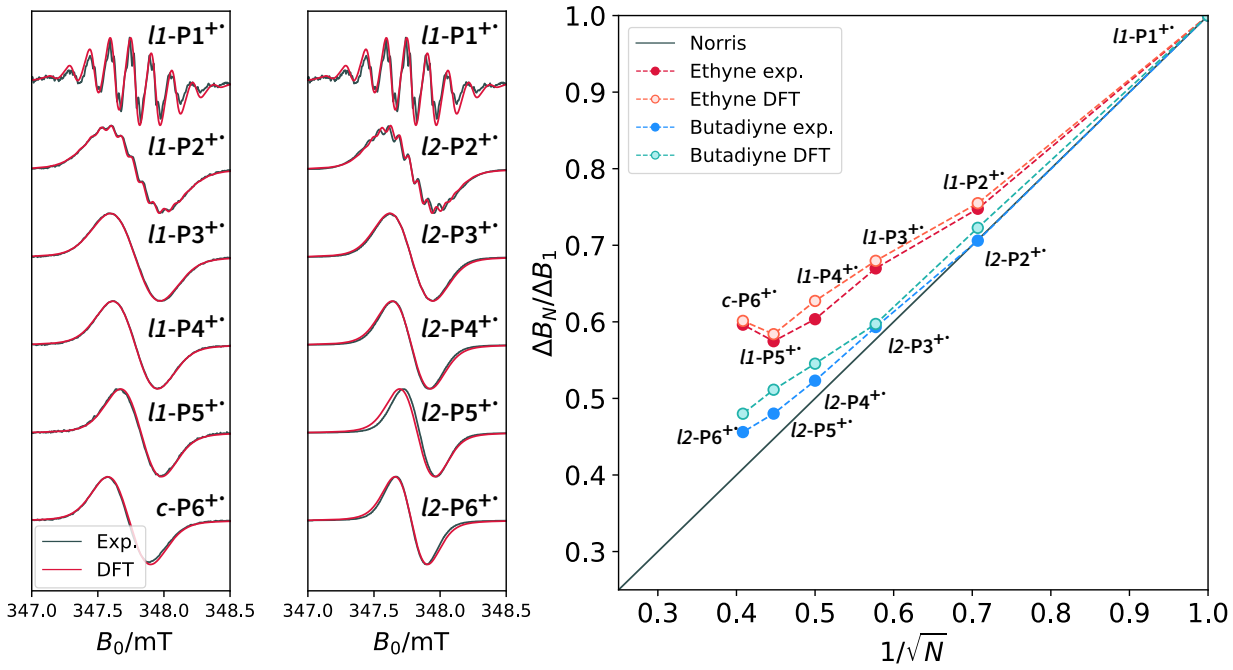


Figure 2.11: The experiemental and DFT predicted cwEPR spectra for the ***l1*-PN**$^{+\cdot}$ and ***l2*-PN**$^{+\cdot}$ series are depicted in the left and middle panels, respectively. The DFT cwEPR spectra were generated from the Mulliken spin densities in figure 2.10, as described in the previous methodology section. The DFT predicted spectra were analysed using the same principles as used for the experimental data. The resulting DFT predicted values of ΔB_N are plotted in the right panel along with the experimental values which have also been shown in figures 2.6 and 2.7.

2.5.3 Dihedral angle dependence of ^{14}N spin densities

By comparison with previous experimental and computational studies on similar porphyrin structures, it might be argued that the trends in ΔB_N observed here could be caused by differences in inter-porphyrin dihedral angle distributions. More precisely, it could be argued that for the butadiyne-linked series, the dihedral angle dependence of the ^{14}N spin densities is averaged to a unique characteristic value for all the nuclei in a porphyrin unit due to the fact that the barrier for rotation (minimum is at ~ 0° with a barrier in the neutral dimer of ~3 kJ mol^{-1}) is similar to the thermal-energy at room temperature (~2.5 kJ mol^{-1}). For the ethyne-linked series, the barrier for rotation is larger (~5.9 kJ mol^{-1} in the neutral dimer) and the minimum energy conformation corresponds to a dihedral angle of ~ 20°. These rotation barriers are quoted from references [37–40, 47]. In light of the above, one might expect this difference in energy profiles to be the reason for the deviation of the ***l1*-PN**$^{+\cdot}$ series from the Norris equation.

To test this hypothesis, the spin density on the ^{14}N nuclei of the ethyne- and butadiyne-linked dimers was calculated as a function of the dihedral angle between the porphyrin units. The results of these calculations are summarized in figure 2.12. First of all, at the equilibrium angle (~ 20° for ***l1*-P2**$^{+\cdot}$ and ~ 0° for ***l2*-P2**$^{+\cdot}$), the spin density on the peripheral ^{14}N nuclei (ρ_p) is larger than the spin density on the central ^{14}N nuclei (ρ_c) for both dimer systems. For ***l2*-P2**$^{+\cdot}$, it can be seen that in the range 0–50°, ρ_p is larger than ρ_c, whereas in the range 50–90°, ρ_c is the largest. This implies that, in an ensemble, there will be approximately just as many conformers with $\rho_p > \rho_c$ as with $\rho_c > \rho_p$. This is further illustrated by the fact that the average central and peripheral spin densities are very similar, as shown in the right

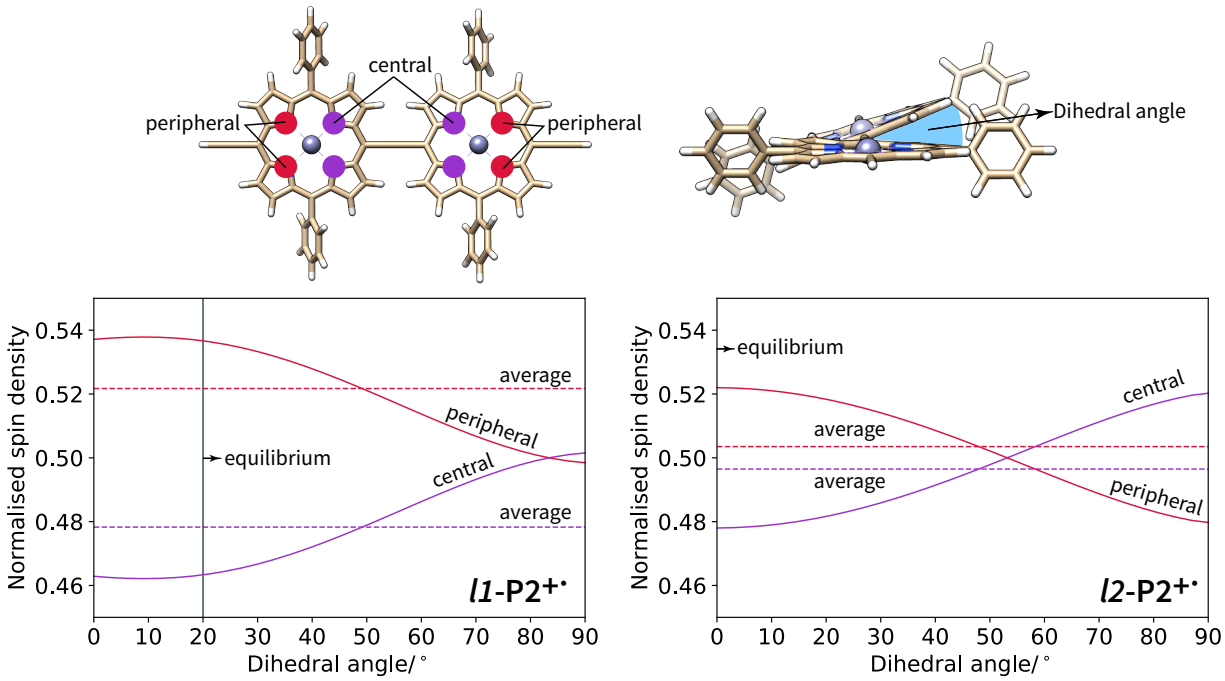


Figure 2.12: Dihedral angle dependence of the DFT predicted ^{14}N Mulliken spin density of the central and peripheral sets of equivalent nitrogen nuclei in the ethyne- (left) and butadiyne- (right) linked dimers. The dashed lines show the averaged spin density, whereas the vertical line indicates the equilibrium geometry of ***l1*-P2**$^{+\cdot}$.

panel of figure 2.12 –the ratio of the averages is ρ_c/ρ_p = 98%.

However, for ***l1*-P2**$^{+\cdot}$, figure 2.12 reveals a different trend compared to ***l2*-P2**$^{+\cdot}$. We observe that the value of ρ_p is larger than ρ_c over a much wider range of dihedral angles (0– 85°). Moreover, the ratio of the average spin densities is ρ_c/ρ_p = 91%. This difference in the ratios of ρ_c/ρ_p (which is, in essence, a measure of the non-uniformity of the spin density averaged over all angles) between the two dimers is sufficient to cause a –small– change in the appearance of the two cwEPR spectra, as illustrated in the simulations in figure 2.13.

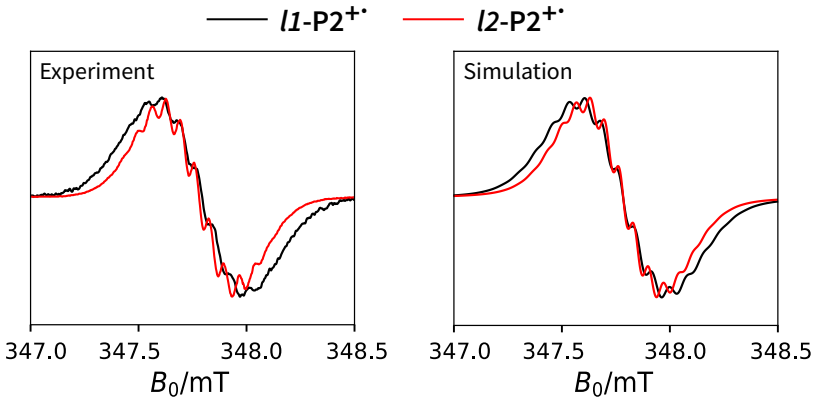


Figure 2.13: (Left) The experimental cwEPR spectra of ***l1*-P2**$^{+\cdot}$ and ***l2*-P2**$^{+\cdot}$. (Right) The corresponding simulations of the two dimers performed using the dihedral averaged spin densities marked with the dashed lines in figure 2.12. The inherent Lorentzian linewidth was kept the same as the one used to generate the DFT predicted EPR spectra in the previous section.

The experimental (left panel of 2.13) difference between the two dimers is more pronounced than predicted in the simulation (right panel of 2.13). As a result, it is unlikely for the dihedral angle dependence of the ^{14}N spin density to be the sole cause of the observed deviations from the Norris equation. It might nonetheless be argued that for the longer ethyne-linked oligomers, the dihedral averaged non-uniformity in spin density could be more pronounced than in the dimer.

However, based on these calculations alone, the dihedral averaged distortion in spin density is likely not to be sufficient to account for the experimental trend for the longer oligomers. In summary, these DFT calculations seem to indicate a less uniform spin delocalisation in the ***l1*-PN**$^{+\cdot}$ series, albeit the degree of non-uniformity seems to be underestimated (more so when the dihedral angle dependence is included).

2.6 ^{1}H-ENDOR measurements

2.6.1 Experimental method

Pulse EPR experiments were carried out at 85 K at Q-band microwave frequencies (~34 GHz) on a Bruker Elexsys 580 spectrometer equipped with an Oxford Instruments gas flow cryostat. The Mims ENDOR spectra reported in this section were acquired with the pulse sequence $\pi/2-\tau-\pi/2-T-\pi/2-\tau-echo$ with microwave pulse lengths of 44 ns and τ = 260 ns. A 16 μs radiofrequency π–pulse was applied during the mixing period, T. The power of the radiofrequency pulse was adjusted to form a π–pulse using a nutation experiment at the Larmor frequency of ^{1}H (ca. 51 MHz) for the field position corresponding to the maximum echo intensity. The spectra were recorded using different τ values in order to rule out the presence of distortions due to the blind-spots characteristic of the Mims ENDOR pulse sequence. Figure 2.14 presents a summary of all the recorded ^{1}H-ENDOR spectra.

The ^{1}H-ENDOR measurements reported in this thesis have been focused primarily on the ethyne-linked oligomers, with the exception being the spectrum of ***l2*-P2**$^{+\cdot}$ which has also been reproduced for the purpose of the proceeding discussion. The full set of spectra for the ***l2*-PN**$^{+\cdot}$ series is discussed in the previous work of Peeks, Tait, et al. [41]. The ***l2*-P2**$^{+\cdot}$ spectrum reported here is almost indistinguishable from the one in reference [41] (measured at W-band microwave frequencies).

2.6.2 Summary of ^{1}H-ENDOR results

Mims ENDOR is a complementary method for determining hyperfine couplings not typically accessible in cwEPR. While a direct and quantitative correlation between the room-temperature cwEPR data and frozen solution measurements is not always possible, the pulse ENDOR spectra in figure 2.14 give us valuable insight into the electronic communication between the porphyrin units and, with accompanying spectral simulations, can validate the accuracy of the DFT calculations presented in the previous section.

These ENDOR spectra are typical of ^{1}H nuclei in the weak coupling regime[14]. In this regime, the ENDOR peaks are centered at the Larmor frequency of ^{1}H and split by the hyperfine coupling constants of all the individual protons present in the molecule. By contrast to the room temperature cwEPR measurements,

[14] *i.e.* the hyperfine coupling is much smaller than the Larmor frequency (~51 MHz at these field positions).

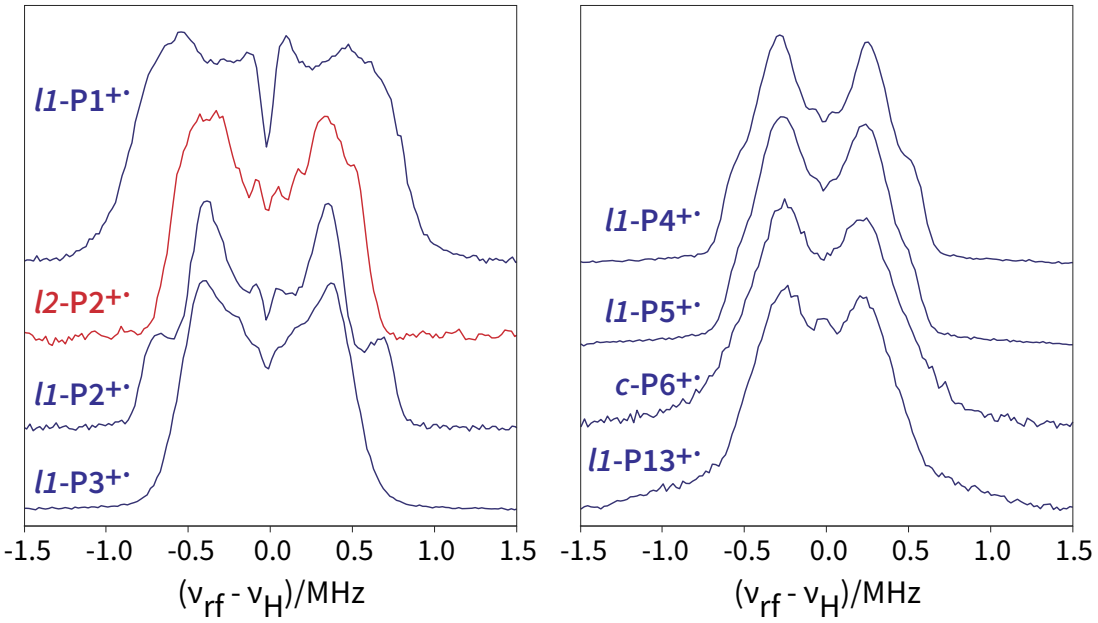


Figure 2.14: The ^{1}H-ENDOR spectra of the linear and cyclic ethyne-linked oligomers (blue) and of the butadiyne-linked dimer (red). All spectra were recorded at Q-band microwave frequencies and at the field position corresponding to the maximum stimulated echo signal.

these ^{1}H-ENDOR spectra are acquired at cryogenic temperatures [15] and as a result, the anisotropy of the hyperfine coupling interactions is resolved and the interpretation of the spectra is more complicated.

A direct deconvolution of the monomer spectrum involves performing a simultaneous fit of 84 parameters corresponding to 3 eigenvalues and 3 Euler angles describing the hyperfine coupling tensor of each one of the 14 protons. As a consequence, a deconvolution of the spectra for the longer oligomers would involve a simultaneous fit of $84N$ independent parameters. Such an analysis is impractical, if not impossible, and as a result, a quantitative interpretation of these spectra relies on an *a priori* knowledge of the hyperfine coupling tensors (*e.g.* from DFT calculations; see next section).

Nonetheless, there are a few conclusions to be drawn from a qualitative analysis of the shape of the ^{1}H-ENDOR spectra in figure 2.14. Firstly, by comparing the spectra of the ***l1*-P2**$^{+\cdot}$ and ***l2*-P2**$^{+\cdot}$ dimers, the width of the former is seen to be larger than the width of the latter spectrum. The ***l2*-P2**$^{+\cdot}$ dimer spectrum (red line in 2.14) has half the width of the monomer spectrum, which was previously interpreted as an indication of complete delocalisation of the proton spin density [41].

By contrast, the ***l1*-P2**$^{+\cdot}$ spectrum reveals that there are two distinct groups of protons with hyperfine couplings of ~0.7 MHz and ~1.4 MHz. This observation is in agreement with the previous discussion of the cwEPR spectra whereby the ethyne linker was shown to cause distortions in the spin density thus leading to non-uniform spin delocalisation. In turn, this causes groups of protons (or nitrogens for the cwEPR spectra) to have larger hyperfine couplings.

Closer inspection of figure 2.14 reveals a decrease in spectral width by a factor of 1.6 from ***l1*-P1**$^{+\cdot}$ to ***l1*-P5**$^{+\cdot}$. This result is significant: if the spin density were uniformly delocalised over the porphyrin units, the width of the ^{1}H-ENDOR spectra would be inversely proportional to N, by analogy with the Norris equation. Noteworthy is that the ^{1}H-ENDOR spectrum of ***l1*-P13**$^{+\cdot}$ is essentially identical to

[15] 85 K; necessary because of the fast spin-spin relaxation times in liquid solution.

that of ***l1*-P5**$^{+\cdot}$, whereas the room temperature cwEPR spectrum of ***l1*-P13**$^{+\cdot}$ is narrower than that of ***l1*-P5**$^{+\cdot}$ (figure 2.6).

Previously, it was conjectured that the saturation of the width of the low temperature ENDOR spectra for oligoporphyrins beyond the trimer is due to a decrease in the rate of thermally activated hopping [41]. Such arguments could, at first sight, be used to explain why the room temperature cwEPR spectra of the longer oligomers indicate a greater extent of spin delocalisation compared with the low temperature ENDOR measurements.

However, there are three key issues associated with such arguments: (1) at room temperature, fast hopping would appear indistinguishable from the static delocalisation pattern proposed in this thesis[16], (2) at low temperatures, the effects of slower hopping on the linewidth of the ENDOR spectra would be indistinguishable from the effects of hyperfine anisotropy resolution, and (3) these arguments completely neglect the non-uniformity of the spin density which also leads to a narrowing or broadening of the cwEPR and ENDOR spectra alike. In fact, as will be shown in the next section, and in appendix F (figure F.1), all the ENDOR spectra can be simulated relatively accurately using the static spin densities obtained from DFT, similarly to the way in which the same DFT calculations yielded a good explanation for the observed trends in ΔB_N (figure 2.11).

In summary, all the data and calculations presented thus far in this chapter, are consistent with a static spin delocalisation pattern over the molecular backbone of these oligoporphyrin radical cations. Within the rigid experimental and theoretical framework set out here, no justifiable conclusion can be drawn about the rate of thermally activated polaron hopping, even if such a phenomenon were to take place in these systems. The only potential outlier of this framework is the ***l1*-P13**$^{+\cdot}$ oligomer, which due to its record chain length, lies outside the boundary in which the Norris equation is applicable and additionally, its spin density is not currently obtainable by DFT.

2.6.3 ^{1}H spin densities and hyperfine tensors of ***l1*-P1**$^{+\cdot}$, ***l1*-P2**$^{+\cdot}$, and ***l2*-P2**$^{+\cdot}$

The above discussion of the ENDOR data is partially supported by a more theoretical approach to disentangling the contributions of individual groups of protons to the total spectrum. In an equivalent manner to how the ^{14}N Mulliken spin densities were used to evaluate the cwEPR spectra in the previous section, the ^{1}H spin densities can be used to evaluate the hyperfine coupling tensors, and hence, the ^{1}H-ENDOR spectra. The results for the entire series are shown in figure F.1 of appendix F, whilst figure 2.15 summarises the analysis only for the ***l1*-P1**$^{+\cdot}$, ***l1*-P2**$^{+\cdot}$, and ***l2*-P2**$^{+\cdot}$ systems, which offer the most insight. Similar calculations were reported in reference [49] for the ***l2*-P2**$^{+\cdot}$ system.

It can be seen in figure 2.15 that for the monomer, there is a set of larger hyperfine couplings corresponding to the ortho- and para-phenyl protons of the aryl side chains, as well as a set of smaller couplings to the porphyrin protons. By contrast, the majority of the largest hyperfine couplings in the dimers belong to porphyrin protons, and especially to the protons close to the ethyne/butadiyne linker (marked with an asterisk in 2.15). These α-pyrole protons can be assigned to the shoulders in the experimental ^{1}H-ENDOR spectrum of ***l1*-P2**$^{+\cdot}$. Given these results, it would seem that the monomer and dimer ^{1}H-ENDOR spectra should not be interpreted in terms of the observed narrowing of the spectral width because the couplings do not correspond to the same groups of protons.

[16] based on the (time independent) DFT spin densities shown in the previous section.

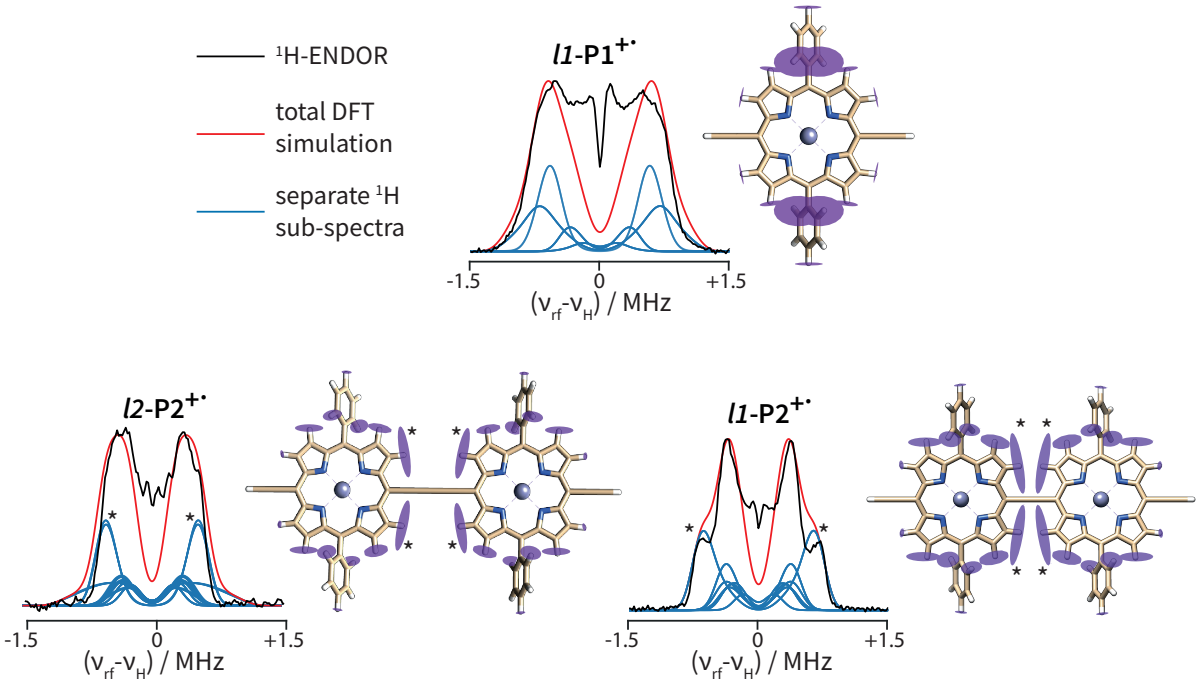


Figure 2.15: The blue lines are separate simulations of the individual ^{1}H-ENDOR spectra using the DFT derived hyperfine coupling tensors. The red line is the sum of the spectra of the individual protons and it is shown overlaid on the experimental spectrum (black). To the right of each ENDOR spectrum is the pictorial representation of the hyperfine coupling tensors as ellipsoids centred at the position of the corresponding proton. The asterisks mark the largest hyperfine couplings (to the α-pyrole protons) and the corresponding sub-spectra. The simulations were obtained using the function *saffron* in EasySpin [9].

Furthermore, the fact that the α-pyrole protons have an enhanced hyperfine coupling in ***l1*-P2**$^{+\cdot}$ *versus* ***l2*-P2**$^{+\cdot}$ is entirely mirrored by the previous observation [17] of an enhanced non-uniformity in the ^{14}N spin density. In as far as these ENDOR results are concerned, it is now clear that neither series of oligoporphyrins could be classed as being more suitable than the other for molecular devices. The extent of spin delocalisation in both series is very similar, and the minute changes observed in both the cwEPR and ENDOR spectra can be attributed to the effects of non-uniformity/ non-equivalence of the different nuclei of each type.

2.7 Concluding remarks

The spin delocalisation in the radical cations of a series of ethyne- and butadiyne-linked oligoporphyrins was investigated using EPR spectroscopy. The room temperature spectral envelope for the ethyne-linked oligomers deviates significantly from the benchmark $1/\sqrt{N}$ trend in linewidth expected for a completely delocalised spin density, in contrast to the butadiyne-linked analogues measured previously (figure 2.6)[41]. Here, we show, using DFT calculations and complementary low-temperature Mims ^{1}H-ENDOR measurements, that this deviation is primarily driven by a more pronounced inequivalence of the ^{14}N spins within individual sub-units for the ethyne-linked oligoporphyrins. Once this ^{14}N inequivalence is taken into consideration, the room temperature cwEPR and low temperature EN-

[17] in the cwEPR spectra

DOR spectra for both series can be simulated by similar static delocalisation patterns derived from DFT (figures 2.11 and 2.15).

In summary, this work illustrates clearly that EPR is a powerful tool for investigating the spin delocalisation in molecular wires when employed in combination with careful simulation and theory. As shown throughout this chapter, for the ethyne-linked oligomers, the assumptions behind the Norris equation, typically employed to probe the extent of spin delocalization at room temperature within such wires, break down. The observation of a significant deviation from the $1/\sqrt{N}$ trend could, at first sight, be easily misinterpreted as arising from reduced spin delocalisation across the wire in the ethyne-linked as compared to the butadiyne-linked structures, which follow this trend neatly. However, it became apparent that the differences between the cwEPR and ENDOR spectra exhibited by the two oligomer series have a more subtle origin, which does not negate the viability of either series as molecular wires.

Chapter 3

EPR spectroscopy of photo-generated triplet states

There are certain spin systems which only exist for periods ranging from a few tens of nanoseconds to a few hundreds of microseconds after they are produced. In this thesis, only two types of such transient radicals are considered: triplet states and spin-correlated radical pairs both of which are formed after photo-excitation of a diamagnetic ground state. The detection of the cwEPR spectra of such radicals is possible using two methods: continuous illumination and pulsed laser excitation.

In the former, a continuous source of light causes the build-up of a steady state concentration of the transient paramagnetic species which can then be detected using the usual cwEPR scheme described previously. On the other hand, the detection of short lived transient paramagnetic species formed after a nanosecond long laser pulse requires a modified version of the cwEPR experiment: namely, transient EPR (trEPR). This experiment will be described in this chapter, with particular emphasis on the photo-excited triplet states of organic chromophores. The discussion of spin-correlated radical pairs will be the subject of the final chapter.

As a substantial amount of the discussion in Chapters 4 and 5 is dedicated to the description of the ZFS in porphyrin triplet states, the origin of this interaction will be described below in detail and from first principles. Before however, it is necessary to introduce the spin-orbit coupling (SOC) interaction which leads to the phenomenon of **g**-tensor anisotropy, to certain contributions to the **D**-tensor, as well as to intersystem crossing.

3.1 The spin-orbit coupling interaction

By applying a non-relativistic approximation to the Dirac equation it is possible to predict successfully that the spin of electrons interacts with a magnetic field and that this interaction contains a relativistic correction factor $g_e = 2$. A first-order expansion of the Dirac equation leads to a general expression for the SOC interaction which takes the following form:

$$\hat{H}_{\mathrm{SOC}} = -\frac{i}{4m^2c^2}\hat{\boldsymbol{\sigma}} \cdot \left(\hat{\mathbf{p}} \times \left[\hat{\mathbf{p}}, \hat{V}\right]\right) \tag{3.1}$$

where $\hat{\boldsymbol{\sigma}}$, $\hat{\mathbf{p}}$, and $\hat{V}$ represent the Pauli, linear momentum, and potential energy operators. This equation is applicable to one electron atoms and molecules. The potential energy operator in such systems is defined as:

$$\hat{V} = -\frac{e^2}{4\pi\epsilon_0}\sum_k \frac{Z_k}{|\hat{\mathbf{r}} - \mathbf{r}_k|} \tag{3.2}$$

where Z_k and $\mathbf{r}_k$ are the charge and position of nucleus k. According to this equation, the electron is subjected to a net Coulombic potential which is a sum over all the nuclear potentials. By substituting equation 3.2 into 3.1 and performing a number of rearrangements, the well-known expression for the SOC interaction in one electron molecules is obtained:

$$\hat{H}_{\mathrm{SOC}} = \sum_k \hat{\xi}_k(r)\hat{\mathbf{s}} \cdot \hat{\mathbf{l}}_k \tag{3.3}$$

where the $\hat{\xi}_k(r)$ operator is defined as:

$$\hat{\xi}_k(r) = \frac{1}{4\pi\epsilon_0}\frac{e^2 Z_k}{2m^2c^2\,|\hat{\mathbf{r}} - \mathbf{r}_k|^3}. \tag{3.4}$$

A noteworthy aspect of equation 3.3 is the presence of the $\hat{\mathbf{l}}_k$ operator, which represents the orbital angular momentum of the electron relative to nucleus k. Unlike the usual angular momentum operator, the origin of $\hat{\mathbf{l}}_k$ cannot be chosen arbitrarily, it is pre-defined with respect to nucleus k.

In many electron molecules, the most general form of the SOC interaction is given by the Breit-Pauli equation [6]:

$$\hat{H}_{\mathrm{SOC}} = \frac{1}{4\pi\epsilon_0}\frac{e^2}{2m^2c^2}\left[\sum_i\sum_k \frac{Z_k}{\hat{r}_{ik}^3}(\hat{\mathbf{r}}_{ik}\times\hat{\mathbf{p}}_i)\cdot\hat{\mathbf{s}}_i - \sum_i\sum_{j\neq i}\frac{1}{\hat{r}_{ij}^3}\left(\hat{\mathbf{r}}_{ij}\times\hat{\mathbf{p}}_i\right)\cdot\left(\hat{\mathbf{s}}_i + 2\hat{\mathbf{s}}_j\right)\right] \tag{3.5}$$

One of the complications involved in calculating EPR parameters using equation 3.5 is that it contains a two-electron pairwise interaction [50, 51]. However, even in the presence of heavy atoms, this interaction is smaller than the one-electron term (with a few exceptions *e.g.* references [52, 53]). There are many methods with varying levels of precision for taking into account the two-electron SOC interaction in an approximate manner [50]. For example, many quantum chemistry software packages make use of the very successful spin-orbit mean field approach [51, 54, 55]. As far as this chapter is concerned, for simplicity, the crudest possible approximation, which does not completely neglect the effects of the two-electron terms in $\hat{H}_{\mathrm{SOC}}$ will be employed. This involves reducing the SOC Hamiltonian to the following equation:

$$\hat{H}_{SOC} \approx \frac{1}{4\pi\epsilon_0}\frac{e^2}{2m^2c^2}\sum_i\sum_k \frac{Z_k^{\mathrm{eff}}}{\hat{r}_{ik}^3}\hat{\mathbf{l}}_{ik}\cdot\hat{\mathbf{s}}_i \tag{3.6}$$

which is taking the two-electron contributions into account by the use of an effective (screened) nuclear charge, Z_k^{eff}, for every nucleus, k [56–60]. Apart from the effective nuclear charge, expression 3.6 is analogous to equation 3.3 used for one-electron molecules. The $\hat{\mathbf{l}}_{ik} = (\hat{\mathbf{r}}_{ik}\times\hat{\mathbf{p}}_i)$ operator corresponds to the orbital angular momentum of electron i relative to the origin at nucleus k.

3.2 The origin of the g-tensor

Whilst the most important spin Hamiltonian parameter for the discussion in chapters 4 and 5 is the **D**-tensor, the derivation of the **g**-tensor provides crucial insight into the origin of **D**. As such, this section will be focused on a derivation of the general form of the **g**-tensor as a preliminary step for the later derivations.

Apart from the SOC Hamiltonian in equation 3.6, the other interaction Hamiltonian needed for deriving a formula for the elements of the **g**-tensor is the spin and orbit Zeeman (SOZ) term:

$$\hat{H}_{SOZ} = \frac{\mu_B}{\hbar} \sum_i \mathbf{B} \cdot \left(\hat{\mathbf{l}}_i + g_e \hat{\mathbf{s}}_i \right). \tag{3.7}$$

Consider now the unperturbed Born-Oppenheimer eigenstates of multiplicity $(2S + 1)$:

$$\hat{H}_0 |aSM\rangle = E_a^{(0)} |aSM\rangle \tag{3.8}$$

where $M = -S, -S + 1, \ldots, S - 1, S$. Apart from the spin degeneracy, the states under consideration here are taken to be orbitally non-degenerate *i.e.* the 'a' part of the wavefunction, $|aSM\rangle$, is a real-valued function of the spatial coordinates. As aforementioned, the perturbation Hamiltonian will be taken as the sum of SOC and SOZ, and thus, the first-order correction to the energy is given by:

$$E_a^{(1)} = \langle aSM|\hat{H}_{SOZ}|aSM\rangle + \langle aSM|\hat{H}_{SOC}|aSM\rangle \tag{3.9}$$

After substituting equations 3.6 and 3.7 into the above, the results can be simplified further because the only non-vanishing term is the one involving the spin operator in SOZ. This is because all other operators are purely imaginary, and the expectation value of a purely imaginary operator over real-valued wavefunctions is exactly zero [1]. Thus, the first order correction to the energy is:

$$E_a^{(1)} = \frac{\mu_B}{\hbar} g_e \mathbf{B} \cdot \sum_i \langle aSM|\hat{\mathbf{s}}_i|aSM\rangle = \frac{\mu_B}{\hbar} g_e \mathbf{B} \cdot \langle aSM|\hat{\mathbf{S}}|aSM\rangle. \tag{3.10}$$

Therefore, by direct comparison of the last equation with the form of the EZ Hamiltonian used in the spin Hamiltonian formalism it can be concluded that the first-order contributions to the **g**-tensor are given by:

$$\mathbf{g}^{(1)} = g_e \mathbf{1} \tag{3.11}$$

where **1** is the (3×3) Cartesian unit matrix, *i.e.* the first-order contributions are isotropic.

When we move to second order corrections, it becomes necessary to generalise the perturbation theory expansion to states of different M. This is done in detail in McWeeny's exposition of the origin of spin Hamiltonian parameters [61].[1] The same procedure is briefly outlined by Neese and Solomon [56]. According to these references, the second-order contribution to the matrix elements between states of

[1] McWeeny's approach is referred to as the 'partitioning method', whereby the eigenvalues and eigenvectors of a relatively large matrix are grouped into sets which interact weakly (the cross entries in the original matrix are small). This allows one to diagonalize a smaller matrix which only describes the eigenstates of interest.

different M is given by:

$$\mathcal{E}^{a}_{MM'} = -\sum_{bM''} \Delta_b^{-1} \langle aSM|\hat{H}_{SOZ} + \hat{H}_{SOC}|bS'M''\rangle\langle bS'M''|\hat{H}_{SOZ} + \hat{H}_{SOC}|aSM'\rangle \tag{3.12}$$

where $\Delta_b = E_b^{(0)} - E_a^{(0)}$ is the unperturbed energy difference between states a and b. We see that, in principle, we have to consider the effect of four terms that occur from the expansion of the above equation. The terms that contribute to the electron Zeeman Hamiltonian have to be linear in magnetic field and also linear in the spin operators. Therefore, the parts of equation 3.12, that are relevant for the **g**-tensor are:

$$\mathcal{E}^{a}_{MM'}\left(\mathbf{B},\hat{\mathbf{S}}\right) = -\sum_{bM''} \Delta_b^{-1} \left[\langle aSM|\frac{\mu_B}{\hbar}\sum_i \mathbf{B}\cdot\hat{\mathbf{l}}_i|bS'M''\rangle\langle bS'M''|\hat{H}_{SOC}|aSM'\rangle + \right.$$
$$\left. + \langle aSM|\hat{H}_{SOC}|bS'M''\rangle\langle bS'M''|\frac{\mu_B}{\hbar}\sum_i \mathbf{B}\cdot\hat{\mathbf{l}}_i|aSM'\rangle \right] \tag{3.13}$$

And thus, only two types of matrix elements need to be calculated. First of all, because it does not act on the spin degree of freedom, the first orbital Zeeman matrix element cannot mix states with $S \neq S'$ and $M \neq M''$, whereas the second cannot mix states with $M'' \neq M'$. This restriction, together with the fact that $\langle SM|SM\rangle = 1$, reduces equation 3.13 to:

$$\mathcal{E}^{a}_{MM'}\left(\mathbf{B},\hat{\mathbf{S}}\right) = -\frac{\mu_B}{\hbar}\mathbf{B}\cdot\sum_b \Delta_b^{-1}\left[\langle a|\sum_i \hat{\mathbf{l}}_i|b\rangle\langle bSM|\hat{H}_{SOC}|aSM'\rangle + \langle b|\sum_i \hat{\mathbf{l}}_i|a\rangle\langle aSM|\hat{H}_{SOC}|bSM'\rangle\right] \tag{3.14}$$

Next, we turn our attention to the SOC matrix element, and apply the Wigner-Eckart theorem after expanding the dot product in the spherical basis [56]:

$$\langle bSM|\hat{H}_{SOC}|aSM'\rangle = \mathcal{C}\sum_q (-1)^q \langle bSM|\sum_i\sum_k \frac{Z_k^{eff}}{\hat{r}_{ik}^3}\hat{l}_{ik,-q}\hat{s}_{i,q}|aSM'\rangle \tag{3.15}$$
$$= \sum_q (-1)^q \langle SM'1q|SM\rangle \mathcal{L}_{ba}(-q) \tag{3.16}$$

where all the fundamental constants are grouped into $\mathcal{C} = \frac{1}{4\pi\epsilon_0}\frac{e^2}{2m^2c^2}$, and the q^{th} component of the vectorial reduced matrix element, $\boldsymbol{\mathcal{L}}_{ba}$, is defined as follows:

$$\mathcal{L}_{ba}(-q) = \mathcal{C}\langle bS||\sum_i\sum_k \frac{Z_k^{eff}}{\hat{r}_{ik}^3}\hat{l}_{ik,-q}\hat{\mathbf{s}}_i||aS\rangle. \tag{3.17}$$

Furthermore, the Clebsch-Gordan coefficient in 3.16 can easily be shown to be proportinal to the matrix elements of the total spin operator, $\hat{S}_q$, by retro-active application of the Wigner-Eckart theorem:

$$\langle SM'1q|SM\rangle = \frac{1}{\hbar\sqrt{S(S+1)}}\langle SM|\hat{S}_q|SM'\rangle \tag{3.18}$$

To simplify the notation, the following vector quantity is defined:

$$\boldsymbol{\Lambda}_{ab} = \Delta_b^{-1}\langle a|\sum_i \hat{\mathbf{l}}_i|b\rangle \tag{3.19}$$

Therefore, by combining equations 3.14-3.19 the second-order perturbation to the energy can be written in a more compact form:

$$\mathcal{E}^{a}_{MM'}\left(\mathbf{B},\hat{\mathbf{S}}\right) = -\frac{\mu_B}{\hbar^2\sqrt{S(S+1)}}\langle SM|\mathbf{B}\cdot\left\{\sum_b \mathbf{\Lambda}_{ab}\left(\boldsymbol{\mathcal{L}}_{ba}\cdot\hat{\mathbf{S}}\right)+\left(\boldsymbol{\mathcal{L}}_{ab}\cdot\hat{\mathbf{S}}\right)\mathbf{\Lambda}_{ba}\right\}|SM'\rangle \tag{3.20}$$

Given four vectors **a**, **b**, **c**, and **d**, the following identity will allow equation 3.20 to be simplified further:

$$\mathbf{a}\cdot(\mathbf{b}\,(\mathbf{c}\cdot\mathbf{d})) = \mathbf{a}^{\dagger}\cdot(\mathbf{b}\otimes\mathbf{c})\cdot\mathbf{d} \tag{3.21}$$

where the '⊗' symbol denotes the outer product of two vectors.[2] The final expression for the perturbation expansion can thus be written as:

$$\mathcal{E}^{a}_{MM'}\left(\mathbf{B},\hat{\mathbf{S}}\right) = -\frac{\mu_B}{\hbar^2\sqrt{S(S+1)}}\langle SM|\mathbf{B}\cdot\left(\sum_b \mathbf{\Lambda}_{ab}\otimes\boldsymbol{\mathcal{L}}_{ba}+\boldsymbol{\mathcal{L}}_{ab}\otimes\mathbf{\Lambda}_{ba}\right)\cdot\hat{\mathbf{S}}|SM'\rangle \tag{3.22}$$

By comparison with the Zeeman matrix elements of the spin Hamiltonian, the most general expression for the second-order correction to the **g**-tensor is thus:

$$\mathbf{g}^{(2)} = -\frac{2}{\hbar\sqrt{S(S+1)}}\sum_b \mathbf{\Lambda}_{ab}\otimes\boldsymbol{\mathcal{L}}_{ba} \tag{3.23}$$

In light of the above discussion, the final equation for the **g**-tensor up to second-order is simply:

$$\mathbf{g} = \mathbf{g}^{(1)} + \mathbf{g}^{(2)} + \ldots \tag{3.24}$$

where $\mathbf{g}^{(1)}$ and $\mathbf{g}^{(2)}$ are given by equations 3.11 and 3.23. This expression for the **g**-tensor is widely used by electronic structure software packages [45, 56]. The symmetry properties of the $\mathbf{\Lambda}_{ab}$ and $\boldsymbol{\mathcal{L}}_{ba}$ reduced matrix elements will be discussed after the elements of the **D** tensor are derived. The fundamental link between the fine-structure interaction tensors and the symmetry of the SOC interaction will therefore become apparent.

3.3 The origin of the D-tensor

EPR experiments can allow a detailed description of the electronic structure of paramagnetic species only if the spin Hamiltonian parameters can be reconciled with the true electronic Hamiltonian. Therefore, in the following sections, we will derive expressions for the D and E parameters of molecular triplet states. Equivalent expressions are also obtainable for the general case of arbitrary spin quantum number, however, the algebra is slightly more involved.

The **D**-tensor can thought of as the sum of two contributions:

$$\mathbf{D} = \mathbf{D}_{\mathrm{SSC}} + \mathbf{D}_{\mathrm{SOC}} \tag{3.25}$$

where the SSC and SOC subscripts refer to the spin-spin coupling and spin-orbit coupling terms. Whilst these two types of perturbations are sufficient to account for the ZFS parameters reported in this thesis,

[2] Not to be confused with the direct product denoted by '×'.

they are not generally the only contributions. There is also a crystal field contribution in systems where the spin density resides primarily on one atom (typically a transition metal) which interacts weakly with other parts of the molecule (typically the ligands)[5].

The two contributions will be derived separately using perturbation theory. Since the desired ZFS Hamiltonian is quadratic in the spin operators, the SSC contribution can be calculated using only first-order perturbation theory. The SOC contribution to ZFS arises from one of the terms in the expansion of equation 3.12, namely: the term which contains the SOC interaction twice (because it is field-independent and quadratic in spin).

3.3.1 The SSC contribution to ZFS

The discussion that follows is inspired by McWeeny's general treatment [61], however, it is considerably less general (only triplets are considered here) and the notation is significantly different (in order to be consistent with the modern notation employed in this thesis). We begin the derivation by writing the eigenvalue equation of an orbitally non-degenerate triplet state solution to the Born-Oppenheimer Hamiltonian:

$$\hat{H}_{BO}|aSM\rangle = E_a^{(0)}|aSM\rangle \tag{3.26}$$

where $E_a^{(0)}$ is the unperturbed energy, a labels the spatial part of the wavefunction, $S = 1$, and $M = +1, 0, -1$. The Hamiltonian for the SSC perturbation, $\hat{V}$, is given by:

$$\hat{V} = \mathcal{C} \sum_i \sum_{i<j} \underbrace{-\frac{8\pi}{3}\left(\hat{\mathbf{s}}_i \cdot \hat{\mathbf{s}}_j\right)\delta^3(\mathbf{r}_{ij})}_{\hat{V}_1} + \underbrace{\frac{\hat{\mathbf{s}}_i \cdot \hat{\mathbf{s}}_j}{\hat{r}_{ij}^3}}_{\hat{V}_2} - 3\underbrace{\frac{\left(\hat{\mathbf{r}}_{ij} \cdot \hat{\mathbf{s}}_i\right)\left(\hat{\mathbf{r}}_{ij} \cdot \hat{\mathbf{s}}_j\right)}{\hat{r}_{ij}^5}}_{\hat{V}_3} \tag{3.27}$$

where the dipolar constant is $\mathcal{C} = \frac{\mu_0}{4\pi} g_e^2 \gamma_e^2$. Therefore, we can write the first-order contribution to the matrix elements of the triplet sub-levels as:

$$\mathcal{V}_{MM'} = \langle aSM|\hat{V}|aSM'\rangle = \mathcal{V}^{(1)}_{MM'} + \mathcal{V}^{(2)}_{MM'} + \mathcal{V}^{(3)}_{MM'} \tag{3.28}$$

where the superscripts (1), (2), and (3) refer to the three contributions to the SSC perturbation in equation 3.27.

The first term, $\mathcal{V}^{(1)}_{MM'}$, can be evaluated trivially by separating the spatial and spin components of the matrix elements:[3]

$$\mathcal{V}^{(1)}_{MM'} = -\frac{8\pi}{3} \sum_i \sum_{i<j} \underbrace{\langle a|\delta^3(\mathbf{r}_{ij})|a\rangle}_{=0} \langle SM|\hat{\mathbf{s}}_i \cdot \hat{\mathbf{s}}_j|SM'\rangle = 0 \tag{3.29}$$

and noting that for a triplet state comprised of exactly two electrons, the spatial wavefunction is antisymmetric with respect to exchange of coordinate labels and thus the probability that any two electrons occupy the same position vanishes.[4] Although this interaction does not vanish if the triplet state is comprised of more than two electrons, it only results in a shift of the barycenter of the entire multiplet *i.e.*

[3] Generally, the separation of the spatial and spin components of the total electronic wavefunction is not valid in computational methods such as Hartree-Fock or DFT. Nevertheless, analogous derivations can be carried out for these frameworks as well. Regardless of this additional complication, the final equation for the $\mathbf{D}_{\text{SSC}}$ obtained here is invaluable for understanding the physical picture behind the origin of the ZFS interaction.

[4] This consequence of the Pauli exclusion principle can be seen if we write the matrix element over the spatial wave-

it cannot contribute to the traceless **D**-tensor.

The second matrix element, $\mathcal{V}^{(2)}_{MM'}$, also contributes a uniform shift in energy but, unlike $\mathcal{V}^{(1)}_{MM'}$, it will be included in the final **D**-tensor for reasons which will soon become apparent. By separating the integration over the spin and space degrees of freedom we obtain:

$$\mathcal{V}^{(2)}_{MM'} = \sum_i \sum_{i<j} \langle a| \frac{1}{\hat{r}^3_{ij}} |a\rangle \langle SM|\hat{\mathbf{s}}_i \cdot \hat{\mathbf{s}}_j|SM'\rangle. \tag{3.30}$$

To make progress the dot product is expanded in the spherical basis, and the unit operator is inserted:

$$\langle SM|\hat{\mathbf{s}}_i \cdot \hat{\mathbf{s}}_j|SM'\rangle = \sum_q (-1)^q \langle SM|\hat{s}_{i,q}\hat{s}_{j,-q}|SM'\rangle = \sum_{M''}\sum_q (-1)^q \langle SM|\hat{s}_{i,q}|SM''\rangle\langle SM''|\hat{s}_{j,-q}|SM'\rangle \tag{3.31}$$

It is a matter of applying the Wigner-Eckart theorem twice to show that the matrix elements of the spin operators for the individual electrons are proportional to the matrix elements over the total spin operator:

$$\langle SM|\hat{s}_{i,q}|SM''\rangle = \frac{\langle S||\hat{\mathbf{s}}_i||S\rangle}{\langle S||\hat{\mathbf{S}}||S\rangle}\langle SM|\hat{S}_q|SM''\rangle = \frac{\langle S||\hat{\mathbf{s}}_i||S\rangle}{\hbar\sqrt{S(S+1)}}\langle SM|\hat{S}_q|SM''\rangle \tag{3.32}$$

By combining the previous three equations and setting $S = 1$ in the square root denominator, the following is obtained:

$$\mathcal{V}^{(2)}_{MM'} = \frac{1}{2\hbar^2}\langle SM| \sum_q (-1)^q \hat{S}_q \hat{S}_{-q}|SM'\rangle \left\langle \frac{\underset{\sim}{\mathbf{s}}^2}{\hat{r}^3} \right\rangle = \frac{1}{2\hbar^2}\langle SM|\hat{S}^2|SM'\rangle \left\langle \frac{\underset{\sim}{\mathbf{s}}^2}{\hat{r}^3} \right\rangle \tag{3.33}$$

where the average value of the inverse cube of the inter-electron distance has been written in a more compact form:

$$\left\langle \frac{\underset{\sim}{\mathbf{s}}^2}{\hat{r}^3} \right\rangle = \sum_i \sum_{i<j} \langle a| \frac{1}{\hat{r}^3_{ij}} |a\rangle \langle S||\hat{\mathbf{s}}_i||S\rangle\langle S||\hat{\mathbf{s}}_j||S\rangle \tag{3.34}$$

i.e. the double summation sign over the electronic coordinates is suppressed, and the expectation value is contracted.

The final piece of the derivation is the evaluation of the $\hat{V}_3$ term in equation 3.27:

$$\mathcal{V}^{(3)}_{MM'} = -3\sum_i \sum_{i<j} \langle aSM| \frac{\left(\hat{\mathbf{r}}_{ij}\cdot\hat{\mathbf{s}}_i\right)\left(\hat{\mathbf{r}}_{ij}\cdot\hat{\mathbf{s}}_j\right)}{\hat{r}^5_{ij}} |aSM'\rangle \equiv -3\langle aSM| \frac{\left(\hat{\boldsymbol{\epsilon}}\cdot\hat{\mathbf{s}}_i\right)\left(\hat{\boldsymbol{\epsilon}}\cdot\hat{\mathbf{s}}_j\right)}{\hat{r}^3} |aSM'\rangle \tag{3.35}$$

where, for brevity, the double sum and the indexes of the inter-electron separation operator have been

---

function explicitly: $\langle a|\delta^3(\mathbf{r}_{ij})|a\rangle = \int\cdots\int \psi^*_a(\ldots,\mathbf{r}_i,\mathbf{r}_j,\ldots)\delta^3(\mathbf{r}_{ij})\psi_a(\ldots,\mathbf{r}_i,\mathbf{r}_j,\ldots)\,d^3V$. For a triplet state, the spatial wavefunction must be antisymmetric with respect to exchange of the spatial coordinates of any two electrons. Therefore: $\int\cdots\int \psi^*_a(\ldots,\mathbf{r}_i,\mathbf{r}_j,\ldots)\delta^3(\mathbf{r}_{ij})\psi_a(\ldots,\mathbf{r}_i,\mathbf{r}_j,\ldots)\,d^3V = -\int\cdots\int \psi^*_a(\ldots,\mathbf{r}_i,\mathbf{r}_j,\ldots)\delta^3(\mathbf{r}_{ij})\psi_a(\ldots,\mathbf{r}_j,\mathbf{r}_i,\ldots)\,d^3V$. This equation holds regardless of the operator placed between the two wavefunctions. However, the $\delta^3(\mathbf{r}_{ij})$ operator is special because when the integration over $\mathbf{r}_i$ and $\mathbf{r}_j$ is performed, we simply obtain the value of the wavefunction when $\mathbf{r}_i = \mathbf{r}_j$ (this kind of integral is often called a 'sifter integral'). Thus, the previous equality becomes: $\int\cdots\int \psi^*_a(\ldots,\mathbf{r}_i,\mathbf{r}_i,\ldots)\psi_a(\ldots,\mathbf{r}_i,\mathbf{r}_i,\ldots)\,d^3V' = -\int\cdots\int \psi^*_a(\ldots,\mathbf{r}_i,\mathbf{r}_i,\ldots)\psi_a(\ldots,\mathbf{r}_i,\mathbf{r}_i,\ldots)\,d^3V'$, where d^3V' refers to the volume element of all electrons except i and j (because we integrated over them in this step). Since the two multiple integrals over the 'other electrons' are the same, the last equality implies that the integral must be zero. Clearly, this argument does not hold for symmetric spatial wavefunctions *e.g.* for singlet states. The result is a direct consequence of the Pauli exclusion principle and the 'sifting' property of the Dirac delta function.

suppressed as before (it is crucial to remember that the summation is *always* present). Furthermore, the unit vector for the inter-electron separation is defined as:

$$\hat{\boldsymbol{\epsilon}}_{ij} = \frac{\hat{\mathbf{r}}_{ij}}{|\hat{\mathbf{r}}_{ij}|} \Longleftrightarrow \hat{\boldsymbol{\epsilon}} = \frac{\hat{\mathbf{r}}}{|\hat{\mathbf{r}}|} = \begin{pmatrix} \sin\theta\cos\phi \\ \sin\theta\sin\phi \\ \cos\theta \end{pmatrix} \tag{3.36}$$

where θ represents the angle between the $\mathbf{r}_{ij}$ vector and the (arbitrarily chosen) z-axis, whilst ϕ is the angle between the projection of $\mathbf{r}_{ij}$ on the xy-plane and the x-axis.

Similarly to the analysis of $\mathcal{V}^{(2)}_{MM'}$, expansion of the product of dot products in equation 3.35, and separation of the integration over the space and spin components of the eigenstates leads to:

$$\mathcal{V}^{(3)}_{MM'} = -3\sum_{p,q}(-1)^{q-p}\langle a|\frac{\hat{\epsilon}_q\hat{\epsilon}_{-p}}{\hat{r}^3}|a\rangle\langle SM|\hat{s}_{i,-q}\hat{s}_{j,p}|SM'\rangle \tag{3.37}$$

Using equation 3.32 for $S = 1$, the above equation becomes:

$$\mathcal{V}^{(3)}_{MM'} = -\frac{3}{2\hbar^2}\sum_{p,q}(-1)^{q-p}\left\langle\frac{\hat{\epsilon}_q\hat{\epsilon}_{-p}\underset{\sim}{\mathbf{s}}^2}{\hat{r}^3}\right\rangle\langle SM|\hat{S}_{-q}\hat{S}_p|SM'\rangle \tag{3.38}$$

Before an expression for the elements of the **D**-tensor can be written, it is necessary to combine equations 3.33 and 3.38. However, there is a slight complication due to the fact that $\mathcal{V}^{(3)}_{MM'}$ contains a double sum over p and q, whereas $\mathcal{V}^{(2)}_{MM'}$ is a single sum over q. To overcome this, equation 3.33 is modified by employing the Kronecker delta, δ_{pq}:[5]

$$\mathcal{V}^{(2)}_{MM'} = \frac{1}{2\hbar^2}\sum_{p,q}\left\langle\frac{\delta_{qp}\underset{\sim}{\mathbf{s}}^2}{\hat{r}^3}\right\rangle\langle SM|\hat{S}_q\hat{S}_p|SM'\rangle \tag{3.39}$$

By combining equations 3.38 and 3.39, and changing from spherical to Cartesian coordinates,[6] the total SSC perturbation becomes:

$$\mathcal{V}_{MM'} = \frac{1}{2\hbar^2}\sum_{p,q}\left\langle\frac{\delta_{qp} - 3\hat{\epsilon}_q\hat{\epsilon}_p}{\hat{r}^3}\underset{\sim}{\mathbf{s}}^2\right\rangle\langle SM|\hat{S}_q\hat{S}_p|SM'\rangle \tag{3.40}$$

Comparison of the matrix elements of the ZFS Hamiltonian with equation 3.40 implies the following expression for the elements of the $\mathbf{D}_{\mathrm{SSC}}$-tensor:

$$D_{\mathrm{SSC},pq} = \frac{1}{2\hbar^2}\mathcal{C}\underset{\sim}{\mathbf{s}}^2\left\langle\frac{\delta_{pq} - 3\hat{\epsilon}_p\hat{\epsilon}_q}{\hat{r}^3}\right\rangle \tag{3.41}$$

[5] Which is just the pq entry of the Cartesian unit matrix.

[6] *i.e.* $p, q \in \{+1, 0, -1\} \longrightarrow \{x, y, z\}$

When written explicitly, the final traceless $\mathbf{D}_{\mathrm{SSC}}$-tensor is:

$$\mathbf{D}_{\mathrm{SSC}} = \frac{1}{2\hbar^2}\mathcal{C}\underset{\sim}{\mathbf{s}}^2 \begin{pmatrix} \left\langle \frac{\hat{r}^2 - 3\hat{x}^2}{\hat{r}^5} \right\rangle & \left\langle \frac{-3\hat{x}\hat{y}}{\hat{r}^5} \right\rangle & \left\langle \frac{-3\hat{x}\hat{z}}{\hat{r}^5} \right\rangle \\ \left\langle \frac{-3\hat{x}\hat{y}}{\hat{r}^5} \right\rangle & \left\langle \frac{\hat{r}^2 - 3\hat{y}^2}{\hat{r}^5} \right\rangle & \left\langle \frac{-3\hat{y}\hat{z}}{\hat{r}^5} \right\rangle \\ \left\langle \frac{-3\hat{x}\hat{z}}{\hat{r}^5} \right\rangle & \left\langle \frac{-3\hat{y}\hat{z}}{\hat{r}^5} \right\rangle & \left\langle \frac{\hat{r}^2 - 3\hat{z}^2}{\hat{r}^5} \right\rangle \end{pmatrix} \tag{3.42}$$

Despite the fact that perturbation theory was used, this expression becomes very accurate if the energy difference between the triplet state of interest and any other triplet state is much larger than the dipolar interaction. Typically, in organic chromophores, triplet-triplet energy gaps are in the visible to IR region of the electromagnetic spectrum. By contrast, dipolar interactions are in the radio or microwave region, and are thus much smaller (by at least three orders of magnitude) than the former. If the perturbation in 3.27 were to be used to generate second-order corrections, the result would not be a billinear ZFS interaction. The outcome would be a so-called 'high-order ZFS interaction' (*e.g* the spin operators would be raised to the fourth power), and such interactions have thus far not been necessary to simulate or interpret the EPR spectra of photo-induced organic triplet states in this thesis or beyond.

3.3.2 The relationship between $\mathbf{D}_{\mathrm{SSC}}$ and molecular symmetry

The equation for the elements of the ZFS tensor given in 3.42 is widely used to calculate and interpret EPR spectra. Often, the arguments revolve around the relationship between the symmetry of the **D**-tensor and the symmetry of the molecule, hence, we will expand on these ideas in the following section.

If the system under investigation is spherically symmetric, then the absolute square of the spatial part of the non-degenerate wavefunction (the probability density; used in taking the expectation values in equation 3.42) is independent of the θ and ϕ angles:

$$|\psi(r, \theta + \delta\theta, \phi + \delta\phi)|^2 = |\psi(r, \theta, \phi)|^2 \equiv |\psi(r)|^2 \tag{3.43}$$

As a direct consequence of equation 3.43, the elements of the $\mathbf{D}_{\mathrm{SSC}}$-tensor can be decomposed into the product of three independent integrals:

$$D_{pq} = \int_0^{2\pi} f_{pq}(\phi)\, d\phi \int_0^{\pi} g_{pq}(\theta) \sin\theta\, d\theta \int_0^{\infty} |\psi(r)|^2 h_{pq}(r) r^2\, dr \tag{3.44}$$

where $f_{pq}(\phi)$, $g_{pq}(\theta)$, and $h_{pq}(r)$ are only functions of ϕ, θ, and r, respectively. For example, the off-diagonal elements of the $\mathbf{D}_{\mathrm{SSC}}$-tensor are:

$$\begin{cases} D_{xy} \propto \int_0^{2\pi} \sin\phi\cos\phi\, d\phi \int_0^{\pi} \sin^3\theta\, d\theta \int_0^{\infty} \frac{|\psi(r)|^2}{r}\, dr = 0 \\ D_{xz} \propto \int_0^{2\pi} \cos\phi\, d\phi \int_0^{\pi} \cos\theta\sin^2\theta\, d\theta \int_0^{\infty} \frac{|\psi(r)|^2}{r}\, dr = 0 \\ D_{yz} \propto \int_0^{2\pi} \sin\phi\, d\phi \int_0^{\pi} \cos\theta\sin^2\theta\, d\theta \int_0^{\infty} \frac{|\psi(r)|^2}{r}\, dr = 0 \end{cases} \tag{3.45}$$

all of which can trivially be shown to vanish. Similarly, the diagonal elements can also be shown to vanish, because the following angular integrals are all zero:

$$\begin{cases} \int_0^{\pi}\int_0^{2\pi} (1 - 3\sin^2\theta\cos^2\phi)\sin\theta\, d\theta\, d\phi = 0 \\ \int_0^{\pi}\int_0^{2\pi} (1 - 3\sin^2\theta\sin^2\phi)\sin\theta\, d\theta\, d\phi = 0 \\ \int_0^{\pi}\int_0^{2\pi} (1 - 3\cos^2\theta)\sin\theta\, d\theta\, d\phi = 0 \end{cases} \tag{3.46}$$

Therefore, there is no SSC contribution to ZFS in spherically symmetric systems *e.g.* in free atoms and ions or the SSC contribution is small in systems where the electrons are located primarily on a single atom and interact very weakly with the surrounding atoms (such as certain transition metal complexes).

In non spherically symmetric systems, an equivalent demonstration of the symmetry properties of the $\mathbf{D}_{\mathrm{SSC}}$-tensor can be obtained if we consult the group theoretical character tables for the molecular point group of interest. For any molecule with an axis of rotational symmetry, the irreducible representations spanned by the xy, yz, and xz functions are never equal to the totally symmetric irreducible representation.[7] For example, in the D_{4h} point group, the functions xy, yz, and xz span the irreducible representations B_{2g}, E_g, and E_g, respectively. Hence, the off-diagonal entries of the $\mathbf{D}_{\mathrm{SSC}}$-tensor must vanish.[8]

Character tables can also reveal valuable information about the diagonal entries of the $\mathbf{D}_{\mathrm{SSC}}$-tensor. A particularly pertinent example is the comparison of the character tables for the D_{2h} and D_{4h} point groups; the former is given in Appendix D since it will become important in the next chapter. Within these two point groups the following are the transformation properties of the functions relevant for the diagonal elements of the $\mathbf{D}_{\mathrm{SSC}}$-tensor:

$$\begin{aligned} D_{4h} &: A_{1g} \longrightarrow (x^2 + y^2), z^2 \quad \text{and} \quad B_{1g} \longrightarrow (x^2 - y^2) \\ D_{2h} &: A_g \longrightarrow x^2, y^2, z^2 \end{aligned}$$

The above information implies that within the D_{2h} point group, the three diagonal elements of the $\mathbf{D}_{\mathrm{SSC}}$-tensor *could* be non-zero and that they *could* all be distinct. More precisely, the $\mathbf{D}_{\mathrm{SSC}}$-tensor could be orthorhombic ($\lambda > 0$) within the D_{2h} point group.

By contrast, in the D_{4h} point group, $(x^2 - y^2)$ is not totally symmetric and therefore the difference $D_{xx} - D_{yy}$ must vanish. As such, the $\mathbf{D}_{\mathrm{SSC}}$-tensor is expected to be purely axial ($\lambda = 0$) within the D_{4h} point group.

3.3.3 The sign of D and the spheroidal symmetry of the spin density

The symmetry of the molecule has been shown to dictate which entries of the $\mathbf{D}_{\mathrm{SSC}}$-tensor are expected to be zero/non-zero *i.e.* group theory gives the selection rules for the entries of the ZFS tensor. However,

[7] The only exception is the C_2 point group, in which xy is totally symmetric. This does not necessarily imply a non-zero D_{xy} element. Character tables can only provide a criterion to establish whether integrals must be zero, not if they are necessarily non-zero.

[8] The direct product is $\Gamma_n \otimes \Gamma_0 = \Gamma_n \neq \Gamma_0$ if $n \neq 0$, where Γ_0 is totally symmetric and is spanned by $|\psi|^2$ (if ψ is non-degenerate, which it has to be for equation 3.40 to hold).

under certain approximations, the expectation values in equation 3.42 have some further symmetry properties which dictate the relationship between the sign of the D-value and the average shape of the spin density.

First of all, for a single pair of electrons, $\underset{\sim}{\mathbf{s}}^2$ can be evaluated using the Wigner-Eckart theorem to be given by $\hbar^2/2$, and therefore from equation 3.42 the D-value is given by:

$$D = \frac{3}{2} D_{\mathrm{SSC},zz} = \frac{3\mathcal{C}}{8} \left\langle \frac{1 - 3\cos^2\theta}{r^3} \right\rangle \tag{3.47}$$

By assuming that this pair of electrons are restricted to the same distance from one another *i.e.* if r is a constant, then the sign of the D-value is dictated by the average value of $1 - 3\cos^2\theta$. There are three possible symmetries for spin densities that achieve a constant r. Clearly, if the $\mathbf{r}$ vector is permitted to take any orientation on a sphere with equal probability, the D-value vanishes, as per the discussion in the previous section. However, if the spin density is 'disk-like' *i.e.* the angle θ is restricted to $\pi/2$, then the D-value is positive:

$$D_{\mathrm{disk}} = \frac{3\mathcal{C}}{8} \frac{1}{r^3} \tag{3.48}$$

whereas if the spin density is 'rod-like' with the angle $\theta = 0$, then the D-value is negative:

$$D_{\mathrm{rod}} = -\frac{3\mathcal{C}}{8} \frac{2}{r^3} \tag{3.49}$$

Furthermore, we notice that for the same inter-spin distance r, the D-value of the disk has half the magnitude of the D-value of the rod *i.e.* we expect rod-like systems to have larger $|D|$ values.

The real spin density of an arbitrary molecule is neither a disk nor a rod. At most, we might be able to claim that the three-dimensional object corresponding to an iso-level of the spin density can be classified by the moments of inertia of a spheroid: oblate ('pancake-like') or prolate ('cigar-like') with respect to some arbitrarily chosen z-axis (figure 3.1). Furthermore, the inter-spin vector is not a constant, it depends on θ.

Equations 3.48 and 3.49 establish the sign of D for two limiting situations: the pancake to disk limit, and the cigar to rod limit. The question thus arises about the sign of D everywhere else in between these two limits: should we expect $D > 0$ for an oblate spheroid and $D < 0$ for a prolate spheroid? Whilst the absolute proof of this fact is difficult to achieve, this observation can be justified in a semi-quantitative fashion.

Consider performing the integration 3.47 for a given iso-level of the spin density *i.e.* over a particular surface with a uniform probability of finding an unpaired electron. If the spin density is spheroidal, it is constant over the following surface:

$$\frac{x^2}{R_\perp^2} + \frac{y^2}{R_\perp^2} + \frac{z^2}{R_\parallel^2} = 1 \tag{3.50}$$

where $R_\perp$ and $R_\parallel$ are the semi-axes of the spheroid along the x/y- and z– axes, respectively. The spheroid

can be classified via the parameter η defined such that:

$$\eta = \frac{R_\parallel}{R_\perp} \begin{cases} < 1 \Leftarrow \text{oblate} \\ = 1 \Leftarrow \text{spherical} \\ > 1 \Leftarrow \text{prolate} \end{cases} \tag{3.51}$$

Having thus defined the spheroid corresponding to a particular iso-surface of the spin density, the expectation value in equation 3.47 can be evaluated by integration over the surface of the spheroid, thus yielding the following elliptic integral:

$$D(\eta) = \frac{3\mathcal{C}}{8} \frac{1}{2^3 R_\perp^3} \int_0^{2\pi} \int_0^{\pi} \frac{1 - 3\cos^2\theta}{\cos^2\theta + \eta^2 \sin^2\theta} \sin\theta \, d\theta d\phi \tag{3.52}$$

$$= \frac{3\mathcal{C}}{8} \frac{1}{2^3 R_\perp^3} 2\pi \int_{-1}^{1} \frac{1 - 3x^2}{(1-\eta^2)x^2 + \eta^2} \, dx \tag{3.53}$$

This definite integral does not have a *unique* closed form solution for all values of η. Whilst it is clearly zero when $\eta = 1$, it takes different functional forms: $D_<$ when $\eta < 1$, and $D_>$ when $\eta > 1$ (the explicit form of $D_<$ and $D_>$ is irrelevant). This complication is, mathematically speaking, a statement of the fact that the above integral, $D(\eta)$, is the analytic continuation of $D_<$ and $D_>$ to the set of real numbers (except the singularities at $\eta = 0$ or $\eta = 1$).

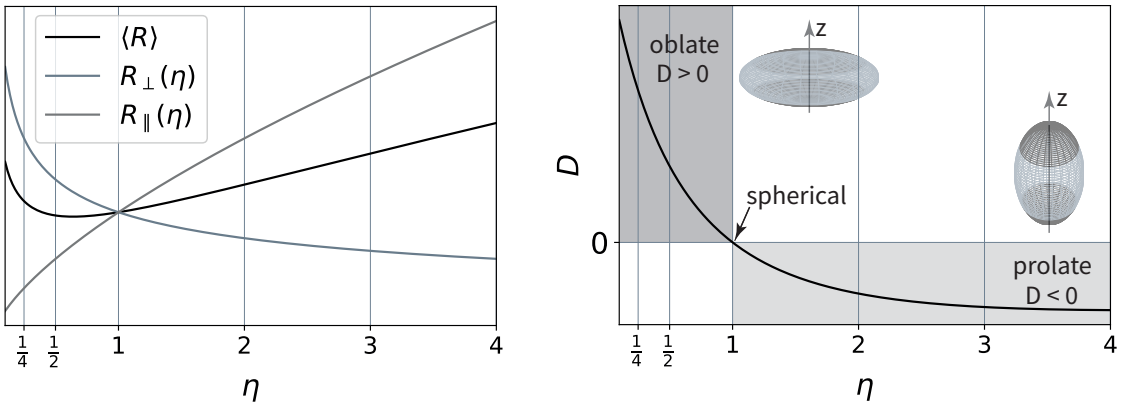


Figure 3.1: (Left) The semi-axes, $R_\perp$ and $R_\parallel$, of the unit volume spheroid as a function of η. The mean value of the inter-spin distance, $\langle R \rangle$, is also plotted as a function of η. For a sphere, $\eta = 1$, and hence all three values are equal. (Right) The integral in equation 3.53 as a function of η for a spheroid of unit volume *i.e.* $R_\perp = \sqrt[3]{\frac{3}{4\pi\eta}}$. The function crosses zero when the spheroid is a sphere. The D-value is shown to be positive for oblate spin densities and negative for prolate spin densities. Note: the z-axis in this figure is an arbitrarily chosen Cartesian axis with respect to which the spheroid was defined as shown in the inset of the right panel.

Equation 3.53 is plotted in figure 3.1 as a function of η for a spheroid of constant volume. Clearly, the behaviour of this function as the spheroid is deformed from oblate to prolate is in line with the qualitative arguments presented above.

Finally, it is important to stress that equation 3.53 is approximate and should only be used to derive qualitative conclusions regarding the sign of the D-value. Nonetheless, for simple systems, equation 3.53 is not an entirely unreasonable approximation. As an example, consider the benzene molecule. The

C-C bond length is 0.14 nm and assuming a perfectly hexagonal geometry, the 'in-plane' semi-major axis can be approximated to be $R_\perp \approx 0.1212$ nm (the radius of the inscribed circle). The semi-minor axis could be estimated as the average distance of an electron in a $2p_z$ orbital from the origin. This gives $R_\parallel = \frac{5a_0}{Z_{\text{eff}}} \approx 0.08436$ nm. Substituting these values into equation 3.53 gives $D \approx 5190$ MHz. Given how crude the assumptions behind this formula are, this predicted D-value is surprisingly close to the experimental D-value of 4766 MHz. A similar calculation for pyrene yields $D \approx 3162$ MHz which is comparable to the experimental value of 2572 MHz. These quoted experimental values were taken from reference [62].

3.3.4 The SOC contribution to ZFS

In most organic triplet states, the SSC contribution to the ZFS is sufficient to account for the observed EPR spectra. However, occasionally, and especially in the presence of heavy atoms, the SOC interaction also contributes to the ZFS spin Hamiltonian. This will prove to be the case in the investigation of the photo-excited triplet state of palladium porphyrin systems in Chapter 4.

The derivation of the $\mathbf{D}_{\text{SOC}}$-tensor will be outlined below following the original derivation of Neese and Solomon [56]. As was the case for the SSC contribution, the notation will be adapted and the analysis will be restricted to triplet states.

As before, the derivation begins with the Born-Oppenheimer eigenstates for a spatially non-degenerate triplet state:

$$\hat{H}_{BO}|aSM\rangle = E_a^{(0)}|aSM\rangle \tag{3.54}$$

where the symbols are the same as in equation 3.26. The first-order perturbation due to SOC (equation 3.9), does not contribute to the ZFS, only to the EZ interaction. However, the second-order SOC contribution is non-zero and it is given by the final term in the expansion of equation 3.12:

$$\mathcal{T}_{MM'} = -\sum_{bM''} \Delta_b^{-1} \langle aSM|\hat{H}_{SOC}|bS'M''\rangle\langle bS'M''|\hat{H}_{SOC}|aSM'\rangle \tag{3.55}$$

In the derivation of the $\mathbf{g}$-tensor, only matrix elements where $S = S'$ had to be considered, because the orbital angular momentum operators cannot mix states of different multiplicity. However, the SOC can mix states of different multiplicity. This can be seen by application of the Wigner-Eckart theorem to the matrix elements in 3.55:

$$\begin{cases} \langle aSM|\hat{H}_{SOC}|bS'M''\rangle = \sum_q (-1)^q \langle S'M''1q|SM\rangle \mathcal{L}_{ab}(-q) \\ \langle bS'M''|\hat{H}_{SOC}|aSM'\rangle = \sum_q (-1)^q \langle SM'1q|S'M''\rangle \mathcal{L}_{ba}(-q) \end{cases} \tag{3.56}$$

where the $\mathcal{L}_{ab}(-q)$ and $\mathcal{L}_{ba}(-q)$ are the same reduced matrix elements introduced in equation 3.17, except that now they could have $S \neq S'$. The Clebsch-Gordan coefficients are zero unless either $S' \pm 1 = S$ or $S' = S$. This simple fact implies that the perturbation in equation 3.55 is non-zero only for triplet-triplet, singlet-triplet, and triplet-quintet contributions. Thus, the ZFS that arises from these three cases

can be considered individually, by separating the expression for $\mathcal{T}_{MM'}$ in equation 3.55 into three parts:

$$\mathcal{T}_{MM'} = \mathcal{T}^{tt}_{MM'} + \mathcal{T}^{st}_{MM'} + \mathcal{T}^{tq}_{MM'} \tag{3.57}$$

where the superscripts tt, st, and tq correspond to the individual contributions with $S' = 1$, $S' = 0$, and $S' = 2$, respectively.

The triplet-triplet contribution. By combining equations 3.55 and 3.56, the explicit form of the triplet-triplet perturbation sum can be written as:

$$\mathcal{T}^{tt}_{MM'} = -\sum_{bM''} \Delta_b^{-1} \sum_{q,p} (-1)^{q-p} \langle SM''1q|SM\rangle \langle SM'1-p|SM''\rangle \mathcal{L}_{ab}(-q)\mathcal{L}_{ba}(p) \tag{3.58}$$

Due to the result in equation 3.18, the product of Clebsch-Grodan coefficients can be replaced by a product of matrix elements of spin operators. For $S = 1$, the above summation becomes:

$$\mathcal{T}^{tt}_{MM'} = -\frac{1}{2\hbar^2} \sum_{bM''} \Delta_b^{-1} \sum_{p,q} (-1)^{q-p} \langle SM|\hat{S}_q|SM''\rangle \langle SM''|\hat{S}_{-p}|SM'\rangle \mathcal{L}_{ab}(-q)\mathcal{L}_{ba}(p) \tag{3.59}$$

A few rearrangements of the above equation need to be performed before the form of the $\mathbf{D}^{tt}_{\mathrm{SOC}}$-tensor can transpire: the unit operator $\hat{1} = \sum_{M''} |SM''\rangle\langle SM''|$ can be removed, the spherical coordinates $p, q \in \{-1, 0, +1\}$ can be replaced by the Cartesian coordinates $p, q \in \{x, y, z\}$, and the summation signs are reversed (whilst keeping track of the indices):

$$\mathcal{T}^{tt}_{MM'} = -\langle SM| \sum_{p,q} \hat{S}_q \sum_b \frac{\mathcal{L}_{ab}(q)\mathcal{L}_{ba}(p)}{2\hbar^2\Delta_b} \hat{S}_p |SM'\rangle \tag{3.60}$$

And by comparison of the above equation with the matrix elements of the ZFS Hamiltonian in equation 1.28, the equation for the triplet-triplet SOC contribution to the ZFS tensor can immediately be written:

$$D^{tt}_{\mathrm{SOC},qp} = -\sum_b \frac{\mathcal{L}_{ab}(q)\mathcal{L}_{ba}(p)}{2\hbar^2\Delta_b} \quad \Longleftrightarrow \quad \mathbf{D}^{tt}_{\mathrm{SOC}} = -\sum_b \frac{1}{2\hbar^2\Delta_b} \boldsymbol{\mathcal{L}}_{ab} \otimes \boldsymbol{\mathcal{L}}_{ba} \tag{3.61}$$

The consequences of this formula for the elements of the **D**-tensor will be discussed in due course. Before however, the tensor in equation 3.61 needs to be converted to a traceless form. This is readily achieved by subtracting a third of the trace from each diagonal entry to obtain the final formula:

$$\mathbf{D}^{tt}_{\mathrm{SOC}} = \sum_b \frac{1}{6\hbar^2\Delta_b} \left(\mathbf{1}_3 \boldsymbol{\mathcal{L}}_{ab} \cdot \boldsymbol{\mathcal{L}}_{ba} - 3\boldsymbol{\mathcal{L}}_{ab} \otimes \boldsymbol{\mathcal{L}}_{ba}\right). \tag{3.62}$$

The singlet-triplet contribution. For $S' = 0$, the corresponding perturbation sum is:

$$\mathcal{T}^{st}_{MM'} = -\sum_{bM''} \Delta_b^{-1} \sum_{q,p} (-1)^{q-p} \langle 0M''1q|SM\rangle \langle SM'1-p|0M''\rangle \mathcal{L}_{ab}(-q)\mathcal{L}_{ba}(p) \tag{3.63}$$

Note that $S = 1$ in this equation, yet it has been kept as 'S' for comparison with the previous formula for $\mathcal{T}^{tt}_{MM'}$. Both Clebsch-Gordon coefficients are zero unless $M'' = 0$, the first one is also zero unless $M = q$, and the second one is zero unless $M' = p$. In light of these selection rules, for triplet states the

above sum collapses to:

$$\mathcal{T}^{st}_{MM'} = \sum_b \Delta_b^{-1} \frac{(-1)^M}{\sqrt{3}} \mathcal{L}_{ab}(-M)\mathcal{L}_{ba}(M') \tag{3.64}$$

In the case of this (*st*) contribution, it is no longer immediately obvious by visual inspection of the perturbation sum (equation 3.64) how the ZFS Hamiltonian emerges. The main issue is that this matrix is not traceless. Hence, subtracting a third of the trace from each diagonal entry:

$$\mathcal{T}^{st}_{\text{traceless}} = \mathcal{T}^{st} - \frac{1}{3}\,\text{tr}\left[\mathcal{T}^{st}\right]\mathbf{1}_3 \tag{3.65}$$

gives rise to the following explicit matrix representation of $\mathcal{T}^{st}_{\text{traceless}}$ in the Cartesian basis:

$$\mathcal{T}^{st}_{\text{traceless}} = \frac{1}{\sqrt{3}} \sum_b \Delta_b^{-1} \times$$
$$\begin{pmatrix} \frac{1}{2}\left(\mathcal{L}^x_{ab}\mathcal{L}^x_{ba} + \mathcal{L}^y_{ab}\mathcal{L}^y_{ba}\right) - \frac{1}{3}\boldsymbol{\mathcal{L}}_{ab}\cdot\boldsymbol{\mathcal{L}}_{ba} & -\frac{1}{\sqrt{2}}\mathcal{L}^x_{ab}\mathcal{L}^z_{ba} + \frac{i}{\sqrt{2}}\mathcal{L}^y_{ab}\mathcal{L}^z_{ba} & -\frac{1}{2}\left(\mathcal{L}^x_{ab}\mathcal{L}^x_{ba} - \mathcal{L}^y_{ab}\mathcal{L}^y_{ba}\right) + i\mathcal{L}^x_{ab}\mathcal{L}^y_{ba} \\ & \mathcal{L}^z_{ab}\mathcal{L}^z_{ba} - \frac{1}{3}\boldsymbol{\mathcal{L}}_{ab}\cdot\boldsymbol{\mathcal{L}}_{ba} & +\frac{1}{\sqrt{2}}\mathcal{L}^x_{ab}\mathcal{L}^z_{ba} - \frac{i}{\sqrt{2}}\mathcal{L}^y_{ab}\mathcal{L}^z_{ba} \\ & & \frac{1}{2}\left(\mathcal{L}^x_{ab}\mathcal{L}^x_{ba} + \mathcal{L}^y_{ab}\mathcal{L}^y_{ba}\right) - \frac{1}{3}\boldsymbol{\mathcal{L}}_{ab}\cdot\boldsymbol{\mathcal{L}}_{ba} \end{pmatrix} \tag{3.66}$$

The elements of $\mathcal{T}^{st}_{\text{traceless}}$ below the principal diagonal have been suppressed for simplicity (the matrix is Hermitian). The analogous expression for the elements of the (traceless) ZFS spin Hamiltonian is obtained from equation 1.28:

$$\mathcal{H}_{\text{ZFS}} = \hbar^2 \begin{pmatrix} -\frac{D_{xx}+D_{yy}}{2} & \frac{1}{\sqrt{2}}(D_{zx} - iD_{zy}) & \frac{1}{2}(D_{xx} - D_{yy}) - iD_{xy} \\ \frac{1}{\sqrt{2}}(D_{zx} + iD_{zy}) & -D_{zz} & -\frac{1}{\sqrt{2}}(D_{zx} - iD_{zy}) \\ \frac{1}{2}(D_{xx} - D_{yy}) + iD_{xy} & -\frac{1}{\sqrt{2}}(D_{zx} + iD_{zy}) & -\frac{D_{xx}+D_{yy}}{2} \end{pmatrix} \tag{3.67}$$

In order to obtain the elements of the ZFS tensor, equation 3.66 is set equal to equation 3.67. This results in a set of six simultaneous equations which can be solved to yield the following singlet-triplet contribution to the $\mathbf{D}_{\text{SOC}}$-tensor:

$$\mathbf{D}^{st}_{\text{SOC}} = \sum_b \frac{1}{3\sqrt{3}\hbar^2\Delta_b}\left(\mathbf{1}_3\boldsymbol{\mathcal{L}}_{ab}\cdot\boldsymbol{\mathcal{L}}_{ba} - 3\boldsymbol{\mathcal{L}}_{ab}\otimes\boldsymbol{\mathcal{L}}_{ba}\right) \tag{3.68}$$

Note that the expressions for the singlet-triplet contribution (above) and the triplet-triplet contribution (equation 3.62) have the same form except for the pre-factors of $\frac{1}{6}$ and $\frac{1}{3\sqrt{3}}$. The origin of these pre-factors is in the evaluation of the Clebsch-Gordan coefficients (in the original perturbation sums), and they depend on the multiplicity of the state for which the $\mathbf{D}_{\text{SOC}}$-tensor is computed, and the multiplicity of the ad-mixing states. General expressions for these coefficients for arbitrary multiplicities are found by Neese and Solomon [56]. Note that, the pre-factors found in the above derivation for triplets are *not* the same as the pre-factors computed by Neese and Solomon. This is not a problem because the final expressions given by Neese and Solomon are not written in terms of the *reduced* SOC matrix elements $\boldsymbol{\mathcal{L}}_{ab}$, but rather in terms of the *full* SOC matrix elements. It is a simple matter of applying the Wigner-Eckart theorem to show that the equations presented here are exactly equal to the ones of Neese and

Solomon. The reason for choosing this representation for the **D**-tensor equations is to facilitate the qualitative discussions that will follow.

The triplet-quintet contribution The perturbation sum for the $S' = 1$ contribution can also be expanded similarly to the previous section:

$$\mathcal{T}^{tq}_{MM'} = -\sum_{bM''} \Delta_b^{-1} \sum_{q,p} (-1)^{q-p} \langle 2M'' 1q|SM\rangle\langle SM'1-p|2M''\rangle \mathcal{L}_{ab}(-q)\mathcal{L}_{ba}(p) \tag{3.69}$$

The selection rules for the Clebsch-Gordan coefficients drastically reduce the number of non-zero terms to those which satisfy $M'' = M - q = M' + p$. After setting the traceless form of equation 3.69 equal to the matrix elements of the ZFS Hamiltonian and performing some algebraic manipulations, the triplet-quintet contribution to the **D**-tensor eventually emerges as:

$$\mathbf{D}^{tq}_{\mathrm{SOC}} = \sum_b \frac{1}{6\sqrt{15}\hbar^2\Delta_b} \left(\mathbf{1}_3 \boldsymbol{\mathcal{L}}_{ab} \cdot \boldsymbol{\mathcal{L}}_{ba} - 3\boldsymbol{\mathcal{L}}_{ab} \otimes \boldsymbol{\mathcal{L}}_{ba}\right) \tag{3.70}$$

As seen before, this formula is the same as the other contributions except for the factor of $\frac{1}{6\sqrt{15}}$ which is due to the Clebsch-Gordan coefficients.

3.3.5 Relationship between $\mathbf{D}_{\mathrm{SOC}}$ and molecular symmetry

Further insight can be gained into the SOC contribution to the **D**-tensor by analysing equations 3.62, 3.68, and 3.70 from a group theoretical perspective. The important quantity to consider is the reduced matrix element of the SOC Hamiltonian:

$$\boldsymbol{\mathcal{L}}_{ab}(q) = \mathcal{A} \underbrace{\langle aS||}_{\Gamma_a} \underbrace{\sum_i \sum_k \frac{Z_k^{eff}}{\hat{r}_{ik}^3} \hat{l}_{ik,q}\hat{\mathbf{s}}_i}_{\Gamma(R_q)} \underbrace{||bS'\rangle}_{\Gamma_b} \tag{3.71}$$

where $q \in \{x, y, z\}$, and Γ_a/Γ_b are the symmetry species of the irreducible representations spanned by the a and b wavefunctions , respectively. The orbital angular momentum operator, $\hat{l}_{ik,q}$, transforms under the symmetry operations of the point group as a rotation around the q-axis followed by a translation along the vector connecting the origin to the position of nucleus k. The effects of the translation can often be ignored,[9] and the entire operator in equation 3.71 can be assumed to span an irreducible representation of the same symmetry species as the q-axis rotation matrix, *i.e.* it is $\Gamma(R_q)$. The presence of the integration over the spin degree of freedom in 3.71 is not problematic: it gives rise to a factor which only depends on $\Delta S = S - S'$. The selection rules for this factor are already accounted for by the derivation in the previous sections whereby it was established that only $\Delta S = 0, \pm 1$ admixtures have to be considered. More precisely, after integrating over the spin variable in equation 3.71, only the symmetry of the spatial degrees of freedom needs to be considered.

Let Γ_0 denote the symmetry species spanned by the totally symmetric irreducible representation (*e.g.* A_{1g} and Σ_g^+ for D_{4h} and $D_{\infty h}$, respectively). The selection rules for the elements of the **D**-tensor can be

[9] For example, in cases where the SOC only needs to be considered for heavy elements situated at the origin of the coordinate system defined by the molecular point group.

formulated very concisely as follows:

$$\Gamma_0 \notin \left\{\Gamma_a \otimes \Gamma(R_p) \otimes \Gamma_b\right\} \cap \left\{\Gamma_b \otimes \Gamma(R_q) \otimes \Gamma_a\right\} \Longrightarrow D_{\mathrm{SOC},pq} = 0 \tag{3.72}$$

Note that the converse of the above condition is not necessarily true. The condition in 3.72 is the quantitative equivalent of El Sayed's rule as applied to the SOC contribution to the ZFS interaction.[10] This can easily be verified: $\Gamma(R_q)$ is rarely equal to Γ_0, hence, state a must have a different symmetry compared to b, otherwise, the SOC contribution to ZFS will vanish.

As an example, consider the orbitally non-degenerate triplet ground state of molecular oxygen. The term symbol for this state is ${}^3\Sigma_g^-$. The first two excited states are ${}^1\Delta_g$ at ca. 7,888 cm^{-1}, and ${}^1\Sigma_g^+$ at ca. 13,120 cm^{-1}. In order to calculate the D_{SOC} value of oxygen, the following direct product involving only $\Gamma(R_z) = \Sigma_g^-$ needs to be considered:

$$\begin{cases} \Sigma_g^- \otimes \Sigma_g^- \otimes \Sigma_g^+ = \Sigma_g^+ \\ \Sigma_g^- \otimes \Sigma_g^- \otimes \Delta_g = \Delta_g \end{cases} \tag{3.73}$$

Hence, despite the fact that the ${}^1\Delta_g$ state is lower in energy, it does not contribute to the ZFS of the ground state of molecular oxygen. Indeed, as shown in reference [64], the D_{SOC} value arising from mixing with the ${}^1\Sigma_g^+$ amounts to 2.374 cm^{-1}. Combined with the D_{SSC} value of 1.440 cm^{-1}[64], the result is D_{total} = 3.814 cm^{-1} which is in good agreement with the experimental value of ca. 4.0 cm^{-1} (especially given that all other excited states have been omitted).

3.3.6 Relationship between $\mathbf{D}_{\mathrm{SOC}}$ and $\mathbf{D}_{\mathrm{SSC}}$

The natural question that arises is whether the eigenframes of $\mathbf{D}_{\mathrm{SOC}}$ and $\mathbf{D}_{\mathrm{SSC}}$ coincide. More precisely, is there a $\mathbf{U}_D$ transformation, as defined in equation 1.30, which is unique for both SSC and SOC contributions to the **D**-tensor? However, note that we are not interested in whether the z-axis of $\mathbf{D}_{\mathrm{SOC}}$ is the same as the z-axis of $\mathbf{D}_{\mathrm{SSC}}$, but whether the axes of the two tensors are collinear regardless of the labelling. As mentioned before, a knowledge of the correct labelling scheme requires a knowledge of the absolute magnitudes of the eigenvalues of the tensors (by equation 1.34). Therefore, the labels are unlikely to be coincident given the fundamental difference in the origin of the two contributions.

In the discussion of the relationship between $\mathbf{D}_{\mathrm{SSC}}$ and molecular symmetry it was noted that if a molecule has an axis of n-fold rotational symmetry, a C_n-axis, then the $\mathbf{D}_{\mathrm{SSC}}$-tensor is diagonal in any Cartesian frame which has one of its axes aligned with C_n (*i.e.* $\mathbf{D}_{\mathrm{SSC}}$ is diagonal in the 'natural' molecular frame). On the other hand, if such a C_n-axis exists, then the symmetry species of the rotation matrices cannot be all equal.[11] Typically, $\Gamma(R_z)$ is distinct from both $\Gamma(R_x)$ and $\Gamma(R_y)$, whereas the latter two could be equal or distinct. Furthermore, Γ_a and Γ_b could also be equal or distinct. Hence, it is not generally true that $\mathbf{D}_{\mathrm{SOC}}$ and $\mathbf{D}_{\mathrm{SSC}}$ have a common eigenframe.

Nonetheless, there are certain situations in which the two contributions are collinear. To illustrate one such possibility, consider an organic chromophore which, apart from the ground state, has a singlet and a triplet excited state ${}^1\Gamma_b$ and ${}^3\Gamma_a$. Often, ${}^1\Gamma_b$ and ${}^3\Gamma_a$ are much closer in energy to each other than

[10] El Sayed's rule was originally formulated for ISC from an excited singlet state to a triplet state. The rule states that such a process must be accompanied by a change in symmetry of the spatial wavefunction [63].

[11] Except, of course, the full rotation group.

to any other electronic state. As such, only the singlet-triplet contribution to the $\mathbf{D}_{\mathrm{SOC}}$-tensor needs to be considered. In this case, there is a simple criterion for the elements of the $\mathbf{D}_{\mathrm{SOC}}$-tensor:

$$\Gamma_a \otimes \Gamma_b \in \left\{\Gamma_0, \Gamma(R_q)\right\} \Longrightarrow D_{\mathrm{SOC},qp} = 0, \quad \forall p \neq q \tag{3.74}$$

which means that, in such special cases, the $\mathbf{D}_{\mathrm{SOC}}$-tensor is diagonal and hence, coincident with the $\mathbf{D}_{\mathrm{SSC}}$-tensor.[12]

3.3.7 Relationship between $\mathbf{D}_{\mathrm{SOC}}$ and the g-tensor

The formula for the anisotropic g-tensor was derived in an earlier section and, for a triplet state, it is given by:

$$\mathbf{g} = g_e \mathbf{1}_3 - \frac{\sqrt{2}}{\hbar} \sum_b \mathbf{\Lambda}_{ab} \otimes \boldsymbol{\mathcal{L}}_{ba} \tag{3.75}$$

As a reminder, $\mathbf{\Lambda}_{ab}$ is a matrix element of the orbital angular momentum divided by the energy difference between states a and b. Hence, $\mathbf{\Lambda}_{ab}$ has the same symmetry species as $\boldsymbol{\mathcal{L}}_{ba}$, and the selection rules for the elements of the g-tensor are given by:

$$\Gamma_0 \notin \left\{\Gamma_a \otimes \Gamma(R_p) \otimes \Gamma_b\right\} \cap \left\{\Gamma_b \otimes \Gamma(R_q) \otimes \Gamma_a\right\} \Longrightarrow g_{pq} = g_e \delta_{pq} \tag{3.76}$$

which is equivalent to the selection rules for the $\mathbf{D}_{\mathrm{SOC}}$-tensor. However, the g-tensor contains only contributions from states of the same multiplicity as the state of interest. This means that meaningful conclusions can be drawn by comparing the g-tensor with the triplet-triplet contribution to $\mathbf{D}_{\mathrm{SOC}}$.

Comparison of the selection rules in 3.76 and 3.72 leads to the conclusion that the off-diagonal zeros of the $\mathbf{D}^{tt}_{\mathrm{SOC}}$-tensor coincide with the off-diagonal zeros of the g-tensor:

$$D^{tt}_{\mathrm{SOC},pq} \overset{\diamond}{=} 0 \Longleftrightarrow g_{pq} \overset{\diamond}{=} g_e \delta_{pq} \tag{3.77}$$

where the diamond '$\diamond$' above the equality means 'by symmetry' (as opposed to accidental zeros). This relationship between the two tensors implies that if the $\mathbf{D}^{tt}_{\mathrm{SOC}}$ is diagonal in the molecular frame (*e.g.* if condition 3.74 is satisfied), then so is the g-tensor. Interestingly, this situation also implies that $\mathbf{D}^{tt}_{\mathrm{SOC}}$ and g are both collinear with $\mathbf{D}_{\mathrm{SSC}}$.

3.3.8 Summary of fine-structure interaction tensors

Thus far, the effects of the EZ and ZFS spin Hamiltonians on the spin states and energy levels has been discussed, and, with the aid of perturbation theory, expressions for the two fine-structure interaction tensors relevant to this work have been derived. The formulas and selection rules for the elements of the g- and D-tensors are summarised in table 3.1. The symbols in this table have all been introduced earlier. Nonetheless, their meaning is summarised below:

- $\mathbf{\Lambda}_{ab}$ is a purely imaginary vector given by the matrix elements of the orbital angular momentum

[12] Note that if $\Gamma_a \otimes \Gamma_b = \Gamma_0$ then the entire $\mathbf{D}_{\mathrm{SOC}}$ is necessarily zero. This is the 'trivial' case for coincidence with $\mathbf{D}_{\mathrm{SSC}}$. Furthermore, when $\Gamma_a \otimes \Gamma_b = \Gamma(R_q)$, then the only element of the $\mathbf{D}_{\mathrm{SOC}}$-tensor which could be non-zero is $D_{\mathrm{SOC},qq}$.

operators:

$$\mathbf{\Lambda}_{ab} = \Delta_b^{-1} \langle a | \sum_i \hat{\mathbf{l}}_i | b \rangle \tag{3.78}$$

- $\boldsymbol{\mathcal{L}}_{ab}$ is a purely imaginary vector whose components are given by the reduced matrix elements of the SOC Hamiltonian:

$$\boldsymbol{\mathcal{L}}_{ab}(q) = \mathcal{A} \langle aS \| \sum_i \sum_k \frac{Z_k^{eff}}{\hat{r}_{ik}^3} \hat{l}_{ik,q} \hat{\mathbf{s}}_i \| bS' \rangle \tag{3.79}$$

- $\hat{\boldsymbol{\epsilon}}$ is the unit inter-spin vector,

- $\underset{\sim}{\mathbf{s}}^2$ is a shorthand for the following reduced matrix element (the summation sign is suppressed):

$$\underset{\sim}{\mathbf{s}}^2 = \langle S \| \hat{\mathbf{s}}_i \| S \rangle \langle S \| \hat{\mathbf{s}}_j \| S \rangle \tag{3.80}$$

- For a triplet state, $f(\Delta S)$ takes the following values (where ΔS is the difference in S for the admixing states):

$$f(0) = \frac{1}{6}, \quad f(+1) = \frac{1}{3\sqrt{3}}, \quad f(-1) = \frac{1}{6\sqrt{15}} \tag{3.81}$$

- Γ_0, Γ_i, $\Gamma(R_q)$, and $\Gamma(q)$ are the symmetry species of the totally symmetric, electronic wavefunction i, q-axis rotation matrix, and q-axis irreducible representations, respectively.

Tensor	Formula	Perturbation Order	Selection rules
$\mathbf{g}^{(1)}$	$g_e \mathbf{1}_3$	1^{st}	-
$\mathbf{g}^{(2)}$	$-\frac{\sqrt{2}}{\hbar} \sum_b \mathbf{\Lambda}_{ab} \otimes \boldsymbol{\mathcal{L}}_{ba}$	2^{nd} $(\Delta S = 0)$	$\Gamma_0 \in \left\{ \Gamma_a \otimes \Gamma(R_p) \otimes \Gamma_b \right\} \cap \left\{ \Gamma_b \otimes \Gamma(R_q) \otimes \Gamma_a \right\}$
$\mathbf{D}_{\text{SSC}}$	$\frac{1}{2\hbar^2} \mathcal{C} \underset{\sim}{\mathbf{s}}^2 \left\langle \frac{\mathbf{1}_3 - 3\hat{\boldsymbol{\epsilon}} \otimes \hat{\boldsymbol{\epsilon}}}{\hat{r}^3} \right\rangle$	1^{st}	$\Gamma_0 \in \{ \Gamma(p) \otimes \Gamma(q) \}$
$\mathbf{D}_{\text{SOC}}$	$\mathbf{D}_{\text{SOC}} = f(\Delta S) \sum_b \frac{1}{\hbar^2 \Delta_b} (\mathbf{1}_3 \boldsymbol{\mathcal{L}}_{ab} \cdot \boldsymbol{\mathcal{L}}_{ba} - 3\boldsymbol{\mathcal{L}}_{ab} \otimes \boldsymbol{\mathcal{L}}_{ba})$	2^{nd} $(\Delta S = 0, \pm 1)$	$\Gamma_0 \in \left\{ \Gamma_a \otimes \Gamma(R_p) \otimes \Gamma_b \right\} \cap \left\{ \Gamma_b \otimes \Gamma(R_q) \otimes \Gamma_a \right\}$

Table 3.1: Summary of the fine-structure interaction tensors derived in this chapter. Note on the units: $\mathbf{\Lambda}_{ab}$ and $\boldsymbol{\mathcal{L}}_{ab}$ are measured in $\hbar\times$ Joules^{-1} and Joules, respectively; thus, the $\mathbf{g}$-tensor is unitless. The $\mathbf{D}$-tensors are expressed in units of Joules$\times\hbar^{-2}$, thus rendering the ZFS energy in Joules (all spin and orbital angular momentum operators in this thesis have an implicit factor of $\hbar$ *i.e.* they are in SI units).

3.4 Transient EPR on photoexcited triplet states

As mentioned at the outset of this chapter, short lived transient species can be detected using the transient EPR technique, which will henceforth be denoted as 'trEPR'. The following sections will give a brief outline of this technique with particular emphasis on the detection of triplet states and on the general appearance of their trEPR spectra.

3.4.1 Acquisition and instrumentation

TrEPR spectra can be acquired using the same type of cwEPR spectrometer as depicted in figure 1.5 with a few key modifications. The first, and most obvious modification, is that EPR signal detection needs to be synchronised with a laser pulse. A delay generator can be used to trigger both the laser pulse and the EPR detection circuits. Furthermore, cwEPR spectrometers are often times equipped with a 'transient recorder' which is an electronic circuit designed to process (*e.g.* by filtering, amplification, quadrature) and recover the time dependent absorption (and indeed emission) of microwaves by comparison with a reference microwave signal. The typical time resolution achievable in a trEPR experiment is of the order of a few nanoseconds.

There is a second, and very consequential, modification to the trEPR detection scheme as compared to the usual cwEPR set-up. In trEPR, the spectra are recorded *without* field modulation *i.e.* phase-sensitive detection is not employed. There is a simple reason for this: since the trEPR signal decays very rapidly, typically over a period of the order of say ~10 μs, the external magnetic field would have to be modulated at very large frequencies. The modulation frequency would have to be tuned to allow multiple field oscillations to take place over a time frame in which the EPR signal is constant. This requires a very accurate and versatile device to generate precise modulation amplitudes at a user defined frequency. Technical difficulties aside, the frequency itself would be in the radio or even microwave region of the electromagnetic spectrum. The field modulation could, therefore, induce magnetic resonance transitions of either the nuclear or electronic spin energy levels or interfere with the usual incoming radiation.

Due to the absence of phase-sensitive detection, we might be tempted to say that the resulting trEPR spectra would be dramatically weaker than usual cwEPR spectra. Indeed, if the transient species is formed in a thermal equilibrium of its spin energy levels (Boltzmann radical), the trEPR signal would be very weak unless very large magnetic fields and very low temperatures were employed. However, more often than not, transient radicals are not formed in thermal equilibrium *i.e.* they are *spin polarised*. Hence, if spin polarisation is significant, trEPR spectra will be intense and detectable without field modulation.

3.4.2 Triplet states in thermal equilibrium

The discussion below draws on the ideas introduced in section 1.2.2 of Chapter 1. The porphyrin based photo-excited triplet states in this thesis are formed by a cascade of rapid events amongst which there is an intersystem crossing (ISC) step from an excited singlet state to a triplet state. This ISC event is mediated by the SOC interaction. As a result of this, the final triplet state measured in trEPR is spin polarised. This spin polarisation can reveal valuable information regarding the electronic structure

of the system, and hence, we need to understand its consequences on the appearance and analysis of spectra. Before we delve more deeply into the topic of spin polarisation, it is helpful to consider the trEPR spectrum of a fictitious Boltzmann triplet state (assuming that such a spectrum is obtainable in an idealized, noiseless trEPR experiment).

The positions of the EPR peaks in field domain are determined by the following Hamiltonian:

$$\hat{H} = \frac{\mu_B}{\hbar}\mathbf{B}\cdot\mathbf{g}\cdot\mathbf{S} + D\left(\hat{S}_z^2 - \frac{1}{3}\hat{S}^2\right) + E\left(\hat{S}_x^2 - \hat{S}_y^2\right) \tag{3.82}$$

The analytical eigensolutions of this Hamiltonian were described in detail in section 1.2.2. Now, we will employ a numerical solution of 3.82 for different magnitudes and orientations of the magnetic field in order to show the emergence of the trEPR spectrum for a simple illustrative case.

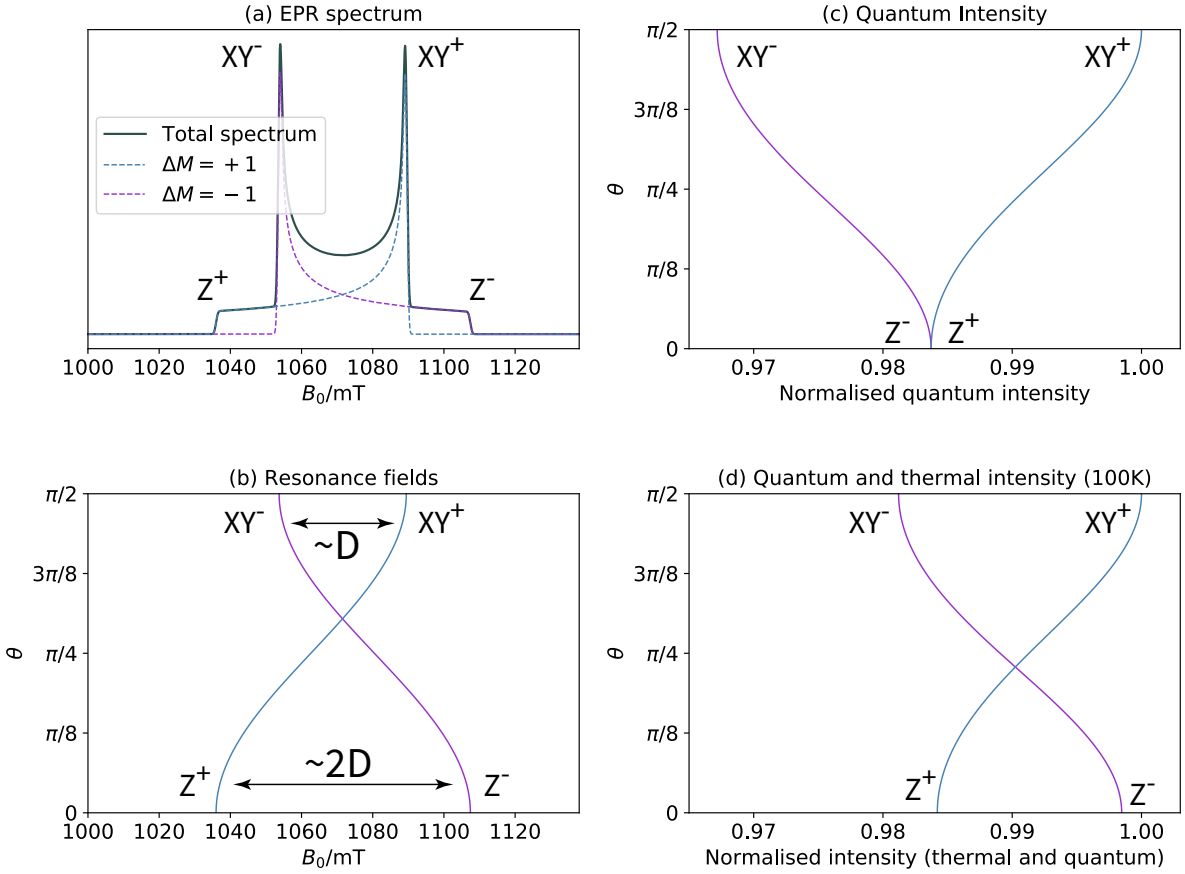


Figure 3.2: (a) Model EPR spectrum of a triplet state generated using the function *pepper* in EasySpin. The simulation parameters are as follows: $g_{iso} = 2$, a $D = 1$ GHz, $E = 0$, a Lorentzian line-width of 1 mT, and a microwave frequency of 30 GHz (chosen to show the high field limit for the ZFS parameters, $h\nu \gg D$). The spectra of the two allowed transitions are shown as the blue and purple lines, and the turning points are labelled according to the ΔM manifold and the orientation of the magnetic field relative to the **D**-tensor *e.g.* Z^+ corresponds to the $\Delta M = +1$ transition (*i.e.* $-1 \longrightarrow 0$) occurring when $\mathbf{B} \parallel D_Z$. (b) The dependence of the resonance fields on the angle, θ, between the external magnetic field and the D_Z-axis of the **D**-tensor. (c) The quantum intensity of the transitions as a function of θ, obtained according to equation 1.98. The values are normalised to the maximum value. (d) The product of the quantum intensity in panel (c) and the thermal/Boltzmann factor for a temperature of 100 K. Note: panels (c) and (d) do not contain the sin θ orientational weighting factor.

For simplicity, only the high-field limit will be considered which, in a field-swept EPR spectrum, cor-

responds to a ZFS much smaller than the spectrometer frequency, *i.e.* $h\nu \gg D$. Figure 3.2 shows an idealised EPR spectrum of a triplet state with $D > 0$ and $E = 0$ in the high-field limit. The positions of the peaks in the EPR spectrum, *i.e.* the resonance fields shown in panel (b) of figure 3.2 can be related to the magnitude of the D-value, whereas the barycenter of the spectrum is proportional to the g-value. For anisotropic **g**-tensors, the spectrum becomes significantly asymmetric with respect to the high and low field transitions.

Noteworthy is that the crossover of the resonance fields occurs at $\theta \approx 54.7^\circ$, the so-called 'magic angle'. At this angle, the spin system behaves analogously to one without any zero-field splitting interaction *i.e.* the energy levels are only separated by the Zeeman interaction and hence, this point determines the position of the barycenter of the EPR spectrum. Furthermore, if E had been set to a non-zero value in the simulation in figure 3.2, the $XY^{\pm}$ transitions would split into an $X^{\pm}$ and $Y^{\pm}$ transition. The assignment of the '$\pm$' label to the turning points in the EPR spectrum is not possible if the sign of D is unknown. The determination of the sign of D will be discussed in a later section.

Apart from the positions of the peaks and turning points, the origin of the transition intensities is also important to consider. Panel (c) in figure 3.2 shows that, despite being formally allowed, the two $\Delta M = \pm 1$ transitions do not have exactly the same quantum intensity (calculated using equation 1.98) for all orientations of the magnetic field vector relative to the D_Z-axis. For a positive D-value, the $\Delta M = +1$ transition becomes slightly more 'allowed'/intense, by ~ 3%, when the field vector is perpendicular to the D_Z-axis. This subtle difference in intensity is a result of the fact that the high-field limit is never truly reached. Hence, the M-values are never truly good quantum numbers except, of course, for the case when the magnetic field vector is exactly aligned with D_Z. For all other orientations, one can never prescribe an M label to the quantum states, and thus, the simplified $\Delta M = \pm 1$ selection rule is never entirely applicable.

The second factor which contributes to the intensity of the transitions is the Boltzmann population difference between the energy levels. As shown in panel (d) for a temperature of 100 K, the effect of the thermal equilibrium populations is to slightly ameliorate the difference in quantum intensity of the transitions. Furthermore, the intensity crossover point is seen to shift to $\theta > 0$ as a result of the Boltzmann contribution. This leads to a slight asymmetry between the intensity of the $XY^{\pm}$ transition. The asymmetry can be used to determine the sign of the D-value of triplet states in thermal equilibrium, a point which will be illustrated later.

Notwithstanding the above discussion, the overall shape of the total EPR spectrum is, all else considered, primarily the result of orientational averaging. In a frozen solution, all values of θ will contribute to the EPR spectrum. Whilst it might seem counter-intuitive, not all ranges of θ contribute in an equal measure to the final spectrum. Choosing an angle θ, is mathematically speaking, equivalent to choosing a random point on the surface of a sphere.

A truly random distribution of θ angles corresponds to a uniform distribution of points on the sphere. However, if points are distributed uniformly on a sphere, then the density of points in a given range, say between θ and $\theta + \delta\theta$, is proportional to the surface of that region:

$$\mathcal{S}(\theta \longrightarrow \theta + \delta\theta) = 2\pi r^2 \int_{\theta}^{\theta+\delta\theta} \sin\theta' \, d\theta' \tag{3.83}$$

which, for example, implies that there are $(\sqrt{2}+1) \approx 2.4$ more points within 45° around the equator ver-

sus the poles *i.e.* a much larger factor compared to the 2% difference in quantum and thermal intensities in figure 3.2. This argument is only warranted once the poles of the sphere are chosen, which is always the case in an EPR experiment: the poles of the sphere are by definition the ones passed through by the D_Z-axis. The resulting 'sin θ- weighting factor' is nothing other than the probability density of the spin system/**D**-tensor adopting an angle in the range $(\theta, \theta + \delta\theta)$ with **B**. Ultimately, this is the main reason why the $XY^{\pm}$ transitions in figure 3.2 are significantly more intense compared to the $Z^{\pm}$ transitions, and not the inherent quantum and thermal contributions to the intensity.

3.4.3 Spin polarised triplet states

Throughout this thesis the phrase 'spin polarisation' has a rather subtle meaning. In a simplified definition, a spin polarised triplet means that the population differences at a fixed magnitude, B, and orientation, (θ, ϕ), of the magnetic field are non-Boltzmann. This definition is, however, rather broad: the resulting EPR spectra could be arbitrarily complicated depending on the exact dependence of the population difference on B, θ and ϕ. The spin polarisation relevant to this thesis has some specific characteristics which simplify the interpretation of EPR spectra.

First of all, it is assumed that the photo-excitation event leads to the initial formation of a unique excited singlet state. As will be seen in the next section, a small perturbation due to the SOC interaction leads to non-zero populations being established in the triplet sub-levels. Whilst not entirely general, it is sufficient for this work to assume that the singlet and triplet eigenstates are not mixed.[13] Furthermore, within the triplet manifold, the eigenstates are not necessarily the same as the pure T_0 and $T_{\pm}$ eigenstates of $\hat{S}_z$ due to presence of the ZFS and EZ interactions.

Suppose that in the absence of the EZ interaction (at zero-field), the triplet sub-levels (X, Y, Z) from equation 1.45 are populated according to three quantities denoted by (P_X, P_Y, P_Z). If we now switch on a magnetic field of arbitrary orientation, the eigenstates of the system will be given by a linear combination of the ZFS eigenstates:

$$|n\rangle = \sum_{Q} c_Q^n |Q\rangle \tag{3.84}$$

where $Q = X, Y, Z$, and c_Q^n are the complex coefficients of $|n\rangle$ in the basis of $|Q\rangle$ (defined as $\langle Q|n\rangle$). Note that the perturbation which drives the ISC is the same whether the magnetic field is on or off. Hence, if we also assume that the ISC take places instantaneously, the spin system will initially be formed in one of the $|Q\rangle$ states with probability P_Q. However, because the magnetic field is switched on, the initial $|\psi(0)\rangle = |Q\rangle$ state is not an eigenstate of the Hamiltonian, and is thus non-stationary. The solution of the time-dependent Schrödinger equation gives us the future behaviour of the system following its

[13] *i.e.* the SOC interaction is not large enough to mix the eigenstates, but it is sufficiently large to mediate ISC (these two are not mutually exclusive).

creation in the non-eigenstate $|Q\rangle$:

$$\begin{aligned}|\psi(t)\rangle &= \exp\left[-\frac{i}{\hbar}\hat{H}t\right]|\psi(0)\rangle = \\ &= \exp\left[-\frac{i}{\hbar}\hat{H}t\right]|Q\rangle = \\ &= \exp\left[-\frac{i}{\hbar}\hat{H}t\right]\sum_n c_n^Q|n\rangle = \\ &= \sum_n c_n^Q \exp\left[-\frac{i}{\hbar}E_n t\right]|n\rangle.\end{aligned}$$

Therefore, if the system is initially in state $|Q\rangle$, the probability of the system being in eigenstate $|n\rangle$ is given by:

$$P_n = P_Q\left|c_n^Q\right|^2 \tag{3.85}$$

(whereby the probability P_Q of being in state $|Q\rangle$ at $t = 0$ has also been included). We observe that P_n is independent of time despite the fact that $|\psi(t)\rangle$ has an explicit time dependence. The presence of the coherent evolution in the expression for $|\psi(t)\rangle$ is, in principle, detectable in a transient EPR experiment. However, throughout this thesis, we will neglect this complication owing to the fact that such coherences decay rapidly.[14]

State $|n\rangle$ can also be generated starting from the other zero-field states, not just $|Q\rangle$. Hence, the final population of eigenstate $|n\rangle$ will be summed over all possible initial states:

$$P_n = \sum_Q P_Q\left|c_n^Q\right|^2 \tag{3.86}$$

In spite of neglecting the short lived coherences present in the true wavefunction, this final formula is remarkably accurate at predicting the appearance of a vast number of photo-excited triplet state spectra, particularly the ones investigated in this thesis. It is interesting to investigate the implications of equation 3.86 in more detail.

First of all, it can be seen that the effects of spin polarisation are quantified with the aid of only three additional parameters, P_Q. The effect of the magnitude and orientation of the magnetic field is predetermined by the coefficients $c_n^Q = (c_Q^n)^\star = \langle n|Q\rangle$ which are readily obtained from the spin Hamiltonian. Computationally speaking, the presence of spin polarisation of this kind has virtually no negative impact on the efficiency of EPR spectral simulations. The coefficients c_n^Q are computed regardless of spin polarisation, as they are required for obtaining the quantum intensity. Hence, the only additional step is the simple sum of three numbers shown in 3.86 with P_Q supplied in the input. The simulation of spin polarisation based on equation 3.86 is featured in the EasySpin toolbox as part of the functions *pepper* and *resfields*.

Notwithstanding the value of numerical simulations, it is also possible in certain cases to evaluate the effects of spin polarisation analytically. For instance, when the magnetic field is along the D_Z-axis, the

[14]These coherences will decay on the time-scale of spin-spin relaxation which is significantly faster than the decay due to spin-lattice relaxation (which eliminates spin polarisation). The presence of these coherences could, in principle, be refocused in a pulse EPR experiment, provided that signals can be recorded at very short delays after the laser pulse.

coefficients c_n^Q of the eigenstates $|n\rangle$ are given in equation 1.54 which is repeated here for clarity:

$$\begin{cases} |0\rangle = |Z\rangle \\ |\pm\rangle = \pm\frac{1}{\sqrt{2}}\sqrt{1 \mp \frac{E}{\sqrt{E^2 + \hbar^2\gamma_z^2}}}|X\rangle \\ \qquad\qquad + \frac{1}{\sqrt{2}}\sqrt{1 \pm \frac{E}{\sqrt{E^2 + \hbar^2\gamma_z^2}}}|Y\rangle \end{cases} \tag{3.87}$$

Without loss of generality, we can set the zero-field populations to satisfy the following two constraints:

$$\begin{cases} P_X + P_Y + P_Z = 1 \\ \min P_Q = 0 \end{cases} \tag{3.88}$$

because only relative, rather than absolute, sub-level populations are important for the intensity of EPR spectra. This constraint reduces the number of zero-field populations required to simulate triplet spectra to only two instead of three.

Application of equation 3.86 to the triplet eigenstates in 3.87 leads to the following sub-level populations in the presence of a magnetic field along the D_Z-axis:

$$\begin{cases} P_0 = P_Z = 1 - (P_X + P_Y) \\ P_\pm = \frac{1}{2}(P_X + P_Y) \pm \frac{E}{\sqrt{E^2 + \hbar^2\gamma_z^2}}(P_Y - P_X) \end{cases} \tag{3.89}$$

and thus, the sum of the populations is conserved.

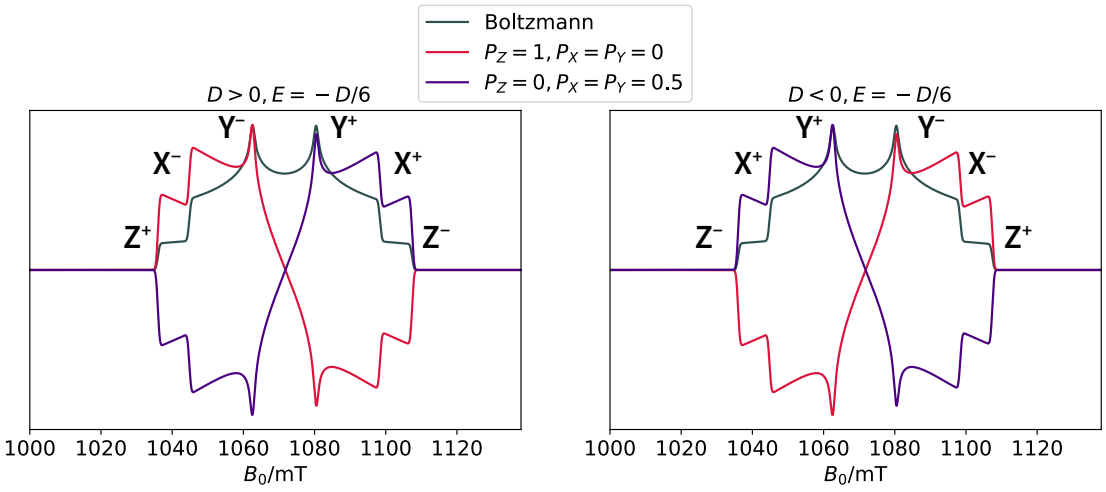


Figure 3.3: The effect of the zero-field sub-level populations on the EPR spectrum of a triplet with $D = +1000$ MHz and $E = +D/6$ (left) and $D = -1000$ MHz and $E = +D/6$ (right). The simulations are shown for out-of-plane and in-plane spin polarisation patterns, as the red and blue lines, respectively. The thermal equilibrium spectrum is shown for reference in grey. The transitions are labelled by the convention introduced in figure 3.2. Noteworthy, is that a change in the sign of D can be compensated by changing the ZFS populations (and thus, the sign of D and the populations cannot be determined simultaneously from these types of spectra).

Furthermore, we see that the $|\pm\rangle$ states can have equal populations either if $E = 0$ or if $E \neq 0$ but we are in the high-field limit ($\hbar\gamma_z \longrightarrow \infty$). If these populations are also the smallest, then convention 3.88 also sets them to be exactly zero. Hence, the polarisations of the allowed $|0\rangle \longrightarrow |\pm\rangle$ EPR transitions will have equal magnitude (P_Z) and opposite signs (because $|-\rangle$ is lower in energy than $|0\rangle$, whereas $|+\rangle$ is higher in energy; see figure 1.3). An equivalent result is obtained if P_Z is the smallest and is set to zero. Also due to equation 3.89, we note that at this field orientation, the $P_\pm$ populations can only be different if both ($P_Y \neq P_X$) and $E \neq 0$ are satisfied simultaneously. These observations highlight the link between the symmetry of the ZFS interaction, the eigenstates, and the sub-level populations.

In summary, spin polarisation manifests itself as a sequence of both absorptive and emissive features in the trEPR spectrum. The particular pattern will depend on the sign of D, the ZFS sub-level populations, and the orthorhombicity of the ZFS interaction. This is illustrated in figure 3.3 for a variety of scenarios. First of all, that if the D-value is positive (left panel), an out-of-plane (P_Z-only) spin polarisation pattern results in an absorptive low-field Z^+ transition and an emissive high-field Z^- transition. If the polarisation pattern is kept the same and the sign of D is inverted (right panel), the spectrum is also inverted (and so are the ± labels). Alternatively, if the sign of D is inverted, the spectrum can be kept the same by adjusting the populations from in-plane to out-of-plane, or vice versa. This can be seen by comparison of the red and blue spectra in the left and right panels of figure 3.3. This final observation is important because it illustrates the fact that the sign of the D-value cannot be determined from these EPR spectra unless the sub-level populations are known *a priori*.

A knowledge of the sign of the D-value and the zero-field spin polarisation pattern can provide crucial insights into the electronic structure of molecular triplet states. As per the discussion in the previous section, the sign and magnitude of the D-value are intrinsically linked to the symmetry of the spin density and the average inter-spin distance between the electrons comprising the triplet state.[15] The populations, on the other hand, offer insight into the mechanism of ISC and often times into the origins of the SOC interaction. This latter point will be the topic of the next section.

3.5 Spin-orbit driven intersystem crossing

Once a molecule is photo-excited, there are a variety of photo-physical processes that can take place. These processes can be grouped into radiative (involving light) and non-radiative events. Internal conversion and intersystem crossing (ISC) are just two examples of non-radiative processes. Both of them involve a change in the electronic wavefunction: the former conserves the total spin of the molecule and changes the spatial part of the wavefunction, whereas the latter changes the total spin of the molecule and can also change (or not) the spatial part. In this section, we will focus exclusively on ISC events, as these are the processes which lead to spin polarisation in organic, photo-induced triplets. In particular, we will delve more deeply into the theory behind SOC mediated ISC events. Much of the proceeding discussion draws on two review articles which contain a significantly more detailed discussion [50, 65].

Consider a single pair of electronic states of a molecule, one of which is an excited singlet and the other a triplet, as illustrated in figure 3.4. The singlet state is formed by a photo-excitation event from the ground singlet state under spin conservation. Assume that immediately after photo-excitation, a rapid (and radiationless) vibrational relaxation cascade leads to the lowest vibrational level of the excited sin-

[15] And occasionally, the sign of D is a reflection of the strength of the SOC interaction.

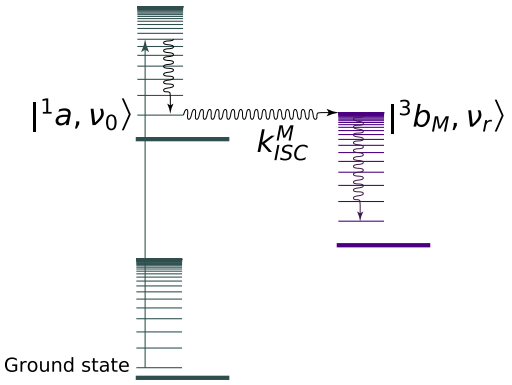


Figure 3.4: Jablonski diagram for the model system considered in this section. The singlet and triplet manifolds correspond to the grey and magenta lines, respectively. Thick long lines represent the adiabatic energies of the states, whereas thin short lines denote the vibrational states of a particular mode. The vertical arrow denotes photo-excitation, and the curly arrows denote non-radiative events; vibrational relaxation is vertical and ISC is horizontal. All other fates of these excited states are neglected in the discussion. The labelling scheme used for the electronic vibrational states is detailed in the main text; in short, state $|^1a, v_0\rangle$ is the excited singlet which intersystem crosses to the M sub-level of the triplet state, $|^3b_M, v_0\rangle$, with a rate constant denoted as k^M_{ISC}.

glet state to be populated. This state will be labelled as $|^1a, v_0\rangle$, where the '1' superscript indicates the multiplicity, a corresponds to the spatial wavefunction, and v_0 denotes the ground vibrational wavefunction (quantum number 0).

The singlet-triplet energy gap is typically larger than the spacing between the vibrational energy levels. Hence, as shown in figure 3.4, the energy of $|^1a, v_0\rangle$ corresponds to a high density of vibrational states in the triplet manifold. If the triplet wavefunction is labelled as $|^3b_M, v_r\rangle$ where v_r denotes a high energy vibrational state ($r \gg 0$) and M labels the spin sub-level, then application of Fermi's Golden Rule to find the rate of ISC [1] gives:

$$k^M_{ISC} = 2\pi \sum_r \left|\langle {}^1a, v_0|\hat{V}|{}^3b_M, v_r\rangle\right|^2 \delta(E_{a0} - E_{br}) \tag{3.90}$$

whereby, for the moment, the ZFS interaction is assumed to be absent. The $\hat{V}$ operator represents the interaction which mediates the ISC event. As mentioned before, SOC is the major contributor to ISC, however, the nuclear kinetic energy operator, $\hat{T}_n$, can also play a role to second order in perturbation theory, as proposed in reference [66]:

$$\begin{aligned}\langle {}^1a, v_0|\hat{V}|{}^3b_M, v_r\rangle = \langle {}^1a, v_0|\hat{H}_{SOC} + \hat{T}_n|{}^3b_M, v_r\rangle \approx \underbrace{\langle {}^1a, v_0|\hat{H}_{SOC}|{}^3b_M, v_r\rangle}_{\text{spin-orbit}} + \\ \underbrace{+ \sum_{c\neq b}\sum_j \frac{\langle {}^1a, v_0|\hat{H}_{SOC}|{}^3c_{M'}, v_j\rangle\langle {}^3c_{M'}, v_j|\hat{T}_n|{}^3b_M, v_r\rangle}{E_{cj} - E_{br}} + \sum_{d\neq a}\sum_p \frac{\langle {}^1a, v_0|\hat{T}_n|{}^1d, v_p\rangle\langle {}^1d, v_p|\hat{H}_{SOC}|{}^3b_M, v_r\rangle}{E_{dp} - E_{a0}}}_{\text{spin-vibronic (neglected)}}\end{aligned} \tag{3.91}$$

where we have identified the so-called spin-vibronic and spin-orbit contributions.[16] As mentioned in reference [50], the spin-vibronic contribution is often neglected in favour of the much larger first-order spin-orbit contribution. The calculation of the spin-orbit matrix element in the above equation proceeds by performing a Herzberg-Teller expansion of the vibrational parts of the wavefunction [66]:

$$\langle {}^1a, v_0|\hat{H}_{SOC}|{}^3b_M, v_r\rangle \approx \underbrace{\langle v_0|v_r\rangle\langle {}^1a|\hat{H}_{SOC}|{}^3b_M\rangle\Big|_{q_0}}_{\text{direct spin-orbit}} + \underbrace{\sum_\kappa \frac{\partial\langle {}^1a|\hat{H}_{SOC}|{}^3b_M\rangle}{\partial q_\kappa}\Big|_{q_0}\langle v_0|q_\kappa|v_r\rangle + \cdots}_{\text{vibronic spin-orbit}} \tag{3.92}$$

where q_0 is a suitably chosen set of nuclear coordinates representing the fixed point of the expansion, κ is an index running over the vibrational modes of the molecule, and q_κ is the respective canonical vibrational coordinate of mode κ. Essentially, the Herzberg-Teller expansion is nothing other than a Taylor series around a static point q_0 representing the geometry of the molecule at the crossing point of the two potential energy surfaces. A similar example of such an expansion can be found in Atkins' and Freedman's textbook, *e.g.* equation 11.11 relating to vibronically allowed electronic transition dipole moments [1]. By substituting the terms in equation 3.92 into the Fermi Golden Rule in equation 3.90 we can derive two major contributions to the ISC rate: the direct/Franck-Condon contribution and the vibronic/Herzberg-Teller contribution.

3.5.1 The Franck-Condon ISC mechanism

This contribution to the ISC rate is obtained by simply taking the square modulus of the direct spin-orbit matrix element in equation 3.92:

$$k^M_{ISC,FC} = 2\pi\left|\langle {}^1a|\hat{H}_{SOC}|{}^3b_M\rangle\right|^2_{q_0}\sum_r |\langle v_0|v_r\rangle|^2\,\delta(E_{a0}-E_{br}) = \tag{3.93}$$

$$= 2\pi\left|\langle {}^1a|\hat{H}_{SOC}|{}^3b_M\rangle\right|^2_{q_0}\rho(E_{a0}) \tag{3.94}$$

where $\rho(E_{a0})$ is the Franck-Condon weighted vibrational density of final states at the energy of the initial state, abbreviated VDOS. [17] The symmetry properties of the square absolute value of the SOC Hamiltonian matrix element will be discussed shortly.

Before however, the VDOS, $\rho(E_{a0})$ requires some further clarification. Explicit evaluations of this quantity are not trivial, and a variety of sophisticated methods, with differing levels of accuracy, have been employed throughout the literature [67–69]. The main complicating features of $\rho(E_{a0})$ are as follows: (1) the evaluation of the Franck-Condon factors, $|\langle v_0|v_r\rangle|^2$, for pairs of different electronic states with potentially quite different equilibrium geometries, (2) the computationally demanding summation over a large number of vibrational levels, and (3) the accurate modelling of Dirac's delta function.

In the high-temperature limit, the VDOS can be approximated by an Arrhenius-Marcus-type equation with an exponential dependence on the singlet-triplet energy gap [68]:

$$\lim_{kT\gg\Delta E}\rho(E_{a0}) = \frac{1}{\sqrt{4\pi\lambda kT}}\exp\left[-\frac{(\Delta E+\lambda)^2}{4\lambda kT}\right] \tag{3.95}$$

[16] Note that the spin-vibronic term is *not* the same as the vibronic spin-orbit term. The latter will be discussed shortly.
[17] Vibrational Density Of States. Sometimes also abbreviated Franck-Condon Weighted Density of states, FCWD.

where λ is the reorganization energy, and ΔE is the energy difference between the two states (including the vibrational energies). This equation is consistent with the so-called *energy gap law* for radiationless transitions according to which, the rate of a radiationless transition (such as ISC) is smaller the larger the adiabatic energy difference between the states.

If the high-temperature limit is not applicable, the calculation of $\rho(E_{a0})$ requires a more explicit modelling of the Franck-Condon overlap. In a time-independent approach, $|\langle \nu_0|\nu_r\rangle|^2$ is evaluated over a small interval around the energy of the initial state where the overlap of the vibrational wavefunctions is likely to be at its largest [67]. In a more sophisticated time-dependent approach, the time-domain representation of the Dirac delta function is combined with the density matrix formalism for vibrational states [69].

3.5.2 The vibronic/ Herzberg-Teller ISC mechanism

This contribution to the ISC rate can be further divided into two sub-parts: the Franck-Condon-Herzberg-Teller (FC-HT) contribution and the 'pure' Herzberg-Teller (HT) contribution. The former is a result of the cross term obtained from the direct spin-orbit and the vibronic spin-orbit parts of equation 3.92 [50, 65]:

$$k^M_{ISC,FC-HT} = 4\pi \sum_r \mathbb{Re}\left\{ \langle {}^1a|\hat{H}_{SOC}|{}^3b_M\rangle\Big|_{q_0} \langle \nu_0|\nu_r\rangle \times \right. \\ \left. \times \sum_\kappa \frac{\partial\langle {}^1a|\hat{H}_{SOC}|{}^3b_M\rangle}{\partial q_\kappa}\Big|_{q_0} \langle \nu_0|q_\kappa|\nu_r\rangle \right\} \delta(E_{a0} - E_{br}) \quad (3.96)$$

with $\mathbb{Re}$ denoting the real part of the expression enclosed by the curly brackets. The pure HT contribution is the product of the vibronic spin-orbit term with itself:

$$k^M_{ISC,HT} = 2\pi \sum_r \left\{ \sum_\kappa \frac{\partial\langle {}^1a|\hat{H}_{SOC}|{}^3b_M\rangle}{\partial q_\kappa}\Big|_{q_0} \langle \nu_0|q_\kappa|\nu_r\rangle \times \right. \\ \left. \times \sum_{\kappa'} \frac{\partial\langle {}^1a|\hat{H}_{SOC}|{}^3b_M\rangle}{\partial q_{\kappa'}}\Big|_{q_0} \langle \nu_0|q_{\kappa'}|\nu_r\rangle \right\} \delta(E_{a0} - E_{br}) \quad (3.97)$$

Note that both equations 3.96 and 3.97 are correct to first-order in perturbation theory and first-order in the Herzberg-Teller expansion (on the other hand, the neglected spin-vibronic terms in equation 3.91 are second-order in perturbation theory). This means that the FC-HT and HT contributions to the ISC are not always expected to be weaker than the direct mechanism. Indeed, in certain systems, the vibronic mechanism can dominate *e.g.* in the free-base porphyrin systems in the next chapter.

3.5.3 The emergence of spin polarisation

First of all, by using the Wigner-Eckart theorem, similarly to the result in equation 3.56, we can expand the SOC matrix element as follows:

$$\langle {}^3b_M|\hat{H}_{SOC}|{}^1a\rangle\Big|_{q_0} = \underbrace{\langle 0010|1M\rangle}_{M=0\Longrightarrow 1} \mathcal{L}_{ba}(0)\Big|_{q_0} - \underbrace{\langle 0011|1M\rangle}_{M=1\Longrightarrow 1} \mathcal{L}_{ba}(-1)\Big|_{q_0} - \underbrace{\langle 001-1|1M\rangle}_{M=-1\Longrightarrow 1} \mathcal{L}_{ba}(+1)\Big|_{q_0} \quad (3.98)$$

where we see that all three Clebsch-Gordan coefficients are equal to unity if the indicated selection rules for M are satisfied. In light of this, the SOC matrix elements between the singlet and the individual triplet manifolds take the following form:

$$\begin{cases} \langle {}^3b_0|\hat{H}_{SOC}|{}^1a\rangle = +\mathcal{L}_{ba}(0)\Big|_{q_0} \\ \langle {}^3b_{+1}|\hat{H}_{SOC}|{}^1a\rangle = -\mathcal{L}_{ba}(-1)\Big|_{q_0} \\ \langle {}^3b_{-1}|\hat{H}_{SOC}|{}^1a\rangle = -\mathcal{L}_{ba}(+1)\Big|_{q_0} \end{cases} \tag{3.99}$$

It should also be noted that the derivatives of the SOC matrix elements satisfy analogous relations to 3.99 because the differentiation with respect to the mode coordinate, q_κ, has no effect on the Clebsch-Gordan coefficients. In other words, the M sub-level dependence of the ISC rate is fully specified by the Clebsch-Gordan coefficients, for all contributions to the ISC rate (direct/vibronic).

By substituting equation 3.99 into equation 3.94, we obtain the following relations for the rates of ISC into the three spin sub-levels:

$$\begin{cases} k^0_{ISC,FC} = 2\pi\,|\mathcal{L}_{ba}(0)|^2_{q_0}\,\rho(E_{a0}) \\ k^{+1}_{ISC,FC} = 2\pi\,|\mathcal{L}_{ba}(-1)|^2_{q_0}\,\rho(E_{a0}) \\ k^{-1}_{ISC,FC} = 2\pi\,|\mathcal{L}_{ba}(+1)|^2_{q_0}\,\rho(E_{a0}) \end{cases} \tag{3.100}$$

In the Cartesian basis,[18] the above can be re-written as:

$$\begin{cases} k^0_{ISC,FC} = 2\pi\,|\mathcal{L}^z_{ba}|^2_{q_0}\,\rho(E_{a0}) \\ k^{+1}_{ISC,FC} = k^{-1}_{ISC,FC} = \pi\left\{|\mathcal{L}^x_{ba}|^2_{q_0} + |\mathcal{L}^y_{ba}|^2_{q_0}\right\}\rho(E_{a0}) \end{cases} \tag{3.101}$$

These final two equations are the origin of spin polarisation in the photo-induced triplet state of molecules. Entirely equivalent expressions can be derived for the vibronic mechanism, starting from 3.96 and 3.97, and the results will contain the vibrational mode derivatives of the reduced matrix elements, $\mathcal{L}^q_{ba}$. It should be noted that these two equations apply only to a single crossover event within an individual pair of singlet and triplet states. For real systems, this would be only one step in the entire photo-physical cascade of events initiated by light excitation.

Interestingly, equation 3.101 predicts that there should be no difference in the rate of populating the $M = \pm 1$ triplet manifolds. This is because we have so far neglected both the effects of the ZFS interaction and the magnetic field. The latter magnetic field dependence was addressed in the previous section and can be quantified with equations such as 3.89.

As far as the influence of ZFS on ISC is concerned, if $\mathbf{D}$ is much smaller than the singlet-triplet energy gap, the M dependence of the VDOS, $\rho(E_{a0})$, can be neglected. Also, if the ZFS interaction is quantified by an E-value of exactly zero, equation 3.101 remains accurate. This is obvious for the $|Z\rangle$ sub-level which is always equivalent to the $M = 0$ state, regardless of E. On the other hand, the $|X\rangle$ and $|Y\rangle$ states

[18] which is defined as $\mathcal{L}_{ba}(0) = \mathcal{L}^z_{ba}$ and $\mathcal{L}_{ba}(\pm 1) = \mp\frac{1}{\sqrt{2}}\left(\mathcal{L}^x_{ba} \pm i\mathcal{L}^y_{ba}\right)$.

are degenerate and therefore, can also be set equal to the $M = \pm 1$ states (when $E = 0$).

If the E-value is non-zero, the ISC to the non-degenerate $|X\rangle$ or $|Y\rangle$ zero-field states can be computed as:

$$
\begin{aligned}
k_{ISC}^{Y/X} &= 2\pi \sum_r \left| \langle {}^1a, v_0 | \hat{H}_{SOC} | {}^3b_{Y/X}, v_r \rangle \right|^2 \rho(E_{a0}) = \\
&= \pi \sum_r \left| \langle {}^1a, v_0 | \hat{H}_{SOC} | {}^3b_{+1}, v_r \rangle \pm \langle {}^1a, v_0 | \hat{H}_{SOC} | {}^3b_{-1}, v_r \rangle \right|^2 \rho(E_{a0}) = \\
&= \underbrace{\frac{1}{2}(k_{ISC}^{+1} + k_{ISC}^{-1})}_{\pi \sum_r \left(\left| \mathcal{L}_{ba}^{y} \right|^2 + \left| \mathcal{L}_{ba}^{x} \right|^2 \right) \rho(E_{a0})} \underbrace{\pm 2\pi \sum_r \mathbb{R}\mathrm{e} \left\{ \langle {}^1a, v_0 | \hat{H}_{SOC} | {}^3b_{+1}, v_r \rangle \langle {}^1a, v_0 | \hat{H}_{SOC} | {}^3b_{-1}, v_r \rangle^\star \right\} \rho(E_{a0})}_{\pm\pi \sum_r \left(\left| \mathcal{L}_{ba}^{y} \right|^2 - \left| \mathcal{L}_{ba}^{x} \right|^2 \right) \rho(E_{a0})}
\end{aligned}
$$

whereby we have grouped together both the direct and vibronic contributions (which is why q_0 does not appear in this equation). The expression simplifies to the remarkably elegant (and rather unsurprising) result:

$$k_{ISC}^{Y/X} = 2\pi \sum_r \left| \mathcal{L}_{ba}^{y/x} \right|^2 \rho(E_{a0}) \tag{3.102}$$

according to which the X, Y, and Z triplet sub-levels are populated by the x, y, z components of the SOC Hamiltonian (the same is true for both direct and vibronic contributions to ISC). However, the important caveat is that this entire derivation takes place in the eigenframe of the **D**-tensor. Often times, electronic structure software packages will yield numerical values for $\mathcal{L}_{ba}^{x/y/z}$. However, these numbers cannot be associated with the rate of ISC into the ZFS sub-levels, unless the molecule was already supplied (to the algorithm) in the ZFS eigenframe, which is often not possible without knowing the sub-level populations. Hence, it is clear that in order to understand the ISC mechanism, we need to understand the ZFS interaction, and vice-versa.

3.5.4 Selection rules for ISC

The most famous selection rule for ISC is *El Sayed's rule* [63], which is applicable only to the direct and FC-HT mechanisms. In its simplest formulation, the rule states that ISC is expected to be preferentially accompanied by a change in the spatial symmetry of the electronic wavefunction. The origin of this criterion can be seen most elegantly by examining the symmetry properties of the direct spin-orbit coupling matrix element in 3.92. Analogously to the discussion of the SOC contribution to ZFS, the strongest possible statement of El Sayed's rule is:

$$\Gamma_0 \notin \left\{ \Gamma_a \otimes \Gamma(R_q) \otimes \Gamma_b \right\} \Longrightarrow \left(k_{ISC,FC}^{q} = 0 \quad \text{and} \quad k_{ISC,FC-HT}^{q} = 0 \right) \tag{3.103}$$

where $\Gamma(R_q)$ is the irreducible representation spanned by the rotations around the q-axis (x, y, or z). For example, in the D_{2h} point group, the x, y, and z rotations transform as B_{1g}, B_{2g}, and B_{3g}. Hence, the direct and FC-HT crossovers between ${}^1B_{1g}$ states and ${}^3B_{2g}$ states are expected to lead to preferential $|Z\rangle$ sub-level populations because ISC is mediated by the B_{3g} rotation.

There is a second selection rule which applies to the derivative terms in the expressions for the FC-HT and pure HT contributions to ISC (3.96 and 3.97). To derive these rules, we require the following

condition to be satisfied for vanishing populations in the $|q\rangle$ zero-field sub-level:

$$\Gamma_0 \notin \left\{ \Gamma \left[\left. \frac{\partial \mathcal{L}^q_{ab}}{\partial q_\kappa} \right|_{q_0} \right] \right\} \tag{3.104}$$

i.e. the mode derivatives of the reduced SOC matrix elements (at the equilibrium geometry) must not span the totally symmetric irreducible representation. Whilst this condition is easy to state, some rearrangements are required to derive usable selection rules. First, we use the product rule for differentiation along the mode coordinate:

$$\frac{\partial \mathcal{L}^q_{ab}}{\partial q_\kappa} = \left(\frac{\partial \langle {}^1 a|}{\partial q_\kappa} \right) |\hat{\mathcal{L}}^q||^3 b\rangle + \langle {}^1 a||\left(\frac{\partial \hat{\mathcal{L}}^q}{\partial q_\kappa} \right)||^3 b\rangle + \langle {}^1 a||\hat{\mathcal{L}}^q| \left(\frac{\partial |^3 b\rangle}{\partial q_\kappa} \right) \tag{3.105}$$

If the sum of three functions spans a unique irreducible representation Γ, then each term in the sum will also span Γ. Thus far we have not shown that $\partial \mathcal{L}^q_{ab}/\partial q_\kappa$ spans a single irreducible representation rather than a sum of irreducible representations. The arguments for each of these three terms follow in an equivalent manner to the middle term which will be discussed in detail below. In order to derive selection rules, we require that:

$$\Gamma_0 \notin \left\{ \Gamma \left[\langle {}^1 a||\left(\frac{\partial \hat{\mathcal{L}}^q}{\partial q_\kappa} \right)||^3 b\rangle \right] \right\} \tag{3.106}$$

To make progress, we need to establish the irreducible representation of the derivative of the $\hat{\mathcal{L}}^q$ (reduced) operator. This is relatively easy to deduce if we perform a Herzberg-Teller expansion:

$$\underbrace{\hat{\mathcal{L}}^q}_{\Gamma(R_q)} = \hat{\mathcal{L}}^q\Big|_{q_0} + \underbrace{\sum_\kappa \left. \frac{\partial \hat{\mathcal{L}}^q}{\partial q_\kappa} \right|_{q_0} \underbrace{q_\kappa}_{\Gamma_\kappa}}_{\Gamma_{\text{deriv}}} + \cdots \tag{3.107}$$

where we have denoted the irreducible representations of each of the relevant components. We deduce that:

$$\Gamma_{deriv} \otimes \Gamma_\kappa = \Gamma(R_q) \Longrightarrow \Gamma_{deriv} = \Gamma(R_q) \otimes \Gamma_\kappa \quad \text{for non-degenerate } \Gamma_\kappa \tag{3.108}$$

Equations 3.106 and 3.108 allow us to formulate the following selection rule for the vibronic contributions to the ISC mechanism:

$$\Gamma_0 \notin \left\{ \Gamma_a \otimes \Gamma_\kappa \otimes \Gamma(R_q) \otimes \Gamma_b \right\} \Longrightarrow \left(k^q_{ISC,FC-HT} = 0 \quad \text{and} \quad k^q_{ISC,HT} = 0 \right) \tag{3.109}$$

This selection rule essentially states that vibrations can be coupled with the SOC Hamiltonian to give a non-zero ISC rate to a particular $|q\rangle$ zero-field sub-level, akin to vibronically allowed electronic transitions.[19] All of the above selection rules will be applied in a number of discussions throughout this thesis to aid the qualitative interpretation of the trEPR data. Note that for the FC-HT mechanism, both 3.109 and 3.103 need to be satisfied simultaneously.

[19]For degenerate vibrations, selection rules can also be derived, but the arguments are more intricate. In such cases, it is best to proceed on a case-by-case basis.

A brief note on computing ISC rates. As can be seen from the above survey into the origins of the various ISC mechanisms, the computation of the various rates requires an algorithm which can combine both the calculation of SOC matrix elements and the evaluation of SOC vibrational derivatives. Since version 4.2.0, the ORCA software provides the option to calculate ISC rates (both direct and vibronic) as part of the excited-state dynamics package [45].[20] Whilst valuable, this new feature of the ORCA software is still in development and unfortunately, except for some of the simpler porphyrin systems, calculations of ISC rates using ORCA have not been successful. Regardless, the symmetry arguments presented above will prove to be essential for the interpretation of the data in the next chapter.

3.6 Determining the orientation of the ZFS tensor

It was established in a previous section that the orientation of the $\mathbf{D}_{SSC}$-tensor is linked to the spheroidal symmetry of the spin density (figure 3.1) whereas the orientation of $\mathbf{D}_{SOC}$ depends on the spatial selection rules associated with the SOC operator (see table 3.1). In principle, computational methods can yield the correct orientation of either type of **D**-tensor. However, the usual trEPR experiment cannot be used to confirm the orientation of the **D**-tensor, unless the zero-field sub-level populations are known *a priori* (figure 3.3).

In principle, the best way to determine the orientation of **D** is to perform single crystal trEPR measurements. From the point of view of EPR spectroscopy, the measurement and the interpretation of single crystal spectra is, in many regards, less ambiguous than solid state/ frozen solution spectra.[21] However, from the point of view of sample preparation, single crystals are often unavailable (as is the case for all the molecules investigated in this thesis). In such cases, the orientation of the **D**-tensor can be determined using different methods, which will form the topic of this section.

In particular, two methods will be outlined: low temperature cwEPR and magneto-photo-selection (MPS) experiments. The former approach is applicable only to triplet states in thermal equilibrium whereas the latter is specifically designed for light induced spin polarised triplet states. Despite the fact that the former method is not used in this thesis, its power and limitations are essential to understand before the MPS experiment is considered in greater detail.

There is one crucial caveat associated with the determination of the orientation of the **D**-tensor with either of these two experiments: it is impossible to distinguish between *right-handed* and *left-handed* **D**-tensors. We will define the 'handedness' of the **D**-tensor shortly and illustrate the significance of this caveat.

3.6.1 Low temperature cwEPR

Consider a triplet state similar to the model spin system with $D = \pm 1000$ MHz and $\lambda = 1/6$ considered in figure 3.3. As alluded to before, the thermal equilibrium cwEPR spectrum will have a small temperature dependence which can be used to determine the orientation of the **D**-tensor and hence the sign of the D-value.

[20] And only in the framework of time dependent DFT.

[21] *e.g.* one would not need to perform the costly orientational averaging which greatly slows down the simulation of complex spin systems

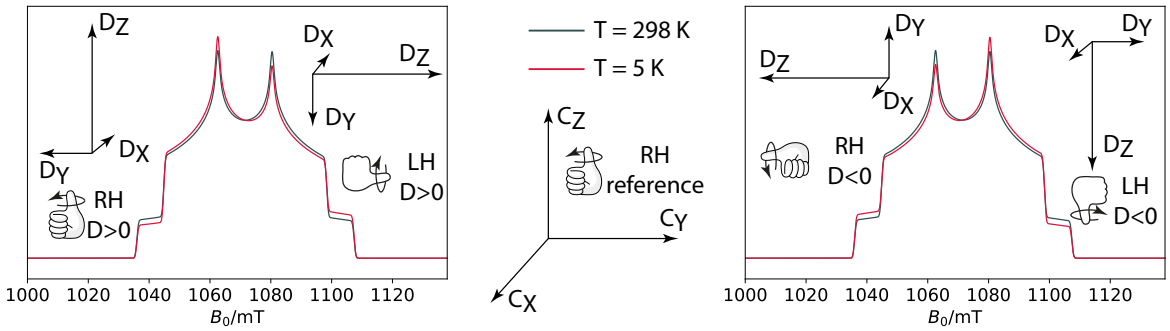


Figure 3.5: The high-temperature (298 K) and low-temperature (5 K) cwEPR spectra of the spin system described in the main text, shown as black and red lines, respectively. The spectra were obtained using the same method and parameters as the ones used for figures 3.2 and 3.3, except for the orientation of the **D**-tensor. The left panel corresponds to $D = +1000$ MHz for a LH and RH **D**-tensor, whereas the right panel refers to ZFS tensors which give rise to $D = -1000$ MHz. The orientation of the **D**-tensor axes are shown in each case relative to a common RH Cartesian coordinate frame depicted in the central diagram. The meaning and interpretation of all the ZFS axes and spectra in this figure will be clarified towards the end of this section.

For the purpose of this example, suppose that the **D**-tensor is known either from some highly accurate calculation or from an independent experiment. The more formal way of expressing the fact that the **D**-tensor is known, is to say that the three axes of the **D**-tensor can be calculated or independently measured (*i.e.* not using EPR) along a set of suitably chosen molecular/ Cartesian axes denoted by C_X, C_Y, and C_Z. This Cartesian reference frame is chosen to be a fixed, right-handed (RH) coordinate system as depicted in the center of figure 3.5.

Having defined this RH reference frame, let us consider the possible results of our independent measurements or calculations of the **D**-tensor. If the spin-orbit contribution is neglected and the spin density is assumed to be a quasi-oblate spheroid, *i.e.* compressed along C_Z and slightly elongated along C_X (with an orthorhombicity of 1/6), then the eigenvalues of the **D**-tensor could be the following (in MHz):

$$\begin{cases} D(C_X) = -166.\dot{6} \equiv D_X \\ D(C_Y) = -500 \equiv D_Y \\ D(C_Z) = +666.\dot{6} \equiv D_Z \end{cases} \tag{3.110}$$

As shown in the leftmost diagram in figure 3.5, this type of **D**-tensor is right-handed and its axes coincide with the Cartesian axes (except for the reversal of the directions of the D_X and D_Y axes, which is due to the fact that the tensor is traceless). This particular assignment of the D_X, D_Y, D_Z labels to the Cartesian values $D(C_X)$, $D(C_Y)$, $D(C_Z)$ is always done to satisfy the convention for the ZFS parameters set out in Chapter 1. Having assigned these labels, we can now deduce that this case corresponds to a positive D-value (because D_Z is positive).

The cwEPR spectrum corresponding to the **D**-tensor in 3.110 is also shown in the left panel of figure 3.5 for a room temperature and a low-temperature Boltzmann distribution. We see that the Boltzmann factor contribution to the intensity is only a minor effect which, as the temperature is decreased, causes a slight asymmetry in the cwEPR spectrum. For instance, the low-field Z^+ transition is less intense than the high-field Z^- transition, whereas the opposite effect is observed for the $X^\pm$ or $Y^\pm$ transitions. As

we shall see shortly, this asymmetry can be used to identify a RH **D**-tensor with a positive D-value and $D_Z \parallel C_Z$.

The next step in this discussion is to distort the spin density of this fictitious triplet state. In particular, we will perform a distortion which keeps the magnitude of the D-value the same, the orthorhombicity the same, and only changes the orientation of the **D**-tensor relative to the fixed Cartesian frame. Crucially, the distortion will be devised such that it maintains the handedness of the tensor (the final **D** will be RH). After some consideration,[22] it can be shown that we can achieve all of these results if we distort the spin density such that it becomes rod-like/cigar-like along the C_Y axis (a prolate spin density).[23] The eigenvalues of the tensor will become:

$$\begin{cases} D(C_X) = +166.\dot{6} \equiv D_X \\ D(C_Y) = -666.\dot{6} \equiv D_Z \\ D(C_Z) = +500 \equiv D_Y \end{cases} \tag{3.111}$$

which corresponds to a *negative* D-value and a D_Z axis which is parallel to the C_Y axis, $D_Z \parallel C_Y$, as shown in the right panel of figure 3.5. As can be seen, the effect of this distortion is to produce an EPR spectrum which is the mirror image of the spectrum with $D > 0$. As such, by measuring low-temperature cwEPR, it is possible to establish the orientation of the **D**-tensor: if the intensity of the low-field Z transition decreases with temperature, then we may conclude that the D-value is positive, the D_Z axis is parallel to the Cartesian C_Z-axis, and the spin density is an oblate spheroid.[24]

The critical turning point is the realization that the above mentioned distortion from oblate to prolate spin density (from 3.110 to 3.111) is not the only one that results in a negative D-value. As shown in figure 3.1, if we elongate the oblate spheroid along the C_Z axis, then the D-value also becomes negative. More precisely, if we impose the conservation of the magnitudes of D and λ (the orthorhombicity parameter), then elongation along the C_Z axis results in the following **D**-tensor:

$$\begin{cases} D(C_X) = +166.\dot{6} \equiv D_X \\ D(C_Y) = +500 \equiv D_Y \\ D(C_Z) = -666.\dot{6} \equiv D_Z \end{cases} \tag{3.112}$$

In other words, this distortion is equivalent to reversing the signs of all the eigenvalues of the **D**-tensor. The resulting D-value is still negative, yet, the D_Z-axis is now once more parallel to C_Z (see rightmost panel in figure 3.5). However, the EPR spectrum is identical to the one obtained from a prolate distortion along C_Y. It would thus seem that there is a paradox, a negative D-value corresponds to both $D_Z \perp C_Z$ and $D_Z \parallel C_Z$ EPR spectra. Similarly, the same can be shown to hold for positive D-values.

This paradox is a result of an error in interpretation, and particularly, in the terms of comparison. The resolution comes in the form of an additional convention/constraint on the **D**-tensor (complementary to the conventions in equations 1.34 in Chapter 1). Notwithstanding that the elongation along C_Z does truly lead to a negative D-value and to D_Z being parallel to C_Z, this distortion does not preserve the

[22] based on the results in figure 3.1.

[23] As will be shown shortly, elongation along the C_Z axis, as performed in the previous section, does not preserve the handedness of the tensor. This is in fact one of the major final points of this discussion.

[24] If there is also a non-zero SOC contribution, then it becomes more difficult to draw a conclusion about the symmetry of the spin density.

handedness of the **D**-tensor. The result is a left-handed tensor, as is immediately obvious from the resulting values in 3.112.

However, the handedness of the **D** tensor cannot be measured in a cwEPR experiment, as can be seen directly from figure 3.5. This is not surprising, elongation along any axis, be it C_Z or C_Y, will lead to the exact same prolate spin density.[25].

What is not invariant to a handedness inversion, is our interpretation of what it means to have a positive and negative D-value. If only RH tensors are compared in a RH reference frame, then the link between the sign of D and the orientation of **D** is as follows:

$$\text{RH } \mathbf{D}\text{-tensor and RH reference frame} \begin{cases} D > 0 \iff D_Z \parallel C_Z \\ D < 0 \iff D_Z \perp C_Z \end{cases} \tag{3.113}$$

whilst comparing LH tensors in a RH frame leads to the reverse of the above. In order to avoid the complications associated with the handedness of interaction tensors, the convention in this thesis will be the following: *all reported* **D***-tensors are right-handed tensors in a right-handed coordinate system.* Hence, equation 3.113 will be applicable from this point onwards.

This final convention for the ZFS interaction will become relevant in the discussion of the orientation of the **D**-tensor in the photo-induced triplet state of palladium porphyrin systems, for which the SOC contribution is of the opposite handedness to the SSC contribution.

3.6.2 Principles of the magneto-photo-selection experiment

Since spin polarisation is independent of temperature, the above method cannot be used to determine the orientation of **D** in photo-excited triplet states. However, the electronic transition dipole moment vector, $\boldsymbol{\tau}$, of the ground to excited singlet excitation can be used as an internal reference frame of the molecule with respect to which the orientation of **D** can be determined. Often times, the orientation of the optical vector, $\boldsymbol{\tau}$, is readily determined from group theory and in certain more difficult circumstances one might have to perform a more sophisticated calculation. Nonetheless, the orientation of the optical vector will be assumed to be known (and immutable) in the remaining discussion.[26]

The aim of an magneto-photo-selection (MPS) experiment is to establish the orientation of the **D**-tensor relative to the optical axis, $\boldsymbol{\tau}$, by using excitation with polarised light. Before we outline the principles of the MPS experiment, we define the following additional vector quantities: the external magnetic field vector, **B**, and the electric field vector of the incoming laser light, **E**. Figure 3.6 shows an example of how the four quantities (**D**, $\boldsymbol{\tau}$, **B**, **E**) can be oriented in space.

If photoexcitation occurs from every possible direction and the laser light is not polarised, then no orientation of $\boldsymbol{\tau}$ relative to **B** is preferred. In other words, the resulting excited state species will correspond to a uniform distribution of the optical vector *i.e.* the resulting EPR spectrum will be a typical powder average spectrum because the **D**-tensor will also have a uniformly distributed orientation relative to **B**.

An MPS experiment involves measuring the trEPR spectrum by setting the incident light (typically, a laser beam) to be polarised along one of two orientations: parallel to the magnetic field, **E** $\parallel$ **B**, or

[25] provided of course that we preserve $|D|$ and λ

[26] The terms 'optical vector' or 'optical axis' will be used throughout this thesis to refer to the transition dipole moment vector.

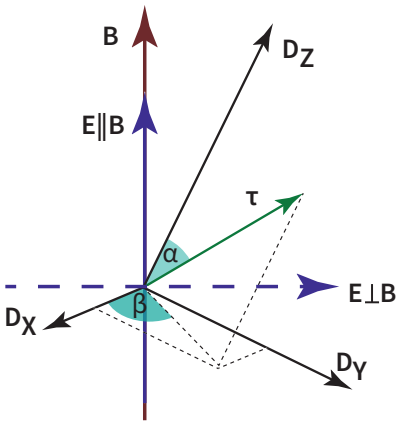


Figure 3.6: The vectors relevant to the description of the MPS experiment: the external magnetic field **B** (brown), the electric field of the incident laser light **E** (solid blue or dashed blue depending on its orientation with respect to **B**), the optical vector $\boldsymbol{\tau}$, and the three axes of the **D**-tensors ($\mathbf{D}_X$, $\mathbf{D}_Y$, and $\mathbf{D}_Z$). The angle α is taken to be between the $\mathbf{D}_Z$-axis and $\boldsymbol{\tau}$, whereas β is the angle between $\mathbf{D}_X$ and the projection of $\boldsymbol{\tau}$ onto the $\mathbf{D}_X\mathbf{D}_Y$ plane.

perpendicular to the magnetic field, $\mathbf{E} \perp \mathbf{B}$ (as shown in figure 3.6). The probability of the optical transition is at its largest when $\mathbf{E} \parallel \boldsymbol{\tau}$, and it vanishes when $\mathbf{E} \perp \boldsymbol{\tau}$. More formally, the probability of exciting a molecule with a particular $\boldsymbol{\tau}$ is proportional to the following dot product:

$$P(\hat{\boldsymbol{\tau}}) \propto \hat{\boldsymbol{\tau}} \cdot \hat{\mathbf{E}} \tag{3.114}$$

where the carets indicate unit vectors. Clearly, certain optical vectors in the ensemble, which are most closely aligned with **E**, will be excited preferentially *i.e.* certain orientations are photo-selected relative to **E**. Since the orientation of **E** is fixed relative to **B**, the resulting orientational distribution around **B** will not be uniform *i.e.* we may say that certain orientations are magneto-photo-selected. Finally, since the orientation of **D** relative to $\boldsymbol{\tau}$ is also fixed, the final trEPR spectra measured with $\mathbf{E} \parallel \mathbf{B}$ and $\mathbf{E} \perp \mathbf{B}$ will show a different intensity pattern. This pattern will depend on which orientations of **D** relative to **B** are preferentially excited.

As a clarification, consider the case when the optical axis is along the ZFS X-axis, $\boldsymbol{\tau} \parallel \mathbf{D}_X$, and the electric field of the incident light is set to $\mathbf{E} \parallel \mathbf{B}$. This setting of the laser polarisation means that molecules which have $\boldsymbol{\tau} \parallel \mathbf{B}$ are preferentially excited. In turn, this means that orientations of the **D**-tensor which satisfy $\mathbf{B} \parallel \mathbf{D}_X$ will contribute to the final EPR spectrum more than in a typical powder average. This effect is illustrated by the spherical density in the left of figure 3.7 whereby we see that orientations of the magnetic field closer to the $\mathbf{D}_X$-axis have a larger weighting. Conversely, if the polarisation of the laser is set such that $\mathbf{E} \perp \mathbf{B}$, then orientations of the field close to $\mathbf{D}_X$ will contribute the least to the EPR spectrum, as per the middle spherical density plot in figure 3.7.

Interestingly, excitation with depolarised light does not lead to a completely uniform distribution of **D** relative to **B** (right density plot in figure 3.7). This is because excitation is usually performed with a laser beam travelling in a single direction through the sample. The electric field vector will thus always be perpendicular to the beam direction. As a consequence, molecules with $\boldsymbol{\tau}$ exactly in the plane perpendicular to the direction of the beam are preferentially excited. However, as can be seen in figure 3.7, this effect is only a minor deviation from the powder average distribution.

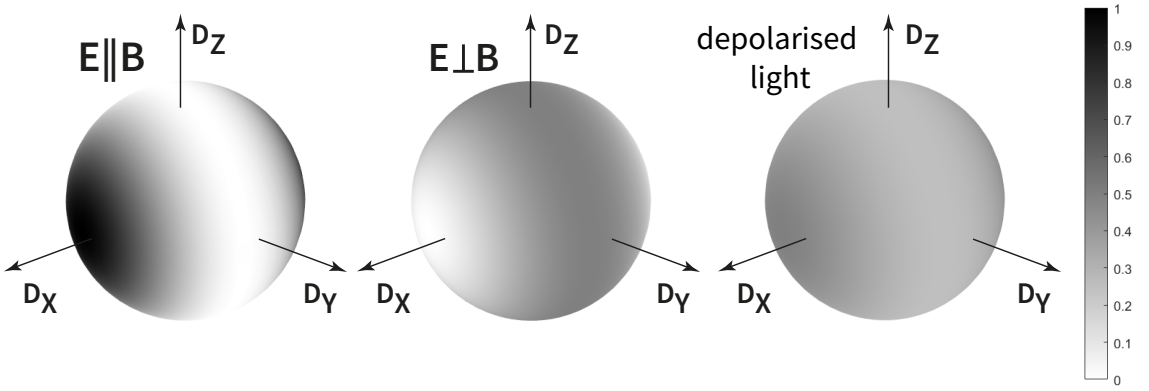


Figure 3.7: Spherical density plots showing the magneto-photo-selected orientations of the **D**-tensor relative to the external magnetic field for a molecule which has the optical vector, $\boldsymbol{\tau}$, along the $\mathbf{D_X}$-axis. In other words, each point on the sphere corresponds to a particular orientation of **B** relative to **D**, and the darkness of that point is proportional to the weighting of the corresponding orientation. The densities are shown for $\mathbf{E} \parallel \mathbf{B}$ and $\mathbf{E} \perp \mathbf{B}$ polarisations of the incident light as well as for depolarised light in the left, center, and right plots, respectively. The densities were generated by employing the formulas in reference [70] (final values were normalised to the maximum value across all three densities). The darker shades correspond to larger relative weights.

For the purpose of clarity, the above discussion of the MPS experiment has been qualitative rather than quantitative. A derivation of the mathematical formulas behind the principles of MPS and of the weighting factors used to generate the model density plots in figure 3.7 can be found in the doctoral thesis of Christiane R. Timmel [70]. In the remaining section, the MPS experiment will be described from the perspective of the resulting trEPR spectra of the same model system as used for the description of spin polarisation (see figure 3.3).

3.6.3 Model simulations of the MPS experiment

The original analysis of the MPS experiment was reliant on a semi-quantitative analysis of the changes in the intensity of the transitions in the EPR spectrum. As described in references [71, 72], the intensities of each of the $X^{\pm}$, $Y^{\pm}$, and $Z^{\pm}$ transitions in the trEPR spectrum are compared between spectra acquired with $\mathbf{E} \parallel \mathbf{B}$ and $\mathbf{E} \perp \mathbf{B}$. The changes can then be equated to the orientation of the **D**-tensor in a qualitative fashion. However, this analysis method is limited to trEPR spectra which display clearly resolved peaks corresponding to the different canonical orientations of the magnetic field relative to the ZFS axes.

In certain instances, the complex symmetry of triplet states combined with large spin Hamiltonian strains (distributions in the interaction parameters) greatly inhibit the qualitative methods mentioned above. For these situations, an MPS simulation algorithm is required in order to extract the orientation of **D** by least-squares fitting of the α and β angles (figure 3.6) to the data.

An initial working version of such an algorithm was developed as part of the work carried for this thesis in collaboration with Ashley J. Redman. This algorithm combines some of the functionalities of the EasySpin package together with the MPS equations in reference [70], and is presented in detail in the Part II thesis of Ashley J. Redman. However, at the time of writing this thesis, an open-source version of the EasySpin package was released. In turn, this facilitated the development of a greatly improved version of the MPS simulation script, called *pepper_MPS*, using some of the features of the original

pepper function which had previously been unavailable. This new *pepper_MPS* script was developed by Ashley J. Redman and will be published elsewhere in due course. *Pepper_MPS* is based on the same original theory and formulas behind MPS as used in the code written collaboratively between myself and Mr. Redman, but improves the efficiency of the code. As a result, only simulations obtained with *pepper_MPS* will be presented in the analysis of subsequent MPS data.

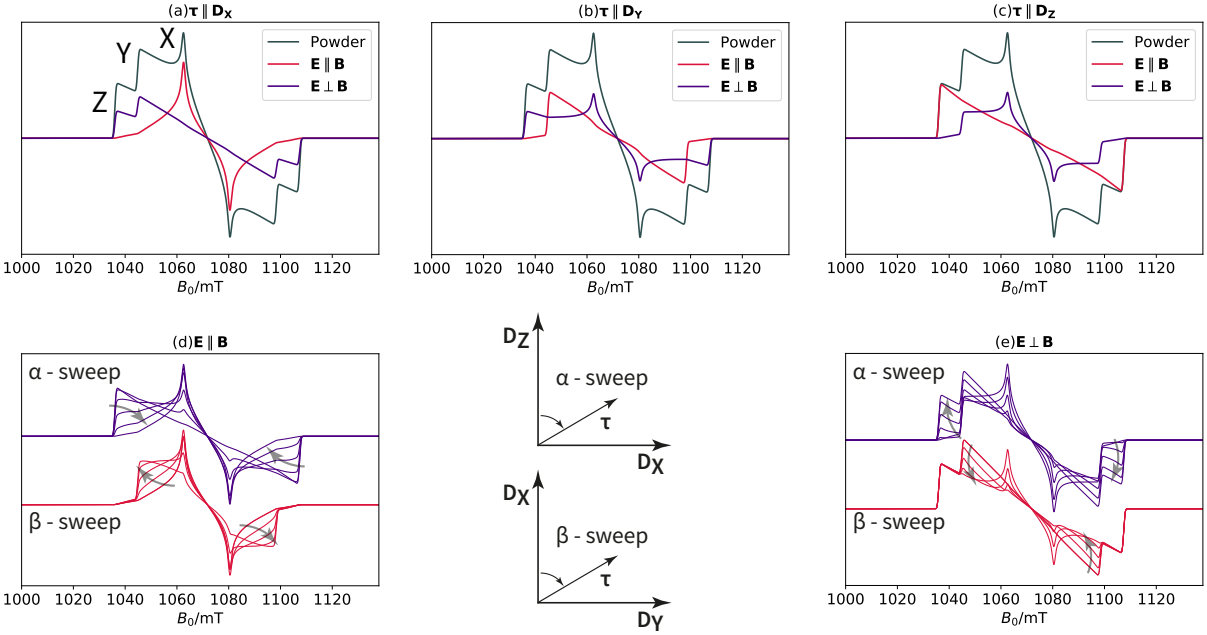


Figure 3.8: Simulations of the powder and MPS trEPR spectra at 30 GHz of a triplet state with $|D|$ = 1000 MHz and an orthorhombicity λ = 1/6. All other simulations parameters are the same as the ones in figures 3.2 and 3.3. In each panel, the spectra are normalised to the double integral of the powder spectrum. Panels (a)–(c) highlight the changes in intensity observed when the optical vector is along each of the three ZFS axes. Panels (d) and (e) show the changes in the spectra as a function of α and β for $\mathbf{E} \parallel \mathbf{B}$ and $\mathbf{E} \perp \mathbf{B}$, respectively. The '$\alpha$-sweep' entails keeping β fixed to zero, whereas the 'β-sweep' is done by keeping α fixed to $\pi/2$.

Panels (a)–(c) in figure 3.8 depict idealised MPS spectra for a model system with $|D|$ = 1000 MHz and an orthorhombicity λ = 1/6. In all cases, the sign of the E-value was chosen to be the same as the sign of the D-value. Thus, the ordering of the transitions in each EPR spectrum is ZYX–XYZ. As per the discussion associated with figure 3.7 we see the effects of the laser polarisation as an increase or decrease in intensities of the features corresponding to the different canonical orientations. For instance, the left density plot in figure 3.7 indicates that orientations of the **D**-tensor which have the $\mathbf{D}_X$-axis parallel to the magnetic field are preferred when $\boldsymbol{\tau} \parallel \mathbf{D}_X$ and $\mathbf{E} \parallel \mathbf{B}$. The resulting EPR spectrum shown as the red line in panel (a) of figure 3.8 is entirely reflective of this MPS effect. By contrast, the blue line in panel (a), which corresponds to $\mathbf{E} \perp \mathbf{B}$ displays an enhancement in the intensity of the Z and Y transitions.

Qualitatively, by inspection of panels (b) and (c), we also see that the discussion of the $\boldsymbol{\tau} \parallel \mathbf{D}_X$ case can be generalised to the other possible orientations of the optical vector relative to the **D**-tensor axes. In each case, the EPR spectra corresponding to the different polarisations are dramatically different. In fact, for these simple cases one can simply 'read' directly from the spectrum the relative orientation of **D**.

Panels (d) and (e) indicate that when the optical vector is not precisely aligned with a specific ZFS axis,

the qualitative analysis of the MPS experiment becomes slightly more ambiguous. The behaviour of the MPS spectra as a function of the α and β angles shown in figure 3.8 is both a testament to the power of this experiment and to the importance of having a reliable simulation algorithm. Together, MPS experiments and simulations can, in principle, be used to determine the orientation of **D** relative to $\boldsymbol{\tau}$ with high precision. Furthermore, most molecules have multiple optical axes, all of which (usually) correspond to different excitation wavelengths. In many cases, regardless of excitation wavelength, the photo-physics of the system can be such that all excitation wavelengths lead to the same final triplet state. Hence, MPS spectra recorded at different wavelengths, with two laser polarisations for each, can lead to a rather large and comprehensive set of experimental data. Since the orientation of **D** is the common variable in all these spectra, a global least-squares fitting can yield very accurate results.

Finally, it is necessary to emphasize that the MPS simulations and discussions presented in this section are based on a fictitious, ideal triplet state. In reality, both the experiment and the electronic structure of the actual triplet states can be significantly more subtle. For MPS in particular, data interpretation is often obscured by a number of different factors; for instance: the inability to guarantee the conservation of the laser polarisation inside the resonator leads to 'powder-like' contributions to the final MPS data, or the inability to guarantee that one, and only one, transition dipole moment is excited at a fixed wavelength [27] can lead to complex intensity patterns. Nonetheless, MPS is still an integral part of the 'EPR toolbox' of techniques which can shed light onto the origin of the **D**-tensor in the most challenging of systems, one of which will be encountered in this thesis.

3.7 ENDOR spectroscopy of triplet states

The Mims ENDOR technique was introduced in Chapter 1 as the primary method of this thesis for the determination of small hyperfine interactions. The technique was subsequently applied to the porphyrin radical cation systems explored in Chapter 2. As far as triplet states are concerned, the Mims ENDOR experiment can also be employed, however, the interpretation of the data requires further considerations. These considerations will be presented in the next section by means of a set of model simulations of Mims ENDOR spectra for an electronic triplet coupled to a proton with an anisotropic hyperfine interaction. Afterwards, it will be shown that Mims ENDOR can be used not only to quantify the distribution of the spin density but also to determine the orientation of the **D**-tensor.[28]

3.7.1 Model Mims ENDOR spectra

Consider the same electronic triplet state as discussed in section 3.6.1 *i.e.* one with an isotropic g-value of 2, and the following **D**-tensor in MHz:

$$\begin{cases} D(C_X) = -166.\dot{6} \equiv D_X \\ D(C_Y) = -500 \equiv D_Y \\ D(C_Z) = +666.\dot{6} \equiv D_Z \end{cases} \tag{3.115}$$

[27] Due to overlap of vibronic bands from different electronic transitions, or due to the overlap of optical transitions due to different molecular conformations

[28] Relative to a hyperfine tensor of known orientation.

As before, this corresponds to a right-handed tensor, in a right-handed Cartesian (or molecular) frame, with a positive D-value of 1000 MHz, and an orthorhombicity $\lambda = 1/6$. The orientation of this **D**-tensor is shown in figure 3.9, and if it were to originate only in the SSC interaction, it would correspond to an oblate spin density compressed along C_Z. The 30 GHz transient EPR spectrum corresponding to this triplet state is shown in the left panel, whereby the transitions are labelled as before by the orientation of the magnetic field at which they resonate and the ΔM manifold to which they belong. The zero-field populations were set to be exclusively in the $|Z\rangle$ sub-level.

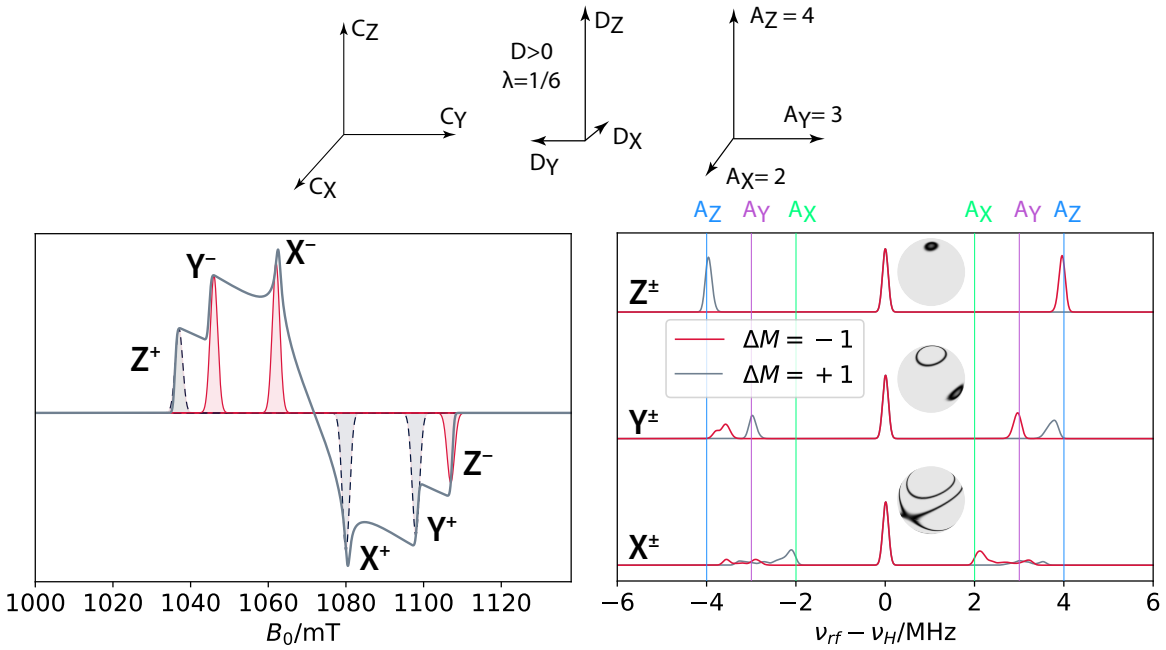


Figure 3.9: (Top) Right-handed Cartesian frame, **D**-tensor, and hyperfine tensor axes; (Bottom left) Simulated EPR spectrum of a spin polarised triplet state generated with the parameters detailed in the main text and Gaussian functions indicating the positions at which the ENDOR simulations were carried out; (Bottom right) Mims ENDOR simulations and spherical density plots showing the resonant orientations of the magnetic field vector relative to the Cartesian frame. The ENDOR spectra were generated using the function *saffron* in EasySpin [9]. The coloured vertical lines indicate the magnitudes of the three hyperfine coupling values. The ideas behind the interpretation of this figure are elaborated throughout this section.

Additionally to the electronic triplet, the spin system considered here also comprises a proton with an anisotropic hyperfine tensor (in MHz):

$$\begin{cases} A(C_X) = 2 \equiv A_X \\ A(C_Y) = 3 \equiv A_Y \\ A(C_Z) = 4 \equiv A_Z \end{cases} \tag{3.116}$$

which is aligned with the **D**-tensor, as depicted in figure 3.9. This hyperfine interaction is orders of magnitude smaller than the ZFS, and in most cases, it would also be much smaller than the inherent linewidth of the trEPR spectrum. Hence, the spectrum in the left panel of figure 3.9 shows no evidence of a hyperfine interaction.

Figure 3.9 depicts the simulated Mims ENDOR spectra of this spin system which would be obtained by

measuring at field positions corresponding to the six turning points in the trEPR spectrum. These turning points are marked in the left panel as Gaussian functions with a width of 62.5 MHz corresponding to the excitation profile of a 16 ns $\pi/2$ microwave pulse. The red Gaussians in the left panel correspond to the red ENDOR spectra of the $\Delta M = -1$ manifolds in the right panel, whilst the grey Gaussians correspond to the gray ENDOR spectra of the $\Delta M = +1$ spectra. Note that by design, all of these spectra are in the weak-coupling regime, since the Larmor frequency of a proton at the indicated field positions is of the order of 44 MHz which is significantly greater than A_X, A_Y, A_Z. This coupling regime is sufficient for this thesis.

The first important observation regarding the appearance of triplet state ENDOR spectra is that there is always a peak centred at the Larmor frequency $\nu_{rf} = \nu_H$. This so-called 'Larmor peak' corresponds to the rf π pulse being resonant with protons which are coupled to electrons in the $M = 0$ state. When the electron is in the $M = 0$ state, the nucleus does not experience a hyperfine field and hence, the splitting of the nuclear states is only due to the nuclear Zeeman interaction. The Larmor peak is not affected by the central blind spot at $\nu_{rf} - \nu_H = 0$ because blind spots only depend on the free evolution under the hyperfine coupling interaction (see equation 1.125 for the ENDOR efficiency).

Secondly, note that triplet ENDOR spectra are asymmetric relative to the Larmor frequency. All the peaks at $\nu_{rf} \neq \nu_H$ can be related to the magnitudes of the hyperfine interaction. Importantly, positive hyperfine couplings appear at $\nu_{rf} - \nu_H > 0$ if the spectrum is measured on a $\Delta M = -1$ electronic transition. Furthermore, corresponding measurements taken on pairs of $\Delta M = -1$ and $+1$ transitions with the same canonical orientation relative to the field will be the mirror image of each other. This effect is particularly clear in the $Z^{\pm}$ ENDOR spectra in figure 3.9; apart from the Larmor peak, there is a peak centred at A_Z in the $\Delta M = -1$ manifold which swaps to being centred at $-A_Z$ in the $\Delta M = +1$ manifold.

The remaining, $Y^{\pm}$ and $X^{\pm}$ ENDOR spectra, also show a similar minor peak centred at the corresponding A_Y and A_X values. However, these spectra also contain other peaks which occur because at these field positions, it is not just the X or Y transition which is excited (there is an overlap of resonance fields of different manifolds). As can be seen in the spherical density plots in the inset in the right panel, the $Z^{\pm}$ turning point is the only one which can truly be classified as 'purely Z' (within the limits of the pulse bandwidth). For this reason, it is typically the Z transition which is easiest to interpret in real applications, despite the fact that the intensity of this transition is lowest in the EPR spectrum (and hence, the stimulated echo will also be less intense).

3.7.2 The orientation of D from ENDOR

As mentioned before, the ENDOR spectra can be used to establish the orientation of the **D**-tensor in cases where the orientation of the hyperfine coupling tensor is known (or can be approximated with some confidence). For instance, one may be able to obtain the hyperfine coupling tensor reasonably well from a DFT spin density (*e.g.* in reference [73]) whereas the **D**-tensor calculation would be difficult to perform if the SOC contribution is significant. Alternatively, the hyperfine tensor could be very similar to a different but analogous molecule for which the orientation of **D** is readily known. Of course, ENDOR can also be used to determine the orientation of the hyperfine tensor if the orientation of **D** is known from an MPS experiment.

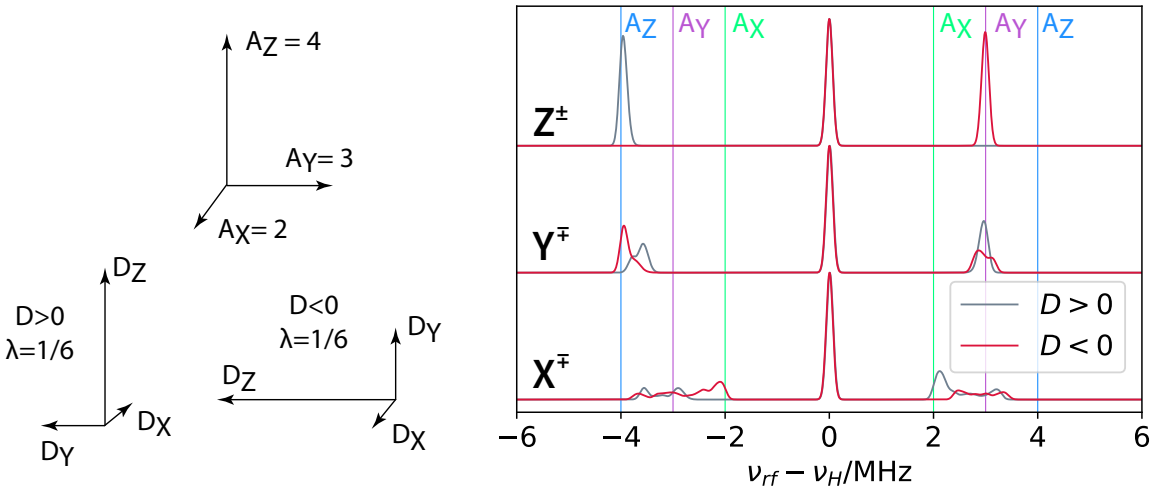


Figure 3.10: (Left) The orientations of the **D**-tensor axes relative to the hyperfine coupling tensor (kept fixed in the Cartesian frame, shown in figure 3.9). The two orientations of **D** correspond to a positive and negative D-value. (Right) Simulated ENDOR spectra for the three consecutive low-field transitions on the EPR spectrum in figure 3.9. By contrast to the previous figure, the grey and red lines now correspond to differing signs of D. The coloured vertical lines indicate the magnitudes of the three hyperfine coupling values.

To see how this might be achieved, we will consider the same spin system as in the previous section. Additionally, a second situation is simulated by keeping the hyperfine tensor identical and reorienting the **D**-tensor such that D becomes negative, and D_Z is along the $-C_Y$ axis (figure 3.10). In the dipolar only picture, this second scenario would correspond to a prolate spin density elongated along the C_Y axis.[29]

The effect of changing the orientation of the **D**-tensor on the ENDOR spectra is illustrated by the simulations in figure 3.10 for $D > 0$ and $D < 0$. The pairs of gray and red spectra correspond to the three consecutive low-field transitions in the trEPR spectrum shown in figure 3.9. In other words, these ENDOR spectra are simulated on the same (low-field) side of the barycenter of the trEPR spectrum.

By changing the orientation of **D** in this way, the D_X axis remains parallel to the C_X axis, but it changes sign. As a result, the ENDOR spectra at the low-field X position are mirror images of each other. In particular the +2 MHz peak corresponding to A_X when $D > 0$ becomes a -2 MHz peak also originating from A_X but with $D < 0$ instead.

The remaining two axes are not conserved, they are swapped relative to their corresponding Cartesian axes.[30] Inspection of the simulated ENDOR spectra reveals that the effect of this axis swap, is to both invert the sign of the peak position and to swap the magnitudes. For example, at the $Z^{\pm}$ field positions, the $-A_Z$ peak becomes the $+A_Y$ peak.

In light of the above, we can formulate a strategy for determining the orientation/ sign of the ZFS interaction given two molecules with similar spin densities and hence similar hyperfine coupling tensors.[31] One can search for two pairs of peak positions in the EPR spectra of both molecules such that: one pair

[29] As usual, both **D**-tensors are right-handed.

[30] This is not surprising. In order to maintain the handedness of the D-tensor, inversion of one of the axes, must be accompanied by a swap of the other two axes.

[31] In fact, for this strategy to work, it is sufficient to require that the hyperfine couplings do not change sign from one molecule to the other.

will have identical/very similar ENDOR spectra whereas the other pair will be perfect/approximate mirror images in ENDOR. If the former pair was acquired on the same side of the barycenter of the trEPR spectrum, then the orientation of the two **D**-tensors is the same.

The important caveat which often limits the effectiveness of this method is the assumption that the hyperfine coupling tensors in both molecules are sufficiently similar. Furthermore, the orientation of **D** needs to be known in at least one member of a series *i.e.* a reference system is needed. Nonetheless, these ideas will be employed in the next two chapters. In summary, this strategy for determining the orientation of **D** is not flawless, yet it can prove to be very fruitful in combination with the MPS method and, whenever possible, theoretical predictions.

3.8 Chapter summary

At the outset of this chapter the SOC coupling interaction was introduced. In conjunction with perturbation theory, the SOC Hamiltonian was then used to showcase the emergence of **g**-tensor anisotropy. This derivation provided the stepping stone for obtaining the SOC contribution to the **D**-tensor in triplet states. Furthermore, the important SSC/dipolar contribution to the **D**-tensor was also derived. The latter contribution is typically said to dominate the fine structure of organic triplet states. Nonetheless, in the next chapter we will encounter a counter-example, namely a palladium porphyrin triplet state with both an anisotropic **g**-tensor as well as a non-zero SOC contribution to ZFS.

Having described the origin of the **g** and **D** interaction tensors, the interplay between these parameters was investigated from a symmetry point of view using group theoretical arguments. Afterwards, the way in which these interactions, especially **D**, manifest themselves in the trEPR spectra of photo-excited triplet states was considered by means of a series of model spectral simulations. In particular, the effects of spin polarisation, *i.e.* non-Boltzmann sub-level populations, on the appearance of EPR spectra were considered in relation to the **D**-tensor. Furthermore, we outlined both the origin of the main type of spin polarisation considered in this thesis as well as its link to the symmetry of the SOC interaction.

Particular emphasis was placed on methodologies which can be used to determine the sign and orientation of the **D**-tensor. Of these methods, the MPS experiment will prove most fruitful. The importance of establishing and understanding the orientation of the **D**-tensor in triplet states cannot be underestimated: it is inherently linked both to the symmetry of the spin density via the SSC interaction (and hence the average distance between the electrons), as well as to the symmetry of the SOC interaction. Both SSC and SOC interactions are needed in order to fully understand the fine-structure magnetic properties of excited triplets.

Finally, the application of ENDOR spectroscopy to triplet states was also considered from the vantage point of a series of model simulations. This technique is shown to be useful not only for determining the spatial distribution of the triplet spin density (from the hyperfine couplings) but also for confirming the orientation of the **D**-tensor in difficult cases. In summary, this chapter contains all the necessary ideas and methods for understanding all the results and discussions presented in the next two chapters.

Chapter 4

Spin-orbit effects in the triplet states of porphyrins

The theoretical EPR framework outlined thus far will be showcased in this chapter in an exploration of the triplet state of palladium (II) porphyrin systems. Apart from a single paper which mentions in passing the ZFS of a palladium porphyrin [74],[1] the magnetic properties of these systems have not been described in any satisfying detail until now. This is a significant gap in the field of porphyrin molecular wires and EPR spectroscopy thereof. The presence of the heavier Pd^{2+}metal center is known to increase the triplet yield and it is bound to have a profound effect on any interaction which is mediated by the relativistic SOC Hamiltonian. It will also be shown that, in spite of the increased complexity of the fine-structure interactions caused by Pd^{2+}, this ion can be exploited to control not only spin delocalisation but also spin polarisation in molecular wires.

Most of the arguments that will follow stem from the group theory considerations of the previous chapter. Nevertheless, the results of electronic structure calculations will also be examined at various key stages. Some of these calculations have, until now, not been attempted on porphyrin molecules, whether with Pd^{2+}or otherwise.[2] These encouraging computational results have the potential to stimulate the development of theoretical methodologies for tackling the elusive nature of fine-structure interactions.

4.1 Context and motivation

EPR spectroscopy has been at the forefront of research dedicated to the understanding of the electronic structure of the excited triplet states of biologically relevant π-conjugated systems [72, 75–79], and molecular wires [73, 80–89]. The relatively recent work of Claudia Tait and Sabine Richert, former members from the group of Prof. Christiane R. Timmel, has helped to establish a modern perspective on the use of trEPR and ENDOR spectroscopies for studying spin delocalisation in porphyrin systems. A particularly important observation is that the ZFS tensor of a Zn^{2+} porphyrin dimer is reoriented compared with the analogous monomer structure [49, 73]. This simple fact will be explored in greater detail in this chapter, since it is linked to the extent of spin delocalisation. For longer oligoporphyrins,

[1] *i.e.* the only paper of which the author is aware of.
[2] *Especially* for the calculation of ZFS parameters.

the magnitudes of the hyperfine couplings are seen as being most revealing about the distribution of the spin density over the molecular framework [80, 82].

One of the difficulties with studying the triplet states of ever longer porphyrin molecular wires is that the EPR signals become weaker and the acquisition of ENDOR spectra requires exceedingly long accumulation times.[3] This experimental complication was the initial driving force for studying the triplet states of porphyrin systems containing Pd^{2+}(low-spin, $4d^8$) rather than Zn^{2+}or free-base systems. More precisely, the molecules depicted in figure 4.1 were synthesised in the group of Prof. Harry L. Anderson precisely with the aim of testing the feasibility of EPR studies on the triplet states of palladium porphyrins. The motivation for doing this was to increase the triplet yield (by intercalation of Pd^{2+} into the porphyrin macrocycle) and hence, facilitate EPR studies of ever longer oligoporphyrin molecular wires.

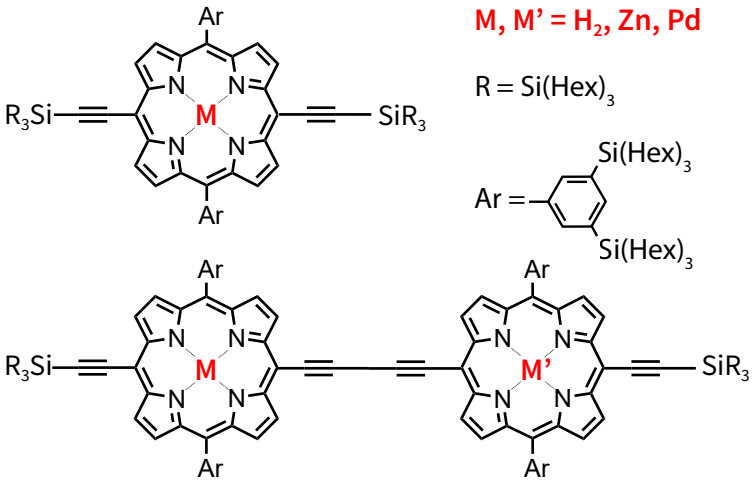


Figure 4.1: Structures of the monomer systems (top) and dimer systems (bottom) investigated in this chapter. Throughout the following sections, the **^{3}Fb**,**^{3}Zn**, and **^{3}Pd** labels will be used to denote the triplet states of free-base, zinc, and palladium monomers, respectively. The homodimers and heterodimers will be labelled as: **^{3}FbFb**, **^{3}ZnZn**, **^{3}PdPd**, **^{3}FbPd**, and **^{3}ZnPd** (the **^{3}FbZn** sample could not be synthesised with sufficient purity). The systems were synthesised in their neutral and spinless ground state by Dr. Jibin Sun from the group of Prof. Harry L. Anderson.

It was indeed found that the trEPR and ENDOR spectra of the longer palladium oligomers (up to five units)[4] could be obtained in similar acquisition times as the monomer/dimer systems.[5] However, the focus of the investigation shifted drastically when an unusually large ZFS interaction, and significant **g**-anisotropy was observed in all the Pd^{2+} systems. Whilst it seemed entirely reasonable to note an increase in the triplet signal intensity, owing to the first-order nature of the SOC contribution to ISC, it was remarkable to note a two-fold increase in the D-parameter (which is only second-order in SOC). The fact that the second-order SOC contributions to **D** (and **g**) are as relevant as the first-order SSC contributions motivated the investigations in this chapter into the relativistic nature of these fine-structure parameters.

Initially, the monomer systems, denoted **^{3}Fb**,**^{3}Zn**, and **^{3}Pd** in figure 4.1 will be described in detail and

[3] Although not a proven fact, this was attributed to a decrease in triplet yield with increasing oligomer chain length.

[4] The linear palladium oligoporphyrin systems will be discussed in more detail at the end of this chapter.

[5] This fact will not be proven in this thesis, nor is this necessary for the conclusion. It is merely mentioned here as an observation.

with a particular emphasis on the similarities and differences between the three compounds, as revealed by trEPR, ENDOR, and computational chemistry. The ^{3}**Fb** and ^{3}**Zn** systems have been studied and published before by Claudia Tait, and hence, the majority of the results will be stated only briefly and referenced accordingly. Nonetheless, the new data on the ^{3}**Pd** system also helps to further our understanding of the previously studied systems, and thus, it is important to reconsider the former as well as the latter.

As mentioned, the presence of Pd^{2+}complicates the analysis of the ZFS interaction. However, it will be shown using the dimers in figure 4.1 that palladium porphyrins can be used as a way of controlling spin delocalisation and spin polarisation in molecular devices. The EPR spectra and analysis of these dimers was carried out in collaboration with Ashley J. Redman. Finally, despite the more relativistic nature of the fine-structure parameters, the ENDOR spectra of the longer palladium oligoporphyrins are remarkably similar to the zinc analogues. In other words, apart from a few modifications, EPR studies can still be used as before to investigate systems with large SOC interactions.

4.2 Monomer systems

4.2.1 TrEPR spectra

Figure 4.2 shows the frozen solution X-band trEPR spectra of the three porphyrin monomer systems along with the results of numerical spectral simulations. The corresponding simulation parameters are summarised in table 4.1. There are several noteworthy points from a qualitative analysis of both the shapes of the spectra and the simulation parameters.

The trEPR spectra of ^{3}**Fb** and ^{3}**Zn** are very similar in the positions of the resonance fields, however, they are inverted with respect to each other. This inversion can be caused either by a change in the ISC mechanism (and thus different zero-field sub-level populations), or by a change in the orientation of the **D**-tensor, or both. It has been shown in references [73] and [49] (using MPS and Mims ENDOR experiments) that the D-value of both ^{3}**Fb** and ^{3}**Zn** is positive and the D_Z axis is perpendicular to the porphyrin plane, in keeping with the oblate symmetry of the spin density. For this reason, only the positive D case is shown in table 4.1. The corresponding change in the polarisation pattern from being exclusively in-plane for ^{3}**Fb** ($P_Z = 0$), and almost entirely out-of-plane for ^{3}**Zn**, indicates a change in the ISC mechanism, as will be discussed in the next section.

System	D/ MHz	$\lambda = \lvert E/D \rvert$	$P_X : P_Y : P_Z$
^{3}**Fb**	+1024	0.14	0.50 : 0.50 : 0.00
^{3}**Zn**	+906	0.18	0.00 : 0.13 : 0.87
^{3}**Pd**	+2289	0.00	0.50 : 0.00 : 0.50
^{3}**Pd**	−2289	0.00	0.00 : 1.00 : 0.00

Table 4.1: ZFS and population parameters used for the simulations depicted in figure 4.2. The D-value is known to be positive for ^{3}**Fb** and ^{3}**Zn**[49, 73], whereas for ^{3}**Pd** it will be shown that D is negative. The **g**-tensors for ^{3}**Fb** and ^{3}**Zn** are approximately isotropic with values of 2.00831 and 2.00636, respectively. The **g**-tensor of ^{3}**Pd** is anisotropic and, in the **D**-tensor eigenframe the values are: $g_X = 2.00071$, $g_Y = 1.9656$, $g_Z = 2.00200$ for $D < 0$, and $g_X = 2.00193$, $g_Y = 1.96528$, $g_Z = 2.00083$ for $D > 0$. These g-values were obtained by global fitting of X-band and W-band data (appendix F, figure F.2).

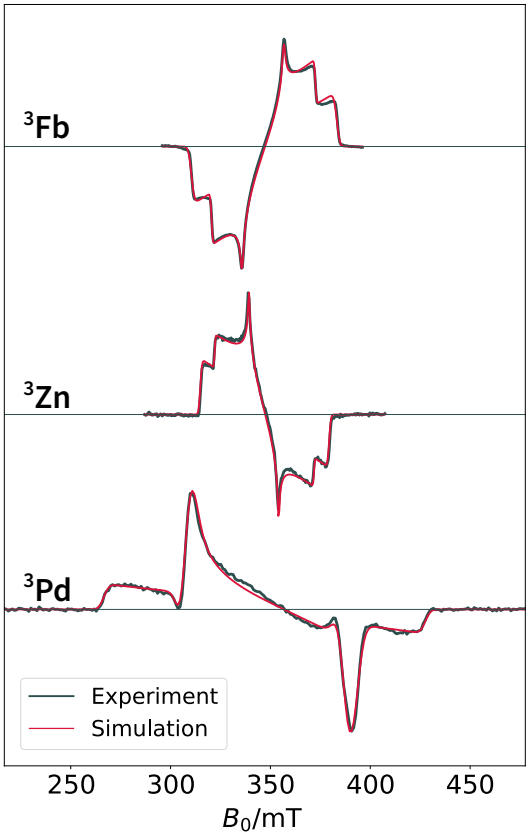


Figure 4.2: Experimental and simulated TrEPR spectra of the triplet states of the monomer systems. The spectra were acquired at X-band and 80 K using laser excitation at 532 nm. The resulting two dimensional data sets were baseline corrected in both the field and time domains. The experimental spectra depicted here represent the time averaged EPR signal over a range of 1μs following laser excitation (no significant change in spectral shape occurs during this period). Further experimental details are provided in appendix F and the simulation parameters are in table 4.1. The spectrum of ^{3}**Fb** was acquired and simulated by Claudia Tait [49].

By contrast to the other two monomers, the ^{3}**Pd** spectrum is markedly different. It is wider and significantly asymmetric with respect to the barycenter. These two observations indicate that in ^{3}**Pd** the D-value is larger (by more than a factor of two) and that the **g**-tensor is significantly anisotropic, as reflected in the simulation parameters. Since at this stage no proof has been provided for the sign of the D-value in the ^{3}**Pd** system, both possibilities are shown in table 4.2. Qualitatively, by analogy with the ^{3}**Zn** case, we expect the increased SOC in ^{3}**Pd** to drive the populations out-of-plane. If $D < 0$, it is also likely that the D_Y axis is out-of-plane, and hence P_Y is exclusively populated as shown in table 4.1. At this stage, this is only a conjecture, which will be justified further from the point of view of more experimental evidence as well as group theoretical arguments.

4.2.2 Understanding the ^{3}Fb and ^{3}Zn systems

As mentioned, the ^{3}**Fb** and ^{3}**Zn** systems are well characterised experimentally (references [49, 73, 80]) and hence, they are a suitable playground for computational studies. In this section, the results of **D**-tensor and spin polarisation calculations will be presented.

D-tensor calculations

In many cases, a first estimate of the D-value can be obtained from DFT calculations, however, the outcomes are not always entirely reliable. Figure 4.3 shows the results of a DFT calculation of the spin density and the SSC contribution to the **D**-tensor.

These DFT calculations predict the correct orientation of the **D**-tensor in these systems, as is confirmed by experiment [49, 73]. As can be seen in figure 4.3 the spin density is compressed along the molecular z-axis (it is pancake-like relative to C_Z), and hence, the D-value is positive. The fact that the orthorhombicity is non-zero is in line with the approximate D_{2h} symmetry of the molecule.

However, there is a rather large discrepancy between the calculated D_{DFT} values in figure 4.3 and the experimental values of table 4.1. Not only are the magnitudes underestimated by almost a factor of two, the orthorhombicity parameter, λ, predicted by DFT is much larger than is observed experimentally. Furthermore, these DFT calculations indicate a slight increase in the D-value for ^{3}**Zn** (versus ^{3}**Fb**), by contrast with experiment.

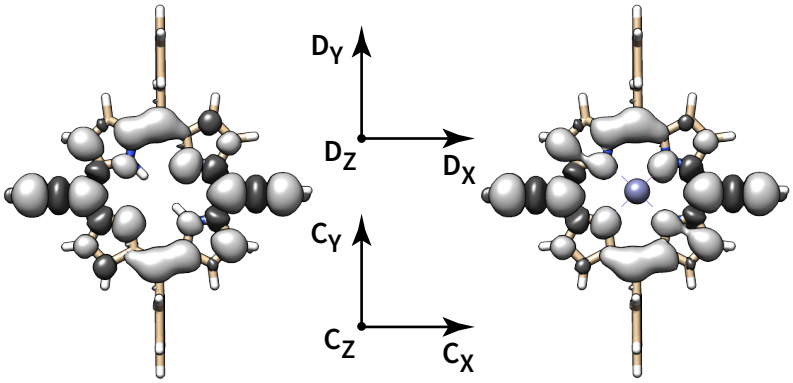


Figure 4.3: The spin density obtained from DFT for the ^{3}**Fb** (left) and ^{3}**Zn** (right) systems. The orientation of the **D**-tensor axes are shown with respect to the Cartesian/molecular axes. The calculation was performed using the ORCA software [45], employing the following input parameters: unrestricted Kohn-Sham, def2-SVP basis set for H, C, and N atoms, def2-TZVP for Zn, and the B3LYP functional.

Method	D(^{3}**Fb**)/MHz	D(^{3}**Zn**)/MHz	λ(^{3}**Fb**)	λ(^{3}**Zn**)
Experimental	+1024	+906	0.14	0.18
DFT	+501	+513	0.23	0.27
CAS(4,4)	+1027	+910	0.14	0.15

Table 4.2: Comparison of the experimental ZFS parameters, D and λ, for the ^{3}**Fb** and ^{3}**Zn** systems with the predictions based on the DFT spin densities in figure 4.3 and the results of a complete active space calculation employing four electrons in the four frontier molecular orbitals in figure 4.4 *i.e.* a CAS(4,4) calculation.

Such a mismatch between DFT and experiment is not easily overlooked, especially if an interpretation of the ZFS interaction is sought. Whilst it is true that porphyrin systems tend to be more complicated than many other π-conjugated molecules,[6] this failure of DFT persists even in simple molecules. For example, an equivalent DFT calculation of the D-value of the triplet state of naphthalene predicts $D_{\mathrm{DFT}} = 1733$ MHz, whereas the value found by experiment is 3022 MHz [62], *i.e.* there is a ca. 50–60%

[6] For example, due to the presence of the nitrogen heteroatoms, and generally, the relatively larger number of atoms.

discrepancy. Similar problems are faced when calculating the ZFS parameters for the triplet states of benzene and anthracene. However, it is highly unlikely that the experimental values are inaccurate because the typical errors associated with the extraction of D-values from trEPR spectra (with a signal-to-noise ratio akin to the data shown here) is in the range of 10–20 MHz.

One of the tactics for improving on the accuracy of DFT calculations of ZFS parameters is to test different functionals and basis sets. Whilst in many cases, such an approach is reasonable, it adds little value or scope in the calculation of fine-structure parameters for a variety of reasons. First of all, if a particular combination of functional and basis set leads to better agreement with experiment for a given system, there is no guarantee that this will be the case in a different system *i.e.* there is a lack of generality, the calculation has to be tuned to the system, without any justification. Furthermore, tuning the calculation to the system eliminates the predictive power of such computational studies. Moreover, the time cost of performing DFT calculations with ever more complicated input parameters on ever more complicated molecules seems unwarranted when a better understanding of the system can be gained by qualitative arguments[7] or different electronic structure methods.

Among the methods which are proposed in the literature as being a better approach for calculating the ZFS interaction is the Complete Active Space Self Consistent Field (CASSCF) method [90], which aims to account for the multireference character of the triplet state wavefunction.[8] In recent years, the ORCA software has been expanded to allow the calculation of the SSC contribution to the **D**-tensor in the framework of CASSCF. However, this feature of ORCA is still under development and hence it can be unstable in some instances,[9] and presently it is 'hard-wired' to compute the ZFS parameters only for the lowest energy multiplet. Other software packages such as MOLCAS, which are optimised for CASSCF calculations, do not currently support the computation of the SSC contribution to **D**. Nonetheless, in spite of these technical difficulties, it is clear from table 4.2 that CASSCF calculations on the ^{3}**Fb** and ^{3}**Zn** systems give very promising results, and the future development of these software packages will likely be invaluable for this field of research.

A detailed description of the CASSCF electronic structure method is beyond the scope of this work. Instead, we will only outline very briefly how the CAS(4,4) results in table 4.2 were obtained. The calculation started with an 'initial guess' step, whereby the electronic structure of the molecule was estimated with an easily implemented algorithm. In the case at hand, a Hartree-Fock calculation was performed using the def2-SVP basis set for all atoms except Zn; for the latter, the def2-TZVPP basis was chosen. The resulting frontier molecular orbitals from this Hartree-Fock calculation are plotted in figure 4.4. Alternatively, a set of Kohn-Sham DFT orbitals can be generated, however, it was found that the resulting D-values are marginally less accurate.

The next step is the selection of the active space, which will act as the basis for the electronic states. There is no clear criterion for this orbital selection step. In principle, due to the variational nature[10] of the later steps in the calculation, any choice of active orbitals will result in a final wavefunction which is a better approximation of the true wavefunction. However, despite being closer to the true wavefunction, not every choice of active orbitals leads to the same level of improvement in the quality of the

[7] For example, the rudimentary considerations at the end of section 3.3.3 give better agreement with experiment than DFT (as illustrated for benzene).

[8] DFT is a single reference method, *i.e.* it is formulated with the assumption that electronic states are single Slater determinants. In other words, effects such as configuration interaction or excited state mixing are neglected in the DFT framework.

[9] unexpected software crashes are occasionally observed in the computation of the SSC contribution to the **D**-tensor.

[10] *i.e.* due to the variational principle.

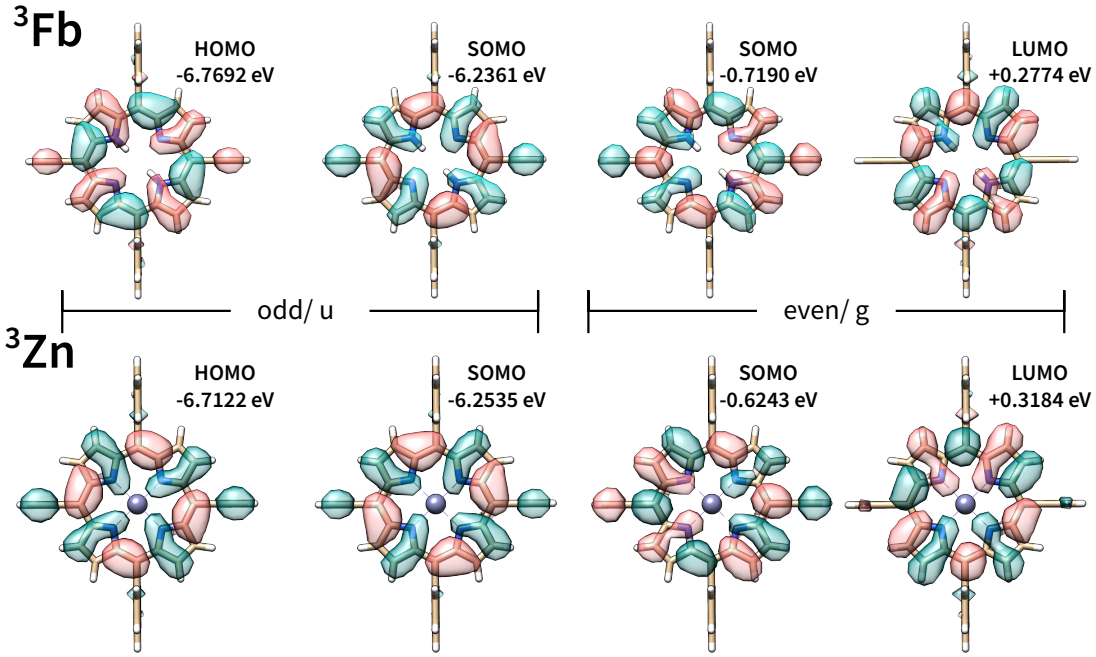


Figure 4.4: The energies (in eV) and shapes of the frontier molecular orbitals of the ^{3}**Fb** and ^{3}**Zn** systems. The acronyms are expanded as follows: HOMO– highest occupied molecular orbital, SOMO– singly occupied molecular orbital, LUMO– lowest unoccupied molecular orbital. The classification of the orbitals by their inversion symmetry is also shown. These orbitals were obtained from a Hartree-Fock calculation employing the same basis set as used for the DFT calculation shown in figure 4.3.

wavefunction (or of the electronic energy). It is a good rule of thumb to assume that the configuration interaction within the frontier molecular orbitals of similar character (*e.g.* predominantly porphyrin based π orbitals rather than the core orbitals of the Zn^{2+}) are likely to be most consequential for the observable molecular properties. It is for this reason that the frontier orbitals shown in figure 4.4 were chosen: these are the famous Goutermann orbitals, which have long been known (since 1963) to be the most important for the understanding of the optical properties of porphyrins [91].[11]

Having defined this active space comprised of four electrons and the four Gouterman orbitals, denoted CAS(4,4), the next step involves formulating the configuration state functions (CSFs). A CSF is a Slater determinant or linear combination of Slater determinants which describes one of the many possible electronic states derived from the orbitals and electrons in the active space. For example, in this CAS(4,4) calculation, there are 15 possible CSFs which correspond to triplet states.[12]

Finally, the calculation proceeds by performing a self consistent iteration which is variational both in the composition/coefficients of the active orbitals and in the configuration interaction coefficients between admixtures of CSFs. The fact that both the active orbitals and the CSFs are optimised makes the CASSCF method more computationally demanding. The criterion for the optimisation[13] is often set to be the average energy of the electronic states of interest. In the case of the ^{3}**Fb** and ^{3}**Zn** systems, the criterion was chosen to be the average energy of the lowest four triplet states. Afterwards, the ZFS of the lowest energy triplet root, which is now a linear combination of the original triplets, is calculated

[11] Referred to as the Goutermann 'four orbital model' for porphyrins.

[12] The number of CSFs in a calculation with n orbitals, N electrons, and total spin S, can be obtained using the Weyl formula: $\#(\text{CSFs}) = \frac{2S+1}{n+1} C^{n+1}_{N/2-S} C^{n+1}_{N/2+S+1}$.

[13] *i.e.* that which is optimised

(results shown in table 4.2). The energies and compositions of the states are provided in Appendix E as excerpts from the ORCA output files. The resulting CAS(4,4) spin densities are plotted in figure 4.5, whereby it is clear that the two systems have a very similar spin density, hence why, the corresponding D-values are similar, and the orientation of the **D**-tensor is the same.

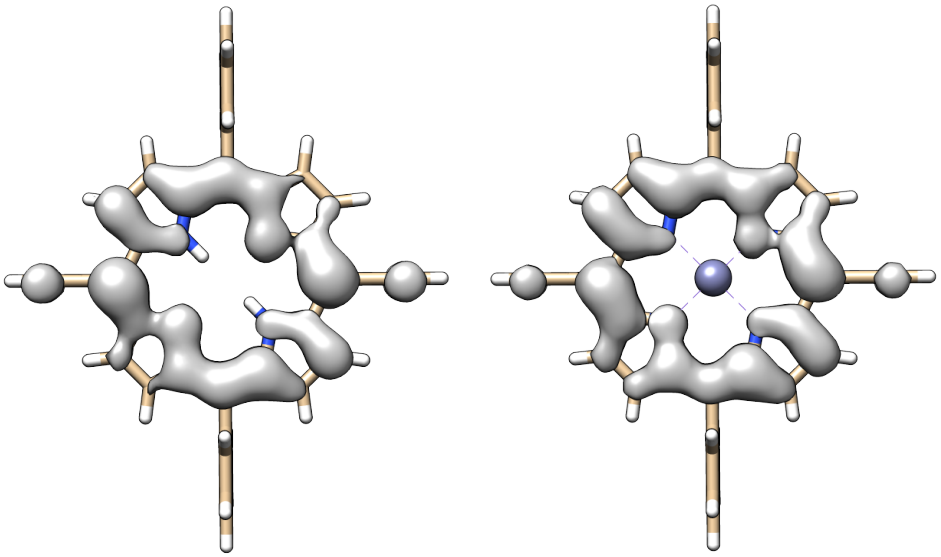


Figure 4.5: Spin densities for ^{3}**Fb** (left) and ^{3}**Zn** (right), obtained from the CAS(4,4) calculation described in the main text. These are the spin densities from which the D-values in the bottom row of figure 4.2 were derived. These spin densities do not contain negative lobes (like the ones in figure 4.3) because, by definition, a CASSCF calculation is spin restricted. The DFT derived spin density in figure 4.3 is obtained from a spin unrestricted Kohn-Sham calculation.

Although it is not coincidental, we can only hypothesize as to the reason behind the better agreement between experiment and these CAS(4,4) calculations compared to DFT. The four Gouterman orbitals seem to be sufficient to reproduce the ZFS of these two monomer systems, however, there is no guarantee that they are sufficient for different porphyrin systems. Nonetheless, even if the CASSCF methodology needs to be developed further to facilitate the calculation of ZFS parameters in complicated systems, the results in table 4.2 show that this theoretical pursuit is justified.

Predicting the spin polarisation pattern

Before discussing any quantitative spin polarisation calculations, it will prove helpful to consider the symmetry properties of the orbitals displayed in figure 4.4. Although the calculation results within this figure were not obtained by employing symmetry, an approximate symmetry analysis can still be carried out. In particular, it is first necessary to assign an irreducible representation to these frontier orbitals; this can be done by a process of elimination using the character table in appendix D. Although not very precise, the arguments below will offer a useful guide to the physics underpinning the ISC processes in these systems.

The higher energy SOMO and LUMO orbitals are symmetric with respect to inversion, *i.e.* all irreducible representations which are 'u' can be eliminated; hence, these orbitals could be either A_g, B_{1g}, B_{2g}, or B_{3g}. Next, the totally symmetric (A_g) irreducible representation can also be ruled out (for obvious reasons), and B_{1g} which is symmetric with respect to reflection in the molecular plane is also not

possible. Closer inspection of the D_{2h} character table given in Appendix D and the orbitals reveals that the higher energy SOMO is approximately B_{2g} symmetric and the LUMO is approximately B_{3g} symmetric. This assignment is not perfect, yet it is sensible, and in agreement with the analysis of Gouterman in reference [91]: the B_{2g} and B_{3g} irreducible representations of the higher SOMO and LUMO orbitals is expected from a decent in symmetry from the D_{4h} point group, which gives $E_g \longrightarrow B_{2g} + B_{3g}$.

The symmetries of the HOMO and lower energy SOMO are more ambiguous compared to the other two orbitals. However, after some consideration, it can be deduced that the only possibility is that they are an admixture of A_u and B_{1u} symmetry. We will assume that the HOMO is A_u and the lower energy SOMO is B_{1u}, as would have been obtained in an equivalent calculation which employed symmetry (see for example references [91–94]).[14] Note also that the frontier orbitals of both ^{3}**Fb** and ^{3}**Zn** systems have the same symmetry.

Having established the approximate symmetry of these orbitals, it is now possible to assign the symmetry of the excited singlet and triplet states, as follows:

$$\begin{cases} |^1B_{3u}\rangle/|^3B_{3u}\rangle \longrightarrow a_u^2 b_{1u}^1 b_{2g}^1 \\ |^1B_{2u}\rangle/|^3B_{2u}\rangle \longrightarrow a_u^2 b_{1u}^1 b_{3g}^1 \end{cases} \tag{4.1}$$

According to El Sayed's rules in equation 3.103, we conclude that the direct/ Franck-Condon mechanism will only drive ISC from a $|^1B_{2u}\rangle$ state to a $|^3B_{3u}\rangle$ state, or from a $|^1B_{3u}\rangle$ state to a $|^3B_{2u}\rangle$ state. Both of these crossovers would be mediated by the SOC matrix element along the Cartesian C_Z-axis (because R_z is B_{1g} symmetric). Since $D > 0$, the Cartesian C_Z axis is aligned with D_Z. Hence, from symmetry considerations, we expect that the direct SOC mechanism would lead to preferential out-of-plane, *i.e.* P_Z only, spin polarisation in both ^{3}**Fb** and ^{3}**Zn**. It seems that this line of reasoning is contrary to the experimental observation shown in table 4.1: ^{3}**Fb** displays exclusive in-plane spin polarisation, whereas ^{3}**Zn** displays preferential P_Z population combined with a ca. 13% in-plane polarisation.

System	$\langle T\|\|\hat{H}^Z_{\mathrm{SOC}}\|\|S\rangle\Big\|_{\mathrm{eq.}}$ /cm^{-1}	$\tilde{k}^0$	$\tilde{k}^{\pm1}$	$\tilde{k}^0_{FC}$	$\tilde{k}^0_{HT}$	$\tilde{k}^{\pm1}_{FC}$	$\tilde{k}^{\pm1}_{HT}$
^{3}**Fb**	-0.04i	2%	98%	1.5%	0.5%	0.0%	98%
^{3}**Zn**	1.04i	90%	10%	52%	38%	0.0%	10%

Table 4.3: Summary of the results on the ^{3}**Fb** and ^{3}**Zn** systems obtained using the ESD package in ORCA. The reduced SOC matrix element along the Cartesian C_Z axis is shown alongside the normalised relative contributions to the ISC rate; the meaning of the different quantities is explained in the main text. The ORCA input files containing all the computational details are provided in Appendix E. Note: the reduced SOC matrix element in this table is equivalent to the $\mathcal{L}^z_{ab}$ quantity introduced in the previous chapter.

It is possible that the symmetry arguments presented above are too approximate to allow any conclusions to be drawn. However, it is also possible that the direct SOC mechanism is not the only relevant contribution to the rate of ISC into the different triplet sub-levels. To illustrate the possible change in ISC mechanism between ^{3}**Fb** and ^{3}**Zn** a series of model calculations were performed using the Excited State Dynamics (ESD) block of the ORCA software. As mentioned in the previous chapter, this feature of ORCA is relatively new, and at present, it cannot be implemented in the framework of CASSCF.

[14] Unfortunately, the implementation of group theory into the ORCA software is not sufficiently developed to allow all the calculations presented in this thesis to be performed with the inclusion of symmetry.

Nonetheless, we will show the results of ESD using the time-dependent DFT method. Full details of the computation procedure are provided in Appendix E, whereas the main results are summarised in table 4.3.

First of all, the only non-zero reduced SOC matrix elements for both molecules are along the C_Z axis, as expected from group theory, hence why only this one is shown in table 4.3. Moreover, the matrix element of the ^{3}**Zn** system is significantly larger than for the ^{3}**Fb** system. This is already an indication that we expect the Franck-Condon/direct SOC contributions to be more significant in the ^{3}**Zn** system. The reason for this larger SOC matrix element in ^{3}**Zn** is due to the fact that there is a small (yet important) contribution of Zn^{2+} orbitals to the frontier molecular orbitals.[15] In particular, the highest SOMO and LUMO orbitals have the appropriate symmetry to mix with the $d_{xz}(B_{2g})$ and $d_{yz}(B_{3g})$ orbitals of Zn^{2+}. All other Zn^{2+} d-orbitals do not have the correct symmetry to mix with the frontier porphyrin-based π-orbitals.

Table 4.3 also contains a summary of the relative contributions to the ISC rate into the different triplet sub-levels. For clarity, the notation in the table is as follows:

- $\tilde{k}^M$ is the relative contribution of the ISC rate to the $M = 0$ and $M = \pm 1$ triplet sub-levels.
- $\tilde{k}^M_{FC}$ and $\tilde{k}^M_{HT}$ are the relative contributions into sub-level M of the Franck-Condon and Herzberg-Teller ISC mechanisms, respectively.
- the sum of all contributions is normalised: $\sum_M \tilde{k}^M = \sum_M (\tilde{k}^M_{FC} + \tilde{k}^M_{HT}) = 100\%$

Noteworthy is that only the relative rather than the absolute rates of ISC are displayed. There are two reasons for this: (1) only the relative rates are important for spin polarisation, (2) accurate absolute values are only attainable if the adiabatic singlet-triplet energy gap is known exactly, which it is not. Regarding this latter point, as shown in Appendix E, we set the adiabatic energy difference to be the same for both ^{3}**Fb** and ^{3}**Zn**. This approximation should be inconsequential to spin polarisation because the ZFS interaction is much smaller than the singlet-triplet energy gap.

Furthermore, also note that table 4.3 shows only the relative ISC rates to the $M = \pm 1$ sub-levels rather than the (actual) X/Y zero-field eigenstates. This is because, at present, the ESD dynamics package does not account for the ZFS interaction. As shown in the previous chapter, whilst there is a clear relationship between $k^{\pm 1}$ and $k^{X/Y}$ (from equation 3.101):

$$k^{\pm 1} = k^X + k^Y \tag{4.2}$$

unfortunately, the former cannot be extracted from the latter. Nonetheless, the results in table 4.3 are invaluable.

The ISC mechanism in ^{3}**Fb** is clear: it is driven to the in-plane triplet sub-levels by a predominantly vibronic/HT mechanism. The out-of-plane triplet sub-level, $M = 0$, is being populated –only marginally– by a mainly direct mechanism. As far as the ^{3}**Zn** system is concerned, the situation is more nuanced than anticipated based purely on the magnitude of the SOC matrix element in table 4.3. The calculation correctly predicts that the spin polarisation is primarily driven out-of-plane, however, this is not exclusively due to the direct/FC SOC mechanism. Approximately 38% of the net ISC in ^{3}**Zn** is predicted by

[15] This contribution from Zn^{2+} d-orbitals is too small to be noticeable in figure 4.4 with the iso-level chosen therein.

this method to be driven *vibronically* into the out-of-plane level. Also, the fact that $\tilde{k}^{\pm 1}$ is responsible for 10% of the net ISC rate, is entirely consistent with the observation of 13% X sub-level population.[16]

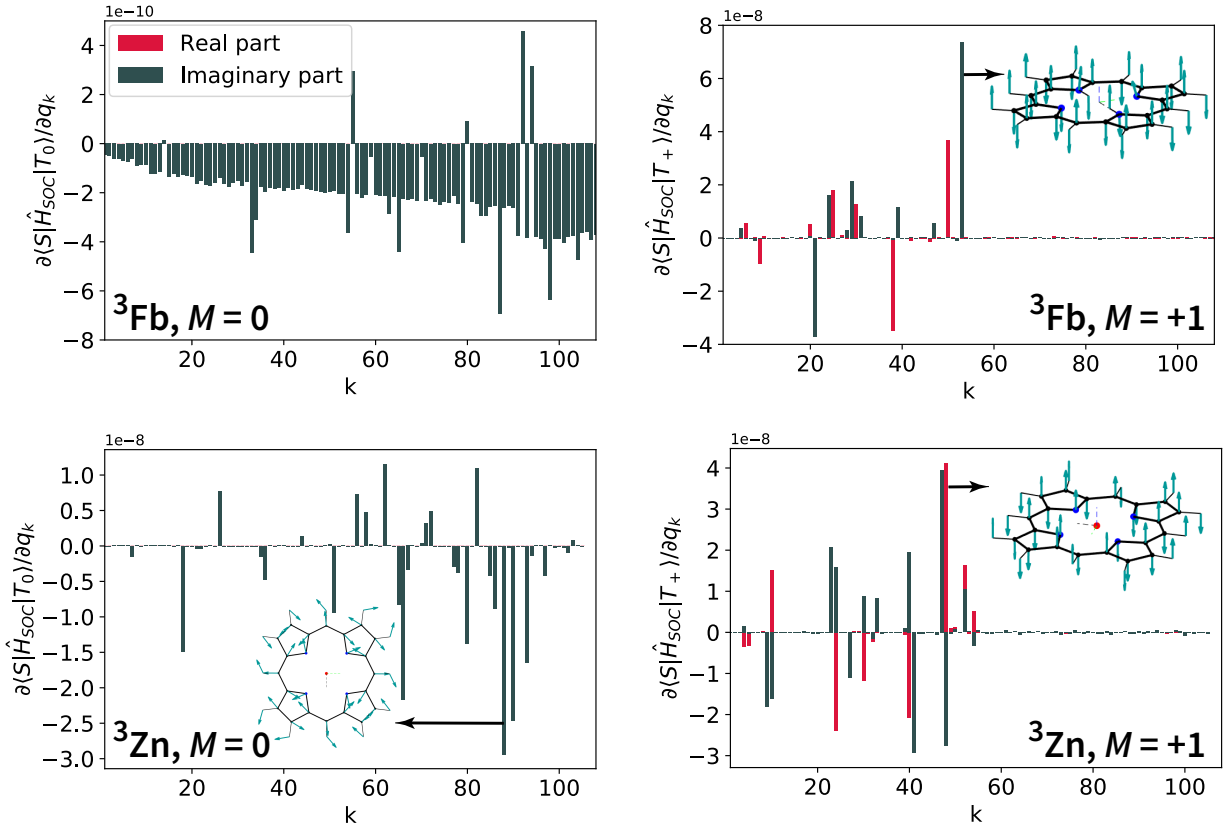


Figure 4.6: Derivatives of the SOC matrix elements between the singlet state and the triplet $M = 0$ and $M = +1$ sub-levels along the vibrational mode coordinate, q_k, of mode k. If all the side groups are neglected, there are 108 vibrations in **^{3}Fb** and 105 in **^{3}Zn**, which are considered separately in the top and bottom panels, respectively. The vibrational mode which induces the largest change in the SOC matrix element is shown as the inset in all panels except the top left. The derivatives in the latter are almost two orders of magnitude smaller than the derivatives in the other three panels (note the scale on the ordinate axis); the units are Hartree (10^{-8} Eh = 65 MHz) because ORCA uses a dimensionless vibrational coordinate (q_k). The red and black colours represent the real and imaginary components of the SOC derivatives.

With regards to the HT contribution to the ISC mechanism, as explained in section 3.5.4, not every vibrational mode will have the correct symmetry to be able to couple with the spin-orbit Hamiltonian. Furthermore, even if the modes have the right symmetry properties, there is no guarantee that the mode derivatives of the SOC matrix elements will be large enough to lead to significant contributions. The magnitudes of the derivatives of the singlet-triplet SOC matrix elements along the vibrational coordinates, q_k, corresponding to all the vibrational modes, indexed by k, are illustrated in figure 4.6. These are the mode derivatives which were used (by ORCA) for the computation of the ISC rates (see also equations 3.96 and 3.97).

The first observation is that all the mode derivatives of the $M = 0$ matrix element for **^{3}Fb** are two orders of magnitude smaller than all other mode derivatives in figure 4.6. This is the reason why $\tilde{k}^0_{HT}$ is only a very small contribution (of 0.5%) to the overall ISC rate. Another statement of this observation is that

[16] Albeit, it is not possible to say whether $\tilde{k}^{\pm 1} = 10\%$ is necessarily due to $\tilde{k}^X$ or otherwise.

no matter how the ^{3}**Fb** structure vibrates, the $\langle S|\hat{H}_{\mathrm{SOC}}|T_0\rangle$ matrix element remains relatively small and unchanged from the equilibrium value (which is given in table 4.3). By contrast, certain vibrations in ^{3}**Fb** are capable of causing sufficiently large deviations of the $\langle S|\hat{H}_{\mathrm{SOC}}|T_+\rangle$ element (from its equilibrium value of zero) to lead to a preferential in-plane, vibronically driven spin polarisation. The inset in the top right panel of figure 4.6 shows the vibrational mode which leads to the largest change in the SOC interaction; similar insets are shown for ^{3}**Zn**.

Such effects have also been reported previously in the literature for free-base porphyrin systems; *e.g.* references [93] and [95] contain more detailed analyses of what are often called 'spin-orbit active modes' (modes which lead to large SOC derivatives). Symmetry considerations aside, it is not clear why certain vibrations should lead to any change in the SOC matrix elements in systems without any heavy elements, yet, the above results also seem to confirm that this is indeed the case.

For the ^{3}**Zn** system, we see that SOC between the singlet state and both the in-plane and out-of-plane triplet sub-levels can be enhanced by certain vibrational modes. The reason why certain modes promote ISC is more easily conceptualised in ^{3}**Zn** compared with the ^{3}**Fb** case. Apart from its symmetry requirements, a vibration of the porphyrin molecular backbone leads to changes in the interaction/bonding between the Zn^{2+} center and the porphyrin orbitals and hence, to small changes in the *d*-orbital composition of the electronic states. Therefore, the strength of the SOC interaction is modulated most by those vibrations which lead to a more drastic increase or decrease of the coefficients of the Zn^{2+} orbitals, or more simply, in the bond strength between Zn^{2+} and the porphyrin macrocycle.

In summary, the above computational results confirm that the spin polarisation observed for ^{3}**Fb** is driven in-plane by certain active vibrations, one of which is depicted in figure 4.6, despite the fact that the in-plane SOC matrix element is zero at equilibrium. For ^{3}**Zn**, the preferential out-of-plane spin polarisation is driven not only by the direct SOC mechanism due to the Zn^{2+} *d*-orbitals, but also by the vibronic mechanism. The minor non-zero in-plane (P_X) sub-level population in ^{3}**Zn** is caused purely by the vibronic/HT mechanism, akin to the ^{3}**Fb** system.

4.2.3 Elucidation of the ^{3}Pd system

Magneto-photo-selection

As can be seen from the simulation parameters in table 4.1, the sign of D and the orientation of the **D**-tensor cannot be determined only from the trEPR spectra, which is why both cases are shown for the ^{3}**Pd** system in the table. However, since an out-of-plane spin polarisation is expected (due to an enhanced SOC interaction) in the presence of the heavy Pd^{2+} ion, it is highly likely that the D-value is negative in ^{3}**Pd**. This conjecture can be justified reasonably well from MPS experiments and accompanying simulations as will be shown in this section.

The excitation wavelengths were set equal to 550 nm and 588 nm which correspond to the two maxima in the Q-band region of the absorption spectrum (rightmost panel in figure 4.7). The results of these MPS experiments are summarised in the top and bottom left panels in figure 4.7 (respectively for 550 nm and 588 nm).

The same figure also contains the results of MPS simulations in the central panels. These simulations were obtained by least-squares fitting of the α and β angles between the **D**-tensor axes and the optical

transition dipole moment, τ. The function *pepper_MPS*, mentioned in the previous chapter, was used in conjunction with the *esfit* function in EasySpin [9]. A number of assumptions have been made in the generation of these simulations, in order to reduce the number of parameters employed to simulate the experimental MPS spectra.[17]

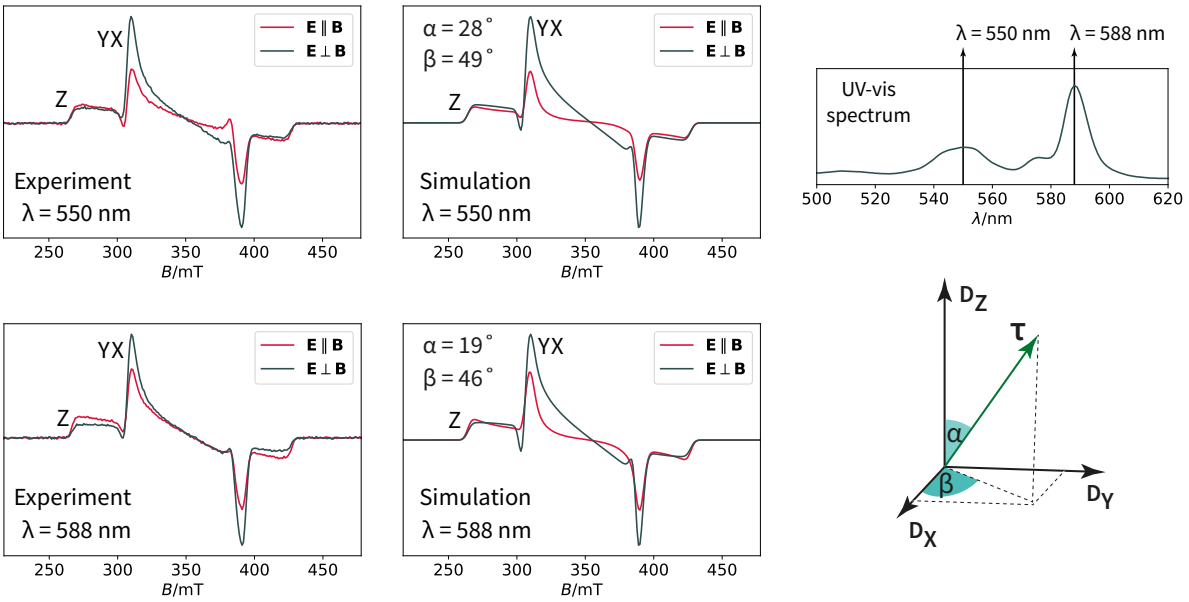


Figure 4.7: MPS experiments (left) and simulations (right) performed at the two wavelengths indicated in the UV-vis spectrum for the ^{3}**Pd** sample. The only two additional parameters required for the MPS simulations are the two angles, α and β, which dictate the orientation of the net optical vector, τ, relative to the **D**-tensor axes.

The assumptions made in generating these simulations and throughout the subsequent discussion are as follows:

1. the optical vectors/transition dipole moments excited at either wavelength in the Q-band region are within the porphyrin plane;
2. there exist only two orthogonal optical vectors;
3. at a given wavelength, the net optical vector is a weighted sum of the two independent in-plane optical moments; the weighting of each component has an unknown wavelength dependence.

Assumptions 1. and 2. follow directly from the symmetries of the electronic states involved in the ground to excited singlet excitation. As will be shown later, apart from a few differences, the states of the ^{3}**Pd** system are very similar in symmetry to the ^{3}**Fb** and ^{3}**Zn** systems described in the previous section. By consulting the D_{2h} character table (Appendix D), we see that the $|^1A_g\rangle \longrightarrow |^1B_{2u}\rangle$ transition is polarised along the molecular y-axis, whereas the $|^1A_g\rangle \longrightarrow |^1B_{3u}\rangle$ transition is polarised along the molecular x-axis.[18] Finally, assumption 3. means that the net optical vector τ will not necessarily be aligned with any of the **D**-tensor axes. This is because at a given wavelength, there could be an overlap

[17] Which is why the simulated spectra in figure 4.7 are not as precise as the powder average simulations in 4.2. Nonetheless, the trade-off is that the interpretation of the results is greatly simplified.

[18] Usually, these transition are labelled Q_x and Q_y.

of the vibronic progression bands of the two allowed transitions, hence, each of the two orthogonal transition dipole moments is excited in a different proportion.

The best fit value of α for either excitation wavelength is significantly less than 45°. This indicates that the D_Z axis of the **D**-tensor in ^{3}**Pd** is highly likely to be close to the porphyrin plane rather than perpendicular to it (*cf.* ^{3}**Fb** and ^{3}**Zn**). Even without performing simulations, qualitative inspection of the experimental data reveals a modest (yet important) increase in the intensity of the Z transitions when **E** ∥ **B**. This indicates that the optical vector is close to or aligned with the D_Z-axis. The decrease of the intensities of the XY transitions (observed in all the spectra) is indicative of the fact that either D_X or D_Y is the out-of-plane axis, and hence, the value of β deviates significantly from 0°. Because the **D**-tensor is approximately axial in this system, we can take either D_X or D_Y to be out-of-plane; D_Y is the choice made in this thesis.

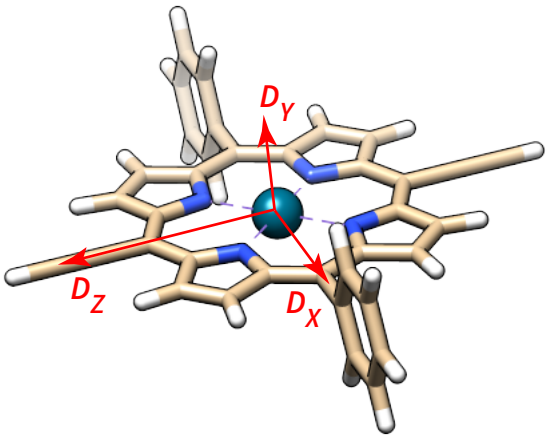


Figure 4.8: The orientation of the **D**-tensor axes in the triplet state of the ^{3}**Pd** system. Based purely on the MPS results in this section, the D_Z and D_X axes could have been placed anywhere in the molecular plane (*i.e.* not necessarily as shown). However, in light of the ENDOR results of the next section, and of the subsequent symmetry arguments, the orientation of **D** relative to the structure of ^{3}**Pd** depicted in this figure is very plausible. Furthermore, because the orthorhombicity is close to zero in this molecule, the D_X and D_Y axes could be swapped, or rotated by any angle (whilst preserving their mutual orthogonality). However, swapping the D_Y and D_X leads to a left-handed tensor, which is not allowed in this thesis. In essence, the only important realisation at this stage of the discussion is that D_Z is very close to being in the porphyrin plane.

In summary, although not perfect, the experimental and computational results in figure 4.7 seem to confirm the fact that the sign of D is negative in ^{3}**Pd**. The assumptions highlighted above are responsible for the slightly ambiguous best-fit values of α and β. However, compromising these assumptions would involve increasing the number of parameters, or degrees of freedom, and thus, the uniqueness of the simulations would become even more questionable. As such, it is reasonable to conclude that the data presented above is in line with the orientation of **D**-tensor in the ^{3}**Pd** system being reoriented compared to ^{3}**Fb** and ^{3}**Zn**, as depicted in figure 4.8.

Mims ^{1}H-ENDOR

Further evidence for the orientation of the **D**-tensor in ^{3}**Pd** being as shown in figure 4.8 can be obtained by comparing the results of ^{1}H-ENDOR measurements on ^{3}**Pd** and ^{3}**Zn**. The interpretation of the

ENDOR spectra in this section is done according to the general principles outlined in section 3.7.2. Figure 4.9 shows the experimental ^{1}H-ENDOR spectra recorded at the low-field Z, low-field X and high-field X turning points in the trEPR spectra of the ^{3}**Zn** and ^{3}**Pd** systems. For the ^{3}**Zn** sample, the original measurements were performed by Dr. Claudia Tait [49, 73], however, they are reproduced in this work as well because they are paramount for the description of the ^{3}**Pd** system.

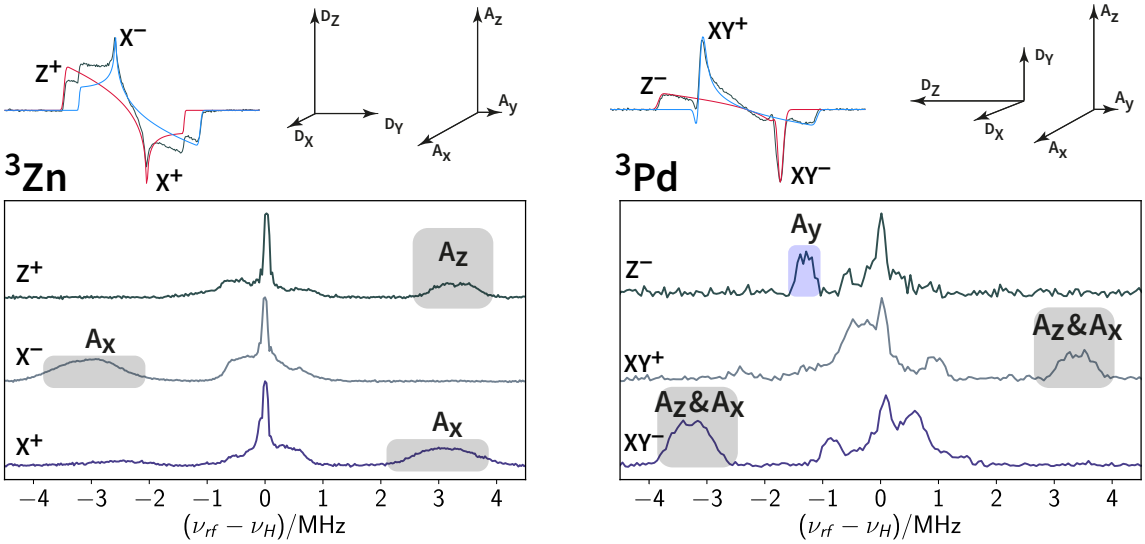


Figure 4.9: Summary of Mims ^{1}H-ENDOR spectra for ^{3}**Zn** and ^{3}**Pd** acquired at the field positions indicated in the diagrams above the two main panels. The relative orientation of the **D**-tensor for ^{3}**Zn** and ^{3}**Pd** is also shown together with the hyperfine tensor axes. The blue and red traces in the top diagrams correspond to the individual $\Delta M = \pm 1$ sub-spectra which comprise the total trEPR spectrum. Note: (1) further experimental details are provided in appendix F, (2) the $Y^{\pm}$ spectra for ^{3}**Zn** have been acquired and analysed previously [49, 73], however, they are not necessary for the present discussion. This figure is the basis for the entire discussion in this section, hence, all the details relating to the interpretation of the diagrams and data will only become clear towards the end of this section.

The low-field Z transition in the trEPR spectrum of ^{3}**Zn** corresponds to the $\Delta M = +1$ electron spin transition (*i.e.* it is a Z^+ transition, as indicated in 4.9) because $D > 0$ in this system [49, 73, 80]. The ENDOR spectrum for this field position displays clear signals corresponding to hyperfine interactions with magnitudes in the range 3–4 MHz (there are also other peaks corresponding to smaller hyperfine interactions). In the left panel of figure 4.9, this signal is indicated by the grey shaded box and the A_z label. When the ENDOR spectrum is recorded on the X^- field position, we observe the appearance of a broad feature in the range from -3 to -4 MHz, which swaps to the other side of the Larmor peak when the spectrum is recorded on the X^+ transition. Equivalent measurements on the $Y^{\pm}$ transitions show only hyperfine couplings with magnitudes smaller than ca. 1.5 MHz together with some residual $Z^{\pm}$ peaks (data not shown). The larger hyperfine couplings observed along Z and X have been attributed to the porphyrin based protons, whereas the smaller hyperfine couplings belong to the phenyl protons [49, 73]. In summary, the ^{1}H-ENDOR data for ^{3}**Zn** is consistent with a net axial hyperfine coupling tensor to the porphyrin based protons which satisfies:

$$\begin{cases} A_x, A_z \approx -3.5\,\text{MHz} > A_y \approx -1.25\,\text{MHz} \\ A_z \parallel D_Z, \quad A_x \parallel D_X, \quad A_y \parallel D_Y \end{cases} \tag{4.3}$$

as indicated in the top left of figure 4.9. Strictly speaking, these peaks are due to more than one proton, however, this complication is irrelevant for the remaining discussion. The fact that A_x and A_z are negative is established by the positions of the hyperfine peaks relative to the Larmor peak: in the Z^+ spectrum, the hyperfine peak (marked with A_Z in figure 4.9) is on the right of the Larmor peak, hence the coupling is negative, in the X^- spectrum the hyperfine peak (marked with A_X) is on the left of the Larmor peak which means that the coupling is also negative. As mentioned, the data for $Y^\pm$ is not shown here, however, the assignment of the sign is analogous to the other field positions [49, 73, 80].

This entire assignment of the ENDOR spectra for the **^{3}Zn** system will be taken as a reference point for the assignment of the **^{3}Pd** ENDOR spectra. More precisely, it will be assumed that the hyperfine coupling tensors in **^{3}Pd** are the same as for **^{3}Zn**. This assumption will be justified in the next section, whereby it will transpire that the spin density distribution in both **^{3}Zn** and **^{3}Pd** is approximately the same. In summary, it is assumed that the **^{3}Pd** system has a net hyperfine tensor which is conserved relative to the Cartesian/molecular axes *and* relative to the **^{3}Zn** system. Therefore, the orientation of **D** can be determined relative to this conserved hyperfine tensor. In turn, this allows the orientation of **D** in **^{3}Pd** to be determined relative to the **D**-tensor in **^{3}Zn**.

In light of the above paragraph (and the assumption therein), the interpretation of the ENDOR data for **^{3}Pd** can now proceed in two ways: (1) the data can be used to *determine* the orientation of **D** relative to the hyperfine tensor **A** in **^{3}Pd** by examining all the possible orientations of **D** and eliminating all the ones that are inconsistent with the data, or (2) the data can be shown to be *consistent* with the orientation of **D** shown in figure 4.8. In the interest of brevity, approach (2) will be taken. This is further motivated because the MPS analysis in the previous section is clear on the fact that D_Z is close to being within the porphyrin plane. Notwithstanding the tedium of approach (1), it is unwarranted in light of the MPS results.

Therefore, in **^{3}Pd** the D_Y axis is now assumed to be aligned with the out-of-plane A_z axis, hence, the 3–4 MHz features will appear in the ENDOR spectra acquired at the $XY^\pm$ positions. The low-field XY for **^{3}Pd** is a $\Delta M = +1$ transition whilst it is $\Delta M = -1$ for **^{3}Zn**. Hence, acquiring ENDOR at field positions on the same side of the zero-crossing in the trEPR spectrum leads to mirror image spectra in **^{3}Zn** versus **^{3}Pd**. Importantly however, the D_Y axis in **^{3}Pd** is approximately degenerate to the D_X axis ($\lambda = 0.00$ in table 4.1). Hence, there are no individual X or Y transitions, there is only an XY transition. For this reason, when the ENDOR spectrum is measured on $XY^\pm$, the resulting hyperfine peaks must belong to both A_z and A_x. *But*, A_x and A_z are the same, so only one peak is observed in the range of ±3 to ±4 MHz.[19]

As a further illustration of the points made in the previous paragraph, this assignment of the $XY^\pm$ spectra of **^{3}Pd** is more easily explained in a visual approach, using the diagrams on the top of figure 4.9 and by a comparison of these diagrams for **^{3}Zn** and **^{3}Pd**. In the **^{3}Zn** diagram (left side of figure 4.9), the D_Z axis is aligned with A_z. Hence, measurements taken on a Z transition will reveal a hyperfine peak centred at $|A_z| = 3-4$ MHz. The fact that $D > 0$ in **^{3}Zn** means that this *low-field* Z transition is actually a Z^+ transition. Peaks on the right of the Larmor peak in a '+' ENDOR spectrum imply negative hyperfine couplings, so $A_z < 0$. Also, for **^{3}Zn**, the D_X axis can be seen to be aligned with A_x, therefore justifying the appearance of the ENDOR spectra acquired on the $X^\pm$ positions. More concretely, a hyperfine peak centred at ~ ±3.5 MHz emerges in these spectra. This peak belongs to A_x, which is also a negative

[19] In **^{3}Zn** the A_z and A_x couplings could be measured independently because the **D**-tensor is not perfectly axial.

hyperfine coupling (as can be determined from the known sign of D).

The exact same visual description can be carried out for the ^{3}**Pd** ENDOR data. As can be seen in the top right side of figure 4.9, the hyperfine tensor is the same in ^{3}**Pd** as it was for ^{3}**Zn**. However, the **D**-tensor in this system is now re-orientated, such that $D_Z \parallel A_y$, $D_Y \parallel A_z$, and $D_X \parallel A_x$. Crucially, there is another difference between the **D**-tensor diagrams for ^{3}**Zn** and ^{3}**Pd** in this figure: in the former, the D_X axis is very similar in magnitude to the D_Y axis (because of the low orthorhomicity determined from trEPR simulation). This means that the measurements taken on the $XY^{\pm}$ peaks reveal a peak which corresponds to *both* A_x and A_z because these hyperfine axes are parallel to D_X and D_Y. Strictly speaking, we have omitted the fact that the $XY^{\pm}$ transition is not a perfect overlap of X and Y,[20] yet the overlap is very much non-negligible, and this is sufficient for all intents and purposes.

Finally, the D_Z axis in ^{3}**Pd** is along A_y, the smallest coupling, which is why there is a peak at ca. -1.25 MHz (marked with blue shading) in the Z^- ENDOR spectrum. In the ^{3}**Zn** system, the equivalent A_y hyperfine coupling is also present, and as expected, it appears in the $Y^{\pm}$ ENDOR spectra published by Tait et al. [73] (see also equations 4.3). Therefore, the Mims ENDOR spectra for the ^{3}**Pd** system strongly suggest a re-orientation of the **D**-tensor compared to the ^{3}**Zn** system.

The origin of the D-tensor in ^{3}Pd

The experimental results of the previous two sections clearly indicate that the **D**-tensor in ^{3}**Pd** has a different orientation relative to the porphyrin backbone compared to the ^{3}**Fb** and ^{3}**Zn** systems: the D_Z axis is in the plane of the porphyrin, and the D_Y axis is perpendicular to the porphyrin plane. It is thus apparent that the dipolar-only picture for the ZFS interaction is no longer applicable to ^{3}**Pd**.[21] In order to better understand the interplay between the SSC and SOC contributions to **D** in this system, a number of different electronic structure calculations were attempted; the final results for the D-value and its two, D_{SSC} and D_{SOC}, components are summarised in table 4.4.

The first (and perhaps most pertinent) conclusion which can be drawn from the results shown in this table is that the DFT methods employed here are not suitable for the description of the either the SSC or the SOC components. The behaviour of the D_{SSC}-value is, on the whole, similar to the DFT results obtained for the ^{3}**Zn** and ^{3}**Fb** systems (table 4.2), *i.e.* the magnitude of this contribution is underestimated by approximately a factor of two. Surprisingly however, it seems that the sign of the D_{SSC}-value behaves erratically, it is sometimes positive or negative, depending on the method used to evaluate the SOC contribution. It is possible that this erratic behaviour is due to a number of errors in the older version 3.0.3 of the ORCA software which have since been addressed in a later release (version 4.2.0). However, the calculations were not re-attempted due to the little promise offered by the eight DFT results already obtained and shown in table 4.4.

Less surprisingly, the SOC contribution, D_{SOC}, shows a very erratic behaviour both in terms of its sign and its magnitude. The reason for this behaviour, is that the def2-TZVP basis set employed in this calculation is not suitable for the description of the core orbitals of the Pd^{2+} ion, some of which can have a

[20] Due to g-anisotropy.

[21] Alternatively, if the dipolar only picture were still applicable then the spin density would have to undergo a drastic change (somehow become more 'contracted' to a vastly smaller average inter-spin distance) to account for the doubling of the D value in ^{3}**Pd** *versus* ^{3}**Zn**. This drastic change in the spin density would then have to be accompanied by a drastic change in the magnitudes of the hyperfine couplings, which is contrary to the ENDOR results.

Method	D_{SSC}/MHz	D_{SOC}/MHz	D/MHz	D_{exp}/MHz
B3LYP-QRO	+539	+3627	+4166	**−2289**
B3LYP-CP	−450	−1229	−1679	
B3LYP-PK	+539	−89	+450	
B3LYP-CVW	+539	−1498	−690	
BP86-QRO	+629	+3807	+4436	
BP86-CP	−539	−1229	−1768	
BP86-PK	+629	0	+629	
BP86-CVW	−89	+869	+780	
CAS(4,4)	+918	−1285	−367	

Table 4.4: The two contributions to the D-value of ^{3}**Pd** obtained from various computational methods. All calculations were performed in ORCA using the def2-TZVP basis set. The first eight rows correspond to DFT calculations employing either the B3LYP or the BP86 functionals. For each functional, all four available methods (QRO, CP, PK, CVW) were employed for the calculation of the SOC contribution. As explained in the ORCA manual, the acronyms for the individual methods are as follows: QRO– quasi restricted orbitals method, CP– coupled perturbed method, PK–Pederson-Khana method, CVW– Christoph van Wüllen method. The final entry is the result of a CASSCF calculation performed equivalently to the calculations presented in table 4.2. As will be explained in the text, the SOC contribution could not be obtained in this particular CAS(4,4) calculation. Also note that all DFT calculations were carried out with ORCA version 3.0.3, whereas the CAS(4,4) was carried out with version 4.2.0 (will be clarified in the main text). The D_{SOC} value highlighted in red in the final row was obtained using MOLCAS in conjunction with the ANO-RCC-TZVP basis set (the significance of this result will be discussed in the main text) [96].

significant impact on the magnitude of the SOC interaction. DFT calculations were attempted in ORCA with a variety of other, more suitable basis sets,[22] however, they were unfortunately unsuccessful.

It is important to note that the same CAS(4,4) calculation which was successful in predicting the D_{SSC}-value of ^{3}**Fb** and ^{3}**Zn** (table 4.2), gives rise to a value of +918 MHz for ^{3}**Pd** which is very close to the value of 910 MHz obtained for ^{3}**Zn**. This result is significant and it is entirely aligned with the experimental findings presented thus far. The fact that the CAS(4,4) derived D_{SSC}-value is similar between ^{3}**Zn** and ^{3}**Pd** indicates that both the symmetry and the distribution of the spin density in the two metalloporphyrin systems is very similar (figure 4.10). This is vindicated by the ENDOR results presented in the previous subsection, whereby both ^{3}**Zn** and ^{3}**Pd** spectra are consistent with a common net hyperfine tensor (attributed to the porphyrin based protons), with a conserved orientation and magnitude. As will be seen shortly, apart from a small difference, the molecular orbitals for ^{3}**Zn** and ^{3}**Pd** are almost indistinguishable, hence why the spin densities and resulting hyperfine tensors are expected to be similar.

The SOC contribution to ZFS could not be obtained from the same CAS(4,4) calculation in ORCA as was used for the SSC part (for either of the systems investigated here). Firstly, although the chosen basis set is entirely suitable for the description of the spin density, it is not suitable for the description

[22]For example, the all-electron atomic natural orbital basis sets (ANO-RCC-DZP and ANO-RCC-TZP) were trialled.

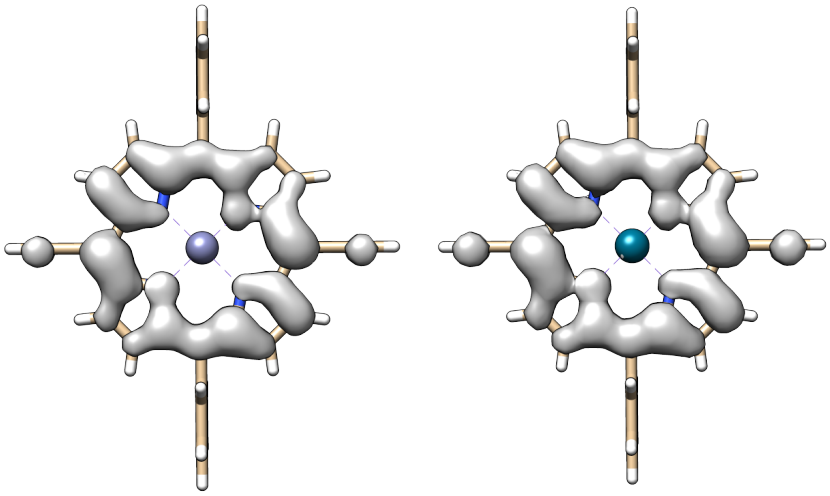


Figure 4.10: Comparison of the spin densities for ^{3}**Zn** (left) and ^{3}**Pd** (right), obtained from the CAS(4,4) calculation described in the main text.

of SOC effects due to the presence of Pd^{2+}. Secondly, whilst for the SSC contribution it is sufficient to obtain an accurate representation for the wavefunction of the triplet of interest, the SOC contribution requires accurate wavefunctions and relative energies for the higher energy triplets as well (because it is a second-order effect). More precisely, the CAS(4,4) calculation performed in ORCA seems to give rise to a sufficiently accurate spin density for the lowest energy triplet to allow an accurate calculation of D_{SSC}, however, both the SOC matrix elements and the relative energies of the states are unlikely to be accurate. As was the case for the DFT calculations, attempts at calculations with more precise basis sets in ORCA, have been unsuccessful. Nonetheless, the D_{SOC} value was obtained from a CAS(4,4) calculation in MOLCAS by employing the ANO-RCC-TZVP basis set, and it is shown in red in table 4.4.

The significance of the D_{SOC}-value highlighted in red will become apparent shortly. This result is not accurate, however, it is important and consistent with expectations based on the symmetry of the ^{3}**Pd** system. As such, it is necessary to describe in more detail the origin of the **D**-tensor in ^{3}**Pd** from the point of view of group theory before interpreting the value highlighted in red any further.

For the purpose of a symmetry analysis, it is, first of all, necessary to consider the symmetry of the ^{3}**Pd** molecular orbitals. Figure 4.11 shows that the main difference between ^{3}**Pd** and ^{3}**Zn** is observed for the higher energy SOMO (B_{2g}) and LUMO (B_{3g}) orbitals. The lower energy SOMO and the HOMO orbitals (neither are shown) are indistinguishable between the two systems, because they do not have the appropriate symmetry to interact with the Pd^{2+} or Zn^{2+} d-orbitals. It is not surprising that the d_{xz} and d_{yz} orbitals of Pd^{2+} interact more favourably with the porphyrin π-system compared to Zn^{2+}; second-row transition metal complexes are often described as having more covalent character in the metal-ligand bond because of the better energy match between the orbitals and due to the fact that $4d$ orbitals are more radially extended compared to $3d$ orbitals (thus leading to better overlap).

As mentioned before, the similarity of these two sets of orbitals is the reason why the CAS(4,4) calculation predicts only a minor difference between the D_{SSC}-values for ^{3}**Zn** and ^{3}**Pd**. For the remainder of the discussion, it will be assumed that the value of D_{SSC} = +918 MHz predicted in the CAS(4,4) calculation for ^{3}**Pd** is accurate.

The general formula for the $\mathbf{D}_{\mathrm{SOC}}$-tensor was derived in the previous chapter and can be found in equa-

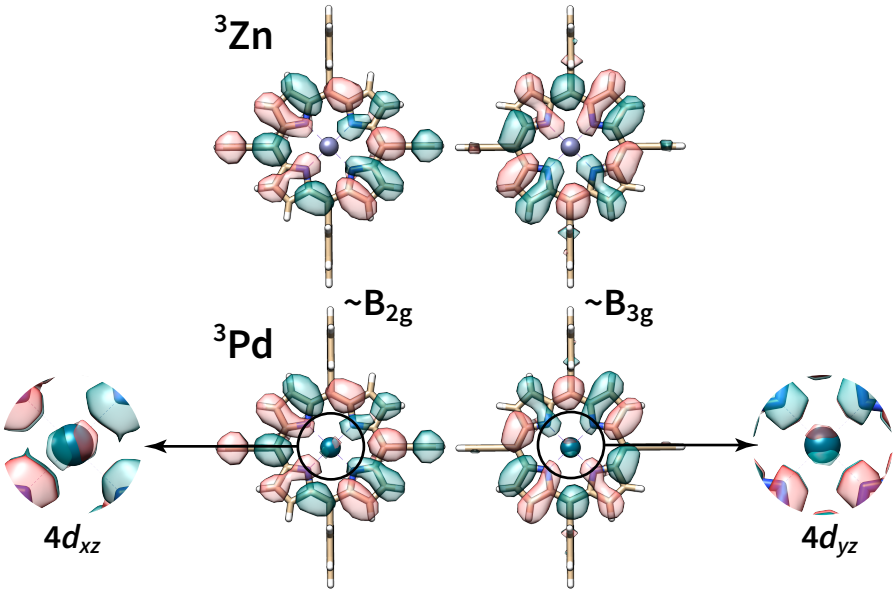


Figure 4.11: The higher energy SOMO (left) and LUMO (right) orbitals for ^{3}**Zn** (top) and ^{3}**Pd** (bottom). The approximate irreducible representation of these molecular orbitals is also given (it is only approximate because the calculation was not carried out by employing symmetry). The contribution from the Pd^{2+} 4d-orbitals is also indicated; for ^{3}**Zn** the equivalent 3d-orbitals are also involved in the molecular orbitals, however, they are not visible at the iso-levels employed in these diagrams, because they are not as radially extended as the 4d-orbitals.

tions 3.62, 3.68, and 3.70. The triplet-triplet contribution is sufficient for a symmetry analysis, although analogous arguments hold for the singlet-triplet contribution. The triplet-quintet contribution is bound to be insignificant due to the much higher energy associated with the quintet states in porphyrins.

All the symmetry properties of the $\mathbf{D}_{\mathrm{SOC}}$-tensor are encapsulated by the outer product of the vectorial reduced SOC matrix elements, *i.e.* the $\mathcal{L}_{ab} \otimes \mathcal{L}_{ba}$ term (see table 3.1). The 'b' index can be taken to be the triplet arising from the $B_{2g} \longrightarrow B_{3g}$ excitation (*i.e.* SOMO $\longrightarrow$ LUMO). Hence, the lowest energy 'b' triplet state which contributes to the ZFS of the 'a' triplet state will be B_{2u} symmetric. The corresponding 'a' triplet is B_{3u} symmetric, and thus, the pq component of the $\mathcal{L}_{ab} \otimes \mathcal{L}_{ba}$ term is expected to be exactly zero unless the following conditions:

$$\Gamma(R_p) = B_{2u} \times B_{3u} \quad \& \quad \Gamma(R_q) = B_{2u} \times B_{3u} \tag{4.4}$$

are satisfied simultaneously. This means that $\Gamma(R_p) = \Gamma(R_q) = B_{1g}$ and as a result $R_p = R_q = R_z$ *i.e.* it can be deduced that the D_{SOC}-value will have the following form (in frequency units):

$$D_{\mathrm{SOC}} = -\frac{2}{9h\Delta_b}|\mathcal{L}^z_{ab}|^2 \tag{4.5}$$

whereby we also assume that the B_{2u} triplet state is the only significant contribution. In other words, we can define the (positive) spin-orbit shift to the net D-value by a positive parameter, $\Lambda = |\mathcal{L}^z_{ab}|^2$, such that:

$$D = D_{\mathrm{SSC}} - \frac{2}{9h\Delta_b}\Lambda \tag{4.6}$$

where Δ_b is the triplet-triplet energy gap. Therefore, if Λ is large enough (which is highly likely in the

presence of Pd^{2+}), then the D-value will be negative, as observed experimentally. It is also necessary to comment on the fact that the overall **D**-tensor for ^{3}**Pd** is measured to have the D_Z axis in the plane of the porphyrin, whilst the spin-orbit interaction acts along the out-of-plane axis. This apparent discrepancy is readily reconciled by noting that the $\mathbf{D}_{SOC}$-tensor is left-handed, whereas the $\mathbf{D}_{SSC}$-tensor is right-handed. Within this thesis, all tensors are by convention reported in their right-handed form, hence why, the orientation of the **D**-tensor in ^{3}**Pd** can be defined as depicted in figure 4.8 for a right-handed **D**-tensor. All of the data so far could have been simulated by employing a left-handed **D**-tensor but this would have caused significant ambiguity in the entire discussion, particularly in the comparison of the ^{3}**Pd** and ^{3}**Zn** data.[23]

The group theory analysis above is accurate except for one 'leap of faith': the assumption that the spin-orbit shift parameter, Λ, is sufficiently large to cause a measurable change in the D-value. Apart from the observed orientation of the **D**-tensor, the first piece of evidence in favour of this assumption is the result of the calculation highlighted in red in table 4.4. Given the aforementioned difficulties with such complicated electronic structure calculations, the value of $D_{SOC} = -1285$ MHz obtained here is sufficiently accurate for the purposes of this work. Reassuringly, if the CAS(4,4) calculation is repeated (using MOLCAS) for both ^{3}**Fb** and ^{3}**Zn** the result is zero.

More compellingly, the observed g-values for ^{3}**Pd** provide further evidence for the fact that Λ is non-negligible in this system. The complete equation for the second-order SOC contribution to **g** in triplet states is shown in table 3.1 of the previous chapter. From this table, the g-shift[24] along a particular axis is subject to the exact same selection rules as the spin-orbit shift to D. Therefore, we expect a negative shift along the out-of-plane Cartesian/molecular axis, *i.e.* $\Delta g_z \propto -\Lambda$. The out-of-plane axis corresponds to the D_Y axis (in the right-handed convention), and hence, we observe a g_Y value of ~1.96 which is significantly lower than the free-electron value. As expected from the same line of reasoning, the other two g-values are much closer to the free-electron value (the g-values are given in the caption to table 4.1).

Finally, the entire discussion in the above section also confirms the conjecture made at the outset of this chapter about the ISC mechanism in ^{3}**Pd**. If the SOC interaction is sufficiently large to cause a simultaneous out-of-plane D-shift and g-shift, it will undoubtedly be sufficient to cause an exclusive population of the out-of-plane triplet sub-level via a direct Franck-Condon mechanism, as quantified in table 4.1. Calculations of the ISC rates and accurate theoretical predictions of the spin polarisation (beyond symmetry arguments) for ^{3}**Pd**, or any similar systems, are unlikely to be feasible before the development of a more versatile theoretical framework for calculating SOC effects in highly delocalised π-systems.

4.3 Dimer systems

As was the case for the work presented in Chapter 2, a precise description of the EPR spectra of the monomer systems paves the way for the analysis and interpretation of the dimer spectra. The dimers represent the next step towards the design of molecular wires derived from oligoporphyrins. Therefore, EPR measurements can be used to establish the extent of spin delocalisation in these systems. However,

[23] For ^{3}**Zn**, **D** is by default right-handed.

[24] The g-shift, Δg_Q, is defined as the difference between the observed g-value along the Q-axis, and the free-electron g-value.

it will be seen that a quantitative description of the EPR parameters of the dimers is more challenging. Nonetheless, the general principles illustrated above for the monomers, will greatly facilitate the discussion.

4.3.1 TrEPR spectra of homodimer systems

Figure 4.12 shows the X-band trEPR spectra of the three homodimer systems, denoted by ^{3}**FbFb**, ^{3}**ZnZn**, and ^{3}**PdPd**. The corresponding simulation parameters obtained from least-squares fitting using the EasySpin toolbox are shown in table 4.5. To facilitate the comparison, the corresponding monomer spectra and simulation parameters are repeated in this subsection as well. As with the monomers, the original spectra and analysis of the ^{3}**FbFb** and ^{3}**ZnZn** are found in references [73] and [49]. These data have been reproduced in this work since they are needed for the description of the new data of the ^{3}**PdPd** system.

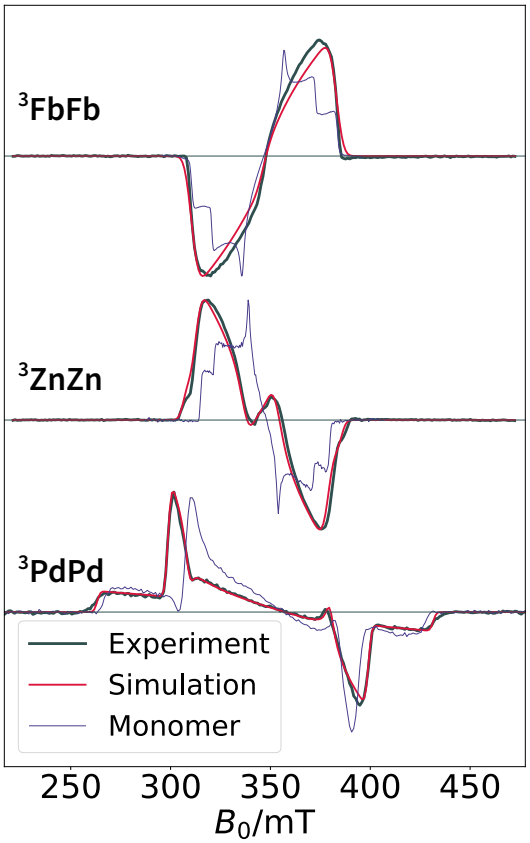


Figure 4.12: Experimental and simulated trEPR spectra of the triplet states of the homodimer systems. The spectra were acquired at X-band and 80 K using laser excitation at 532 nm, equivalently to the spectra reported for the monomer systems in figure 4.2. The experimental monomer spectra are also shown here for comparison purposes.

The most striking differences between these systems occur between the ^{3}**Fb** and ^{3}**FbFb** systems, and between the ^{3}**Zn** and ^{3}**ZnZn** systems. The fact that the sign of the D-value is inverted is a consequence of the fact that the spin density in these molecules is better described by a prolate spheroid (a cigar shape) with the long axis along the axis connecting the two sub-units. Furthermore, the increase in the orthorhombicity parameter is also a reflection of the same change from oblate to prolate spin densities. These observations have been confirmed in the work of Tait et al.[73] by means of MPS and ENDOR

System	D/ MHz	$\lambda = \lvert E/D \rvert$	$P_X : P_Y : P_Z$
^{3}**Fb**	+1024	0.14	0.50 : 0.50 : 0.00
^{3}**FbFb**	−1053	0.30	0.29 : 0.00 : 0.71
^{3}**Zn**	+906	0.18	0.00 : 0.13 : 0.87
^{3}**ZnZn**	−1117	0.23	0.00 : 0.90 : 0.10
^{3}**Pd**	−2289	0.00	0.00 : 1.00 : 0.00
^{3}**PdPd**	−2362	0.06	0.01 : 0.99 : 0.00

Table 4.5: ZFS and population parameters used to obtain the simulations depicted in figure 4.12. The signs of the D-values for the top four zinc and free-base systems have been determined in previous work[49, 73], but have been reproduced in this work. For ^{3}**Pd**, the sign of D was determined in the previous section, whereas for ^{3}**PdPd**, it is negative as will be shown in the proceeding discussion. The **g**-tensor of ^{3}**PdPd** is anisotropic and, in the **D**-tensor eigenframe the values are: $g_X = 2.00463$, $g_Y = 1.98363$, $g_Z = 2.00522$. The **g**-tensors for all non-palladium systems are assumed to be approximately isotropic (the corresponding spectra are symmetric relative to the barycenter).

experiments.

As expected in the dipolar only description of the **D**-tensor in non-palladium dimers, the D_Z axis is in-plane whereas the D_Y axis is perpendicular to the plane containing the two porphyrins. Hence, the direct Franck-Condon ISC mechanism will drive the spin polarisation preferentially into the out-of-plane sub-level in the ^{3}**ZnZn** system, which corresponds to P_Y. On the other hand, the presence of a small in-plane population (P_Z) for ^{3}**ZnZn**, is likely to be due to a vibronic Herzberg-Teller contribution. One might tentatively attribute this vibronic population to the stretching modes of the four ethyne fragments present in these dimers. Whilst this seems a likely explanation, it has yet to be proven and, unfortunately, calculations of the type shown in the previous section have not been successful for this molecule. It is nonetheless clear that the small P_Z sub-level population must be a vibronic effect because the direct SOC interaction due to the Zn^{2+} only acts in the out-of-plane direction.

The change between monomer and dimer is significantly less pronounced for the systems containing Pd^{2+}, in both the appearance of the trEPR spectra and the values of the simulation parameters. The **D**-tensor in ^{3}**PdPd** will be shown in the next section to be negative, akin to its monomer counterpart. In turn this implies that the out-of-plane axis is the D_Y axis, and hence, P_Y is the largest of the sub-level populations. Furthermore, the fact that g_Y is the smallest of the g-values indicates that the SOC interaction is once more acting in the out-of-plane direction.

In light of the above, if we also assume that the dipolar contribution, $\mathbf{D}_{\mathrm{SSC}}$, in ^{3}**PdPd** is very similar to the entire (dipolar only) **D**-tensor of ^{3}**ZnZn**,[25] then it must follow that the SOC contribution in the former has decreased in magnitude by almost a factor of three (otherwise, the two contributions would not add up to a value of -2362 MHz in ^{3}**PdPd**). This is a crucial point; had the SOC interaction been neglected from the discussion of the D-value in the palladium systems, the comparison of the ^{3}**Pd** and ^{3}**PdPd** systems would have been dramatically erroneous. More precisely, if it were assumed that the D-values in both of these triplets were a dipolar only effect, then it would have to be concluded that the spin density is almost exactly the same[26] for the palladium monomer and dimer *i.e.* almost completely

[25] A reasonable assumption given that in the corresponding monomers, the spin density is almost unchanged in shape and symmetry between ^{3}**Pd** and ^{3}**Zn** (figure 4.10).

[26] Because the D-values are almost the same (-2289 MHz *versus* -2362 MHz) and there is no re-orientation of the **D**-tensor between ^{3}**Pd** and ^{3}**PdPd**.

localised to only one unit of the dimer.

4.3.2 The orientation of the D-tensor in ^{3}PdPd

A first indication of the fact that the orientation of the **D**-tensor is conserved between ^{3}**Pd** and ^{3}**PdPd**, can be obtained from the MPS spectra presented in figure 4.13. For porphyrin dimers, the MPS effect is less pronounced by comparison with the effect observed on the corresponding monomers. This decrease in the efficiency of the MPS experiment has been reported previously for the zinc and free-base dimers [49, 73], and is likely due to the increased degree of conformational freedom of the molecules. For example, at a particular excitation wavelength, non-uniform distributions of interporphyrin dihedral angles are selected, and thus the assumptions outlined in section 4.2.3 are not entirely applicable.

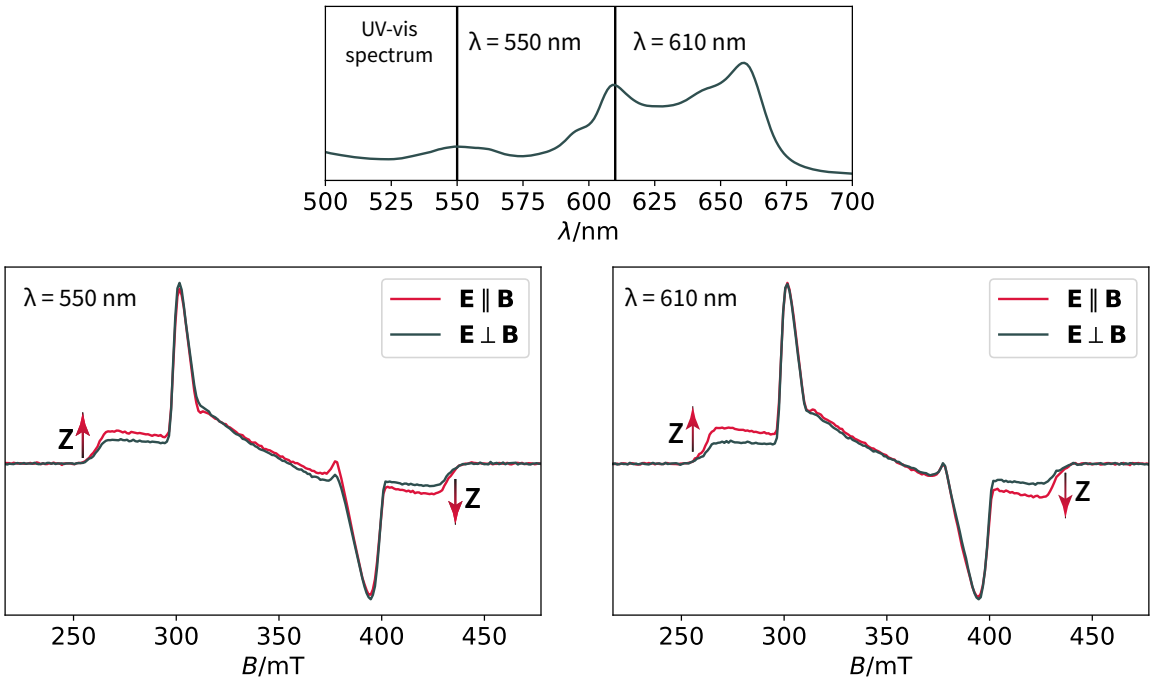


Figure 4.13: The results of MPS experiments (bottom panels) performed on the ^{3}**PdPd** system using the two different excitation wavelengths indicated in the UV-vis absorption spectrum (top panel). All other measurement parameters are identical to the ones used to obtain the usual trEPR spectra. The largest MPS effect is observed on the Z transitions, as indicated by the gradient arrows. Measurements with larger excitation wavelengths (closer to the peak at the red edge at ca. 660 nm) were unsuccessful. Note that in this figure and throughout the entire chapter, the indexes of the hyperfine coupling tensors are *always* Cartesian *i.e.* the 'x' of A_x always corresponds to the Cartesian/molecular x-axis.

Nonetheless, we can safely assume (from the previous work of Tait et al. [73]) that the ^{3}**PdPd** system has at least an optical axis which is aligned with the axis defined by the butadiyne linker *i.e.* the long axis.[27] Depending on the excitation wavelength (here 550 nm and 610 nm are considered), this long axis transition dipole moment will contribute to the UV-vis spectrum in a different proportion. Regardless, the overriding conclusion from figure 4.12 is that when $\mathbf{E} \parallel \mathbf{B}$, the Z transitions are enhanced compared to when $\mathbf{E} \perp \mathbf{B}$. This means that the optical vector is aligned with the D_Z axis, and hence, it is highly likely that D_Z is along the long axis. In turn this would imply a negative D-value, and a **D**-tensor

[27] As far as the ^{3}**PdPd** system investigated here is concerned, there is some flexibility in this assumption. It is sufficient to say that ^{3}**PdPd** has an optical axis which is close to but not perfectly aligned with the interporphyrin axis.

which, overall, is not too dissimilar from the ^{3}**Pd** monomer system. If we only consider the lowest energy conformer (dihedral angle of 0°), then the conclusion is that D_Z is the in-plane axis. Due to the relatively weak MPS effect exhibited by the data in figure 4.13, any further analysis beyond the qualitative description given here is not possible (nor is it necessary).

More conclusive information regarding the orientation of **D** in ^{3}**PdPd** can be obtained from the Mims ^{1}H-ENDOR spectra presented in figure 4.14, especially if the ^{3}**Pd** system is taken as a reference point. It was established in the previous sections that if the following is assumed regarding the couplings to the porphyrinic protons of ^{3}**Pd**:

$$\text{in-plane axes} \begin{cases} D_Z \parallel A_y \\ D_X \parallel A_x \end{cases} \quad \& \quad \text{out-of-plane axis } D_Y \parallel A_z \tag{4.7}$$

then there is a direct correspondence between the assignment of ^{3}**Zn** and ^{3}**Pd** ENDOR peaks, as is shown for the first time in figure 4.9 and repeated here in figure 4.14.

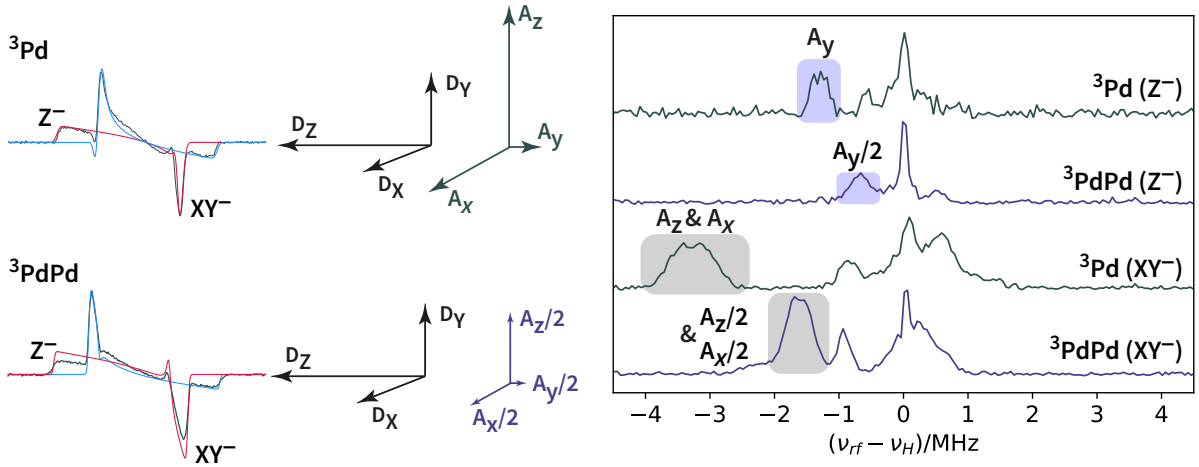


Figure 4.14: Comparison of the Mims ^{1}H-ENDOR spectra for ^{3}**Pd** and ^{3}**PdPd**. The spectra were acquired at the field positions in the trEPR spectra indicated in the leftmost diagrams; the blue and red sub-spectra correspond to the two $\Delta M = \pm 1$ manifolds. The assignment of the ENDOR peaks corresponding to the largest net hyperfine coupling (or set of hyperfine couplings) is done according to the relative axes of the **D**-tensor and hyperfine tensor illustrated in the center of the figure. Under the assumption that the spin density is completely delocalised in the dimer, the hyperfine coupling tensor eigenvalues are shown to become half of the ones for the monomer.

In the ^{3}**PdPd** system, the spin density is delocalised over the two sub-units, and we can therefore write the following:

$$\text{in-plane axes} \begin{cases} D_Z \parallel A_y/2 \\ D_X \parallel A_x/2 \end{cases} \quad \& \quad \text{out-of-plane axis } D_Y \parallel A_z/2.$$

This assumption is sufficient to assign the peaks corresponding to the largest hyperfine couplings in the ENDOR spectra of ^{3}**PdPd**, as illustrated in figure 4.14. Had the D-value been positive in this dimer, then the $\Delta M = -1$ labelling of the peaks in trEPR would have been erroneous, and the accompanying ENDOR spectra would have been the mirror image of the ones which are actually observed in figure 4.14. In summary, both the MPS and ENDOR results presented here are in-line with a conservation of

the orientation of the **D**-tensor in ^{3}**PdPd** *cf.* ^{3}**Pd**.

Finally, it is also important to note that the assignment of ENDOR peaks given in figure 4.14 is equivalent to the assignment of the ENDOR peaks of the analogous zinc dimers [73]. In essence, despite the fact that the SOC interaction due to Pd^{2+} causes the interpretation of the **D**-tensor in this system to be vastly more intricate, the degree of spin delocalisation in the ^{3}**PdPd** dimer system is akin to the ^{3}**ZnZn** system. From the point of view of spin delocalisation, there seems to be no discernible advantage in designing molecular wires by replacing *all* the Zn^{2+} ions of a given oligoporphyrin by Pd^{2+} ions. However, from the point of view spin polarisation along a particular axis of the wire, the palladium dimer has a greater tendency to be out-of-plane polarised (see table 4.5). As a result, replacing the Zn^{2+} ions with Pd^{2+} ions in a porphyrin molecular wire could enable a tuning of the spin polarisation across the wire, whilst preserving the delocalisation length of the spin density.

4.3.3 The heterodimer systems

As suggested at the end of the last section, the SOC effects in palladium porphyrins could be put to use in the design of molecular wires whereby the spin polarisation of the resulting triplet state can be controlled. Whilst promising, the results shown up to this point are not entirely convincing as to the effectiveness of the Pd^{2+} ions *cf.* Zn^{2+} ions at driving the spin polarisation predominantly out-of-plane. It is true that all the simulation parameters in tables 4.5 and 4.1 seem to validate this conclusion *i.e.* if one were to compare only these *best fit* results.

However, the differences in out-of-plane polarisation between the zinc and palladium systems could also be due to uncertainties in the results of the spectral simulations. For instance, it is impossible to guarantee that the exclusively out-of-plane polarisation in ^{3}**Pd** would not be compromised by a concomitant change in the strains (distributions) of the fitted *D*- or *E*-values.

In order to mitigate these uncertainties, and establish whether there is a realistic advantage (or not) in the use of Pd^{2+} ions to control spin polarisation in porphyrin wires, the ^{3}**FbPd** and ^{3}**ZnPd** mixed dimer systems have also been investigated using the same methods as employed up to this point. The trEPR spectra of these two heterodimer systems are shown in figure 4.15 and the accompanying simulation parameters are shown in table 4.6. As always, the parameters for all other systems are also collated in this table for comparison.

By inspection, the trEPR spectrum of ^{3}**FbPd** is vastly different to the trEPR spectra of either ^{3}**Fb** of ^{3}**Pd**. First of all, the *D*-value –which will be shown in due course to be positive– is very similar in magnitude to the ^{3}**Fb** system. This indicates that the spin density is localised primarily on the free-base side of this heterodimer (top right illustration in figure 4.15), and thus, the second-order SOC contribution due to the Pd^{2+} ion is absent. However, the phasing of the spectrum of ^{3}**FbPd** is inverted compared to ^{3}**Fb**. This is reflected by the sub-level populations in table 4.6 which are now consistent with a predominantly out-of-plane spin polarisation. In summary, photo-excitation of the ^{3}**FbPd** heterodimer leads to the formation of a free-base monomer type triplet state in terms of spin delocalisation, but with an out-of-plane rather than in-plane spin polarisation.

The change in spin polarisation observed between the ^{3}**FbPd** and ^{3}**Fb** systems can only be driven by the spin-orbit effects due to Pd^{2+} which, by the symmetry arguments proposed in the previous sections, are always acting in the out-of-plane direction. However, the almost perfect conservation of the orien-

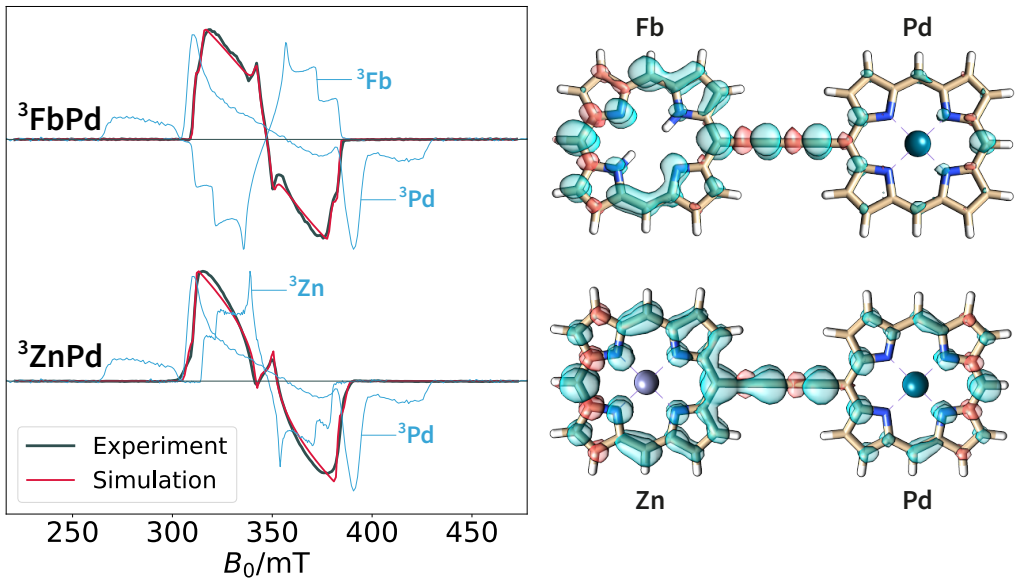


Figure 4.15: (Left) Experimental and simulated trEPR spectra of the triplet states of the **^{3}FbPd** and **^{3}ZnPd** heterodimer systems. The spectra were acquired at X-band and 80 K using laser excitation at 532 nm, under equivalent conditions to all the trEPR spectra reported thus far in this chapter. The experimental monomer spectra are also shown for comparison. (Right) DFT computed spin densities of the heterodimer systems obtained using the B3LYP functional in conjunction with the def2-TZVP basis set. The measurements and DFT calculations in this figure were carried together with Ashley J. Redman, who is one of the main collaborators on this project.

System	D/ MHz	$\lambda = \lvert E/D \rvert$	$P_X : P_Y : P_Z$
^{3}FbPd	+1021	0.26	0.09 : 0.00 : 0.91
^{3}ZnPd	−1114	0.27	0.12 : 0.88 : 0.00
^{3}Fb	+1024	0.14	0.50 : 0.50 : 0.00
^{3}Pd	−2289	0.00	0.00 : 1.00 : 0.00
^{3}Zn	+906	0.18	0.00 : 0.13 : 0.87
^{3}FbFb	−1053	0.30	0.29 : 0.00 : 0.71
^{3}PdPd	−2362	0.06	0.01 : 0.99 : 0.00
^{3}ZnZn	−1117	0.23	0.00 : 0.90 : 0.10

Table 4.6: The first two rows are the ZFS and population parameters used to obtain the simulations depicted in figure 4.15 whereas the remaining rows are the simulation parameters of the monomer and homodimer systems discussed before.

tation and magnitude of the ZFS tensor, implies that the cascade of events initiated by photo-excitation is rather subtle. One consistent and highly likely scenario could be as follows: (1) photoexcitation leads to the formation of either an exclusively palladium-based singlet state or a delocalised singlet wave-function with a significant non-zero contribution on the palladium side of the dimer, (2) a very rapid out-of-plane ISC event takes place, thus carrying the system into the triplet manifold, (3) a polarisation conserving internal conversion cascade within the triplet manifold eventually leads to the final triplet state which is detected by trEPR.

All of these events must take place on a sub-nanosecond timescale, because the trEPR spectra do not change in shape, width, or polarisation as shown in figure F.3 of appendix F. [28] Furthermore, it must

[28]The only change is the net intensity of the entire spectrum. In other words, if the spectra at all times were to be normalised

also be the case that step (2) takes place before any internal conversion to a predominantly free-base localised singlet wavefunction can occur. Otherwise, the in-plane vibronic polarisation specific to free-base porphyrins would be observed. Furthermore, it is essential that step (1) involves a singlet wavefunction which is non-zero on the palladium side of the molecule, because otherwise, the out-of-plane spin polarisation would not ensue. Finally, the wavelength dependent trEPR spectra shown in figure F.4 of appendix F indicate no changes in the polarisation pattern of ^{3}**FbPd**, thus justifying the qualitative mechanism proposed here. Despite not being able to provide any insights into the actual cascade of events in this system (because these ultra-fast processes cannot be resolved in trEPR), the overriding conclusion is that it is the direct SOC of the Pd^{2+} which drives the spin polarisation and not the molecular vibrations. In this sense, when combined with a free-base counterpart, the Pd^{2+} ion can be used to tune the spin polarisation in porphyrin molecular wires.

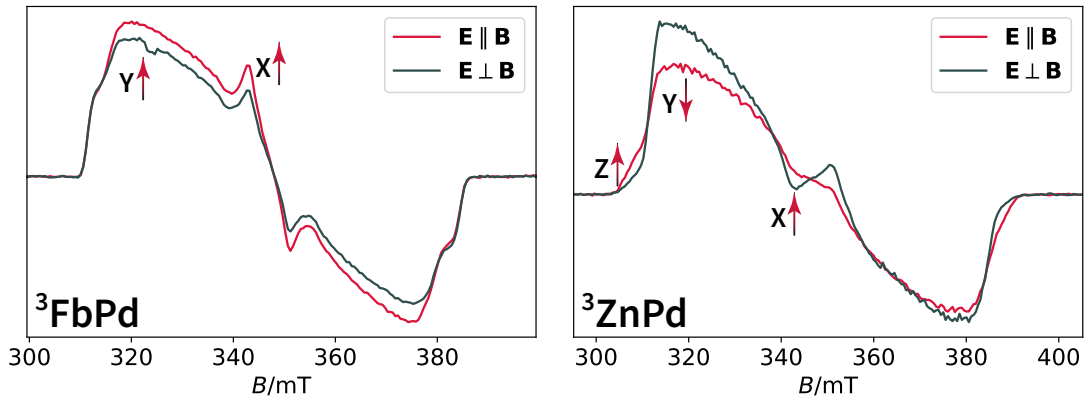


Figure 4.16: MPS spectra for the two heterodimer systems. The data for ^{3}**ZnPd** was acquired with an excitation wavelength of 692 nm and for ^{3}**FbPd** with 550 nm. The observed relative changes between spectra with **E** ∥ **B** and **E** ⊥ **B** in the intensities of the peaks are consistent with a negative D-value for ^{3}**ZnPd** and a positive D-value for ^{3}**FbPd**. MPS spectra at different excitation wavelengths for either of these two systems have been acquired, however, they do not display any interpretable MPS effect (and are therefore omitted).

The issue which has yet to be addressed thus far is the proof of the fact that $D > 0$ in the ^{3}**FbPd** system, which is the origin of the line of reasoning given above. The positive sign of D is clear from the MPS results in the left panels of figures 4.16 and 4.17. The MPS spectrum shows an increase in the intensities of the X and Y transitions when the electric field of the laser is parallel to the external magnetic field. This can only occur if the optical axis (which is presumed to be in the molecular plane) is within the plane defined by D_X and D_Y *i.e.* if D_Z is the out-of-plane axis, and hence, $D > 0$. Furthermore, the spectra in the left panel of figure 4.17 show that by acquiring Mims ENDOR spectra of ^{3}**Fb** and ^{3}**FbPd** at the same field positions leads to almost the same hyperfine peaks, which are on the same side of the Larmor peak. Thus, the orientation of **D** is conserved between ^{3}**Fb** and ^{3}**FbPd**. The slight decrease in the magnitudes of (some of) the hyperfine couplings in the heterodimer is due to the fact that a small amount of spin density can leak onto the palladium side of the molecule (see top right of figure 4.12).

The interpretation of the data for ^{3}**ZnPd** (bottom of figure 4.15 and table 4.6) leads to a different picture to the one uncovered for ^{3}**FbPd**. The trEPR spectrum of the former, and the accompanying simulation parameters, are not similar to either of the component monomer systems. In fact, the ^{3}**ZnPd** system

to the maximum point, they would be identical, albeit the spectra at later times will become ever noisier.

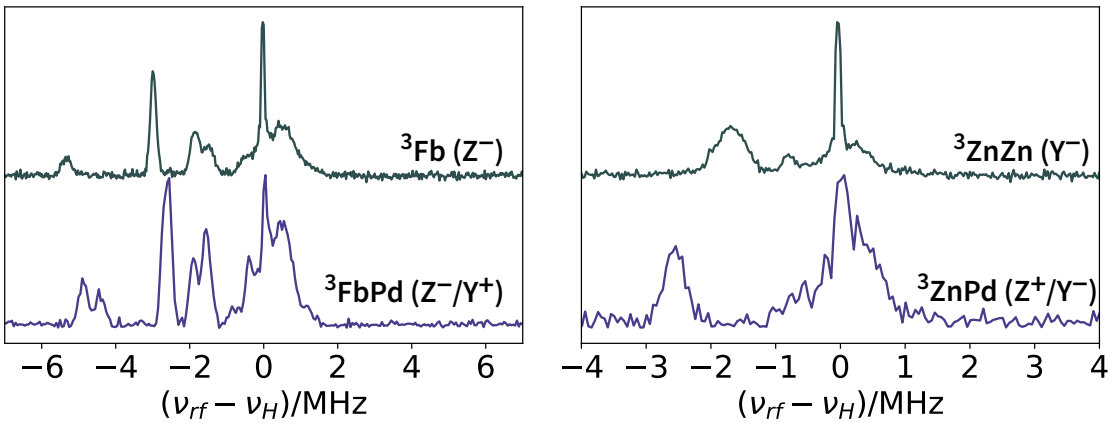


Figure 4.17: (Left) Comparison of the Mims ^{1}H-ENDOR spectrum of ^{3}**Fb** acquired at the (high-field) Z^- field position and the corresponding spectrum for ^{3}**FbPd**. Due to the large value of λ in the latter system (table 4.6), there is significant overlap of the Z^- and Y^+ transitions at this field position. (Right) Comparison of the Mims ^{1}H-ENDOR spectrum of ^{3}**ZnZn** acquired at the Y^- field position and the corresponding spectrum for ^{3}**ZnPd**. Akin to the ^{3}**FbPd** system, there is significant overlap of the Z^+ and Y^- transitions due to the large value of λ. All spectra in this figure are acquired on the high-field side of the zero-crossing in the EPR spectra.

behaves almost entirely like the zinc homodimer, ^{3}**ZnZn**, both in terms of the magnitude and the orientation of **D**. In other words, the spin density is less preferentially localised on the zinc half of the molecule *i.e.* it is more accurately described by a prolate spheroid.

This is confirmed by the MPS results in the right of figure 4.16: changing the polarisation gives rise to a clear orientation selection effect which is consistent with a negative D-value. Furthermore, comparison of the ENDOR data for ^{3}**ZnZn** and ^{3}**ZnPd** in 4.17 reveals that the main hyperfine peak is on the left of the Larmor peak. Given that these spectra were acquired on approximately the same transition in the EPR spectrum, the sign of D must be the same in these compounds. The net hyperfine coupling in ^{3}**ZnPd** is larger than in ^{3}**ZnZn** and it is smaller than in the ^{3}**Zn** and ^{3}**Pd** monomer systems. This is in agreement with the incomplete delocalisation obtained using DFT (bottom right of figure 4.15).

The spin polarisation in ^{3}**ZnPd** is primarily out-of-plane (P_Y = 0.88), however, the in-plane component has shifted along the zero-field X axis, whereas in ^{3}**ZnZn** it was along the (in-plane) Z axis. From this perspective, it might be concluded that the Pd^{2+}does have an influence on the ISC mechanism. However, this interpretation is unclear because if the Pd^{2+} were truly involved in the ISC, the effect should be more pronounced in the out-of-plane direction *i.e.* P_Y should be larger than 0.88. Overall, the data sets presented thus far suggest that the spin-orbit effects caused by Pd^{2+} are more pronounced when this heavy metal is either present in both sub-units of the dimer, or if it is placed in combination with a free-base porphyrin.

4.4 Fine and hyperfine structure trends in linear palladium oligoporphyrins

In order to assess the viability of palladium oligoporphyrins as molecular wires, trEPR and Mims ^{1}H-ENDOR measurements were carried out on a series of linear (butadiyne-linked) oligomers with up to

five sub-units. For simplicity, a change in notation is required in this section: the abbreviation $^3\mathbf{Pd}_n$ will be used to denote the oligomers with n units. Note that despite the change of notation, the $^3\mathbf{Pd}_1$ and $^3\mathbf{Pd}_2$ systems are the exact same molecules as $^3\mathbf{Pd}$ and $^3\mathbf{PdPd}$, respectively. Figure 4.18 is a compilation of the trEPR and ENDOR measurements recorded for this series, whereas table 4.7 contains the trEPR simulation parameters.

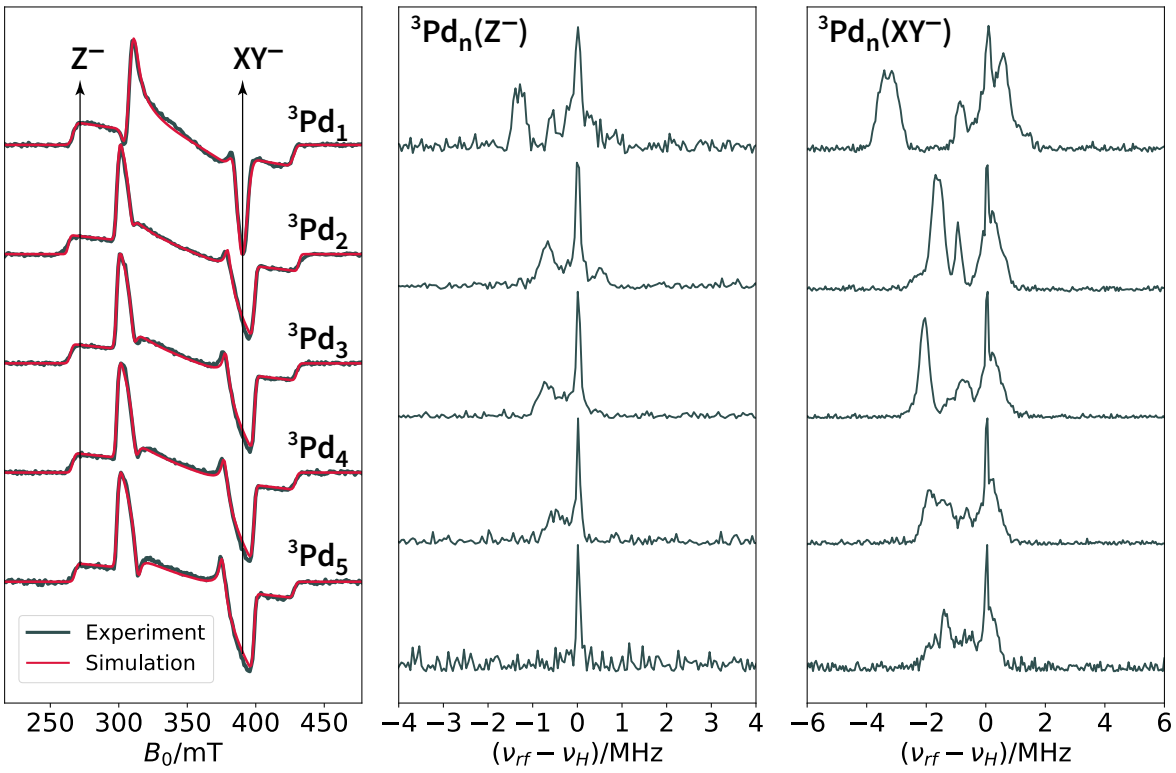


Figure 4.18: (Left) The experimental and simulated trEPR spectra of the linear palladium oligoporphyrins, $^3\mathbf{Pd}_n$. (Center) Mims ^{1}H-ENDOR spectra acquired on the (low-field) Z^- transition for the $^3\mathbf{Pd}_n$ series. (Right) Corresponding Mims ^{1}H-ENDOR acquired on the XY^- transition. Strictly speaking, the X^- and Y^- transition do not overlap as much in the oligomers beyond $^3\mathbf{Pd}_2$, however, the magnitude of the hyperfine couplings measured on either field position around the maximum emissive signal is the same within ±0.5 MHz (*i.e.* the overlap of these transitions is not negligible, and the two **D**-tensor axes are approximately equivalent).

System	D/ MHz	$\lambda = \lvert E/D \rvert$	$P_X : P_Y : P_Z$
$^3\mathbf{Pd}_1$	−2289	0.00	0.00 : 1.00 : 0.00
$^3\mathbf{Pd}_2$	−2362	0.06	0.01 : 0.99 : 0.00
$^3\mathbf{Pd}_3$	−2322	0.07	0.05 : 0.95 : 0.00
$^3\mathbf{Pd}_4$	−2282	0.07	0.03 : 0.97 : 0.00
$^3\mathbf{Pd}_5$	−2242	0.08	0.00 : 0.95 : 0.05

Table 4.7: The best fit values of the ZFS parameters and sub-level populations for the $^3\mathbf{Pd}_n$ series. These parameters give rise to the simulations depicted in figure 4.18. Note that the very small values of the P_X population (and P_Y for $^3\mathbf{Pd}_5$) could be set to exactly zero without any significant change in the quality of the simulation. Thus, there is no change in the populations as a function of the oligomer chain length. Additionally, all of these spectra require a significant shift (relative to g_e) of the g_Y-value which is ca. 1.986 for all oligomers, whilst the other two g-values are very close to the free-electron g-value.

Disregarding the monomer, the trEPR simulation parameters reveal a modest decrease in the magnitude of the D-values with n. For a given consecutive pair of oligomers, $^3\mathbf{Pd}_n$ and $^3\mathbf{Pd}_{n+1}$, the decrease in the D-value is approximately within the error of the spectral simulations. However, the fact that the decrease persists throughout the series, is not within error *i.e.* the change from -2362 MHz in the $^3\mathbf{Pd}_2$ system to -2242 MHz in $^3\mathbf{Pd}_5$ is significant, although it is difficult to quantify the origin of this trend. The conclusion is that the changes in D along this series of oligoporphyrins cannot be interpreted uniquely, whereas for the analogous zinc oligoporphyrins measured by Tait et al. [80], the dipolar only ZFS picture was sufficient to account for the observed trends. The minor increase in the orthorhombicity of the **D**-tensor is also partially mirrored by the trends noted in reference [80] for the zinc oligomers, and hence, it could tentatively be assigned to the SSC contribution to the **D**-tensor.

As noted in the caption to table 4.7, the spin polarisation of the entire $^3\mathbf{Pd}_n$ series is out-of-plane (P_Y-only) within simulation error. This effect is in line with the discussion of the previous sections, whereby the larger SOC due to Pd^{2+} dominates the ISC processes, despite the fact that it does not always influence the ZFS parameters (see the ^{3}**FbPd** and ^{3}**ZnPd** systems).

As noted before, when Pd^{2+} is present in *all* sub-units of the molecular wire, its influence on the D-value obscures the interpretation of the extent of spin delocalisation as far as the ZFS interaction is concerned. Nonetheless, it can be shown clearly that the spin density itself is unaffected by spin-orbit effects, by means of the Mims ^{1}H-ENDOR data in figure 4.18. The hyperfine peaks for either the Z^- or for the XY^- transitions remain on the same (left) side of the Larmor peak, thus confirming the conservation of the negative sign of D for all oligomers. Furthermore, the decrease by a factor of approximately two from $^3\mathbf{Pd}_1$ to $^3\mathbf{Pd}_2$ (highlighted more clearly in figure 4.14) is attributed to complete delocalisation of the spin density over both sub-units of the dimer. The slight increase in the largest hyperfine coupling from $^3\mathbf{Pd}_2$ to $^3\mathbf{Pd}_3$ implies that the spin density is centred on the central unit of the trimer whilst also delocalising partially onto the peripheral porphyrins. Beyond $^3\mathbf{Pd}_3$, there is virtually no change in the magnitude of the hyperfine couplings, indicating that the spin density does not delocalise further than the 2–3 central units of the longer oligomers. The exact same observations and conclusions were drawn from the ENDOR results published by Tait et al. [80] for the analogous zinc oligoporphyrins.

In summary, the distribution of the spin density in either the zinc or palladium oligoporphyrins is identical as far as these particular measurements are concerned. This was also found to be the case in the previous sections. The key difference however between the two series is that the triplet states of the $^3\mathbf{Pd}_n$ oligomers remain out-of-plane spin polarised, whereas the zinc analogues partially lose the out-of-plane polarisation in favour of the vibronically driven in-plane (P_Y) sub-level [80].

4.5 Concluding remarks

Two aspects of spin-orbit effects in photoexcited porphyrin triplets have driven the work presented in this chapter: (1) how the SOC influences the electronic structure of the systems under consideration, (2) how these effects can be exploited to understand molecular wires and guide their design.

The first point was addressed in section 4.2 whereby the monomer systems, ^{3}**Fb**, ^{3}**Zn**, and ^{3}**Pd**, were analysed in detail from the perspective of published and new experimental results, computational methodologies, and group theoretical arguments. It was shown that the CASSCF method leads to a very accurate description of the dipolar part of the ZFS interaction in ^{3}**Fb** and ^{3}**Zn**; these parameters

are invaluable for the interpretation of spin delocalisation in molecular wires. The time-dependent DFT method was also used to quantify the subtle interplay between the ISC mechanisms which produce the different spin polarisations in these systems. The future increase in the ease with which this electronic structure method can be implemented will likely prove to be essential for the description of these fine structure interactions which are ubiquitous in highly delocalised π-systems, such as the triplet states of this work.

Whilst an accurate theoretical description of the D-value in ^{3}**Pd** was not feasible, the group theoretical considerations given in this chapter were crucial. It was shown that the negative sign of D in the ^{3}**Pd** system is entirely encapsulated by the symmetry of the molecule. Furthermore, group theory also allowed the interpretation of the predominantly out-of-plane spin polarisation in all systems containing the heavy Pd^{2+} ion.

The understanding gained about the spin-orbit interaction in the monomer systems facilitated the interpretation of the experimental results for the dimers in section 4.3 and the longer palladium oligoporphyrins in section 4.4. It was found that whenever a Pd^{2+} is present in these oligomers, spin polarisation is predominantly directed to the out-of-plane triplet sub-level. On the other hand, it transpired that, in spite of the intricacies pertaining to the SOC contribution to **D** in palladium porphyrins, the spin delocalisation of the wires is not influenced by the presence of this heavy ion.

All of these findings have also been used throughout this chapter to illustrate the second point raised above regarding the design of molecular wires. The Pd^{2+} ion can be integrated into oligoporphyrin molecular wires as a way of controlling spin polarisation without compromising the delocalisation length of the spin density. For example, it was shown by means of the ^{3}**FbPd** system that it is possible to obtain an almost perfect 'free-base only' spin density, which at the same time, is polarised in the out-of-plane direction (rather than the in-plane polarisation observed for the ^{3}**Fb** system). Similarly, in the longer palladium oligomers, the observed spin density (as quantified by the hyperfine couplings) is almost identical to the analogous zinc oligoporphyrins [80], yet the degree of out-of-plane spin polarisation is significantly enhanced and persistent throughout the entire series.

Chapter 5

The fine-structure of acceptor porphyrin systems

A natural extension of the ideas explored in the previous chapter is the development of methodologies by which the distribution of the spin density can be controlled (*i.e.* not just the spin polarisation). For instance, the introduction of a Pd^{2+} into one of the sub-units of a free-base dimer (*i.e.* the ^{3}**FbPd** system) leads to a preferential out-of-plane spin polarisation, and it also leads to a spin density which is directed preferentially to the free-base side of the molecule. However, it might also be desirable to control the spatial extent of the spin density whilst preserving spin polarisation.

As will be introduced in the next section, one of the proposed schemes for controlling the distribution of the spin density is to alter the electron withdrawing or donating capability of the side groups attached to the porphyrin backbone. If these modifications are introduced in a systematic/well-designed fashion, it should be possible to direct the spin density to certain parts of the molecule whilst preserving the spin polarisation. How such modifications might be achieved, or indeed, how their effects will manifest in EPR experiments have, as of yet, been little explored fields.

In this chapter, these questions are explored by quantifying the trends in fine structure interactions within a series of porphyrin monomers with fluorinated alkyl side groups. This work was carried out in collaboration with Ashley J. Redman, who contributed equally to myself. Furthermore, the work presented in here is presently prepared as a manuscript which will be submitted imminently.

5.1 Context and motivation

The focus of this chapter will be on the five porphyrin systems depicted in figure 5.1 which were synthesised by Erin J. Viere in the group of Prof. Michael J. Therien from Duke University (United States). Each porphyrin system contains a particular distribution of perfluoroalkyl acceptor groups, denoted by **A**, and in three cases, a particular distribution of *meso*-ethyne groups, denoted by **e**.

The fluorinated acceptor groups are known to modulate the electronic structure of the porphyrin core by virtue of their weak π-conjugating ability and strong σ-withdrawing properties [97–100]. Such effects are observed, for instance, in potentiometric measurements which establish that the HOMOs and LUMOs of systems similar to the ones in figure 5.1 are uniformly lowered by ca. 0.15 eV by each

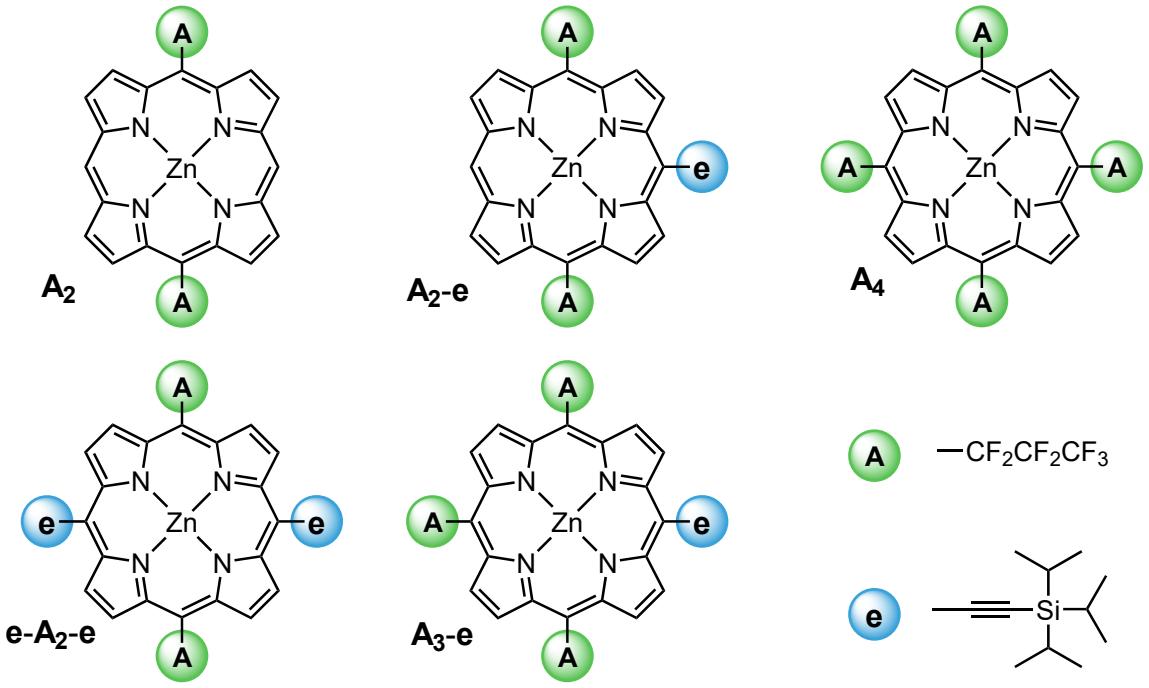


Figure 5.1: Chemical structures of the acceptor substituted porphyrins (denoted $\mathbf{A_2}$, $\mathbf{A_2}$-**e**, $\mathbf{A_4}$, **e**-$\mathbf{A_2}$-**e**, $\mathbf{A_3}$-**e**) investigated in this work.

substitution relative to an analogous meso-aryl porphyrin. As a case in point, the $E_{1/2}^{0/+}$ and $E_{1/2}^{-/0}$ values measured for a tetra(heptafluoropropyl) zinc porphyrin system ($\mathbf{A_4}$) are each 0.67 eV stabilized relative to those determined for the tetra(phenyl) zinc porphyrin benchmark [98]. In certain papers, these findings have been further reconciled with electronic structure calculation such as DFT and its time-dependent variety [100, 101].

By contrast to the fluorinated acceptor groups, the ethyne groups are best regarded as π-acceptors, although this categorisation does not fully capture the properties of these substituents. Apart from providing a versatile bridge for the assembly of longer oligoporphyrin molecular wires, the ethyne groups also influence the symmetry of the triplet state wavefunction, and therefore the extent of spin delocalisation. This was illustrated by Richert et al. [84], in a trEPR and Mims ^{1}H-ENDOR study into the impact of the ethyne groups on the ZFS and spin delocalisation of a series of aryl subsituted oligoporphyrin systems (*i.e.* in the analogues of the structures in figure 5.1 with aryl groups instead of perfluoroalkyl).

In light of these literature findings, three additional avenues are explored throughout this chapter regarding the systems in figure 5.1. Primarily, we would like to establish whether these systematic changes in the number and type of acceptor groups around the porphyrin core are sufficient to realize observable changes in the triplet spin density distributions. This leads to the second question concerning the trends in the ZFS parameters which might be expected amongst these five compounds, and in relation to previously reported ones. And as per the previous chapter, it will also be shown by means of computational results, that the future development of the theoretical methodologies aimed at ZFS calculations will be invaluable for guiding the design of π-conjugated molecular wires.

5.2 Experimental and computational methodology

Sample preparation. Solutions at a concentration of approximately 200 μM in 2-methyltetrahydrofuran were prepared. Prior to preparation, the solvent was passed through a column of activated aluminium oxide to remove any traces of water and peroxides. The solutions were frozen in liquid N_2 before insertion into the spectrometer.

TrEPR measurements. All trEPR experiments were performed on a Bruker ELEXSYS E680 spectrometer at 20 K using a helium gas-flow cryostat in combination with an Oxford Instruments temperature controller. X-band measurements were performed with a Bruker EN 4118X-MD4-W1 resonator and W-band measurements with a Bruker EN 600-1021H TeraFlex resonator. The trEPR experiments were performed in direct detection mode using the transient recorder with a microwave power of 0.2 mW. For W-band measurements, data was collected using a Stanford Research 560 voltage preamplifier with a 3–300 kHz bandpass.

Laser excitation at 532 nm–unless otherwise stated–was performed using an Opotek Opolette HE355 optical parametric oscillator pumped by the third harmonic of a Nd:YAG laser. An excitation energy of ca. 2 mJ for X-/Q-band and 0.6 mJ for W-band was used, at a repetition rate of 20 Hz. The laser power was adjusted through a combination of a Glan-Taylor polariser and a $\lambda/2$ waveplate. For X-/Q-band measurements the laser beam was directed through the optical window of the cryostat into the resonator, whereas, for W-band, the laser beam was directed to the top of the sample *via* an optical fibre inserted into the sample holder. After the last turning mirror, light was depolarised using an achromatic depolariser.

MPS experiments. The experiment was performed according to the X-band trEPR protocol. Light at various wavelengths from the OPO was polarised vertically or horizontally (relative to the applied magnetic field) using a combination of a $\lambda/2$ waveplate and a polariser. The exact same methodology was employed for the MPS experiments presented in the previous chapter.

Pulse EPR measurements. The echo-detected field sweeps and ENDOR measurements were carried out on the same spectrometers and resonators as detailed above. For Q-band, the Bruker ELEXSYS E580 spectrometer was used in conjunction with a Bruker EN 5107D2 resonator. Mims ENDOR measurements (at either 20 K or 5 K) were performed with the pulse sequence: laser pulse – $\frac{\pi}{2}$ – τ – $\frac{\pi}{2}$ – T – $\frac{\pi}{2}$ – τ – echo, with m.w. pulse lengths of 16, 52, and 52 ns for X, Q and W-band, respectively. The mixing time, T, had lengths of 15, 24, and 42 μs at X, Q, and W-band, respectively. The ENDOR spectra at each field position were recorded using several τ values (120, 180, 240 ns) and summed during post-processing. Note: the X-band ENDOR spectra presented here were acquired analogously to the ones reported in the previous chapter.

Electronic structure calculations. All property calculations were performed using the ORCA 4.1.2 program. Single point energy and EPR property calculations for the excited triplet state were performed on structures optimised by DFT. Structures were optimised to the ground singlet state geometry in Turbomole V6.1, using the B3LYP functional and def2-TZVP basis set in combination with the RI approximation. A second optimisation to the triplet state using the B3LYP functional together with the def2-TZVP basis set was performed in ORCA, unless otherwise stated.

EPR parameter calculations for hyperfine couplings and zero-field splittings were performed using the B3LYP functional and the 6-31G(d) basis set for zinc and EPR-II for all remaining nuclides. For the zero-

field splitting parameters, only the spin–spin coupling contribution was considered using the spin-unrestricted natural orbital (UNO) approach.

EPR parameters were also calculated using CASSCF, considering an active space of four electrons and four orbitals, CAS(4,4), using the def2-SVP basis set and def2-TZVPP for zinc. The initial active space orbitals were selected by visual inspection following a restricted open-shell Hartree–Fock (ROHF) calculation.

5.3 Results and discussion

5.3.1 Transient EPR

Figure 5.2 shows the frozen solution trEPR spectra of the acceptor porphyrin systems measured at X-band and W-band microwave frequencies following photoexcitation with a laser pulse at a wavelength of 532 nm. The reason for acquiring the spectra at both frequencies is that after the initial measurements at X-band were obtained, it was noted that the spectra were slightly asymmetric with respect to the barycenter. Hence, W-band measurements were necessary to confirm that the **g**-anisotropy in these systems was indeed significant. The parameters used to obtain the (global) simulations depicted in red in figure 5.2 are displayed in table 5.1.

	D / MHz	λ	g_x	g_y	g_z	P_X	P_Y	P_Z
$\mathbf{A_2}$	−1017	0.33	2.0033	2.0033	2.0003	0.00	0.81	0.19
$\mathbf{A_2}$**-e**	+1033	0.26	2.0041	2.0038	2.0006	0.00	0.10	0.90
e-$\mathbf{A_2}$**-e**	+1074	0.10	2.0034	2.0040	1.9989	0.10	0.00	0.90
$\mathbf{A_3}$**-e**	+1000	0.21	2.0039	2.0037	2.0017	0.00	0.05	0.95
$\mathbf{A_4}$	+967	0.31	2.0035	2.0032	2.0021	0.00	0.22	0.78

Table 5.1: TrEPR simulation parameters: g-values, ZFS parameters (D and λ) and relative sub-level populations (P_X, P_Y, P_Z). The parameters were extracted from a global simulation of the spectra shown in Figure 5.2. The assignment of a negative D-value for $\mathbf{A_2}$ is discussed in detail in the main text.

In many respects, the spectral signature of these acceptor porphyrins seems typical for a photogenerated porphyrin triplet state. However, inspection of table 5.1 reveals the assignment of a negative sign to the D-value of $\mathbf{A_2}$. This assignment–which will be validated in the next section– is as unexpected as it is important for the conclusions of this investigation. Throughout the remaining discussion, the parameters in table 5.1, with particular emphasis on the outlier ($\mathbf{A_2}$), will be justified and interpreted.

For all systems except $\mathbf{A_2}$, the spectra in figure 5.2 display the archetypal polarization pattern, *AAAEEE*, specific to many zinc-porphyrin triplet states [83]. As described in previous EPR work [49, 73, 80] and in the previous chapter, the D-value of monomeric zinc porphyrin systems has been determined to be positive, and thus this polarization pattern is assigned to the preferential population of the out-of-plane triplet Z sub-level, as highlighted by the values in table 5.1.

At W-band microwave frequencies, the enhanced g-value resolution further facilitates the discussion of the subtle effects observed in these porphyrin systems. The asymmetry of the W-band spectra in figure 5.2 relative to the X-band spectra is indicative of an anisotropic **g**-tensor, which is quantified by the simulated g-values reported in table 5.1. In a zinc porphyrin monomer, ISC from the excited singlet state into the observable triplet state has been shown in the previous chapter to be dominated by a direct

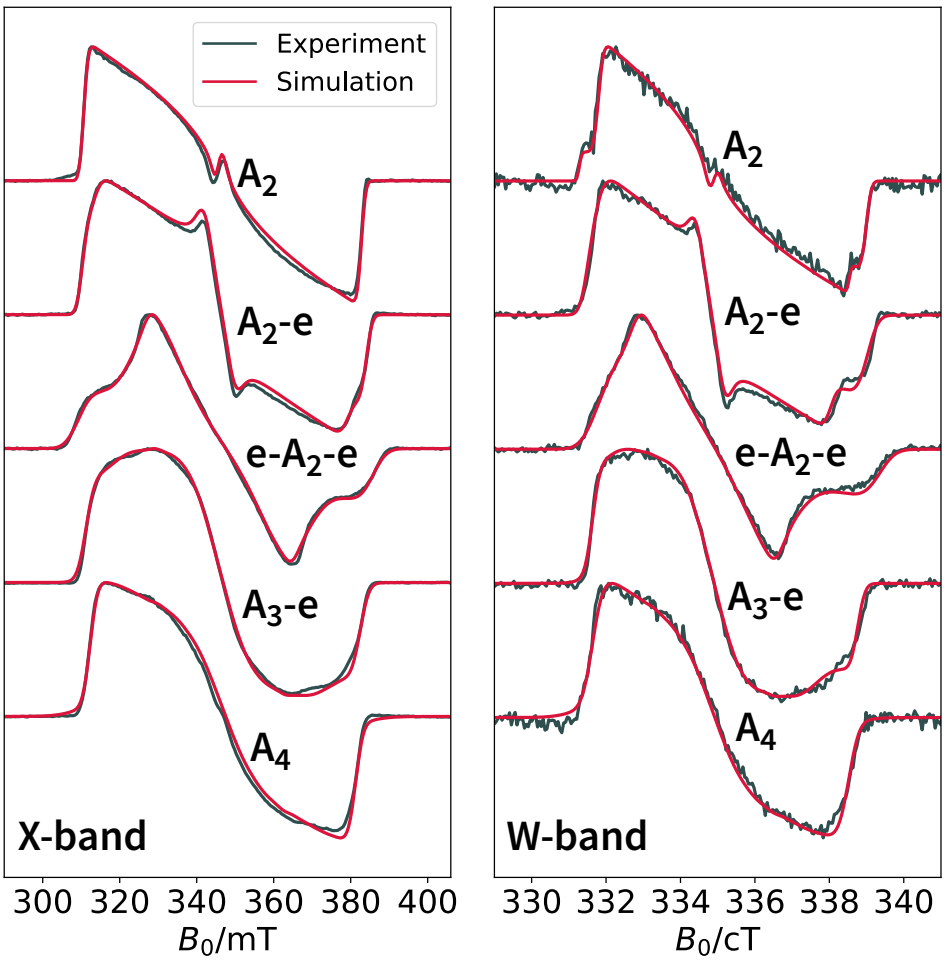


Figure 5.2: Experimental frozen solution trEPR spectra of $\mathbf{A_2}$, $\mathbf{A_2}$-**e**, **e**-$\mathbf{A_2}$-**e**, $\mathbf{A_3}$-**e**, and $\mathbf{A_4}$(black) recorded at 20 K at X- and W-band microwave frequencies. The spectral simulations obtained using the parameters in Table 5.1 are shown in red. Note: the experimental spectra are the average obtained over a 1 μs time window following the laser pulse (at a wavelength of 532 nm). Note that the units of the magnetic field axis in the right panel for the W-band data have been changed to cT (centitesla).

SOC interaction. More concretely, non-zero spin-orbit matrix elements arise from a mixing of zinc d-orbitals with the porphyrin π-orbitals, resulting in a preferential population of the out-of-plane triplet manifold. Since the shifts in the g-values are also a result of perturbations due to spin-orbit coupling, we expect a correlation between the sub-level populations and the g-values. For a typical zinc porphyrin monomer, the g_z-axis and the ZFS Z-axis are collinear and perpendicular to the porphyrin plane. As a result, the triplet Z sub-level is preferentially populated, as is indeed observed in the simulation parameters in table 5.1 for all systems except $\mathbf{A_2}$. For the latter, the observed preferential population of the Y sub-level is in line with a reorientation of the **D**-tensor (D-value sign inversion), such that the Y-axis is now oriented perpendicular to the porphyrin plane.

Overall, the D-values show a modest trend of decreasing magnitude with an increasing number of acceptor groups,[1] whereas the λ-values display no obvious trend. In systems with such complex symmetries, the interpretation of the data cannot solely rely on the link between the D-value and the

[1]For clarity, by comparing a system with more acceptors than another system (*e.g.* $\mathbf{A_4}$ *versus* $\mathbf{A_3}$-**e**), the former will have a smaller D value than the latter. This statement is ambiguous, because, as will become clear, not all pairs of systems are directly comparable.

spheroidal symmetry of the spin density (see section 3.3.3). For example, in reference [84], Richert et al. employ group theory in conjunction with the dipolar picture for ZFS to interpret the decrease in D between a pair of **Ar$_2$-e** and **e-Ar$_2$-e** systems (and similar trends amongst other *meso*-aryl porphyrins);[2] their arguments assume, on account of the relatively axial symmetry of the measured **D**-tensor, that a spheroidal representation of the spin density is sufficient.

However, in the case at hand, there is an increase in D from **A$_2$-e** to **e-A$_2$-e**, contrary to the *meso*-aryl analogues considered by Richert et al. in reference [84]. This observation does not invalidate the framework proposed in this latter reference, yet it highlights that the behaviour of these acceptor substituted porphyrins requires more careful considerations. For example, the fact that λ is close to 1/3 in **A$_2$-e** whereas it is 0.10 in **e-A$_2$-e**, will drastically obscure the interpretation of the D-value in terms of spheroidal densities. This is because as $\lambda \longrightarrow 1/3$, then $|D_Z| - |D_Y| \longrightarrow 0$, and hence, the axis of maximum dipolar coupling (D_Z) is ill-defined (it could be redefined as anything in between the canonical D_Z and D_Y). This means that the spheroidal symmetry of the spin density is far from being a valid presumption. In summary, whilst the D-values for all acceptor porphyrins (and the **D**-tensor in general) still originate in the dipolar only picture, the spin density is not spheroidal,[3] and thus, the trends are difficult to predict or interpret using the same arguments that have been employed throughout the porphyrin triplet state literature (see [83] for a review).

Furthermore, predictions of an 'oblate' to 'prolate' symmetry transition, associated with a change in the sign of the D-value, should be accompanied by a significant magnitude change (due to the $1 - 3\cos^2\theta$ term in equation 3.47). However, as is outlined in the magnetophotoselection section below, the experimental data point with some clarity towards a negative D for **A$_2$**, although this assignment is tentative. Yet, an associated change in $|D|$, as would be expected from a spheroidal symmetry, is clearly not observed (table 5.1). As such, the complicated behaviour of the D- and E-values in these molecules is endemic to all the species in figure 5.1. These complications are most likely a consequence of the distortions in geometry induced by the σ-withdrawing effects of the *meso*-perfluoro groups; this conjecture is supported by electronic structure calculations.

5.3.2 Magneto-photo-selection

We now turn our attention to a more detailed investigation of the sign of D. Figure 5.3 and table 5.2 depict the MPS data and corresponding simulation parameters for the **A$_2$** and **A$_2$-e** systems. Due to the complications in interpretation mentioned above, it was necessary to simulate the MPS data explicitly rather than rely on arguments based on qualitative changes in the appearance of the spectra. This was particularly important for the **A$_2$** system; it can be seen in figure 5.3 that the MPS effect is not particularly pronounced at either excitation wavelength, particularly so at 570 nm. However, the MPS effect *is* present, and importantly, from simulations we can deduce that the data is consistent with a negative D-value for **A$_2$**, and hence, with a D_Z axis reoriented relative to **A$_2$-e**.

The simulations were obtained by employing the same assumptions which were implemented in section 4.2.3, with one (minor) modification: in the cases investigated here, the two porphyrin optical moments (denoted Q_1 and Q_2 in figure 5.3) were included explicitly. For the **^{3}Pd** system discussed in the previous

[2] Note that the notation '**Ar**' refers to aryl groups rather than the fluorinated acceptor groups (**A**) under consideration here.

[3] As will be shown in the final discussion section of this chapter.

System	$\alpha(Q_1)$	$\alpha(Q_2)$	$\beta(Q_1)$	$\beta(Q_2)$
$\mathbf{A_2}$	0.4°	90°	−22°	22°
$\mathbf{A_2}$**-e**	74°	74°	−3°	87°

Table 5.2: Parameters used for the simulation of the MPS data shown in figure 5.3. α and β represent the orientation of the transition dipole moments, Q_1 and Q_2, relative to the **D**-tensor axes. The exact definition of α and β for a given Q_i is as depicted in figure 3.6 in Chapter 3. The approximate orientations of Q_1 and Q_2 relative to the **D**-tensor are also shown in figure 5.3.

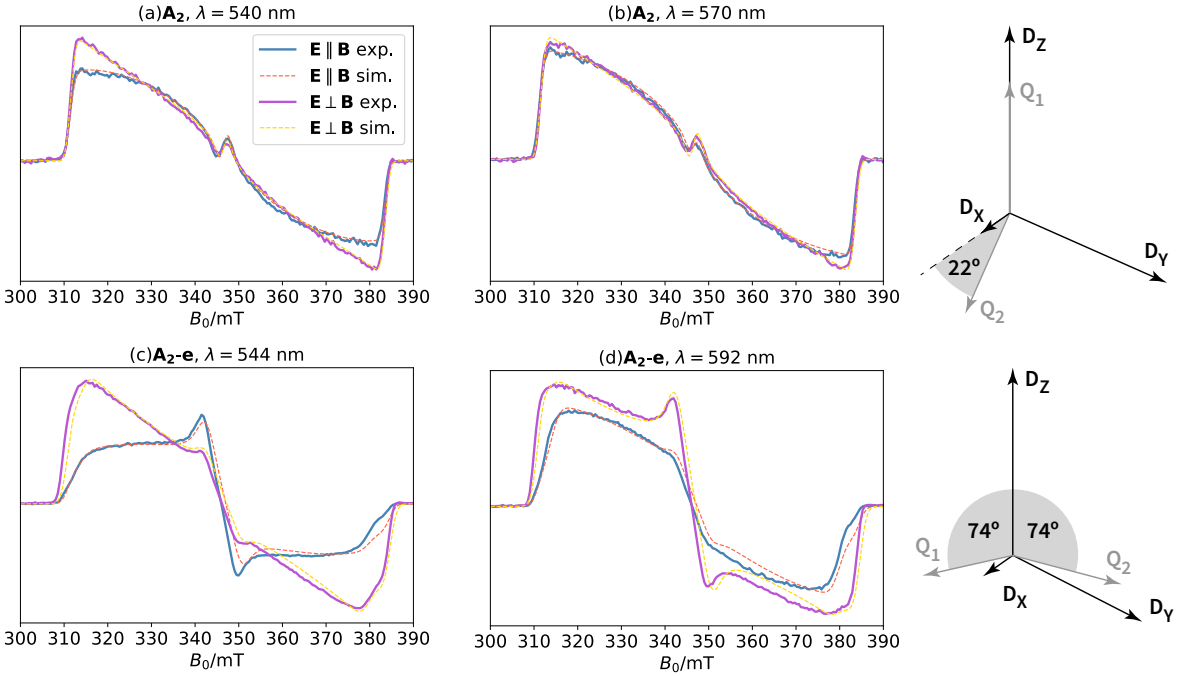


Figure 5.3: Experimental and simulated MPS spectra recorded for $\mathbf{A_2}$ (top) and $\mathbf{A_2}$**-e** (bottom). The laser wavelengths specified in each panel correspond to absorptions in the optical Q-band region of these porphyrins. The approximate relative orientation of the two perpendicular optical vectors, $\mathbf{Q}_1$ and $\mathbf{Q}_2$, relative to the axes of the **D**-tensor are shown adjacent to the MPS spectra as obtained by least square fitting with the *pepper_MPS* function. The assumption that $Q_1 \perp Q_2$ is based on similar symmetry arguments as mentioned in the previous chapter (section 4.2.3). The complete set of angles obtained in the fitting is given in table 5.2. MPS measurements for the other systems have been attempted, however, the data could not be analysed due to a lack of clear intensity changes.

chapter, the simulations were sufficiently accurate by simply assuming one *average* transition dipole moment at each wavelength.[4]

Whilst the MPS results presented here seem to indicate that $D > 0$ for $\mathbf{A_2}$**-e** and $D < 0$ for $\mathbf{A_2}$, there is still the question of the uniqueness of this assignment of the signs of D. More precisely, the MPS simulations shown here do not actually constitute sufficient proof for the statement that $D < 0$ in $\mathbf{A_2}$ because the MPS effect is small in this system, and because the **D**-tensor is significantly orthorhombic. For the $\mathbf{A_3}$**-e** system, the fitting results are less ambiguous because the experimental MPS effect is more pronounced and the **D**-tensor is less orthorhombic ($\lambda = 0.21 < 1/3$) compared to $\mathbf{A_2}$. Nonetheless, in

[4]This is likely a result of the fact that the palladium porphyrins of the previous chapters have a very small orthorhombicity, and the porphyrin backbones are approximately flat. Hence, whether two optical moments or a single net optical vector are considered, makes little difference.

spite of this issue, the simulations in figure 5.3 do still show that the data is *consistent* with $D < 0$ for $\mathbf{A_2}$.

A more extensive series of MPS simulations (which address the issue raised above about the uniqueness of the fitting) have been performed by Ashley J. Redman, and will be published as part of the paper which resulted from this work (joint first authorship between myself and Mr. Redman). These additional simulations will not be shown here, however, they do indicate that simulations with a negative D-value for $\mathbf{A_2}$ are more suitable for describing the MPS effects depicted in figure 5.3.

The fact that $\lambda \approx 1/3$ for $\mathbf{A_2}$ is a much more consequential observation *cf.* the observation that $D < 0$. This large orthorhombicity is the main reason for the complications encountered in the MPS simulations for this system. Furthermore, $\lambda \approx 1/3$ implies that the spin density is neither a prolate nor an oblate spheroid in the $\mathbf{A_2}$ system. Had the orthorhombicity not been quite so large, we might have been able to claim that the *meso*-perfluoro groups in $\mathbf{A_2}$ are withdrawing the spin density away from the porphyrin core, resulting in a prolate distribution, and thus a negative D-value.

5.3.3 Mims ENDOR

ENDOR experiments were carried out on this series of acceptor substituted porphyrins with two aims: (1) to seek confirmation (or refutation) of the sign of D in $\mathbf{A_2}$ relative to the other systems, (2) to understand the effects of the *meso*-perfluoro groups on the spin density. The resulting Mims ENDOR data is shown in figure 5.4 together with the field position at which the data was collected (relative to the trEPR spectra) and the corresponding spherical density plots obtained using the *orisel* function in EasySpin. Measurements at other field positions were also carried out, however, the absence of clear hyperfine peaks precluded any further analysis.

All data sets contain a Larmor peak corresponding to the ^{19}F nuclei (at ca -1 MHz) additionally to the expected Larmor peak of ^{1}H. The assignment of the hyperfine peaks to the individual nuclei is not possible directly from the data shown in figure 5.4; this was achieved using a deconvolution of a series of multifrequency Mims ENDOR measurements (X-, Q-, W-band), and the data and interpretation is shown in figure F.5 of appendix F. The largest hyperfine couplings in all cases have been determined to belong to protons (grey shaded region) and, in each case, it was also established that there exists a non-zero hyperfine coupling to the ^{19}F nuclei. However, the Gaussian deconvolution shown in the appendix is rather approximate and the assignment of the peaks in the blue shaded region to ^{19}F hyperfine couplings is only tentative.

The fact that non-zero ^{19}F couplings are observed for all species indicates that there could be a small degree of delocalisation of the triplet spin density onto the *meso*-perfluoro groups. However, given their small magnitude (less than 1 MHz) and the fact that they remain virtually unchanged throughout the series,[5] it is not possible to claim with any certainty that these couplings do not originate in a purely dipolar –through space– hyperfine interaction. This through space interaction would be present even if the spin density were completely localised on the porphyrin core.[6]

With regard to the ^{1}H couplings, these are also approximately unchanged throughout the series. The minor shifts in frequency of the peaks in the grey shaded region are not sufficient to claim that there

[5] except perhaps for **e**-$\mathbf{A_2}$-**e**.

[6] Which will be shown to be the case in the next section.

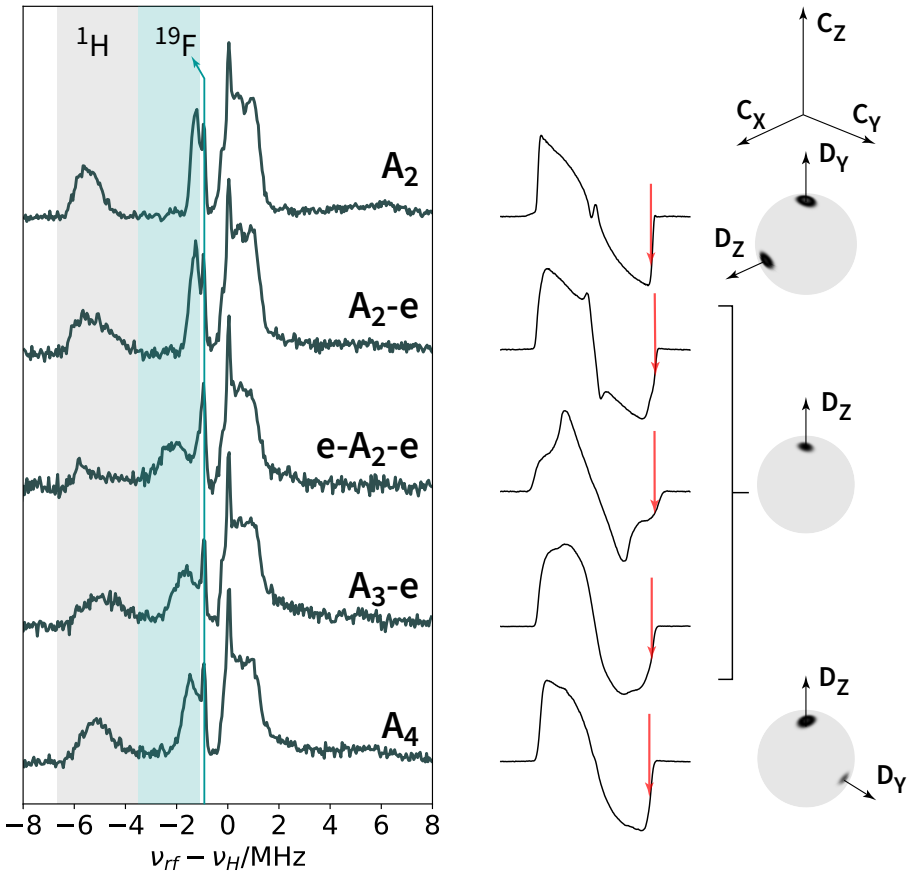


Figure 5.4: X-band Mims ^{1}H-ENDOR spectra of the acceptor porphyrins. The spectra were acquired at the field positions indicated with a red arrow relative to the trEPR spectra which are depicted adjacent to each ENDOR spectrum. The spherical density plots depict the orientations of the magnetic field relative to the **D**-tensor axes which are resonant at those field positions. All spherical densities are defined with respect to the same right-handed Cartesian frame which comprises the C_X, C_Y, C_Z axes shown in the topmost diagram. The D-value was assumed to be negative for $\mathbf{A_2}$, hence the swap of the **D**-tensor labels for this system. Taking the $\mathbf{A_4}$ system as example, the interpretation of these spherical density plots is as follows: the darker shaded areas correspond to the orientations of the magnetic field which are aligned either with D_Z or D_Y, hence, the field position indicated by the red arrow corresponds to a ZY transition. The interpretation can be done analogously for the other systems. The gray and blue shaded regions in the ENDOR graph are used to indicate the nucleus to which the largest hyperfine peaks belong (note that this assignment of the ^{19}F couplings is problematic and should be viewed only as a guide – the important point is that the ^{19}F couplings are very small). The Larmor peak of ^{19}F is indicated with the blue vertical line.

is a depletion of spin density on the porphyrin. In fact, these ^{1}H hyperfine couplings have a magnitude which is on average larger than for the meso-aryl analogues which have been reported in the literature (*e.g.*[73, 80, 84]), as well as in the previous chapter (figure 4.9). If the *meso*-perfluoro groups were to truly withdraw a non-negligible portion of the π spin density *through* the bond (*i.e.* increasing the Fermi-Contact interaction of ^{19}F) then the porphyrinic protons should not experience a larger hyperfine coupling than they would in a *meso*-aryl porphyrin. These protons should then experience a noticeably smaller hyperfine interaction, which they clearly do not. This observation further confirms that the attribution of the ^{19}F hyperfine peaks to a dipolar effect is more likely than a Fermi-Contact (delocalisation) effect.

Regarding the **D**-tensor in the $\mathbf{A_2}$ species, this molecule is in an orthorhombicity regime in which it is impossible to infer the sign of D or orientation of **D** from ENDOR. This is illustrated by the spherical density plots in figure 5.4, whereby for $\mathbf{A_2}$ both the canonical Z and Y orientations resonate in an almost equal measure at the indicated field position. Attempts at measurements of only the 'pure' Z transition have been unsuccessful, because $\lambda \approx 1/3$ for this system. Similarly to $\mathbf{A_2}$, the $\mathbf{A_4}$ species also has a large orthorhombicity ($\lambda = 0.31$) and thus, the ENDOR spectrum is comprised of an overlap between the canonical Z and Y orientations of the magnetic field relative to **D**.

However, for the middle three −ethyne containing −species in figure 5.4 ($\mathbf{A_2}$-**e**, **e**-$\mathbf{A_2}$-**e**, $\mathbf{A_3}$-**e**), the following three points help to establish that $D > 0$ in these systems: (1) only the Z canonical orientation contributes to these ENDOR spectra, (2) all ENDOR spectra are acquired on the high-field side of the barycenter of the trEPR spectrum, (3) all hyperfine peaks are on the left of their corresponding Larmor peaks. The reason why these points are sufficient to prove that $D > 0$ in these three molecules is because the exact same observations are true for the ^{3}**Zn** system (for which $D > 0$) discussed in the previous chapter and in references [49, 73, 80].

The only assumption made in the reasoning of the previous paragraph is that the sign of the hyperfine couplings is preserved in these systems relative to the reference ^{3}**Zn** system. This assumption is supported by the fact that the MPS data for $\mathbf{A_3}$-**e** (figure 5.3) implies that $D > 0$ in this system. Because of this, and because the hyperfine peaks measured on a high-field Z transition for $\mathbf{A_3}$-**e** remain on the same side of the Larmor peak when compared to the analogous ^{3}**Zn** data, imply the conservation of the sign of the hyperfine couplings between $\mathbf{A_3}$-**e** and ^{3}**Zn**.

In summary, the ENDOR data is not sufficient to determine the orientation of **D** for $\mathbf{A_2}$ and $\mathbf{A_4}$. However, the ENDOR spectra of the other systems are consistent with a positive D-value.

5.3.4 Electronic structure calculations

In order to understand the experimental EPR results presented above, quantum chemical calculations were performed using the DFT and CASSCF methods as per section 5.2. The results are depicted as the DFT and CAS(4,4) spin densities in figures 5.5 and 5.6, as well as the numerical values given in table 5.3.

	Experimental		DFT		CASSCF		$R_\perp$	
	D / MHz	$\lvert E/D \rvert$	D / MHz	λ	D / MHz	λ	/Å	#**e**/#**A**
$\mathbf{A_2}$	−1017	0.33	−863	0.16	939	0.29	0.1116	0
$\mathbf{A_2}$-**e**	1034	0.26	−824	0.18	936	0.28	0.0864	0.5
e-$\mathbf{A_2}$-**e**	1074	0.10	575	0.17	976	0.29	0.0479	1
$\mathbf{A_3}$-**e**	1000	0.21	594	0.18	862	0.10	0.1489	$0.\dot{3}$
$\mathbf{A_4}$	967	0.31	−725	0.14	739	0.25	0.3336	0

Table 5.3: A comparison of the experimental ZFS parameters with results from quantum chemical calculations using the DFT and CASSCF methods is given in the first two columns. The next column shows the mean perpendicular distance, $R_\perp$, from the best fit plane derived from the porphyrin core to the atoms of the porphyrin core (*i.e.* excluding the side groups). The last column is the ratio of ethyne to acceptor groups for each system. Computational details are given in section 5.2.

The most striking conclusion that arises from these electronic structure calculations is that, apart from **e**-$\mathbf{A_2}$-**e**, the spin densities of all these species are very different from the spin densities encountered

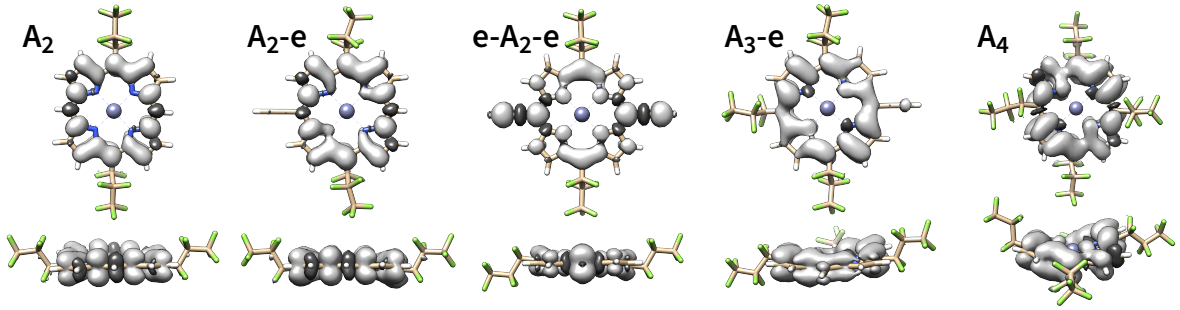


Figure 5.5: Visualization of the spin density distributions of the photoexcited triplet states for the five perfluoroalkyl substituted porphyrins obtained from a DFT calculation. For each species, the spin density is shown from two perspectives: along the molecular z-axis and along an 'in-plane' axis in the top and bottom rows, respectively.

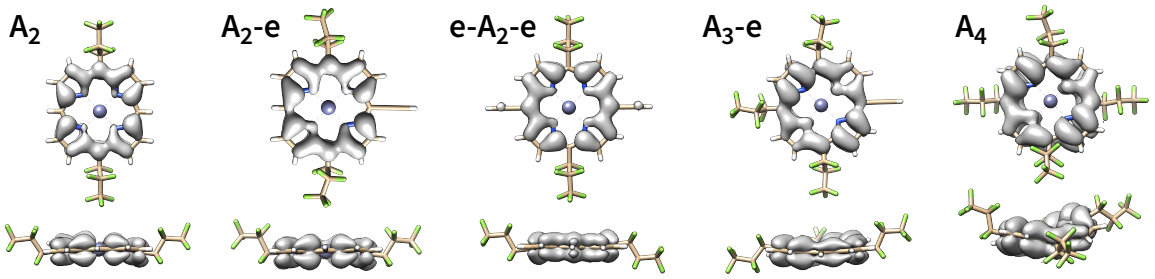


Figure 5.6: The CAS(4,4) predicted spin densities for the lowest energy triplet root of the five species investigated in this chapter.

in the –more usual– *meso*-aryl subsitituted porphyrin monomers (see figures 4.3, 4.5, and 4.10). A first indication as to the origin of these changes in spin density can be gained by inspection of the values of $R_\perp$ in table 5.3. This quantity is obtained by fitting a plane to the atoms which comprise the porphyrin backbone and evaluating the mean displacement (perpendicular distance) of the atoms from the resulting plane. In essence, $R_\perp$ is a measure of the deviation of the porphyrin skeleton from planarity, and it can also act as a guide for the orthorhombicity of the spin density.[7]

It is clear that **e-A$_2$-e** has the lowest value of $R_\perp$ and the lowest experimental value of λ. Furthermore, the experimental values of D and λ for **e-A$_2$-e** are also the closest to the ones observed in typical porphyrin molecules (such as ^{3}**Fb** and ^{3}**Zn**) which are also flat/planar. By contrast, all other systems, **A$_2$**, **A$_2$-e**, **A$_3$-e**, **A$_4$**, are significantly non-planar, and hence the observed values of λ are significantly larger than for **e-A$_2$-e** (or, indeed, compared to λ measured for typical *meso*-aryl porphyrins).

The $R_\perp$ parameter is clearly not sufficient to capture all the minute changes in the observed values of λ, it only captures the overall trend. In a different analysis method, one might suspect a correlation between the experimental value of λ and the ratio between the acceptor groups and the ethyne groups. As can be seen in table 5.3, the **A$_2$** and **A$_4$** species have the largest experimental λ values and the lowest #**e**/#**A** ratios. Similarly, **e-A$_2$-e** has the largest #**e**/#**A** and the lowest orthorhombicity. The **A$_2$-e** and **A$_3$-e** systems have an intermediate value of #**e**/#**A** (between 0 and 1) and an intermediate value of

[7] We emphasize that it is only a 'guide' for orthorhombicity. There is no reason to believe that there should be a simple one-to-one correspondence between the values of λ and $R_\perp$. However, in the absence of a better measure, $R_\perp$ is good enough for the purposes of this investigation.

λ. However, based on the #**e**/#**A** ratio alone, $\mathbf{A_2}$-**e** should have a smaller λ compared to $\mathbf{A_3}$-**e** (to be consistent with the trends observed for the other systems). And thus, the #**e**/#**A** ratio alone is not a sufficient criterion for describing the trends in ZFS parameters, just as the $R_\perp$ value is also not a good enough criterion. Nonetheless, it cannot be completely denied that both #**e**/#**A** and $R_\perp$ could be used as qualitative descriptors for the expected trends in λ.

In spite of all these complications, it can be said that: by comparing any two systems, if one of them has a (strictly) larger #**e**/#**A** ratio, then it will also have a smaller $R_\perp$ value.[8] This observation is entirely justified by the well documented properties of fluorinated alkyl chains, as found in countless organic chemistry textbooks. These perfluoro groups are σ-electron withdrawing groups *i.e.* they alter the σ bonding network of the porphyrin backbone, and induce deviations from planarity. In a different perspective, a σ-acceptor group will strive to turn a planar trigonal sp^2 center into a tetrahedral sp^3 center (hyperconjugation).

As a proof of principle, figure 5.7 shows a comparison of the geometries, spin densities, and DFT computed ZFS parameters for the triplet states of propene and 3,3,3-trifluoro-propene. It is obvious from this figure that the spin density is withdrawn away from the π-system by a small fraction (less than 0.5%) more in the presence of the trifluoro-methyl group compared to the methyl group. Also, the carbon centers of the double bond are less planar in the fluorinated analogue of propene. Finally, the D-value[9] decreases by a small amount because the average interspin distance is marginally larger in 3,3,3-trifluoro-propene *cf.* propene, whilst the λ-value increases slightly with fluorination. If the CF_3 group of the 3,3,3-trifluoro-propene molecule were to be replaced by longer fluorinated alkyl chains, the ruffling of the σ framework is bound to become more pronounced; therefore, the accompanying increase in λ will become larger and obscure the interpretation of the D-value.

By analogy with propene, the porphyrin π system responds to this ruffling of the σ bond framework, and provided the number of fluorinated groups is not too large, it will maintain its relatively flat structure (for which the overlap of the p-orbitals is maximised). In the $\mathbf{A_2}$ and $\mathbf{A_4}$ species, the number of fluorinated groups is large and uncompensated by the π-conjugating ethyne groups which strive to re-planarise the porphyrin backbone, hence these species have the largest deviations from planarity. All of these qualitative arguments are illustrated most clearly by comparing **e**-$\mathbf{A_2}$-**e** and $\mathbf{A_2}$: the two ethyne groups in the former are entirely sufficient to cancel the effects of the acceptor groups in the latter.

Another aspect which arises from an inspection of the spin density plots in figures 5.5 and 5.6 is that, within error, the π spin density in these triplet states does not delocalise onto the *meso*-perfluoro groups. All spin densities are centred on the porphyrin core. Some of the backbones are distorted, *e.g.* $\mathbf{A_4}$, however, this only affects the symmetry of the spin density and the orthorhombicity of the **D**-tensor (any changes in the net D-value will be minute, as observed).

With regards to the calculated D and λ values, it is clear from this chapter as well as from the previous chapter that the DFT derived spin density does not give good agreement with the experimental ZFS parameters. The sign of the DFT predicted D-value is incorrect in $\mathbf{A_2}$-**e** and $\mathbf{A_4}$, and the magnitude of D is also erratic and unreconcilable with experiment for any of the oligomers. On the other hand, the CASSCF results seem to give a better representation for the trends in the magnitudes of the D-values,

[8] This cannot be applied to a comparison between $\mathbf{A_2}$ and $\mathbf{A_4}$, because these two systems have the same #**e**/#**A** ratio.
[9] Which is negative because the π-system of propene resembles a prolate spheroid.

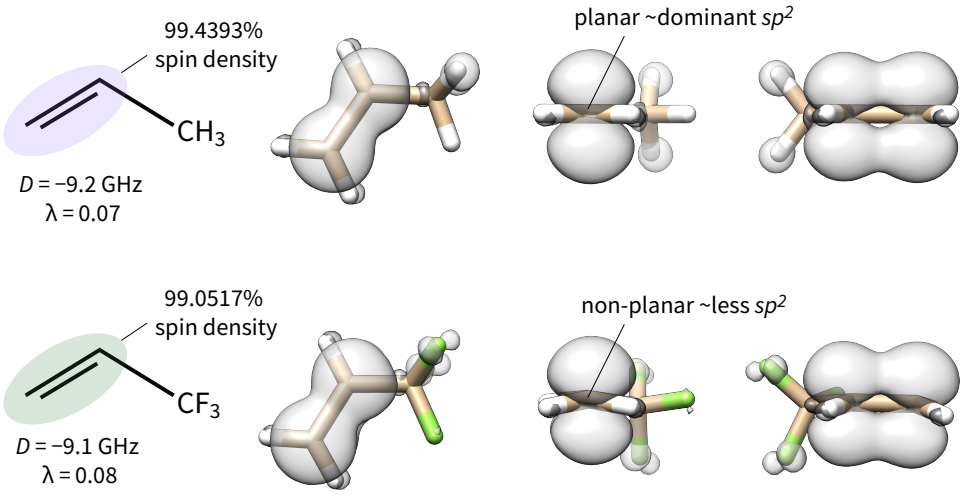


Figure 5.7: Geometries, triplet spin densities, and ZFS parameters of propene (top) and 3,3,3-trifluoropropene (bottom). The calculations were performed in ORCA using the B3LYP functional in combination with the def2-SVP basis set. The spin densities are shown from three perspectives: (left) from above/below the double bond, (middle) side view such that the vinyl end is pointing out of the plane of the paper, (right) side view such that the *cis*-protons are pointing out of the plane of the paper. The perspective on the left shows that the in-plane allylic proton/fluorine center has a greatly reduced spin density compared to the other two allylic centers (because the σ bond is perpendicular to the π-bond when the C–H or C–F bond is in-plane with the double bond). The other two perspectives highlight the enhanced non-planarity of the vinylic carbon atoms in the fluorinated *versus* non-fluorinated species.

albeit the sign of D for $\mathbf{A_2}$ is incorrect. This latter inconsistency in the sign of D for $\mathbf{A_2}$ is, nonetheless, an acceptable error. The CASSCF calculation underestimates the orthorhombicity of the **D**-tensor in this system (λ = 0.29 versus 0.33 in experiment), and hence, the D-value appears positive.[10]

It is however important to note that not all the ZFS parameters predicted by means of these CAS(4,4) calculations are reasonable. Particularly worrying is the fact that the predicted value of λ for $\mathbf{A_2}$ is the same as the one for **e-A$_2$-e** in spite of the vastly different geometries. In summary, the same picture emerges as was found in the previous chapter: the CAS(4,4) calculations are encapsulating the behaviour of the dipolar contribution to D much better than the DFT calculations, despite the fact that the results are not perfect. Whilst it was a step forward when it was found in Chapter 4 (table 4.2) that a CAS(4,4) calculation can reproduce the experimental D-values for ^{3}**Fb** and ^{3}**Zn** to within a few MHz, it is now evident that more work is required on the theoretical front. As far as this project is concerned, the results obtained thus far have been sufficient to understand these acceptor systems in a semi-quantitative manner. However, the predictive value of the electronic structure calculations performed here will continue to remain somewhat questionable until these computational methods become more versatile.

5.4 Concluding remarks

At the outset of this chapter, one of the open ended questions posed was regarding the possibility of using these *meso*-perfluoro groups to achieve control of the spin density distribution in porphyrin

[10]This discrepancy in sign is less easily overlooked in the DFT results, for which $\lambda \ll 1/3$, and hence there should be no issue of degeneracy in the eignvectors of the **D**-tensor.

molecular wires. By investigating the fine-structure interactions of the monomer species $\mathbf{A_2}$, $\mathbf{A_2}$-**e**, **e**-$\mathbf{A_2}$-**e**, $\mathbf{A_3}$-**e**, and $\mathbf{A_4}$, it was shown that these acceptor groups cause the spin density to become orthorhombic without any discernible delocalisation of the spin density away from the porphyrin core. These findings do not invalidate the prospect of using these perfluoro acceptor groups in the design of hetero-dimeric (or even longer) oligoporphyin molecular wires.

However, if EPR spectroscopy is to be used to investigate the extent of spin delocalisation, or the extent to which a control of the spin density was achieved in such novel systems, care should be taken to account for the large orthorhombicity of the resulting ZFS tensors. The large values of λ observed in most of these systems will obscure the interpretation of the sign and magnitude of the D-values, and in certain instances, it will also cause complications in the interpretation of ENDOR data. For circumventing these issues, the development of new computational methods to accurately model fine-structure interactions in delocalized triplet states will be paramount.

In terms of the continuing role of EPR based techniques in guiding the design of porphyrin molecular wires, the results shown in this chapter are a testament to their importance. These findings suggest that future synthetic efforts should consider more carefully the interplay between the distribution of σ- and π-acceptor side groups, **A** and **e**, and the resulting symmetry of the spin density.

Chapter 6

Applications of EPR to the study of cryptochrome proteins

Cryptochromes are blue light photoreceptor proteins which are speculated to be responsible for the magnetic sense of certain avian species, such as the European robin. The leading hypothesis for how cryptochromes carry out this function proposes that upon photo-excitation of a flavin cofactor (non-covalently bound to the protein surface), an electron transfer cascade ensues which eventually leads to the formation of a spin-correlated radical pair (SCRP) between the flavin and a tryptophan residue. The SCRP interacts with the magnetic field of the Earth, and this interaction modulates the kinetics and/or yields of the radical pair recombination reaction. Subsequently, this impacts on a sensory pathway (*via* a signalling state) which starts in the retina and propagates to the brain.

The radical-pair mechanism for magnetoreception in avian species is a fascinating hypothesis not just for scientists, but for the general public as well. This is because it constitutes a prime example of quantum mechanics manifesting on the scale of a macroscopic organism. From a less philosophical perspective, the study of this hypothesis will undoubtedly give rise to new science and new applications such as the development of accurate chemical compasses and field sensors. Much in the same way, the quantum nature of the processes behind photosynthesis in green plants have inspired the development of artificial photosynthesis, and also the use of porphyrin systems as building blocks for molecular wires.

One of the many techniques which can be exploited to further our understanding of cryptochromes in particular, and SCRPs in general is EPR spectroscopy, as will be shown throughout this chapter. The work was carried out in collaboration with Mr. Tommy L. Pitcher (MChem candidate), who contributed equally to myself. Some of the measurement results were initially obtained by Dr. Sabine Richert; these have been independently reproduced and analysed in depth by myself and Mr. Pitcher. Parts of this work are included in a paper which has been submitted for publication in *Nature*.

6.1 Introduction

6.1.1 Cryptochromes as compasses of night-migratory songbirds

Night-migratory songbirds such as the European robin,[1] use a variety of navigational cues to travel over very long distances (*e.g.* from northern Europe to sub-Saharan Africa) [102]. They do so every year and without the help of older, more experienced individuals *i.e.* they have an innate ability to navigate [102].

Many orientational cues are available to these species to aid them in this task, and the magnetic field of the Earth is just one of them [103–105]. Schulten et al. are the earliest (1978) proponents of the idea that the spin dynamics of light generated radical pairs could be at the heart of this biological compass [106]. This idea became more tangible when cryptochromes were identified as prime examples of photo-active proteins, ubiquitously present in Nature, and importantly, in the retinae of the birds, which can host a magnetically sensitive radical pair mechanism [107–112].[2]

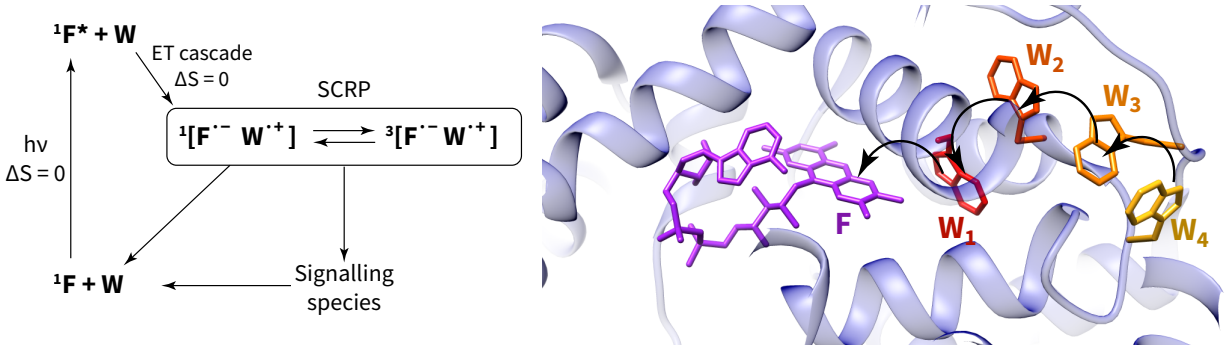


Figure 6.1: (Left) Simplified scheme for the radical pair mechanism involving a spin conserving photo-excitation of a flavin adenine dinucleotide cofactor (denoted **F**), a spin conserving electron transfer cascade across a series of (three or four) tryptophan amino acids (denoted **W**), followed by the non-spin conserving dynamics of the resultant SCRP. (Right) Visual representation of the electron transfer chain from across a tetrad of tryptophan residues to the flavin cofactor bound to the surface of the protein. At this stage, it suffices to say that **W** in the reaction scheme on the left could be either $\mathbf{W}_3$ or $\mathbf{W}_4$ in the cryptochrome structure on the right. The identity of the tryptophan residue is one of the issues addressed in this chapter.

A simplified version of the radical pair mechanism is shown in figure 6.1 alongside a depiction of the structures and relative orientations of the flavin and tryptophan species involved in the mechanism. For simplicity, many details have been omitted from this figure, and the discussion will only outline briefly the processes which are most relevant to this chapter; a more detailed review of the radical pair mechanism of magnetoreception can be found in reference [113].

The first step of the scheme in figure 6.1 involves photo-excitation with blue light of a flavin adenine dinucleotide (**F**). The fact that the flavin absorbs blue light is important because, for example, robins are found to orient in particular under these wavelength conditions [114]. This photoexcitation triggers a rapid electron transfer across a set of nearby tryptophan (**W**) residues. Whilst until recently it was believed that the electron transfer takes place over a triad of tryptophans, it was shown that, in fact, the electron transfer takes place over a tetrad of tryptophans for the common fruit fly [115], in contrast

[1] Or finches, sparrows, blackbirds, and many others

[2] No other proteins have been proposed in the literature for magnetoreception.

to all other previously investigated proteins from the cryptochrome family. As will be shown in this chapter, EPR spectroscopy confirms that this is also the case for the cryptochromes of European robins.

Both photoexcitation and electron transfer events are spin conserving, *i.e.* the resulting **F** –**W** radical pair is formed in an initial singlet state. As will be shown in the next section, this singlet state is not generally an eigenstate of the spin Hamiltonian of the radical pair. Therefore, a coherent and magnetic field dependent evolution will take place under the influence of the spin Hamiltonian giving rise to the SCRP introduced earlier.

The SCRP will oscillate between the singlet and triplet state with a frequency which depends, amongst other factors, on the strength and orientation of the magnetic field.[3] The magnetic field dependence of the singlet-triplet interconversion will modulate the yield and kinetics of the radical pair recombination reaction as the direct decay to the ground state will be altered, because it is spin conserving and thus cannot proceed via the triplet state. The influence of the magnetic field on the recombination reaction can translate into a change in the yield of a downstream signalling species, and this can elicit a sensory response to the magnetic field.

In summary, in its simplest manifestation (figure 6.1), a magnetic field effect (and by extension, a chemical or biological compass) requires, first of all, the formation of a SCRP *i.e.* of a quantum state which evolves coherently between spin states. Secondly, it requires that the singlet and triplet states have different fates because otherwise, the effect of the magnetic field would not be translated into any kind of change further downstream from the SCRP.

6.1.2 Principles of spin-correlated radical pairs

More insight about the general behaviour of SCRPs can be gained from the spin Hamiltonian formalism. In the absence of hyperfine interactions, the simplest possible radical pair problem[4] is defined by the following Hamiltonian:

$$\hat{H} = \gamma_1 \hat{s}_{1z} + \gamma_2 \hat{s}_{2z} + \mathcal{J}\hat{\mathbf{s}}_1 \cdot \hat{\mathbf{s}}_2 + \frac{1}{2}\mathcal{D}(\theta)\left(3\hat{s}_{1z}\hat{s}_{2z} - \hat{\mathbf{s}}_1 \cdot \hat{\mathbf{s}}_2\right) \tag{6.1}$$

where the symbols have the following meaning:

- $\hat{\mathbf{s}}_i = \left(\hat{s}_{ix}, \hat{s}_{iy}, \hat{s}_{iz}\right)$ is the spin vector operator of radical i,
- $\gamma_i = \mu_B g_i B/\hbar$ is the Zeeman interaction factor between radical i with an isotropic g-factor, g_i, and a magnetic field of magnitude B,
- $\mathcal{J}$ is the isotropic exchange interaction parameter,[5]

[3] In cryptochromes, these oscillations are mainly driven by hyperfine coupling interactions. This is called 'the hyperfine mechanism' and it will not be discussed explicitly in this chapter. Instead, the next section will illustrate how singlet-triplet interconversion occurs both as a result of the dipolar and exchange interactions and due to a difference in g-values between the radicals. Despite the fact that these latter interactions are not the main driving forces for singlet-triplet mixing in cryptochromes, the derivation will provide a good starting point for discussing the EPR spectra of SCRPs.

[4] The phrase 'simplest possible' is used here to refer to the simplest radical pair problem which still has some characteristics relevant to the work presented in this chapter. One could also consider a radical pair Hamiltonian with zero inter-electron interactions. Also, note that the radical pair quantified by this Hamiltonian is not necessarily spin-correlated.

[5] The EPR convention is used here: a positive J -value leads to a singlet state which is stabilised by an energy $\mathcal{J}\hbar^2$ compared to the triplet state. Often in the spin chemistry community, the exchange interaction is defined such that a positive $\mathcal{J}$ value leads to a singlet state which is destabilised by $2\mathcal{J}\hbar^2$ compared to the triplet state.

- $\mathcal{D}(\theta)$ quantifies the secular part of the dipolar interaction between the two radicals:

$$\mathcal{D}(\theta) = \frac{\mu_0}{4\pi} g_1 g_2 \gamma_e^2 \frac{1}{r^3}(1 - 3\cos^2\theta) \tag{6.2}$$

  where the angle θ represents the orientation of the inter-spin vector relative to the magnetic field vector.

This spin Hamiltonian will also be used in section 6.2.1 to illustrate a simplified EPR spectrum of a SCRP. Note also that hyperfine interactions are neglected in this section. The eigenstates of $\hat{H}$ are:

$$|1\rangle = |\beta\beta\rangle = |T_-\rangle \tag{6.3}$$

$$|2\rangle = \sin\xi|\alpha\beta\rangle + \cos\xi|\beta\alpha\rangle = \sin\phi|S\rangle + \cos\phi|T_0\rangle \tag{6.4}$$

$$|3\rangle = \cos\xi|\alpha\beta\rangle - \sin\xi|\beta\alpha\rangle = \cos\phi|S\rangle - \sin\phi|T_0\rangle \tag{6.5}$$

$$|4\rangle = |\alpha\alpha\rangle = |T_+\rangle \tag{6.6}$$

where the coupling angles, ξ and ϕ, are defined as follows:

$$\begin{cases} \tan\xi = \dfrac{\gamma_1 - \gamma_2}{\mathcal{J} - \mathcal{D}(\theta)/2} - \sqrt{1 + \dfrac{(\gamma_1 - \gamma_2)^2}{(\mathcal{J} - \mathcal{D}(\theta)/2)^2}} \\ \tan\phi = \dfrac{\sin\xi - \cos\xi}{\sin\xi + \cos\xi} \end{cases} \tag{6.7}$$

and since there is a fixed phase relationship of $\pi/4$ between the uncoupled and coupled representations, there will also be a fixed phase of $\pm\pi/4$ between ξ and ϕ. The corresponding eigenvalues of $\hat{H}$ are:

$$E_1 = +\frac{1}{4}\mathcal{D}(\theta) + \frac{1}{4}\mathcal{J} - \frac{1}{2}\gamma_1 - \frac{1}{2}\gamma_2 \tag{6.8}$$

$$E_2 = -\frac{1}{4}\mathcal{D}(\theta) - \frac{1}{4}\mathcal{J} - \frac{1}{4}\sqrt{(\mathcal{D}(\theta) - 2\mathcal{J})^2 + 4(\gamma_1 - \gamma_2)^2} \tag{6.9}$$

$$E_3 = -\frac{1}{4}\mathcal{D}(\theta) - \frac{1}{4}\mathcal{J} + \frac{1}{4}\sqrt{(\mathcal{D}(\theta) - 2\mathcal{J})^2 + 4(\gamma_1 - \gamma_2)^2} \tag{6.10}$$

$$E_4 = +\frac{1}{4}\mathcal{D}(\theta) + \frac{1}{4}\mathcal{J} + \frac{1}{2}\gamma_1 + \frac{1}{2}\gamma_2 \tag{6.11}$$

Having found the eigensolution of $\hat{H}$ it is now possible to investigate the time evolution of the spin states. As explained in the previous section, the radical pair is formed by a sequence of very rapid and spin conserving processes, *i.e.* we can take the initial wavefunction to be given by $|S\rangle$. Therefore, the system will evolve as follows:

$$|\psi(t)\rangle = \exp\left[-\frac{i}{\hbar}\hat{H}t\right]|S\rangle = \tag{6.12}$$

$$= \exp\left[-\frac{i}{\hbar}E_2 t\right]\sin\phi|2\rangle + \exp\left[-\frac{i}{\hbar}E_3 t\right]\cos\phi|3\rangle = \tag{6.13}$$

$$= \left\{\sin^2\phi\exp\left[-\frac{i}{\hbar}E_2 t\right] + \cos^2\phi\exp\left[-\frac{i}{\hbar}E_3 t\right]\right\}|S\rangle + \tag{6.14}$$

$$+ \sin\phi\cos\phi\left\{\exp\left[-\frac{i}{\hbar}E_2 t\right] - \exp\left[-\frac{i}{\hbar}E_3 t\right]\right\}|T_0\rangle \tag{6.15}$$

A number of conclusions can be drawn directly from equations 6.13–6.15. First of all, from the eigenbasis expansion (6.13) it can be deduced that the system is in a linear superposition of eigenstates $|2\rangle$ and $|3\rangle$ with the following time-independent probabilities:

$$P_2 = \sin^2\phi \quad P_3 = \cos^2\phi \tag{6.16}$$

Despite the fact that the probabilities of being in either one of these two eigenstates is constant, the state of the system is, in fact, changing in time; *e.g.* the real and imaginary parts of the coefficient of eigenstate $|2\rangle$ are oscillating between each other at a frequency of $E_2/\hbar$. As explained in references [116, 117], this evolution is called zero-quantum coherence, and in some instances it can be neglected because it decays rapidly.[6] In the remainder of this section, the zero-quantum coherence will *not* be neglected, however, it will be neglected in the formulation of the trEPR spectra of SCRPs (because the trEPR experiments performed here are usually dominated by single-quantum transitions and coherences).

From equations 6.14 and 6.15, the singlet and triplet, $|S\rangle$ and $|T_0\rangle$, probabilities have a time dependence which can be computed as follows:

$$P_S(t) = |\langle S|\psi(t)\rangle|^2 = \sin^4\phi + \cos^4\phi + 2\sin^2\phi\cos^2\phi\cos\left(\frac{1}{2\hbar}\sqrt{(\mathcal{D}(\theta)-2\mathcal{J})^2+4(\gamma_1-\gamma_2)^2}\,t\right) \tag{6.17}$$

$$P_{T_0}(t) = 1 - P_S(t) \tag{6.18}$$

This expression is the origin of singlet-triplet mixing in this simplified SCRP. At $t = 0$, the system is in a pure singlet state, $P_S = 1$, and then it oscillates coherently between $|S\rangle$ and $|T_0\rangle$ with an angular frequency $\omega_{ST} = \frac{1}{2\hbar}\sqrt{(\mathcal{D}(\theta)-2\mathcal{J})^2+4(\gamma_1-\gamma_2)^2}$. The system does not always lose its singlet character completely because the minimum value of $P_S(t)$ is $\left(\sin^2\phi - \cos^2\phi\right)^2 = \cos^2 2\phi$ which, in general, is non-zero. In summary, the state of the system oscillates between the singlet and triplet states with a frequency given by ω_{ST} and a modulation depth of $1 - \cos^2 2\phi$.

It can also be seen in equation 6.17 that singlet-triplet mixing depends on the exchange and dipolar interaction parameters and on the difference in the strength of the Zeeman interactions of the two radicals, $\gamma_1 - \gamma_2$. The latter dependence is often referred to in the spin chemistry community as the 'Δg-mechanism'.[7]

Whilst it is a useful proof of principle exercise, the above treatment of SCRPs is deficient. In cryptochromes for instance, the inter-radical distance is large and hence, the through-bond exchange coupling, $\mathcal{J}$, is expected to be very small.[8] Furthermore, the differences in the g-values of organic radicals tend to be negligible, because spin-orbit effects are weak in the absence of heavy elements. Therefore, the treatment outlined above is not sufficient to cause an observable magnetic field effect in the Earth strength magnetic fields relevant for avian magnetoreception (ca. 0.5 mT).[9] In fact, for cryptochromes,

[6] Typically, the zero-quantum coherence decays in ca. 100 ns. This is likely a result of interactions with nuclear nuclear spins (which lead to an averaging/dephasing of these oscillations) and due to the fact that relaxation processes, in general, tend to be faster if the energy gap between the states (E_2 and E_3 in this case) is smaller.

[7] The modulation depth reaches unity when the coupling angle ϕ equals $\pi/4$. It can be shown that a coupling angle of $\phi = \pi/4$, is achieved when: $\mathcal{J} = 0$, $\mathcal{D}(\theta) = 0$, and $\gamma_1 - \gamma_2 \neq 0$. In other words, the pure Δg-mechanism leads to oscillations between a singlet probability of 1 and 0. By contrast, the modulation depth becomes exactly zero, *i.e.* there is no singlet-triplet mixing, when $\phi = 0$. It can also be shown that $\phi = 0$ is the strong coupling limit, in which case the initial $|S\rangle$ state is an eigenstate, and there should be no singlet-triplet mixing because eigenstates are stationary, as predicted.

[8] Because it depends on the overlap of the spatial parts of the wavefunctions for the two radicals. This overlap will have a steeply decreasing dependence on r.

[9] However, the Δg-mechanism can dominate the hyperfine mechanism in typical EPR magnetic fields (350 mT at X-band

singlet-triplet mixing is known to be driven primarily by hyperfine interactions [113]. Nonetheless, the eigensolution of $\hat{H}$ given above will be useful for the description of a simple SCRP trEPR spectrum, as will be seen in section 6.2.1, and for generalisations to more complicated systems.

6.1.3 The role of EPR spectroscopy

A substantial amount of information about SCRPs can be gained from optical spectroscopy techniques. For example, transient absorption spectroscopy probes the kinetics and behaviour of the geminate radical pairs on timescales ranging from picoseconds to microseconds. Similarly, one can monitor the yields and lifetimes of species resulting from the SCRP by means of fluorescence techniques. However, optical methods cannot necessarily prove the spin-correlated nature of the radical pairs.[10] Additionally, the hyperfine interactions which drive the magnetic field effects cannot be measured directly on the energy scales of optical spectroscopy.

It is therefore clear that EPR spectroscopy is not only an accessory to the optical methods used for investigating cryptochromes and SCRPs, it is an indispensable part of an artillery of techniques. In brief, EPR can be used to establish the following: (1) that spin-correlated radical pairs are involved in the sequence of events initiated by light excitation, (2) the precise identity of the radicals in the pair, and finally, (3) key structural information can also be extracted from the spin Hamiltonian parameters. These points are not specific to cryptochrome proteins, they relate to any SCRP as reviewed in references [118–120], and they will be explored throughout the remainder of this chapter.

The first direct observation of SCRPs in cryptochrome proteins was achieved in 2009 by Biskup et al. using the trEPR technique introduced earlier in this thesis [121]. In particular, the cryptochrome of the African clawed frog (*Xenopus laevis*) was considered in this reference. It was proven that a SCRP pair is formed between a flavin cofactor and a tryptophan residue, and it was also conjectured that the electron transfer terminates on the third tryptophan residue in cryptochromes ($\mathbf{W_3}$ in figure 6.1). The fact that the radical pair formation terminates on a *tryptophan* residue was an important breakthrough because prior work on similar proteins also considered, amongst other hypotheses, the possibility of a flavin-tyrosine SCRP [122, 123].

In another important publication, the out-of-phase Electron Spin Echo Envelope Modulation (oopESEEM) pulse EPR technique was exploited to show that cryptochromes from the common fruit fly (*Drosophila melanogaster*) host a SCRP derived from electron transfer over a tetrad, rather than a triad, of tryptophan residues [124]. This oopESEEM technique will be shown in this chapter as well to be a particularly versatile technique for determining the dipolar and exchange interactions present in the spin Hamiltonian of SCRPs. The former of these interactions is dependent on the distance between the radicals of the pair. It is precisely by comparing the radical pair distance between a bacterial photolyase protein (a relative of cryptochromes which does not contain $\mathbf{W_4}$) and the cryptochromes from the fruit fly, that Nohr et al. reached their important conclusion about the involvement of $\mathbf{W_4}$ in the latter [124].

There are many crucial unanswered questions about the cryptochrome SCRP mechanism of magnetoreception and EPR will be used in this thesis to address some of these issues. In the first instance, the development of an efficient and reliable simulation algorithm for the trEPR spectra of SCRPs will be

for example).

[10] Albeit, in normal circumstances it can be assumed that the observed magnetic field effects must have originated in a SCRP

presented. The trEPR spectra of these systems are a signature of spin-correlation, a necessary condition for the proposed mechanism of magnetoreception (or, indeed, for any magnetic field effect). However, due to the many fine and hyperfine interactions present in the spin Hamiltonian, the identity of the radicals cannot be confidently extracted without a versatile numerical simulation tool. Thus far, such simulation algorithms have been presented only sporadically, *e.g.* notably in reference [125], and have not been made widely available. The codes developed here will then be exploited in a case study wherein the experimental trEPR spectra of naturally occurring and mutated cryptochromes are simulated and interpreted.

In the second part of this chapter, the inter-spin distance in a range of cryptochromes will be determined using the oopESEEM technique. Complementary to trEPR, the results of this experiment will reveal that the radical separation in the cryptochromes of European robins is consistent with a tetrad of tryptophan residues. Furthermore, variable temperature oopESEEM will also be used to investigate the potential for an equilibrium between $\mathbf{F}$–$\mathbf{W_3}$ and $\mathbf{F}$–$\mathbf{W_4}$ in a range of samples. This equilibrium between two SCRPs is speculated to initiate the sensory chain responsible for magnetoreception and it is a new hypothesis which stemmed from a series of optical spectroscopy results carried out in the group. Addressing the validity (or invalidity) of this hypothesis via EPR, or otherwise, is a key issue.

6.2 Transient EPR of SCRPs

6.2.1 The simplest SCRP spectrum

Analogously to the discussion in Chapter 1 (section 1.3.2), EPR transitions of the radical pair system defined by the spin Hamiltonian in equation 6.1 will be driven by the following microwave interaction operator:

$$\hat{H}_{mw} = \frac{\mu_B}{\hbar} B_1 \left(g_1 \hat{s}_{1x} + g_2 \hat{s}_{2x} \right) \tag{6.19}$$

where B_1 is the amplitude of the magnetic component of the microwaves. This is the equivalent of the $\hat{V}$ operator defined in Chapter 1 in equations 1.85 and 1.86 (used in Fermi's golden rule). When $g_1 \approx g_2$, $\hat{H}_{mw}$ can be simplified to:

$$\hat{H}_{mw} \approx \frac{\mu_B}{\hbar} B_1 \tilde{g} \hat{S}_x = \tilde{\gamma} \hat{S}_x = \frac{\tilde{\gamma}}{2} \left(\hat{S}_+ + \hat{S}_- \right) \tag{6.20}$$

where the mean of the g-values has been defined as $\tilde{g}$ and the variable $\tilde{\gamma}$ is given by $\frac{\mu_B}{\hbar} B_1 \tilde{g}$. This equation is sufficient for the discussion in this section and also, it is implemented in one of the two simulation algorithms of the next section. As mentioned previously, for *organic* radical pairs, the differences between the g-values tend to be small enough for this approximation (equation 6.20) to not cause any significant deviations from the exact treatment (equation 6.19). Nonetheless, this approximation will not be made in the other, more general algorithm presented in the next section.

Application of Fermi's Golden Rule (equation 1.86) to all the possible pairs of states in equations 6.3–6.6 leads to the following non-zero quantum intensities for EPR transitions in this spin system:

$$P_{1\to 2} = P_{2\to 4} = \frac{\tilde{\gamma}^2}{4} \cos^2 \phi \tag{6.21}$$

$$P_{1\to 3} = P_{3\to 4} = \frac{\tilde{\gamma}^2}{4} \sin^2 \phi \tag{6.22}$$

Often, these intensities are interpreted as arising from the fact that the allowed EPR transitions occur with a probability given by the 'triplet character' of the eigen-pair involved in the transition. In frequency domain, the peak positions of these allowed transitions are:

$$\hbar\omega_{1\to2} = \frac{1}{2}(\gamma_1 + \gamma_2) - \frac{1}{2}(\mathcal{D}(\theta) + \mathcal{J}) - \frac{1}{4}\sqrt{(\mathcal{D}(\theta) - 2\mathcal{J})^2 + 4(\gamma_1 - \gamma_2)^2} \tag{6.23}$$

$$\hbar\omega_{1\to3} = \frac{1}{2}(\gamma_1 + \gamma_2) - \frac{1}{2}(\mathcal{D}(\theta) + \mathcal{J}) + \frac{1}{4}\sqrt{(\mathcal{D}(\theta) - 2\mathcal{J})^2 + 4(\gamma_1 - \gamma_2)^2} \tag{6.24}$$

$$\hbar\omega_{2\to4} = \frac{1}{2}(\gamma_1 + \gamma_2) + \frac{1}{2}(\mathcal{D}(\theta) + \mathcal{J}) + \frac{1}{4}\sqrt{(\mathcal{D}(\theta) - 2\mathcal{J})^2 + 4(\gamma_1 - \gamma_2)^2} \tag{6.25}$$

$$\hbar\omega_{3\to4} = \frac{1}{2}(\gamma_1 + \gamma_2) + \frac{1}{2}(\mathcal{D}(\theta) + \mathcal{J}) - \frac{1}{4}\sqrt{(\mathcal{D}(\theta) - 2\mathcal{J})^2 + 4(\gamma_1 - \gamma_2)^2} \tag{6.26}$$

The resulting EPR spectra for a fixed value of θ and for a powder average are shown in figure 6.2 for a Boltzmann distribution of energy levels, whereby each transition has an intensity:[11]

$$I_{j\to k} = P_{j\to k}\exp(-\hbar\beta\omega_{j\to k}). \tag{6.27}$$

The single crystal (fixed θ) spectrum consists of at most four peaks centred at the average Larmor frequency of the two electrons, and the separations between the peaks depend on the two inter-electron couplings, $\mathcal{D}(\theta)$ and $\mathcal{J}$, and on the difference between the Larmor frequencies. Once the integration over θ is performed, the result is the familiar pair of Pake patterns. However, it is important to note that, strictly speaking, these two Pake patterns are only observed in the weak-coupling limit, *i.e.* $|\gamma_1 - \gamma_2| \gg |\mathcal{D}(\theta) + \mathcal{J}|$. In any other coupling regime, the two Pake patterns will overlap and the intensity pattern will become distorted. Nonetheless, all of these complications are already encapsulated by equations 6.23–6.26; figure 6.2 is only a model illustration of a particularly simple case (weak-coupling).

As mentioned, equations 6.23–6.26 quantify the peak positions in frequency/energy domain, whereas the field domain spectrum is required in this thesis. Provided that the high-field limit is satisfied, *i.e.* that $\gamma_i \gg |\mathcal{D}(\theta) + \mathcal{J}|$, then the conversion to field domain can be performed according to:

$$B_{j\to k} = \frac{\hbar\omega_{j\to k}}{\mu_B\tilde{g}} \approx \left(\frac{\omega_{j\to k}/\mathrm{MHz}}{28}\right)\mathrm{mT} \tag{6.28}$$

where $B_{j\to k}$ denotes the resonance field of transition $j \longrightarrow k$, and $\tilde{g}$ is the average g-value of the electrons. Furthermore, in the simplest of cases, the anisotropy of the individual $\mathbf{g}$-tensors is small enough that the generalised $1/g$-factor (equation 1.99) can be omitted because it is a constant scaling factor.[12]

[11] The symbol β in this case refers to the Boltzmann factor $\beta = 1/k_BT$.

[12] In more precise treatment, the $1/g$-factor cannot be neglected and, furthermore, the resonance fields need to be extracted from the resonance frequencies by solving the following resonance polynomial:

$$\hbar\omega_{j\to k}\left(B_{j\to k}\right) = \kappa + \lambda B_{j\to k} + \sqrt{\mu + \eta\left(B_{j\to k}\right)^2} = \hbar\omega_{mw}$$

where the variables κ, λ, μ, and ν can be obtained by simply equating them with the appropriate (free, linear, and quadratic) terms in equations 6.23–6.26 (the equations are not shown in the interest of brevity). The roots of this resonance polynomial are the following:

$$B_{j\to k} = \frac{\pm\sqrt{\kappa^2\eta + \kappa^2\mu - \mu\eta} - \kappa\lambda}{\lambda^2 - \eta}$$

Therefore, a given pair of states, j and k, will have zero, one, or two possible resonance fields, depending on which of the two values of the above equation are positive and real. If both '±' outputs of the above are positive and real, then the transition from j to k is called a 'looping transition'; these are transitions which occur at either side of a level crossing in field domain.

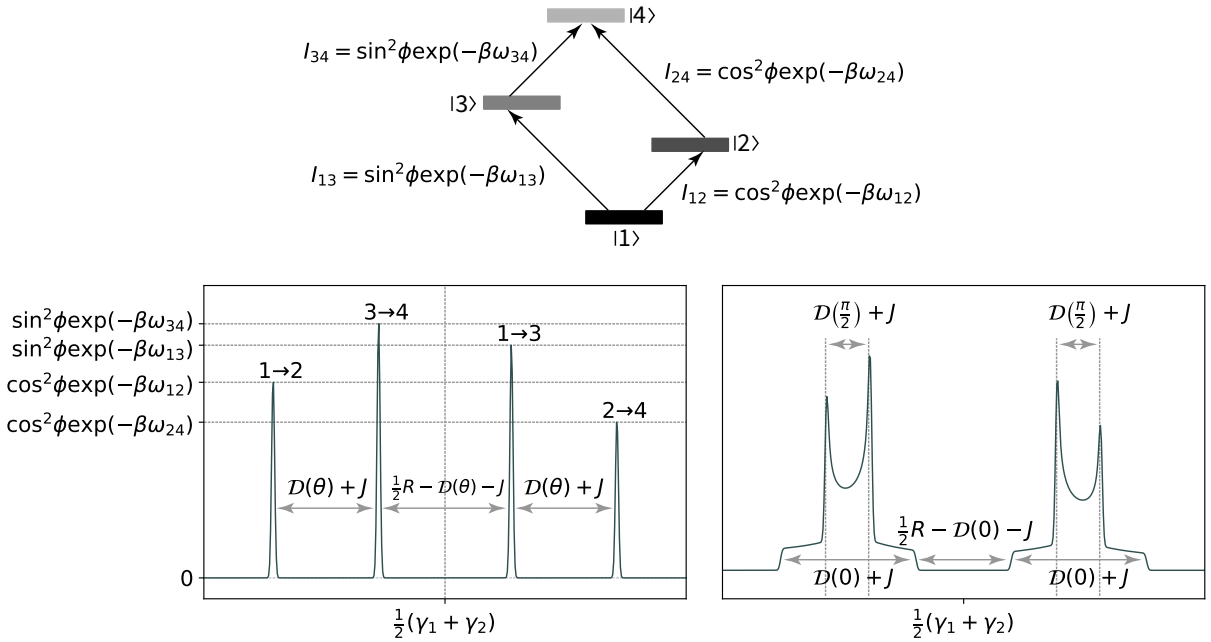


Figure 6.2: (Top) Schematic representation of the energy levels of the eigenstates of the radical pair quantified by equations 6.8–6.11. The arrows indicate the allowed transitions and their corresponding intensity (equation 6.27). A darker shading for a given state corresponds to a greater population for that state. The case illustrated here is for a Boltzmann distribution of the sub-level populations. (Bottom left) EPR spectrum (in frequency/energy domain) at a fixed value of θ of the radical pair system described in the main text. (Bottom right) The powder average EPR spectrum of the model radical pair system obtained by integration over the interval $\theta \in [0, \pi/2]$. Both panels show the results for a Boltzmann distributed radical pair. Note: $R = \sqrt{(\mathcal{D}(\theta) - 2\mathcal{J})^2 + 4(\gamma_1 - \gamma_2)^2}$.

The above discussion has focussed exclusively on a radical pair in thermal equilibrium, hence, the intensities are given by equation 6.27. In other words, there is no spin-correlation in the spectra depicted in figure 6.2. As was shown in the previous section, the SCRPs of interest are formed in an initial singlet state, $|S\rangle$, and as a result of equation 6.13 the system will be in a coherent superposition between eigenstates $|2\rangle$ and $|3\rangle$. More precisely, the system is spin polarised, because the populations of states $|1\rangle$ and $|4\rangle$ are zero, whereas $|2\rangle$ and $|3\rangle$ are populated according to equation 6.16. In light of this, the transition intensities will be given by the following equations for a singlet-born SCRP:

$$I_{1\to2} = P_{1\to2}\,(P_1 - P_2) = -\cos^2\phi\sin^2\phi \tag{6.29}$$

$$I_{1\to3} = P_{1\to3}\,(P_1 - P_3) = -\cos^2\phi\sin^2\phi \tag{6.30}$$

$$I_{2\to4} = P_{2\to4}\,(P_2 - P_4) = +\cos^2\phi\sin^2\phi \tag{6.31}$$

$$I_{3\to4} = P_{3\to4}\,(P_3 - P_4) = +\cos^2\phi\sin^2\phi \tag{6.32}$$

where the factor of $\tilde{\gamma}^2/4$ has been omitted for simplicity. As depicted in figure 6.3, equations 6.29–6.32 imply that the spectrum of this SCRP will comprise two emissive and two absorptive peaks, with the same absolute magnitude for all resonant pairs. It can be seen from this figure that, in the case of a single θ value, the spectrum comprises two anti-phase doublets, whereas the powder average spectrum consists of two polarised Pake patterns (Pake patterns with anti-phase structure).

In the remainder of this chapter, equation 6.28 will be used in one of the simulation algorithms; nonetheless, the code can easily be generalised to the above equation should this ever prove to be necessary.

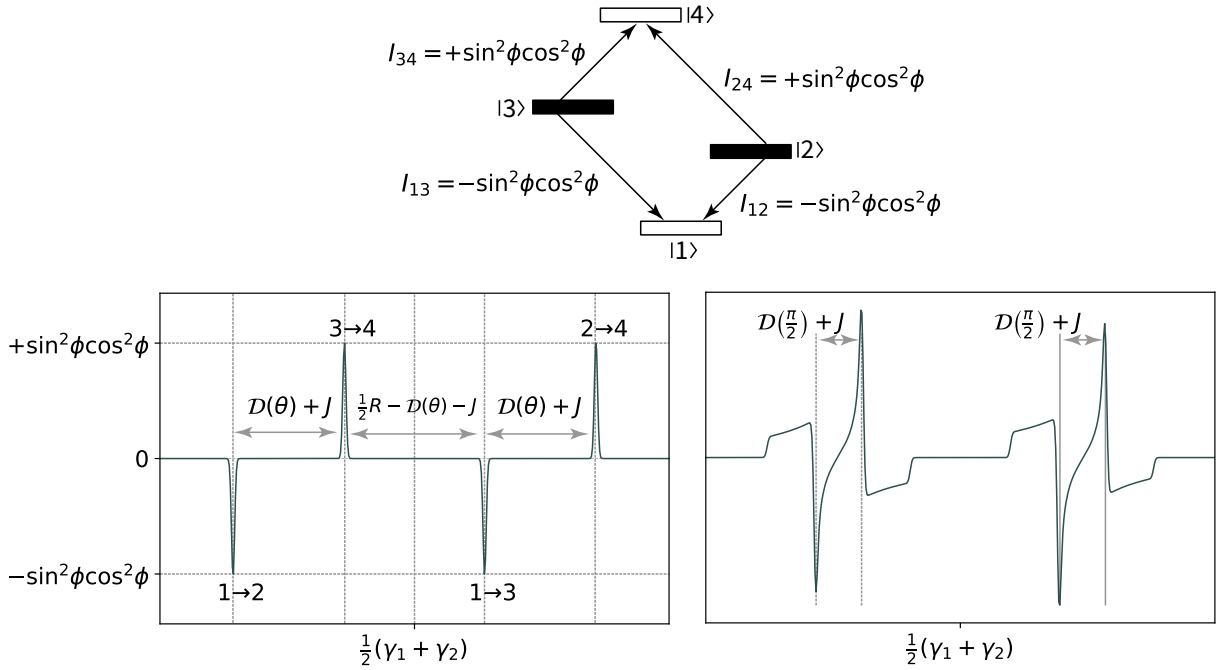


Figure 6.3: (Top) The same schematic energy level diagram as for figure 6.2 *except* that in this case, the populations of the states are non-Boltzmann as a consequence of spin-correlation. For a singlet-born SCRP, states $|2\rangle$ and $|3\rangle$ are preferentially populated due to the fact that they are the only ones with non-zero singlet character. The intensities of the EPR transitions can be negative (emission) or positive (absorption) as shown in equation 6.29–6.32. (Bottom left) EPR spectrum (in frequency/energy domain) at a fixed value of θ for a singlet-born SCRP. (Bottom right) The corresponding powder average EPR spectrum for the same SCRP. The peak positions are the same as in figure 6.2, whereas the intensities are given in equations 6.29–6.32.

The particular sequence of absorptive and emissive features in the EPR spectrum of a SCRP will depend on the magnitudes and relative signs of $\mathcal{D}(\theta)$ and $\mathcal{J}$,[13] as can be computed directly from the equations given in this section. In summary, the following types of information can be gleaned about cryptochromes using trEPR: (1) if the observed spectrum is a sequence of absorptive and emissive signals, then the radical-pair is truly spin-correlated, as required for magnetoreception, (2) in this simple case, from the peak positions it is possible to extract structural information (through $\mathcal{D}(\theta)$), and (3) from the g-values, the identity of the radicals can also be inferred (the inclusion of hyperfine couplings is done in the next section).

6.2.2 Towards simulating complex SCRPs

Apart from a few minor approximations, the above treatment of SCRPs and their EPR spectra is very accurate. However, cryptochrome based SCRPs are significantly more complicated than the system defined by the Hamiltonian in equation 6.1. The radicals of the pair will also exhibit the following features which need to be accounted for in numerical simulations: the **g**-tensors are not necessarily isotropic (albeit this is a minor perturbation for many organic radicals at X-band), anisotropic hyperfine interactions will be present for both radicals, and all of these interaction tensors will not necessarily be

[13] And generally, it will also depend on whether the SCRP is singlet-born or triplet-born. Only the former type are considered in this work.

aligned.

Two simulation algorithms have been developed for numerical simulations of the trEPR spectra of such complex SCRPs: *cockatiel* and *fawns*. The former, *cockatiel*, is an accurate but slow algorithm, whereas *fawns* is fast, yet approximate. Despite being approximate, it will be shown that *fawns* can be used reliably for cryptochrome spectra. The two codes will be outlined briefly below, whereas the complete MATLAB scripts for both are provided in appendix G.

Cockatiel

As was shown for the simple example of the previous section, transitions in the Boltzmann populated system occur at the exact same resonance fields as for a spin-correlated system. These resonance fields will depend only on the eigenvalues of the following general spin Hamiltonian for a radical pair with n nuclear spins, denoted $\hat{\mathbf{I}}_k$:

$$\hat{H} = \underbrace{\frac{\mu_B}{\hbar}\mathbf{B}\cdot\mathbf{g}_1\cdot\hat{\mathbf{s}}_1 + \frac{\mu_B}{\hbar}\mathbf{B}\cdot\mathbf{g}_2\cdot\hat{\mathbf{s}}_2}_{\text{electron Zeeman}} + \underbrace{\mathcal{J}\hat{\mathbf{s}}_1\cdot\hat{\mathbf{s}}_2 + \hat{\mathbf{s}}_1\cdot\mathcal{D}\cdot\hat{\mathbf{s}}_2}_{\text{exchange and dipolar}} + \underbrace{\sum_{k=1}^{n}\gamma_I\mathbf{B}\cdot\hat{\mathbf{I}}_k + \sum_{k=1}^{n}\sum_{i=1}^{2}\hat{\mathbf{s}}_i\cdot\mathbf{A}_{ik}\cdot\hat{\mathbf{I}}_k}_{\text{nuclear Zeeman and hyperfine}} \tag{6.33}$$

where all interaction parameters, except $\mathcal{J}$, can be anisotropic and can have any orientation relative to each other. Apart from the presence of the hyperfine interactions and anisotropic $\mathbf{g}$-tensors, this Hamiltonian differs from the one in equation 6.1 also in the definition of the electronic dipolar interaction tensor, $\mathcal{D}$, which is in this case given by:

$$\mathcal{D} = \frac{\mu_0}{4\pi}\tilde{g}^2\gamma_e^2\frac{\mathbf{1}_3 - 3\boldsymbol{\epsilon}\otimes\boldsymbol{\epsilon}}{r^3} \tag{6.34}$$

whereby $\boldsymbol{\epsilon}$ is the unit vector corresponding to the inter-spin vector $\mathbf{r}$. By contrast, the dipolar term in equation 6.1 contains only the secular parts of the total interaction. The reason for replacing the dipolar interaction tensor with equation 6.34 is done in the interest of generality and precision; for cryptochromes, the non-secular parts of the dipolar interaction are only minor perturbations (because these systems approach the high-field/weak-coupling limit) and can be neglected. The inputs to *cockatiel* can be changed to include only the secular approximation, if this approximation is suitable for the SCRP under investigation. The eigenvalues of $\hat{H}$ depend on $|\mathbf{B}| \equiv B$, θ, and ϕ, the latter of which define the orientation of the magnetic field with respect to the common frame in which all interaction tensors are defined (in the code, it is chosen to be the eigenframe of $\mathbf{g}_1$).

The first step within *cockatiel* is the generation of a grid of orientations, (θ, ϕ), of the magnetic field vector which are then looped over. For every pair (θ, ϕ), the function *resfields* from EasySpin is used to obtain the resonance fields of all the possible EPR transitions (those which satisfy the resonance condition at the given microwave frequency). The function *resfields* also outputs two other important quantities: the quantum intensity of the transition, and the identity of the pair of states between which the transition occurs. At this stage in the program, for a given pair (θ, ϕ), the following is a summary of the available information:

- a list of m resonance fields:

$$\left\{B_{res}^1, B_{res}^2, \ldots, B_{res}^m\right\}$$

- a list of quantum intensities (the analogues of equations 6.21–6.22):

$$\left\{ Q^1, Q^2, \ldots, Q^m \right\}$$

- a list of level pair indexes (in ascending energetic order) denoting the lower state $|l^i\rangle$ and the upper state $|u^i\rangle$ of resonance field B^i_{res}:

$$\left\{ \left(|l^1\rangle, |u^1\rangle\right), \left(|l^2\rangle, |u^2\rangle\right), \ldots, \left(|l^m\rangle, |u^m\rangle\right) \right\}$$

The lists for the resonance fields, B^i_{res}, and corresponding quantum intensities, Q^i, are only sufficient to reconstruct the EPR spectrum of radical pairs in thermal equilibrium *i.e.* not spin-correlated (and in the high-temperature limit). For a SCRP, we require an additional spin polarisation factor, P^i, in order to obtain the total intensity, $Q^i P^i$, of the peak located at B^i_{res}.

The spin polarisation factor is computed as follows:

- Loop over each resonance field B^i_{res}:
  - Diagonalise the Hamiltonian (equation 6.33) by setting the magnetic field vector to have magnitude B^i_{res} and orientation (θ, ϕ). Then, use the list of indexes for the state pairs (defined by *resfields*) to obtain the $|l^i\rangle$ and $|u^i\rangle$ vectors. The resulting state vectors consist of a list of complex numbers corresponding to the expansion coefficients of the eigenstates in the product basis (*i.e.* the completely decoupled basis for all spins).
  - Loop over all the possible nuclear spin states for each nucleus, *i.e.* a loop over $\mu = 1 \longrightarrow \prod_k (2I_k + 1)$ nuclear states:
    - Calculate the spin polarisation factor as follows:

$$P^i = P^i + \left|\langle S_\mu | l^i \rangle\right|^2 - \left|\langle S_\mu | u^i \rangle\right|^2 \tag{6.35}$$

The $|S_\mu\rangle$ state represents the electronic singlet state coupled to the nuclear manifold labelled by μ. As an example, if there is only one proton present in the system, then $|S_1\rangle$ is equivalent to $|S, \alpha\rangle$ and $|S_2\rangle$ is equivalent to $|S, \beta\rangle$, whereby the second label denotes the proton's spin state. For two protons, the correspondence is $\mu = 1, 2, 3, 4 \longrightarrow \alpha\alpha, \alpha\beta, \beta\alpha, \beta\beta$. These electronic singlet state vectors are pre-computed prior to entering the (θ, ϕ) loop, since they only depend on the nuclear spin quantum numbers. It is essential that $|S_\mu\rangle$ are generated in the same basis, with the same ordering, as the basis in which $|l^i\rangle$ and $|u^i\rangle$ are written.

Finally, the set of B^i_{res}, Q^i, and P^i for each (θ, ϕ) are used to assemble the final EPR spectrum in conjunction with an inherent (Gaussian/Lorentzian) linewidth, and an orientational weighting factor of $\sin\theta$. This algorithm is accurate except for the unavoidable approximation that the SCRP is initially created in an electronic singlet state without nuclear coherence and without nuclear polarisation. This is precisely the approximation which allows the spin polarisation factor to be written in the manner given in equation 6.35. The interpretation of this approximation for a SCRP containing a single proton is as follows: when the ensemble of SCRPs is created by the photoexcitation and electron transfer events, half of the systems in the ensemble will be in the $|S, \alpha\rangle$ state and the other half will be in the $|S, \beta\rangle$ state.

Apart from the above mentioned approximation, *cockatiel* suffers from the minor bottleneck of having to re-diagonalise the spin Hamiltonian at each resonance field in order to retrieve the state vectors which were lost as local variables in *resfields*. This was unavoidable at the time when the code was written because the function *resfields* was not publicly available. However, in the near future the open-source version of *resfields* will be modified to allow the computation of P^i within this function at the same time as Q^i. As is, *cockatiel* executes m additional diagonalisation steps (for each orientation on the grid) than would be necessary with an integrated *resfields* function. Nonetheless, *cockatiel* offers a useful consistency check for the approximate, yet much faster, *fawns* algorithm.

Fawns

The *fawns* algorithm is based on a code developed by Prof. Peter J. Hore and modified in the doctoral thesis of Prof. Christiane R. Timmel, called *pqesp*, which allows the computation of the EPR spectra of singlet-born SCRPs using the analytical formulas given in section 6.2.1 [70]. The code was written for the purpose of simulating the trEPR spectra of the SCRPs formed in the reaction centers of photosynthetic bacteria [126].[14] Within *pqesp*, the spectrum is assembled as a sum of Gaussian functions centred at the positions given by $\omega_{j\rightarrow k}$ in equation 6.23–6.26 and with intensities $I_{j\rightarrow k}$ given by equations 6.29–6.32. In addition to these formulas, this original *pqesp* algorithm also supports the inclusion of anisotropic **g**-tensors, of arbitrary orientation relative to each other, as well as a dipolar interaction with an arbitrary orientation.

Both of these features are built into the code by means of an effective g-value for electron i, denoted $g_{i,\mathrm{eff}}$, defined as the sum of the projections of the $\mathbf{g}_i$ tensor axes onto the magnetic field axis:

$$g_{i,\mathrm{eff}} = \sqrt{g_{i1}^2 \cos^2\theta_1 + g_{i2}^2 \cos^2\theta_2 + g_{i3}^2 \cos^2\theta_3} \tag{6.36}$$

where g_{ik} is the k-th eigenvalue of $\mathbf{g}_i$, and θ_k is the angle between the the k-th axis of $\mathbf{g}_i$ and the magnetic field. The validity of this expression comes from the fact that the operator:

$$\frac{\mu_B}{\hbar} B g_{1,\mathrm{eff}} \hat{s}_{1z} + \frac{\mu_B}{\hbar} B g_{2,\mathrm{eff}} \hat{s}_{2z} \tag{6.37}$$

is similar to the Zeeman operator in equation 6.33.[15] Since the eigenvalues of the total Hamiltonian are conserved by similarity transformations, the $g_{i,\mathrm{eff}}$-values defined above will give exact results.

The *pqesp* function does not include any hyperfine interactions, which is the reason for developing the *fawns* function using the former as inspiration. The inclusion of hyperfine interactions can be done relatively simply in the weak-coupling limit, $|\gamma_1 - \gamma_2| \gg |\mathcal{D}(\theta) + \mathcal{J}|$, because transitions $1 \longrightarrow 3$ and $2 \longrightarrow 4$ can be considered as a spin flip of electron 1, whereas $1 \longrightarrow 2$ and $3 \longrightarrow 4$ can be considered a spin flip of electron 2. In other words, the two anti-phase doublets in figure 6.3 can each be thought of as belonging approximately to the resonance of a single electron spin. This resonance of electron i is then shifted with respect to γ_i by the net dipolar and exchange fields due to the other electron (which amounts to an energy shift of $\pm\frac{1}{2}(\mathcal{D}(\theta) + \mathcal{J})$).

In light of the above, the effect of the hyperfine interaction can also be considered as an additional shift

[14] The trEPR signature of these is mainly due to fine-structure interactions rather than hyperfine couplings, hence why the latter were not included explicitly in the algorithm (they were only included as a Gaussian line broadening).

[15] *i.e.* similar in a mathematical sense: A is similar to B if there exists an invertible U such that $A = U^{-1}BU$.

in the resonance frequency of each electron. More precisely, the spectrum of a particular transition $j \longrightarrow k$, attributed mainly to a spin flip of electron i will be split by an effective hyperfine coupling into $(2I_p + 1)$ lines of equal intensity. The positions of the peaks in this hyperfine multiplet will then be given by:

$$\hbar\omega'_{j\longrightarrow k} = \hbar\omega_{j\longrightarrow k} + \hbar^2 a_{ip,\text{eff}} m_{I_p} \tag{6.38}$$

where $\hbar\omega_{j\longrightarrow k}$ is given in equations 6.23–6.26, m_{I_p} is the magnetic quantum number of nucleus p, and $a_{ip,\text{eff}}$ is the effective hyperfine coupling experienced by electron i due to nucleus p.[16] The effective hyperfine interaction is calculated in a similar manner to the effective g-values described above, *i.e.* by projecting the axes of the hyperfine tensor onto the magnetic field direction:

$$a_{ip,\text{eff}} = \sqrt{A^2_{ip,1}\cos^2\xi_1 + A^2_{ip,2}\cos^2\xi_2 + A^2_{ip,3}\cos^2\xi_3} \tag{6.39}$$

where $A_{ip,k}$ is the k-th eigenvalue of hyperfine coupling tensor $\mathbf{A}_{ip}$ between electron i and nucleus p, and ξ_k is the angle between the k-th eigenvector of $\mathbf{A}_{ip}$ and the magnetic field. Qualitatively, $a_{ip,\text{eff}}$ can be considered as the net shift in strength of the external magnetic field experienced by electron i due to the magnetic moment of nucleus p.

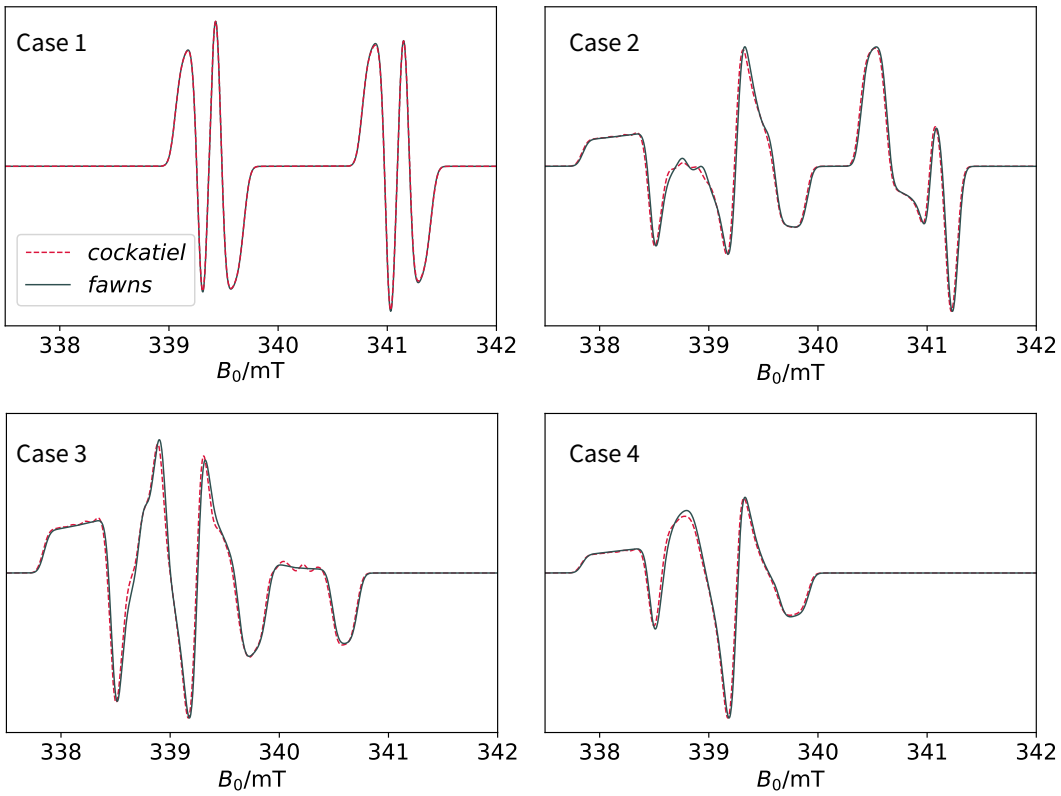


Figure 6.4: Comparison of SCRP simulations obtained with *cockatiel* and *fawns*. The simulation parameters for each case are provided in table 6.1.

The above treatment is expected to yield sufficiently accurate EPR spectra for most singlet-born SCRPs of interest, whilst dramatically improving the simulation time. As a justification, figure 6.4 is a comparison of simulations obtained with *cockatiel* and *fawns* for a relatively simple SCRP with interaction

[16] The factor of $\hbar^2$ attached to the hyperfine coupling constant is superfluous; it is a result of the fact that the spin operators used throughout the thesis are in SI units.

Case #	$\mathbf{g}_1$	$\mathbf{g}_2$	ξ_2	$\mathbf{A}_1$/MHz
1	[2.000 2.000 2.000]	[1.990 1.990 1.990]	[0° 0° 0°]	[0 0 0]
2	[2.000 2.003 2.003]	[1.990 1.990 1.993]	[120° 45° 90°]	[2 2 20]
3	[2.000 2.003 2.003]	[2.003 2.003 1.993]	[120° 45° 90°]	[2 2 20]
4	[2.000 2.003 2.003]	[2.000 2.003 2.003]	[0° 0° 0°]	[2 2 20]

Table 6.1: Parameters used to generate the four simulation cases in figure 6.4: the $\mathbf{g}_i$ column shows the eigenvalues of the $\mathbf{g}$-tensor for electron i, the ξ_2 values represent the Euler angles corresponding to the eigenframe of the $\mathbf{g}_2$-tensor, and $\mathbf{A}_1$ are the eigenvalues of the hyperfine coupling tensor between electron 1 and a nitrogen nucleus ($\mathbf{A}_1$ is taken to be aligned with $\mathbf{g}_1$). Additional simulation parameters are: $\mathcal{D}(0) = \frac{2}{3}D = -14.94\,\text{MHz}$, $\mathcal{J} = +2.8025\,\text{MHz}$, a Gaussian broadening of 0.1 mT, and a microwave frequency of 9.5 GHz. Simulations with *fawns* took ca. 30 seconds to generate, whilst with *cockatiel* they took over 2.5 minutes (measured using the *tic* and *toc* functions in MATLAB).

parameters as summarised in table 6.1. For arbitrary systems, it is impossible to check the validity of the approximations in *fawns* versus the more exact treatment in *cockatiel*, hence why only four particular cases are shown here. The fact that all the pairs of spectra in figure 6.4 are in very good agreement with each other is sufficient justification for the use of *fawns* in simulating the cryptochrome spectra in the next section.

The *fawns* algorithm is expected to yield inconsistent/problematic simulations in the low-field limit (where looping transitions and forbidden transitions become feasible and/or if the exchange, dipolar, and hyperfine interactions are orders of magnitude larger than the difference in the Zeeman energies of the electrons.[17] If such complications are suspected/expected for a given SCRP system, then *cockatiel* is the more appropriate choice for simulations.

6.2.3 Applications to cryptochromes

Samples and methodology

The three cryptochrome proteins summarised in table 6.2 will be investigated in this section using trEPR spectroscopy in combination with the *fawns* simulation script introduced above. Two of these samples, one from the European robin (*Erithacus rubecula*, *Er*Cry4 WT) and the other from the common fruit fly (*Drosphila melanogaster*, *Dm*Cry WT), are wild-type proteins (expressed as they occur naturally) from a migratory and non-migratory species, respectively. Both of these systems are known to contain a tetrad of tryptophans adjacent to the flavin cofactor, as illustrated in figure 6.1. The *Er*Cry4 W369F sample is a single point mutant whereby the fourth tryptophan ($\mathbf{W_4}$ in figure 6.1) was replaced with a phenylalanine residue; this latter amino acid cannot take part in electron transfer. The label '*Er*Cry4 W369F' is used to denote the fact that the tryptophan (W) at position 369, *i.e.* W369, in the protein structure was replaced by a phenylalanine (F) residue. The labelling scheme is introduced in more detail in the caption to table 6.2.

The *Dm*Cry WT system has been studied before by Nohr et al. using EPR spectroscopy [115, 124], and is

[17] For example, in the 500 MHz EPR spectrum of a radical pair with $\mathcal{D}(0) = \mathcal{J} = 2\,\text{GHz}$ and g-values of 2.00 and 2.01 (simulations not shown). Such conditions are very extreme compared to what is normally expected for any SCRPs of relevance, and also, such small microwave frequencies are rarely, if ever, encountered in EPR.

used here as a reference for the new systems, *Er*Cry4 WT and *Er*Cry4 W369F. These two latter systems both show (different) magnetic field effects, and the aim here is to establish the identity of the radical pair, *i.e.* to understand the extent to which the fourth tryptophan residue is involved in the SCRP.

Label	Species	Characteristics
*Er*Cry4 WT	European robin (*Erithacus rubecula*)	wild-type protein, tetrad of tryptophans, migratory songbird
*Er*Cry4 W369F	European robin (*Erithacus rubecula*)	mutated protein, triad of tryptophans, $\mathbf{W}_4$ (= W369) replaced by phenylalanine
*Dm*Cry WT	Common fruit fly (*Drosophila melanogaster*)	wild-type protein, tetrad of tryptophans, (non-migratory) insect

Table 6.2: Summary of the cryptochrome samples investigated in this section using the trEPR technique and their most relevant characteristics. This specific labelling of the samples is done for the purpose of consistency with the cryptochrome literature. The meaning of the labels is as follows: WT– wild-type protein, *Er* and *Dm* are the initials of the binomial nomenclature of the living species to which the cryptochromes correspond, Cry4 represents Cryptochrome 4 of the European robin (the '4' is necessary because avian species have four cryptochromes, and the fourth one is speculated to be responsible for the magnetic sense, see reference [127]), and W369F denotes the specific point mutation of the protein sample (explained in the main text).

The *Dm*Cry WT sample was expressed in the groups of Prof. Erik Schleicher and Prof. Stefan Weber from the University of Freiburg (Germany) according to the procedures published in the reference [115]. The *Er*Cry4 WT and *Er*Cry4 W369F samples were expressed by Ms. Jingjing Xu from the group of Prof. Henrik Mouritsen from the University of Oldenburg (Germany). Upon arrival in Oxford, the samples were prepared by Dr. Kevin B. Henbest and Mr. Tommy L. Pitcher. Initially, the samples are washed with a Tris buffer solution (20%glycerol/water solvent) in order to remove the β-mercaptoethanol (an important additive which prevents oligomersiation of the protein during preparation and transport). Afterwards, a 5 mM solution of Fe^{3+} ions (in the form of potassium ferricyanide) is added in order to ensure a rapid re-cycling to the oxidised state following photo-excitation (without Fe^{3+}, the experiments would require unreasonably long waiting times after each laser shot due to the formation of the long-lived reduced form of the flavin). The final protein concentration is approximately 0.5 mM (20% glycerol/water solvent).

The trEPR experiments were performed following the protocol described in the previous two chapters with a few important exceptions: (1) the temperature was 274 K, (2) photo-excitation was carried out exclusively at 460 nm, (3) the laser repetition rate was set to 1 Hz in order to minimise photo-damaging the samples, (4) the laser power was adjusted to 1 mW (which corresponds to approximately 1 mJ per laser pulse), and crucially, (5) the samples were inserted in a W-band capillary which was placed inside a Q-band tube which was placed inside an X-band tube. This seemingly extravagant W/Q/X sequence of nested tubes was necessary because of the low quality factor of the resonator in the presence of the lossy water/glycerol solvent mixture at 274 K. All reported datasets in the next section represent an average of the transient signals over a range of 500 ns following photo-excitation. No change in spectral shape was observed as a function of time (except for the uniform decrease in intensity across the entire spectrum).

Results and discussion

Figure 6.5 and table 6.3 contain a summary of the trEPR data and simulation results for the three cryptochrome systems considered in this section. First of all, a visual inspection of the experimental trEPR data reveals that for each sample there are absorptive and emissive features which are centred around a g-value of approximately 2.003. Furthermore, the width of each spectrum does not exceed 7–8 mT. In light of these two observations it can be concluded that, in all three cases, the trEPR spectra are a signature of a SCRP, and not of a pair of non-spin correlated (Boltzmann) radicals or of a flavin based triplet state. Boltzmann radicals do not display emissive features[18] and the flavin triplet would have a significantly broader trEPR spectrum owing to a much larger ZFS interaction (of the order of 80 mT) [128]. The similarity between the previously reported *Dm*Cry WT spectrum [115], and the new spectrum of *Er*Cry4 WT shown here is indicative of a fairly conserved SCRP environment between the cryptochromes of the two species. The spectrum of the mutant, *Er*Cry4 W369F is broad and featureless, albeit the spectral width is similar to the other systems. Once again, the spectrum of *Er*Cry4 W369F is consistent with a SCRP, which is an encouraging conclusion, given that both *Er*Cry4 WT and *Er*Cry4 W369F have been shown in our group to exhibit magnetic field effects (results not published at the time of writing).

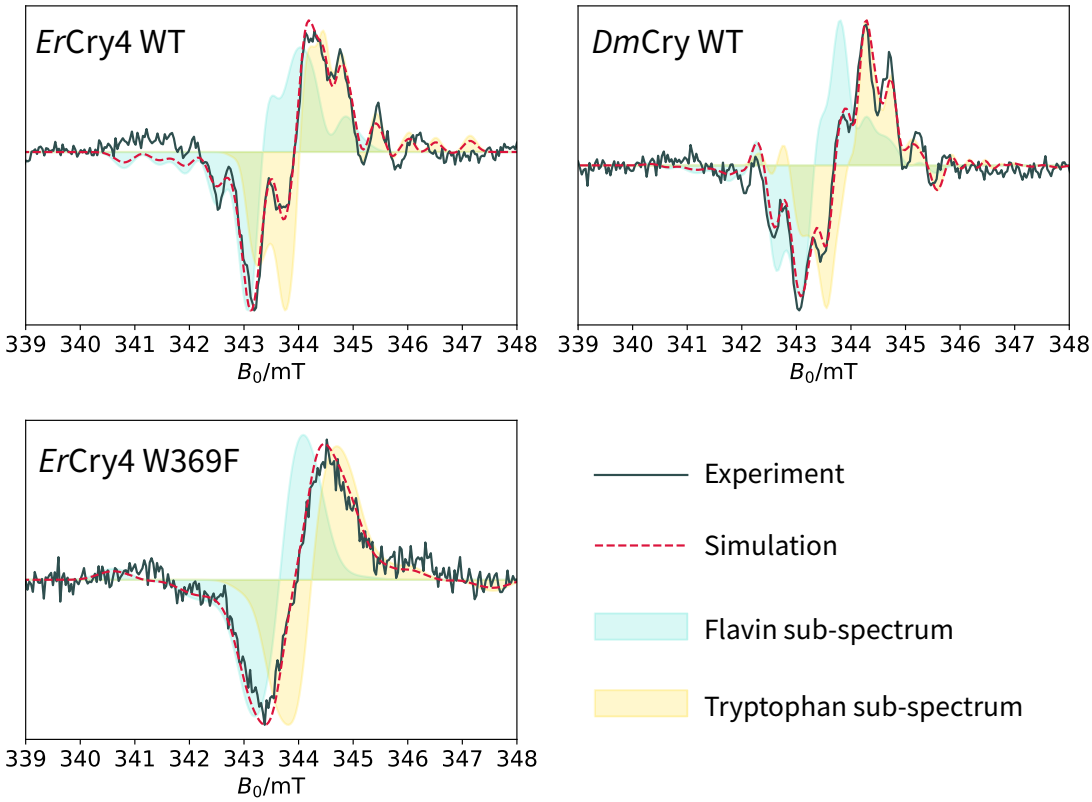


Figure 6.5: X-band trEpr spectra and simulation results for the *Dm*Cry WT, *Er*Cry4 WT, and *Er*Cry4 W369F cryptochrome samples. The simulation parameters are given in table 6.3. The shaded regions represent the sub-spectra of the individual flavin and tryptophan residues. The sum of these is equal to the total simulation (dashed red line).

[18] And they are also silent in a trEPR spectrum (because there is no field modulation to enhance the weak signals of Boltzmann radicals at X-band).

As far as the simulation results and parameters are concerned, the interpretation is highly non-trivial, yet it is still possible to extract –some– quantitative information regarding the SCRP environments of the three cryptochromes. Each simulated spectrum is a result of a least-squares fitting of 21 unique parameters,[19] as illustrated in table 6.3. As will be detailed shortly, some of these parameters are known from the literature. The fact that so many parameters need to be included in the fitting will have a number of consequences: (1) it is impossible to obtain the same level of simulation accuracy as was reported in the previous chapters of this thesis, (2) it is impossible to guarantee the simultaneous uniqueness of all the fitting parameters, (3) these results can only be interpreted as being *consistent* with the expected changes in SCRP environment (and not as ultimate proof of a change in the SCRP environment).

	*Dm*Cry WT			*Er*Cry4 WT			*Er*Cry4 W369F		
$\mathbf{g}_\mathrm{F}$	2.00464	2.00314	2.00131	2.00445	2.00408	2.00273	2.00414	2.00340	2.00247
$\mathbf{g}_\mathrm{W}$	2.00443	2.00245	2.00217	2.00483	2.00259	2.00206	2.00338	2.00241	2.00195
$\boldsymbol{\xi}_\mathrm{W}/^\circ$	63	358	89	64	351	73	237	71	125
J		0.17			0.22			0.78	
D		−8.4			−8.5			−13.9	
$(\theta_D, \phi_D)/^\circ$		(204, 123)			(179, 127)			(118, 107)	
$\mathbf{A}_\mathrm{F}(^{14}\mathrm{N}_1)$	2.4	2.4	64.5	0.1	0.1	47.6	6.1	6.1	67.3
$\mathbf{A}_\mathrm{F}(^{14}\mathrm{N}_2)$	1.6	1.6	31.9	0.4	0.4	31.9	9.3	9.3	25.8
$A_\mathrm{F}(^1\mathrm{H})$		16.7			17.7			11.1	
$\mathbf{A}_\mathrm{W}(^{14}\mathrm{N})$	2.7	2.7	37.6	8.9	8.9	28.9	2.2	2.2	25.3
$A_\mathrm{W}(^1\mathrm{H})$		12.8			6.7			11.6	
λ_F/G		3.44			4.22			6.09	
λ_W/G		2.76			2.89			5.51	

Table 6.3: Best-fit spin Hamiltonian parameters used to generate the simulations in figure 6.5. All simulations were done with the *fawns* function. The 'F' and 'W' subscripts refer to the flavin and tryptophan residues, respectively. The exchange, dipolar, and hyperfine interactions are reported in units of MHz. For each protein, we considered two anisotropic nitrogen hyperfine couplings on the flavin residue and one anisotropic nitrogen coupling on the tryptophan. Additionally, an isotropic proton hyperfine coupling was considered for both residues of the SCRP. The angle sets denoted by $\boldsymbol{\xi}_W$ and (θ_D, ϕ_D) quantify the orientations of the $\mathbf{g}_W$-tensor and dipolar interaction tensor relative to the $\mathbf{g}_F$-tensor. The last two rows, λ_F and λ_W, represent the Gaussian linewidth broadening corresponding to the sub-spectra of the two residues. The dipolar coupling constant, D, is defined as $D = \frac{3}{2}\mathcal{D}(\frac{\pi}{2})$ as per the spin chemistry convention. The J value in this table is also reported in the spin chemistry convention according to which: $J = -\mathcal{J}/2$ (where the calligraphic $\mathcal{J}$ symbol is the one used in the derivations of the previous sections). These conventions are inconsequential for the discussion, yet, they are important for ease of comparison and consistency with the values found in the spin chemistry literature.

Regarding issue (1) raised in the above paragraph, it can be seen clearly that the simulations fail to reproduce all the intricate features of the experimental spectra. In particular, the simulations are less accurate on the low-field and high-field edges of the experimental spectra (especially for *Er*Cry4 WT). Nonetheless, there is an overall agreement between the major turning points of both simulated and

[19] The anisotropic nitrogen hyperfine couplings have been assumed to be perfectly axial, in an attempt to reduce the number of degrees of freedom in the fitting.

experimental spectra for all samples. As will become apparent below, this level of precision is sufficient for the purposes of this investigation; the overall spectral shape is reproduced by a set of sensible parameters (by comparison with literature values; to be cited below).

As mentioned in issue (2) above, the simultaneous uniqueness of all 21 fitting parameters in table 6.3 cannot be guaranteed and neither is this necessary. The most revealing of all the parameters are the dipolar and exchange interactions, quantified by D and J (in particular, as will be detailed shortly, the dipolar interaction is related to the inter-spin distance). Two pertinent observations about D and J can be made at this stage: firstly, if all other parameters in the spin Hamiltonian are kept constant, then an inversion of the sign of both J and D results in a completely inverted simulated spectrum, and secondly, small variations of ±2.5 MHz for D and ±0.1 MHz for J, whilst keeping the same sign as in table 6.3, have very little impact on the goodness of the fit.[20] The fact that the D-value is negative in these simulations is in line with the fact that if the flavin and tryptophan residues are at a sufficiently large distance, then the symmetry of the total spin density is similar to the symmetry of a prolate spheroid.

Having discussed these caveats and complications, it will now be shown that the results in table 6.3 are, in fact, consistent with qualitative expectations regarding the systems. First of all, the reported g-values and hyperfine tensors in this table are all very similar to the ones reported in the literature for free, *i.e.* not protein bound, flavin and tryptophan radicals [130–133] . An approximate assignment (obtained by comparison with literature values) of the hyperfine couplings in table 6.3 to the nuclei of the flavin and tryptophan radicals is presented in figure F.7 of appendix F.

Any small differences between the **g**-tensors and hyperfine parameters in table 6.3 and the ones in the papers cited above are likely a result of small interactions between the radicals and the protein environment (or in the case of $\mathbf{W_4}$ interactions with the solvent; this residue is exposed on the outer surface of the tertiary structure of the protein). Furthermore, the relative orientations of the **g**-tensors and the dipolar interaction tensor in the *Dm*Cry WT system are analogous to the orientations reported in previous trEPR studies of the same protein [115]. Therefore, the similarity of all simulation parameters between *Dm*Cry WT and *Er*Cry4 WT support the fact that the SCRPs and their environments are highly conserved between these two species. Reassuringly, the fact that the **g**-tensors and hyperfine couplings in the mutated *Er*Cry4 W369F system are also very similar to the other two samples, and to the values reported in the literature, is an indication of a SCRP between a flavin and a tryptophan radical.

The first major difference between *Er*Cry4 W369F and *Er*Cry4 WT occurs in the relative orientations of the **g**-tensors and the dipolar interaction tensor, quantified by ξ_W and (θ_D, ϕ_D), respectively, in table 6.3. This is an encouraging result because the absence of $\mathbf{W_4}$ (figure 6.1) in the mutated protein means that the electron transfer terminates on $\mathbf{W_3}$ which is bound to have a different orientation with respect to the flavin residue. More importantly, using the following formula for the relationship between D, and the inter-spin distance, r:[21]

$$r \approx \sqrt[3]{\frac{78}{D/\text{MHz}}}\,\text{nm} \tag{6.40}$$

it can be seen that the inter-spin distance in *Dm*Cry WT and *Er*Cry4 WT is approximately 2.1 nm, whereas in *Er*Cry4 W369F it is approximately 1.8 nm. These distances are in perfect agreement with

[20] These bounds were established by Mr. Pitcher and the accompanying simulations are shown in his Part II thesis [129].
[21] In the EPR convention, the 78 is replaced by 52.

previous EPR studies of the inter-spin distance in cryptochromes [124] and with the crystal structure reported for *Dm*Cry WT [134]. In the next section, they will be confirmed with much greater accuracy by means of the oopESEEM experiment.

In summary, the data for *Er*Cry4 WT and *Er*Cry4 W369F are consistent with flavin/tryptophan SCRPs in both cryptochromes. Notwithstanding the uncertainty of at least ±5 MHz in the *D*-values displayed in table 6.3, we may claim relatively confidently that the data is also consistent with a shorter interspin distance in *Er*Cry4 W369F. In other words, the electron transfer cascade is more extended in the wild-type systems, hence confirming the involvement of the fourth tryptophan. Whilst this was known to be true for the non-migratory fruit fly cryptochrome (*Dm*Cry WT), it is a new finding that the *Er*Cry4 WT cryptochrome from the migratory European robin also has a SCRP which extends to $\mathbf{W_4}$. This realisation, together with the fact that not all cryptochromes have a SCRP which extends over four tryptophans (*e.g.* see references [115, 124, 125]), could have a bearing on future research into the evolution of magnetoreception in avian species.

6.3 Out-of-phase ESEEM of SCRPs

In order to characterise the dipolar interaction and hence the inter-spin distance more thoroughly, the out-of-phase ESEEM –oopESEEM– experiment was employed. Normally in EPR, the distance between two radicals is measured using pulse sequences such as 3– or 4–pulse double electron electron resonance (DEER), or variations thereof. However, by virtue of their spin-correlation, the systems of this chapter can be investigated using the oopESEEM technique. In the next section, this experiment will be introduced briefly from a theoretical perspective, and afterwards, the experimental results will be discussed.

6.3.1 Introduction to oopESEEM

As shown in panel (a) of figure 6.6, oopESEEM consists simply of the Hahn echo sequence applied at a time t after the laser pulse. The laser pulse instantaneously generates a radical pair in a singlet state (and hence, a spin correlated state). The system evolves under the spin Hamiltonian for some time t after being created, and afterwards the two microwave $\pi/2$ and π pulses are applied with an inter-pulse delay τ. As will be seen shortly, this leads to the formation of an echo signal in the imaginary channel, *i.e.* an out-of-phase (oop) echo. The intensity of the oop echo is then monitored as a function of τ; the resulting echo envelope modulations are then analysed, and eventually, the dipolar and exchange interactions can be extracted.

The behaviour of a usual, non-spin correlated radical during the Hahn echo sequence was analysed in Chapter 1. It was seen that by applying a $\pi/2 - \tau - \pi$ pulse sequence with both pulses along $+x$, the result is an echo along the $+y$ axis. These echoes along the $+y$ axis are known as 'real echoes' or equivalently, 'in-phase' echoes. By contrast, spin-correlated radical pairs do not behave like usual radicals under the influence of microwave pulses, and particularly not during the Hahn echo sequence.

The peculiar behaviour of SCRPs in pulse EPR is a direct consequence of their spin correlation as noted in a myriad of literature studies, *e.g.* references [116, 117, 126, 135, 136]. The density matrix formalism can be used to show that, starting from an initial singlet state at time zero, the signal, $S(t, \tau)$ =

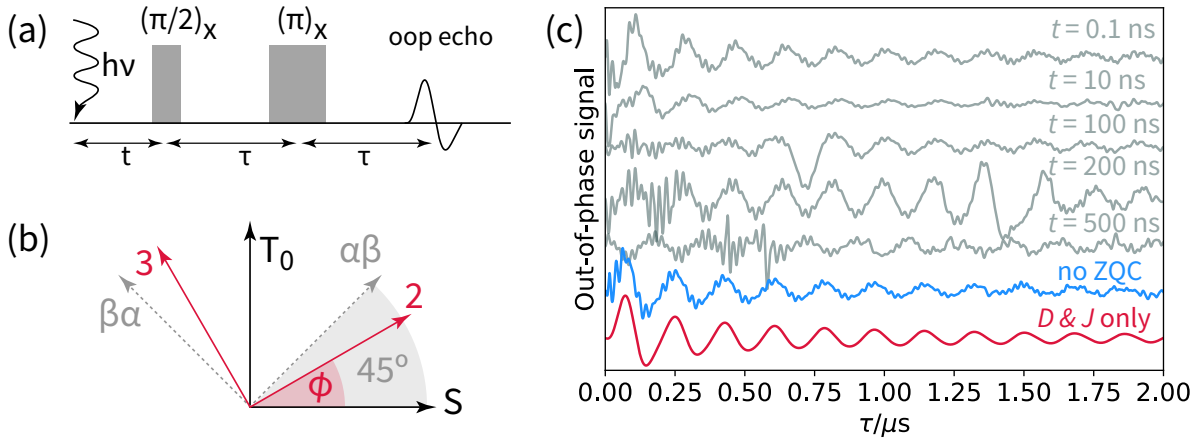


Figure 6.6: (a) The oopESEEM pulse sequence comprised of a laser pulse ($h\nu$), and the Hahn echo sequence. For SCRPs, only the out-of-phase signal (oop echo) has non-zero intensity; this intensity is monitored as a function of τ in order to extract D and J. (b) Diagramatic representation of the phase relationship between the state vectors relevant for SCRPs. ϕ is defined as the coupling angle between eigenstate $|2\rangle$ of the spin Hamiltonian (equations 6.3–6.6) and the singlet state vector. Eigenstate $|3\rangle$ is clearly orthogonal to $|2\rangle$. The $|\alpha\beta\rangle$ and $|\beta\alpha\rangle$ states are also shown as grey arrows. It can be seen that as ϕ approaches 45°, the weak-coupling limit is approached, and the uncoupled basis becomes the eigenbasis. In the strong coupling limit, $\phi \longrightarrow 0$, the eigenstates collapse into the coupled representation. (c) The grey lines represent equation 6.42 plotted for the five indicated values of t. The parameters chosen to generate these plots are as follows: $D = -8.5\,\text{MHz}$, $J = 0.05\,\text{MHz}$, $\phi = 43°$, $T_2 = 3\,\mu\text{s}$. The blue line is the angular average of equation 6.43, which corresponds to the oopESEEM experiment in the absence of zero-quantum coherence. Finally, the red line is a plot of equation 6.46; this corresponds to the oopESEEM experiment in the quasi-weak-coupling limit where the modulations depend only on D and J.

$S_y(t,\tau) + iS_x(t,\tau)$, resulting from the $h\nu - t - \pi/2 - \tau - \pi - \tau$ pulse sequence is given by [136]:

$$\begin{cases} S_x(t,\tau) = \sin^2(2\phi)\cos(2\phi)\left[\cos(\omega_{23}\tau) - 1\right]\left\{\sin(\omega_{23}t)\cos\left[\left(\frac{2}{3}D\left(3\cos^2\theta - 1\right) - 2J\right)\tau\right] + \right. \\ \qquad\qquad \left. + \cos(2\phi)\left[1 - \cos(\omega_{23}t)\right]\sin\left[\left(\frac{2}{3}D\left(3\cos^2\theta - 1\right) - 2J\right)\tau\right]\right\} \\ S_y(t,\tau) = 0 \end{cases} \tag{6.41}$$

The meaning of the symbols within this equation and the assumptions made in its derivation are:

- ϕ is the coupling angle (in Hilbert space) between the singlet state vector, $|S\rangle$, and eigenstate $|2\rangle$ of the SCRP Hamiltonian, as shown in panel (b) of figure 6.6,
- J and D are the exchange and dipolar interaction parameters (the latter is related to the distance by equation 6.40),
- ω_{23} is equal to $(E_3 - E_2)/\hbar$ as defined in equations 6.9 and 6.10,
- θ is the angle between the inter-spin vector and the external magnetic field vector,
- only the secular part of the dipolar interaction is considered,
- hyperfine couplings are neglected.

A direct consequence of equation 6.41 is that a SCRP does not give rise to an in-phase echo, $S_y(t,\tau)$, and furthermore, both t and τ have to be non-zero in order to observe an oop echo. The fact that the

delay between the laser pulse and the first microwave pulse has to be non-zero is easily interpreted: if the system is not given enough time to evolve into a state with more triplet ($|T_0\rangle$) character, then the $\pi/2$ pulse cannot induce coherence, and therefore, the subsequent π pulse has nothing to refocus.

For a powder sample, the final signal is given by the average of $S_x(t, \tau)$ over all orientations:

$$\tilde{S}_x(t, \tau) = 2\pi \exp(-\tau/T_2) \int_0^{\pi} S_x(t, \tau) \sin\theta \, d\theta \tag{6.42}$$

whereby we have defined the phase-memory time due to relaxation processes as T_2. The grey traces in panel (c) of figure 6.6 depict the behaviour of the oop signal, $\tilde{S}_x(t, \tau)$, as a function of τ and t for a fictitious SCRP system with $D = -8.5\,\text{MHz}$, $J = 0.05\,\text{MHz}$, and $\phi = 43^\circ$. We see that for each of the t values shown, these time traces are a complicated superposition of the angular frequencies contained in equation 6.41. Interestingly, at early times, such as $t = 0.1\,\text{ns}$ or $t = 10\,\text{ns}$, the dominant frequency component of the time traces corresponds to the average over all θ of $\left(\frac{2}{3}D\left(3\cos^2\theta - 1\right) - 2J\right)$, *i.e.* the net dipolar and exchange frequencies. We will shortly illustrate that for most systems of interest the complicated behaviour depicted by the grey traces in figure 6.6 is more the exception than it is the rule, and the interpretation of oopESEEM data is less convoluted than this treatment implies.

It is important to note that, had we set $\phi = 45^\circ$, which is the weak-coupling limit, then $S_x(t, \tau)$ would have been exactly zero. This is one of the major peculiarities of SCRPs: in the weak coupling limit, there is neither an in-phase nor an out-of-phase signal following a two-pulse Hahn echo sequence [70, 116, 136]. Nonetheless, in most real experiments, the oop signal is actually observable even in the weak-coupling limit.

There are a few reasons for the above fact. Firstly, real microwave pulses are rarely ideal and completely non-selective, and therefore, not all spin packets in the ensemble experience the nominal $\pi/2$ and π flip angles. It was shown in reference [116] that the oop signal of a SCRP is, in fact, maximised when the flip angles are set to $\pi/4$ and π (albeit, ideal and non-selective pulses were assumed in this reference as well). This observation has also been justified in reference [137], whereby numerically optimised pulses (in a feedback control loop) were used to increase the modulation depth of the oopESEEM experiment.

Secondly, the oop signal is zero only when ϕ is exactly 45°, *i.e.* in the 'idealised' weak-coupling limit. Even in the most weakly coupled of systems, the ϕ angle is rarely exactly 45°, it is more likely to have a distribution of values. Hence, in real systems, $S_x(t, \tau)$ is not expected to be zero even in what might formally be classed as the weak-coupling limit.[22]

The next point that needs to be addressed is that the complicated overlap of oscillation frequencies contained in $S_x(t, \tau)$ (and depicted in figure 6.6) is rarely observed in SCRPs if t is set to be larger than approximately 100 ns [116]. The main source of complication is that equation 6.41 is derived without neglecting the zero-quantum coherence (ZQC) between states $|2\rangle$ and $|3\rangle$. This ZQC is converted to detectable single-quantum coherence under the influence of the microwave pulses, and hence, it can refocus at the time of the echo,[23] and cause the development of the complicated traces depicted in figure 6.6. As shown in reference [116], once this ZQC is neglected owing to the fact that it decays rapidly,

[22] Albeit, if the distribution of ϕ around 45° is very sharp, then the oop signal will be very weak.
[23] This was observed experimentally for the first time in reference [138].

the t dependence of the signal disappears, and we are left with the following equation:

$$S_x(\tau) = \cos^2(2\phi)\sin^2(2\phi)\sin(\omega_e\tau)(1-\cos(\omega_{23}\tau)) \tag{6.43}$$

where we have defined the combination of dipolar and exchange frequencies, ω_e, as:

$$\omega_e = \frac{2}{3}D\left(3\cos^2\theta - 1\right) - 2J \tag{6.44}$$

The angular average of equation 6.43 is plotted as the blue trace in figure 6.6 for the same SCRP system as before. It can once more be seen that in the exact weak coupling limit, $\phi = 45^\circ$, the oop echo vanishes. In the almost-weak-coupling limit, *e.g.* the $\phi = 43^\circ$ situation shown in figure 6.6, the time-dependence of the signal is greatly simplified compared with the results of equation 6.41. However, there is still a high frequency component with a much lower modulation depth which overlaps with the primary frequency (ω_e). This high-frequency component is due to the ω_{23} term in equation 6.43 which originates in the singlet-triplet coherence of the SCRP.[24] In the case at hand, it is easily verified that ω_{23} is large; for $\phi = 43^\circ$ and $\theta = \pi/2$, it is approximately 80 MHz. Therefore, we can approximate $1 - \cos(\omega_{23}\tau) \approx 1$, and write:[25]

$$S_x(\tau) \approx \cos^2(2\phi)\sin^2(2\phi)\sin(\omega_e\tau) \tag{6.45}$$

and by taking the average over all orientations, the oopESEEM signal will obey the following scaling relation:

$$\tilde{S}_x(\tau) \sim 2\pi\exp(-\tau/T_2)\int_0^\pi \sin(\omega_e\tau)\sin\theta\, d\theta \tag{6.46}$$

This final equation (shown as the red trace in figure 6.6) is the most commonly employed formula for the analysis of oopESEEM data of singlet-born SCRPs (applicable in the almost-weak-coupling limit). Hence, this equation is the basis of all analyses which will be presented in the remaining sections of this chapter. The merits of this treatment are evident from the fact that it has lead to the determination of the inter-spin distance in a wide array of naturally occuring SCRP, such as the ones in references [124, 139–142].

To summarise, the formal treatment of the evolution of SCRPs during the Hahn echo sequence leads to modulations in the oop signals which are very complicated (equation 6.41). However, for a system which is close to being in the weak-coupling limit, with a ϕ-value around 45°, the formulas can be simplified to the ones given in equations 6.43 and 6.45. The latter of these equations shows that the oscillations in the oopESEEM trace of the SCRPs relevant to this thesis are dominated by the dipolar and exchange interactions.

6.3.2 Methodology

Samples

The same three samples, *Er*Cry4 WT, *Er*Cry4 W369F, and *Dm*Cry WT, which were investigated with trEPR in section 6.2.3 were also investigated with the oopESEEM pulse sequence. In addition, two

[24] Just like the phase-coherence between states $|2\rangle$ and $|3\rangle$, the singlet-triplet coherence also evolves at the ω_{23} frequency. Naturally, in the relatively large magnetic fields of the EPR spectrometer, the Δg-mechanism dominates, and hence, this frequency is very large compared to the dipolar and exchange frequencies.

[25] The limit of a sine or cosine function as the argument approaches infinity is equal to zero.

other wild-type cryptochrome 4 proteins from avian species will be studied here, namely: *Gg*Cry4 WT, which is from the domestic chicken (*Gallus gallus*), and *Cl*Cry4 WT, which is from the common pigeon (*Columba livia*); both of these are non-migratory species. These additional cryptochromes were also expressed by Ms. Jingjing Xu from the group of Prof. Henrik Mouritsen from the University of Oldenburg.

By contrast with *Er*Cry4 WT and *Er*Cry4 W369F both *Gg*Cry4 WT and *Cl*Cry4 WT cryptochromes exhibit a smaller magnetic field effect (data not published). Therefore, an EPR study could reveal whether a SCRP is formed in these proteins at all, and if so, whether the radical pair environment is in any way different between the robin, chicken, and pigeon. Owing to the fact that the oopESEEM data depends on significantly fewer parameters than trEPR, *i.e.* data analysis is less ambiguous, only this former technique was used for all five cryptochrome samples. Any difference observed between the data for *Er*Cry4 WT, *Er*Cry4 W369F, *Gg*Cry4 WT, and *Cl*Cry4 WT, is likely to help to further our understanding of the evolution of magnetic sensitivity in avian species. As before, the *Dm*Cry WT system has been published before, and will be used here for reference [124].

All samples in this oopESEEM study were prepared in the same manner as for the trEPR study in section 6.2.3. Some additional analyses and simulations of the data were performed independently by Mr. Pitcher and are reported in his Part II thesis [129]. As far as this chapter is concerned, these additional analyses have helped to estimate the error bounds for the fitting parameters; these results will be mentioned when they become relevant for the discussion, however, the accompanying simulation results will not be shown explicitly (they are found in reference [129]).

Acquisition of oopESEEM data

All oopESEEM data was acquired at Q-band on a Bruker Elexsys E580 spectrometer equipped with a D2 resonator. Whilst the typical temperature for oopESEEM measurements on cryptochromes is 80 K, additional measurements at higher temperatures were also taken in order to test the hypothesis of a radical pair equilibrium. The reason for acquiring the pulse EPR data at significantly lower temperatures compared with trEPR was in order to maximise the phase-memory time, T_2, which is one of the limiting factors for these pulse measurements (trEPR signals are independent of the phase-memory time, they are limited by the rate at which spin polarisation decays).

Due to the fact that lower temperatures were employed in oopESEEM, the laser repetition rate could be increased to 4 Hz, rather than the 1 Hz rate used in trEPR.[26] The wavelength was set to 460 nm as for the trEPR spectra. All results in the next section are an average of many individual scans which were acquired separately (usually during the same 12 hour period), and added together in post processing. Each individual scan was designed to take less than approximately 30 minutes; this allows the quality of the signal to be checked before starting the next scan.

The oopESEEM experiments were acquired with the following pulse sequence:

$$(\xi) - T - (h\nu) - t - (\pi/2)_x - \tau - (\pi)_x - \tau - (\text{oop echo})_x$$

[26] Larger repetition rates were also trialled and beyond approximately 10 Hz, significant bleaching (signal reduction) was observed within minutes after the start of the experiment. The chosen 4 Hz repetition rate offered a suitable compromise between the rate of signal decay and the time it takes to acquire the data.

The variable ξ denotes a pre-saturation pulse (nominal flip angle π) which is applied at a time $T = 10\,\mu$s before the laser pulse ($h\nu$). This pre-saturation pulse was necessary because upon illumination, the build-up of an intense dark state radical signal was observed. This signal is likely to belong to the protonated form of the flavin radical,[27] and its contribution to the final data is not desired; after approximately 30 minutes of illumination with the laser at 4 Hz, the build-up of this signal reaches a steady state value. The power of the ξ pulse and the delay T were adjusted so as to cancel the contribution from this dark-state radical signal to the final spectra of the SCRP. At time $t = 200$ ns after the laser pulse, the Hahn echo sequence is applied with pulse lengths of 8 ns and 16 ns for $\pi/2$ and π flip angles, respectively.[28] The inter-pulse delay τ was swept between 100 ns and 2000 ns with an increment of 4 ns. The magnetic field was set to the maximum intensity in the oop component of the echo-detected field swept spectra. This field position also corresponded approximately with the zero-crossing of the in-phase component (as expected). For reference, the echo-detected field sweeps are shown in figure F.6 of appendix F.

Finally, for every individual oopESEEM trace recorded with the laser on, another spectrum was recorded with the laser off. This allowed us to confirm that the signals observed are indeed due to the transient SCRP. As mentioned above, before adding them together, each of the individual scans (which take approximately 30 minutes to acquire) were checked to ensure the persistence of the signal intensity and to ensure that no major microwave phase drift occurred.

6.3.3 Results and discussion

80 K oopESEEM results

Figure 6.7 depicts the experimental (80 K) and simulated oopESEEM data for *Dm*Cry WT, *Er*Cry4 WT, *Cl*Cry4 WT, *Gg*Cry4 WT, and *Er*Cry4 W369F, whilst the best-fit values of D, J, and T_2 are shown in table 6.4. Before the quantitative simulation results are scrutinized and interpreted in more detail, there are a number of important qualitative observations to be made about the appearance of the experimental results.

All of the experimental oopESEEM traces show a damped oscillatory evolution as a function of τ. None of these traces display any discernable high frequency components,[29] therefore suggesting that these SCRPs are very close to the weak-coupling limit as observed qualitatively from the trEPR simulation parameters in the previous section.[30] In other words, the oscillations are highly likely to be driven primarily by the dipolar and exchange interactions. Furthermore, as was shown in the trEPR section, the exchange interaction in cryptochrome systems is expected to be very small, less than ca. 1 MHz, and hence, the primary source of modulation in these data sets is the dipolar interaction.

In light of this observation, and due to the fact that all the wild-type samples display very similar oopESEEM traces, we can conclude fairly confidently that the inter-radical distance is highly conserved between all these species. By contrast, the oopESEEM trace of the mutant, *Er*Cry4 W369F, is very

[27] according to optical absorption measurements performed in the group

[28] The power of the pulses was adjusted by optimising the echo of the dark state radical (in the absence of the pre-saturation pulse).

[29] The time increment in these traces is 4 ns. According to the Nyquist criterion, the largest frequency which can be resolved under these conditions is $1/(8\,\text{ns}) = 125$ MHz.

[30] Unfortunately, it is not possible to extract a unique coupling angle for these cryptochrome SCRPs because the formula for ϕ is only clearly defined for the simple case of isotropic g-values and in the absence of anisotropic hyperfines.

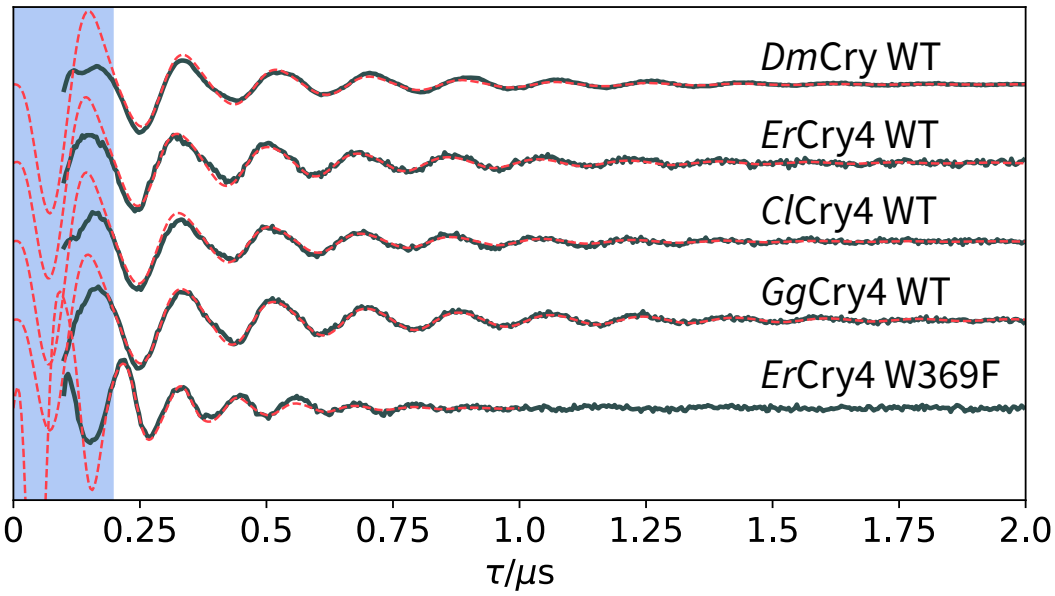


Figure 6.7: Experimental (solid black lines) and simulated (dashed red lines) oopESEEM traces for the five indicated cryptochrome proteins. All data sets were recorded at 80 K. All simulations were obtained using equation 6.46 and the corresponding fitting parameters are displayed in table 6.4. The blue shaded area between 0 and 200 ns indicates the part of the experimental trace which was *not* included in the fitting process.

different, and consistent with a significantly shorter distance between the radicals (a larger dipolar frequency).

The main differences between all the wild-type data sets occurs in the region between $\tau = 100$ ns (the starting point) and $\tau = 200$ ns (highlighted in blue in figure 6.7). Unfortunately, the interpretation of this early time region is problematic in the purely dipolar and exchange picture. This is because anisotropic hyperfine interactions will contribute more to the oopESEEM trace at these early times. Hyperfine modulations have a much smaller modulation depth in oopESEEM compared to the dipolar and exchange contributions, hence why only the interpretation of the data points at early times is compromised. Such effects are discussed in more detail in reference [143].

Sample	D/MHz	r/nm	J/MHz	T_2/μs
*Dm*Cry WT	−8.21	2.12	0.003	0.384
*Er*Cry4 WT	−8.61	2.08	0.050	0.486
*Cl*Cry4 WT	−8.50	2.09	0.030	0.404
*Gg*Cry4 WT	−8.37	2.10	0.030	0.600
*Er*Cry4 W369F	−14.0	1.77	0.330	0.121

Table 6.4: Best-fit parameters used to generate the simulations depicted in figure 6.7 by means of equation 6.46. The inter-spin distance is not directly included in the fit, it is simply obtained from D by application of equation 6.40. The most important observation from this table is the fact that r is almost the same in all wild-type species, whilst it is smaller in the mutant.

Moreover, also in reference [143], it is shown that the precision with which D and J can be extracted from oopESEEM is not compromised significantly by truncating the data such that only the later mod-

ulations (beyond 200 ns in this case) are included in the analysis. This is entirely to be expected if it is assumed that nuclear ESEEM effects are strongest at early times: neglecting the early times leads to a fit which 'focuses' on D and J, despite the signal-to-noise ratio being slightly lower. In fact, in the case of the data shown in figure 6.7, inclusion of the entire data set in the fitting process results in almost the same simulation parameters as table 6.4. However, the resulting fit becomes only marginally more faithful to the initial peaks whilst compromising the goodness of fit for the rest of the oopESEEM trace.

The above considerations are the reason why the simulations depicted in figure 6.7 have been truncated to the experimental data between 200 and 2000 ns. Apart from the truncation, there are a few other aspects concerning the uniqueness of the fitting parameters shown in table 6.4. For example, it is relatively easy to show that the J-value in all cases can be set to zero, and the changes in the fit can be compensated by small changes in D and T_2. Furthermore, it could also be possible that there are two SCRPs contributing to the data as a result of an equilibrium between the third and fourth tryptophan. This radical pair equilibrium could also be responsible for the mismatch between data and simulation at early times.

All of these factors (and many more) which might affect the uniqueness of the fitting parameters have been addressed in an extensive series of simulations performed (independently) by Mr. Tommy L. Pitcher [129], and will be published elsewhere in due course. Whilst valuable, a detailed account of these simulations is not necessary for the purposes of this thesis. The ultimate conclusion is that, regardless of how the fitting is performed, the wild-type species (*Dm*Cry WT, *Er*Cry4 WT, *Cl*Cry4 WT, *Gg*Cry4 WT) exhibit very similar inter-spin distances, in the range of 2.0–2.1 nm, whereas the mutant (*Er*Cry4 W369F) has a significantly shorter distance of 1.75-1.85 nm. Whilst the minute differences between the simulation parameters in table 6.4 are not interpretable, the overriding observation is that the SCRPs of these wild-type cryptochromes are remarkably similar, and that the electron transfer extends to the fourth tryptophan in all of them.

In future work, it might be possible to infer more about these proteins from the differences observed in the oopESEEM data between 100 ns and 200 ns. This would require a simulation method which can reliably account for nuclear modulation effects. As they stand, the conclusions about the inter-spin distance arrived at in this section are unlikely to be influenced by more advanced simulations with an ever growing number of parameters, should these become tangible.

Variable temperature oopESEEM

As alluded to in the above section and throughout the discussion, there is some evidence from optical spectroscopy experiments and molecular dynamics modelling that a radical pair equilibrium could have a bearing on the magnetic sense of certain avian species. In particular, it could be that a dynamic equilibrium between the third and fourth tryptophan residues influences the formation of certain signalling species. Moreover, it is also feasible that certain species, such as the robin, have optimised this equilibrium through the process of evolution.

At this stage, these ideas remain only a hypothesis, and they are also one of the primary motivations for striving to measure the inter-spin distance at ever higher, and more biologically relevant, temperatures.[31] This is particularly interesting in light of the sensitivity of the oopESEEM technique to rather

[31] As it stands, it is not possible to predict with certainty whether this potential equilibrium would be shifted towards $\mathbf{W}_3$

small differences in r, such as the difference between *Er*Cry4 WT and *Er*Cry4 W369F noted in the previous section. Another reason for investigating higher temperatures could be the potential to reveal a difference in conformational changes between different cryptochromes from different species.

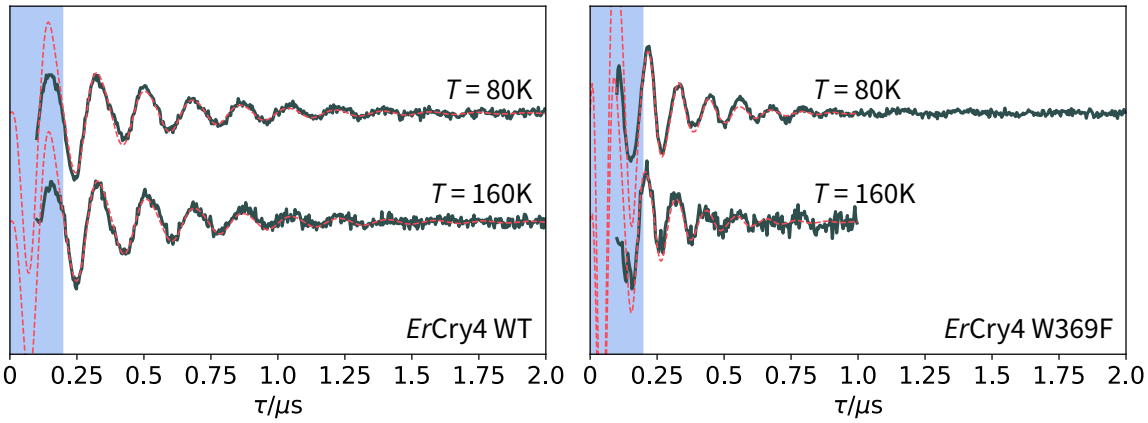


Figure 6.8: (Left) Experimental (solid black lines) and simulated (dashed red lines) oopESEEM traces for the *Er*Cry4 WT sample measured at 80 K and 160 K. (Right) The equivalent oopESEEM data and simulations for the *Er*Cry4 W369F system. The 80 K data in both panels is the same as figure 6.7. The simulation parameters are displayed in table 6.5. The blue shaded region in these panels (and in figure 6.9) represent the part of the experimental trace which was not included in the fitting procedure.

For these reasons, oopESEEM measurements were carried out at 80 K and 160 K on the *Er*Cry4 WT and *Er*Cry4 W369F systems and the resulting experimental and simulated oopESEEM traces are shown in figure 6.8. The corresponding simulation parameters are given in table 6.5. As expected, both samples show a slight decrease in the signal-to-noise ratio at the higher temperature, probably due to a greater rate of signal bleaching.[32] However, it is entirely obvious, even from visual inspection, that increasing the temperature has no effect on the frequency content of these traces. Inspection of the parameters in table 6.5 also proves, without any doubt, that the 80 K and 160 K data sets are identical within signal-to-noise. None of the minute differences between D, J, and T_2 exhibited by the fitting results are interpretable.

Despite the lack of a temperature effect in the data shown in figure 6.8, we cannot completely rule out a potential radical pair equilibrium between the third and fourth tryptophan at higher temperatures. Unfortunately, attempts at measurements with $T > 200$ K have been unsuccessful for all of these cryptochrome systems. Moreover, oopESEEM measurements at physiological temperatures (which for birds correspond to ca. 40°C) are likely to fail regardless of the presence or absence of an equilibrium, because the dipolar interaction averages to zero in the rapid tumbling regime. On the other hand, although the equilibrium hypothesis cannot be ruled out with complete certainty, it is highly implausible that a temperature change of a factor of two, 80 K ⟶ 160 K, would have no impact on the supposed equilibrium (be it fast, slow, or intermediate on the experimental time scale).

As a further case in point, figure 6.9 shows that all the observations made about the *Er*Cry4 WT and *Er*Cry4 W369F systems persist in the comparison of the data recorded at 80 K and 200 K for the *Gg*Cry4 WT sample. If one were to consider only the *Er*Cry4 WT cryptochrome, then the lack of a radical pair

or $\mathbf{W}_4$ by an increase in temperature.

[32] Also, the measurements at the higher temperature were taken on the same sample after the measurements at 80 K. The signal does decrease in intensity after a prolonged period of illumination.

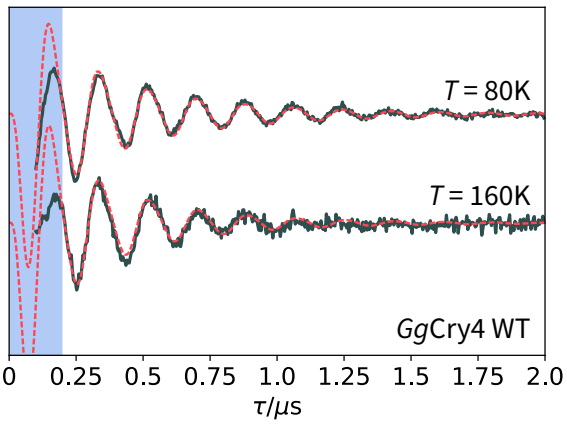


Figure 6.9: Experimental (solid black lines) and simulated (dashed red lines) oopESEEM traces for the *Gg*Cry4 WT sample measured at 80 K and 200 K. The simulation parameters are given in table 6.5. Just like the *Er*Cry4 WT and *Er*Cry4 W369F systems, the *Gg*Cry4 WT system is also unchanged (within signal-to-noise) by increasing the temperature (both in experiment and simulation).

Sample	D/MHz	r/nm	J/MHz	T_2/μs
*Er*Cry4 WT (80 K)	−8.61	2.08	0.050	0.486
*Er*Cry4 WT (160 K)	−8.49	2.09	0.040	0.517
*Er*Cry4 W369F (80 K)	−14.0	1.77	0.330	0.121
*Er*Cry4 W369F (160 K)	−13.9	1.78	0.160	0.195
*Gg*Cry4 WT (80 K)	−8.37	2.10	0.030	0.600
*Gg*Cry4 WT (200 K)	−8.26	2.11	0.020	0.474

Table 6.5: Best-fit parameters used to generate the simulations depicted in figures 6.8 and 6.9 by means of equation 6.46.

equilibrium could also be construed as being a relevant factor in the evolution of avian magnetoreception. However, the data and the simulations for the non-migratory chicken cryptochrome (*Gg*Cry4 WT) are also almost identical between the two temperatures probed here.

In summary, the variable temperature results presented here for the *Er*Cry4 WT, *Er*Cry4 W369F, and *Gg*Cry4 WT cryptochromes neither confirm nor refute the hypothesis of an equilibrium radical pair between the third and fourth tryptophan in the wild-type proteins. However, the similarity between low and high temperature measurements does constitute a rather important issue which will be difficult to explain from the standpoint of a dynamic equilibrium of the kind considered above.

6.4 Concluding remarks

This chapter began with a brief survey into one of the most prominent hypotheses for the mechanism by which certain avian species are able to sense the magnetic field of the Earth. This was the radical pair mechanism, which is believed to occur within cryptochromes by virtue of their ability to host a light-induced, singlet-born SCRP. This SCRP is a result of a sequence of electron transfers (initiated by light excitation) from across a triad/ tetrad of tryptophan residues to a flavin cofactor bound to the surface of the protein (figure 6.1).

The discussion continued with a simplified mathematical description of SCRPs which provided a proof of principle for one of the major requirements of a chemical/biological compass: that a magnetic field can influence the process of singlet-triplet interconversion. The same spin Hamiltonian was then used to show how EPR spectroscopy can be employed both as an unambiguous test for spin correlation and as an analytical tool for quantifying the spin interactions present in SCRPs.

In order to be able to interpret the trEPR spectra of complicated SCRPs, it was necessary to develop a simulation algorithm which is both computer-time efficient and sufficiently accurate to capture both the fine and hyperfine structure interactions of arbitrarily complex SCRP systems. Two such algorithms were presented, *cockatiel* and *fawns*, *i.e.* a slow and accurate procedure, and a fast and 'accurate enough' procedure, respectively.

The latter of these simulation programs proved to be the most suitable for the description of the complicated trEPR spectra of three cryptochrome samples (*Dm*Cry WT, *Er*Cry4 WT, and *Er*Cry4 W369F). It was found that, in spite of the very large number of parameters required to fit the data, the mutated protein, *Er*Cry4 W369F, exhibited larger dipolar and exchange interactions, thus suggesting a shorter inter-spin distance. This provided the first hint that the electron transfer chain in the wild-type *Er*Cry4 WT cryptochrome (belonging to one of the most famous long-distance navigators in nature, the European robin) extends over a tetrad rather than a triad of tryptophan residues.

In the second part of this chapter, the results of a pulse out-of-phase ESEEM investigation provided a convincing quantification of the dipolar and exchange interactions in cryptochromes. It was confirmed that the electron transfer in wild-type *Er*Cry4 WT, *Cl*Cry4 WT, and *Gg*Cry4 WT cryptochromes extends to the fourth tryptophan residue, just as it does in the well-characterised *Dm*Cry WT system. Afterwards, the potential for an equilibrium electron transfer between the third and fourth tryptophans was also considered by comparing oopESEEM data recorded at different temperatures for *Er*Cry4 WT, *Er*Cry4 W369F, and *Gg*Cry4 WT. Whilst these pulse EPR measurements are not feasible at biologically relevant temperatures, the lack of change in the observed inter-spin distance between 80 K and 200 K throws into doubt the hypothesis of a signalling pathway reliant on an equilibrium between the third and the fourth tryptophan.

Appendix A

General eigensolution of the Hamiltonian for triplet states

The secular determinant of the Hamiltonian in equation 1.51 is given by:

$$\det\left(\mathcal{H} - \mathbf{1}_3 E\right) = \begin{vmatrix} -D_x - E & -i\hbar\gamma_y & \hbar\gamma_z \\ +i\hbar\gamma_y & -D_z - E & \hbar\gamma_x \\ \hbar\gamma_z & \hbar\gamma_x & -D_y - E \end{vmatrix} = 0 \tag{A.1}$$

which expands to the following cubic polynomial in the energy:

$$E^3 + E^2(D_x + D_y + D_z) + E(D_xD_y + D_xD_z + D_yD_z - \hbar^2\gamma_z^2 - \hbar^2\gamma_y^2 - \hbar^2\gamma_x^2) + \\ + D_xD_yD_z - \hbar^2\gamma_z^2D_z - \hbar^2\gamma_y^2D_y - \hbar^2\gamma_x^2D_x = 0 \tag{A.2}$$

The free term can be identified with the determinant of $\mathcal{H}$, the linear term is the trace of the adjugate of $\mathcal{H}$, and the quadratic term is the trace of the **D**-tensor. Given that the latter is zero, we can contract the above equation to:

$$E^3 + \mathrm{tr}\left[\mathrm{adj}\left(\mathcal{H}\right)\right] E - \det\left(\mathcal{H}\right) = 0 \tag{A.3}$$

It is known that this equation will only admit real roots because $\mathcal{H}$ is a hermitian matrix. The three solutions given in equation 1.52 are expressed in the trigonometric form of François Viète:

$$E_k = 2\sqrt{-\frac{\mathrm{tr}\left(\mathrm{adj}\left(\mathcal{H}\right)\right)}{3}}\cos\left(\frac{1}{3}\arccos\left(-\frac{3\det\left(\mathcal{H}\right)}{2\,\mathrm{tr}\left(\mathrm{adj}\left(\mathcal{H}\right)\right)}\sqrt{-\frac{3}{\mathrm{tr}\left(\mathrm{adj}\left(\mathcal{H}\right)\right)}} - k\frac{2\pi}{3}\right)\right), \quad \text{for } k \in \{0,1,2\} \tag{A.4}$$

There is no advantage in using this formula for the eigenvalues of $\mathcal{H}$ in spectral simulations. For triplet states, the usual diagonalisation routines of (3×3) matrices are sufficiently fast, so that there is no real advantage of an analytical approach. This equation is derived here purely for interest, and also to illustrate that, in spite of being analytical and general, it offers no further insight compared to numerical approaches. The fact that for a relatively simple system, comprised only of an electronic spin with $S = 1$, the eigenvalues are given by such a complicated formula as A.4 is indicative of the fact that numerical approaches are the only viable option for more complex systems.

Appendix B

The Breit-Rabi equation

The key to the derivation of the eigensolution of equation 1.101 is an analysis of the properties of the $\hat{\mathbf{S}} \cdot \hat{\mathbf{I}}$ operator. These properties can be better seen from the expansion:

$$\hat{\mathbf{S}} \cdot \hat{\mathbf{I}} = \frac{1}{2}\left[\hat{F}^2 - \hat{S}^2 - \hat{I}^2\right] = \hat{S}_z\hat{I}_z + \frac{1}{2}\left[\hat{S}_+\hat{I}_- + \hat{S}_-\hat{I}_+\right] \tag{B.1}$$

where $\hat{\mathbf{F}} = \hat{\mathbf{S}} + \hat{\mathbf{I}}$ is the total electron-nuclear spin operator and $\hat{S}_\pm$, $\hat{I}_\pm$ are raising and lowering operators. Equation B.1 therefore implies that the total projection quantum number, $m_F = m_I + m_S$, is preserved as a good quantum number for the eigenstates of the total Hamiltonian in equation 1.101 because $\hat{\mathbf{S}} \cdot \hat{\mathbf{I}}$ commutes with $\hat{F}_z$. However, F is not a good quantum number because $\hat{F}^2$ does not commute with $\hat{S}_z$ and $\hat{I}_z$ (it only commutes with $\hat{\mathbf{S}} \cdot \hat{\mathbf{I}}$). All in all, these commutation relations imply that we can label the eigenstates by m_F but not by F.

From the final expansion in equation B.1, we can also deduce that the matrix representation of $\hat{H}$ in the $|m_S, m_I\rangle$ basis is block-diagonal. More precisely, the only matrix elements of $\hat{H}$ which are non-zero occur between pairs of the following basis states:

$$|\pm\rangle = |\pm\frac{1}{2}, m_I = m_F \mp \frac{1}{2}\rangle \tag{B.2}$$

Hence, for every $m_S = \pm\frac{1}{2}$ and corresponding m_I, the spin Hamiltonian will consist of blocks which take the following form:

$$\mathcal{H} = \begin{pmatrix} H_{++} & H_{+-} \\ H_{-+} & H_{--} \end{pmatrix} \tag{B.3}$$

where:

$$H_{\pm\pm} = \pm\frac{1}{2}(\gamma_S + \gamma_I)\hbar B - \gamma_I B\hbar m_F \pm \frac{a\hbar^2 m_F}{2} \mp \frac{a\hbar^2}{4} \tag{B.4}$$

$$H_{\pm\mp} = \frac{a\hbar^2}{2}\sqrt{(I + 1/2)^2 - m_F^2} \tag{B.5}$$

The eigenvalues of equation B.3 can trivially be shown to be given by the Breit-Rabi equations in 1.102-1.104.

As mentioned in the main text, for a transition between the $m_S = \pm\frac{1}{2}$ states of the electron (for a particular value of m_I) the fixed-point iteration which converges to the Breit-Rabi resonance fields is

given by [9, 13]:

$$B_{k+1} = \frac{a\hbar}{\gamma_e + \gamma_I} \frac{1}{1 - \left(\frac{a\hbar^2}{2h\nu_k}\right)^2} \left\{ -m_I \pm \sqrt{m_I^2 + \left[1 - \left(\frac{a\hbar^2}{2h\nu_k}\right)^2\right]\left[\left(\frac{h\nu_k}{a\hbar^2}\right)^2 - (I + 1/2)^2\right]} \right\} \tag{B.6}$$

where:

$$\nu_k = \nu + \frac{\gamma_I B_k}{2\pi} \tag{B.7}$$

The starting point, B_0, for the iteration is typically set equal to the value of equation B.6 for $\gamma_I = 0$ *i.e.* by neglecting the nuclear Zeeman interaction. The following is a Python script which performs the above fixed-point iteration:

```
import numpy as np

# Parameter definition
ge = 2 # Electron g-factor
a = 50 # Hyperfine coupling in MHz
I = 1 # Nuclear spin quantum number
gn =  0.4038 # Nuclear g-factor (here it is for 14N)
nu = 10 # Microwave frequency in GHz

# Initial setup
nu = nu*1000 # Convert to MHz
muB = (9.274009e-24/6.6260688e-34)*1e-9 # Bohr magneton MHz/mT
muN = (5.050783e-27/6.6260688e-34)*1e-9 # Nuclear magneton MHz/mT
mI = np.arange(-I,I+1,1) # Generate the mI sub-levels
maxIter = 150
Tolerance = 1e-8
Change = np.ones((len(mI,)))
B = np.zeros((len(mI,))) # Initialize iteration
iteration = 0

# Fixed-point iteration
print('mI = ' + str(mI))
print('Starting point: ' + str(B))
while (iteration<=maxIter) and any(Change>=Tolerance):
    Bold = B
    iteration +=1
    nu_ = nu + gn*muN*B # The new value for nuk in formula
    B = (a/(ge*muB + gn*muN))/((1 - ((a/(2*nu_))**2)))*(
            - mI + np.sign(a)*np.sqrt(
                mI**2 + (1 - ((a/(2*nu_))**2))*(
                    (nu_/a)**2 - (I+0.5)**2))) # The new resonance fields
    Change = abs(B - Bold)
```

```
        print('Change: '+ str(Change))

print('Fixed point iteration has converged!!!\n')
print('Resonance fields are (mT): '+str(B))
```

Appendix C

Adaptive computation of resonance fields

The following is a selection of three scripts (*master*, *stefan*, and *spin*) which illustrate the adaptive computation of resonance fields for a triplet state. The code below is a rudimentary, yet functional, implementation of the advanced algorithm presented by Stefan Stoll and Arthur Schweiger in reference [14]. The code below is not intended as a replacement for the *resfields* function, its aim is to be a suitable starting point for non-MATLAB based simulation scripts.

Master script

```
"""
Master script for adaptive computation of resonance fields
This script works for S = 1, isotropic g, non-zero D.
The orientation is set to theta = 0 and phi = 0.

Gabriel Moise
"""

import stefan

# Parameter definitions
S = 1
g = 2.1
D = 1000

# Experiment definition
B_range = [200,500]
MW = 9.5e3

# Resonance fields
stefan.tic()
(Bres, Si, Sf) = stefan.resonancefields(S,g,D,B_range,MW)
stefan.toc()
print('Resonance fields are: '+ str(Bres)+'mT')
print('Initial state vectore are [S, S-1, ..... -S+1, -S]:\n'+ str(Si))
```

```
print('Final state vectors are [S, S-1, ..... -S+1, -S]:\n'+ str(Sf))
```

The *stefan* script

```
import time
import numpy as np
import spins

def TicTocGenerator():
    ti = 0
    tf = time.time()
    while True:
        ti = tf
        tf = time.time()
        yield tf-ti

TicToc = TicTocGenerator()

def toc(tempBool=True):
    tempTimeInterval = next(TicToc)
    if tempBool:
        print( "Elapsed time: %f seconds.\n" %tempTimeInterval )

def tic():
    toc(False)

def resfxn(E_,MW):
    R = np.zeros((len(E_),len(E_)))
    for k in range(len(E_)):
        for kk in range(k+1,len(E_)):
            R[k,kk] = E_[kk] - E_[k] - MW
    return R

def transfxn(E_):
    D = np.zeros((len(E_),len(E_)))
    for k in range(len(E_)):
        for kk in range(k+1,len(E_)):
            D[k,kk] = E_[kk] - E_[k]
    return D

def SignChangeTest(Emin,Emax,MW):
    Rmin = resfxn(Emin,MW)
    Rmax = resfxn(Emax,MW)
    RminRmax = (Rmin*Rmax<=0)
    SignChange = []
    k = 0
    while (not any(SignChange)) and (k < len(Emin)):
        kk = k + 1
        while (not any(SignChange)) and (kk < len(Emin)) :
            if RminRmax[k,kk] == True:
                SignChange.extend([True])
            kk = kk + 1
        k = k + 1
```

```
    return any(SignChange)

def ParalleloTest(Emin,Emax,Bmin,Bmax,MW,S,g,th,ph):
    mue = (9.274009e-24/6.6260688e-34)*1e-9
    l = mue*S*np.sqrt((g*np.cos(th))**2
                      + (g*np.sin(th)*np.cos(ph))**2
                      + (g*np.sin(th)*np.cos(ph))**2)
    DB = Bmax - Bmin
    Dmin = transfxn(Emin)
    print(Dmin)
    Dmax = transfxn(Emax)
    print(Dmax)
    T = np.abs(((Dmin+Dmax)/2) -MW)
    Checks = (T>l*DB)
    print('Parallelogram test check results: ')
    print(Checks)
    CanRuleOut = []
    for k in range(len(Emin)):
        for kk in range(k+1,len(Emin)):
            if Checks[k,kk]:
                CanRuleOut.extend([True])
            else:
                CanRuleOut.extend([False])
    print('Can we rule out transitions in this segment? '
          + str(all(CanRuleOut)))
    return not all(CanRuleOut)

def HellmannFeynman(A,B,C):
    D = np.zeros(np.shape(C),'float')
    for k in range(len(C)):
        D[k] = np.real(np.transpose(np.conj(B[:,k])) @ A @ B[:,k])
    return D

def FindResPairs(E1,E2,MW):
    R1 = resfxn(E1,MW)
    R2 = resfxn(E2,MW)
    R1R2 = (R1*R2<0)
    lev = []
    for k in range(len(E1)):
        for kk in range(k+1,len(E1)):
            if R1R2[k,kk]:
                lev.append([k,kk])
    return lev

def resonancefields(S,g,D,B_range,MW):
    th = 0
    ph = 0
    print('Setting up spin operators and Hamiltonians...')
    Sz = spins.sop(S,'z')
    Sy = spins.sop(S,'y')
    Sx = spins.sop(S,'x')
    Ssqr = (Sz @ Sz) + (Sy @ Sy) + (Sx @ Sx)
    mue = (9.274009e-24/6.6260688e-34)*1e-9
```

```
F = D*((Sz @ Sz)-(1/3)*Ssqr)
G = mue*g*np.cos(th)*Sz
+ mue*g*np.sin(th)*np.cos(ph)*Sx
+ mue*g*np.sin(th)*np.sin(ph)*Sy
print('Done!')
B = B_range
Bmin = B[0]
Bmax = B[1]
H0 = F
Hmin = F + Bmin*G
Hmax = F + Bmax*G
print('\nPerforming␣initial␣diagonalisation␣and␣'
      +'Hellmann-Feynman␣theorem␣application...')
E0,N0 = np.linalg.eigh(H0)
Emin,Nmin = np.linalg.eigh(Hmin)
Emax,Nmax = np.linalg.eigh(Hmax)
dEmin = HellmannFeynman(G,Nmin,Emin)
dEmax = HellmannFeynman(G,Nmax,Emax)
D1N_0 = transfxn(E0)[0,-1]
print('Done!')
E = [Emin, Emax]
N = [Nmin, Nmax]
dE = [dEmin, dEmax]
finished = [False]
ResonantSegment = [False]
LoopySegment = [False]
print('\nEntering␣adaptive␣segmentation␣procedure:')
print('Segments␣status:␣'+str(finished))
while (not all(finished)):
    for k in range(len(finished)):
        if finished[k] == False:
            s = k
            break
    print('\nTesting␣segment␣'+str(s))
    if transfxn(E[s+1])[0,-1] >= MW:
        if D1N_0 <= MW:
            print('In␣high-field␣limit!'
                  +'␣Looking␣for␣a␣change␣in␣wind␣direction...')
            ResonPossible = SignChangeTest(E[s],E[s+1],MW)
        else:
            print('In␣a␣grey␣area!!!!'
                  +'␣Parallelogram␣will␣tell␣us␣how␣loopy␣we␣are...')
            ResonPossible = ParalleloTest(E[s],E[s+1],B[s],
                                          B[s+1],MW,S,g,th,ph)
    else:
        ResonPossible = False
    if ResonPossible:
        print('Resonance␣possible!')
        B_new = (B[s]+B[s+1])/2
        H_new = F + B_new*G
        E_new, N_new = np.linalg.eigh(H_new)
        dE_new = HellmannFeynman(G,N_new,E_new)
        E_new_approx = np.real(0.5*(E[s]+E[s+1])
```

```
                                + (1/8)*(B[s+1]-B[s])*(dE[s]-dE[s+1]))
            err = np.max(np.abs(E_new-E_new_approx))
            print('Interpolation error within segment '
                  +str(s)+' is '+str(np.round(err,5))
                  + (' << MW/1000' if err<(MW*1e-3) else ' >> MW/1000'))
            B.insert(s+1,B_new)
            E.insert(s+1,E_new)
            N.insert(s+1,N_new)
            dE.insert(s+1,dE_new)
            finished[s] = (err<(MW*1e-3))
            finished.insert(s+1,err<(MW*1e-3))
            ResonantSegment[s] = True
            ResonantSegment.insert(s+1,True)
            LoopySegment[s] = not(D1N_0 <= MW)
            LoopySegment.insert(s+1,not(D1N_0 <= MW))
        else:
            print('Resonance not possible!')
            ResonantSegment[s] = False
            LoopySegment[s] = False
            finished[s] = True
        print('Segments status: '+str(finished))

print('\nResonant Segments: '+str(ResonantSegment))
print('Loopy Segments: '+str(LoopySegment))
print('Actual segment borders: '+str(B))
print('Segmentation done!\n')
print('\nLocating resonances in the Resonant Segment section:\n')
Bres = []
Si = []
Sf = []
for s in range(len(ResonantSegment)):
    if ResonantSegment[s]:
        print('\nLooking in potentially-resonant segment '+str(s))
        if not(LoopySegment[s]):
            print('Phew, segment '+str(s)+' is not loopy!')
            lev = FindResPairs(E[s],E[s+1],MW)
            if not(lev):
                print('Segment has no resonances, never mind...')
            else:
                print('Segment is definitely resonant!!!'
                      +' Trying to solve resonance polynomial...')
            for q in range(len(lev)):
                k = lev[q][0]
                kk = lev[q][1]
                print('Checking level pair '+str(k)+' and '+str(kk))
                p3 = (2*(transfxn(E[s])[k,kk])
                - 2*(transfxn(E[s+1])[k,kk])
                + ((B[s+1]-B[s])*(transfxn(dE[s])[k,kk]))
                + ((B[s+1]-B[s])*(transfxn(dE[s+1])[k,kk])))
                p2 = (-3*(transfxn(E[s])[k,kk])
                + 3*(transfxn(E[s+1])[k,kk])
                - 2*((B[s+1]-B[s])*(transfxn(dE[s])[k,kk]))
                - ((B[s+1]-B[s])*(transfxn(dE[s+1])[k,kk])))
```

```
p1 = (B[s+1]-B[s])*(transfxn(dE[s])[k,kk])
p0 = transfxn(E[s])[k,kk] - MW
rts = np.roots([p3,p2,p1,p0])
print('Resonance polynomial roots:')
print(rts)
for kkk in range(len(rts)):
        if np.isreal(rts[kkk]):
            print('Root '+str(kkk)+' is real!')
            Bres_temp = B[s]+rts[kkk]*(B[s+1]-B[s])
            if (Bres_temp<B[s+1]) and (Bres_temp>B[s]):
                print('...and sensible! (Bres = '
                      + str(Bres_temp)+'mT) is within ('
                      +str(B[s])+','+str(B[s+1])+')')
                Bres.append(np.real(Bres_temp))
            else:
                print('...but not sensible! (Bres = '
                      + str(Bres_temp)
                      +'mT) is NOT within ('+str(B[s])
                      +','+str(B[s+1])+')')
print('Resonant state vectors at lower end of'+
      ' current segment: |initial> = '
      +str(N[s][:,k])+' and |final> = '+str(N[s][:,kk]))
print('Resonant state vectors at upper end of'+
      ' current segment: |initial> = '
      +str(N[s+1][:,k])+' and |final> = '+str(N[s+1][:,kk]))
ket_init_q = N[s][:,k]
ket_init_r = N[s+1][:,k]
ket_final_q = N[s][:,kk]
ket_final_r = N[s+1][:,kk]

print('Checking the phase of the initial state vectors:')
ph_init_q = ket_init_q[np.argmax(np.abs(ket_init_q))]
print('...Maximum absolute component of initial state at'
      +' lower end '
      +str(ph_init_q))
ph_init_r = ket_init_r[np.argmax(np.abs(ket_init_r))]
print('...Maximum absolute component of initial state at'
      +' higher end '
      +str(ph_init_r))
if (np.isreal(ph_init_q) and np.isreal(ph_init_r)
    and ph_init_q>0 and ph_init_q>0):
    print('No phasing issue detected.'+
          ' They are both real and positive.'+
          ' Interpolating initial state vectors...')
    ket_init = (((B[s+1]-Bres[-1])/(B[s+1]-B[s]))*
                ket_init_q
                + ((Bres[-1]-B[s])/(B[s+1]-B[s]))*
                ket_init_r)
print('Initial state for resonance field '
      +str(Bres[-1])+' mT is:\n '+str(ket_init))

print('Checking the phase of the final state vectors:')
ph_final_q = ket_final_q[np.argmax(np.abs(ket_final_q))]
```

```
            print('...Maximum absolute component of final state at'
                  +' lower end '
                  +str(ph_final_q))
            ph_final_r = ket_final_r[np.argmax(np.abs(ket_final_r))]
            print('...Maximum absolute component of final state at'
                  +' higher end '
                  +str(ph_final_r))
            if (np.isreal(ph_final_q) and np.isreal(ph_final_r)
                and ph_final_q>0 and ph_final_q>0):
                print('No phasing issue detected.'+
                      ' They are both real and positive.'+
                      ' Interpolating initial state vectors...')
                ket_final = (((B[s+1]-Bres[-1])/(B[s+1]-B[s]))*
                             ket_final_q
                             + ((Bres[-1]-B[s])/(B[s+1]-B[s]))*
                             ket_final_r)
            print('Final state for resonance field '
                  +str(Bres[-1])+' mT is:\n '+str(ket_final))
            Si.append(ket_init)
            Sf.append(ket_final)
    else:
        print('Segment '+str(s)+' is loopy! Give me a moment...')
        for k in range(len(E[s])):
            for kk in range(k+1,len(E[s])):
                print('Testing transition from level '
                      +str(k)+' to '+str(kk))
                p3 = (2*(transfxn(E[s])[k,kk])
                      - 2*(transfxn(E[s+1])[k,kk])
                      + ((B[s+1]-B[s])*(transfxn(dE[s])[k,kk]))
                      + ((B[s+1]-B[s])*(transfxn(dE[s+1])[k,kk])))
                p2 = (-3*(transfxn(E[s])[k,kk])
                      + 3*(transfxn(E[s+1])[k,kk])
                      - 2*((B[s+1]-B[s])*(transfxn(dE[s])[k,kk]))
                      - ((B[s+1]-B[s])*(transfxn(dE[s+1])[k,kk])))
                p1 = (B[s+1]-B[s])*(transfxn(dE[s])[k,kk])
                p0 = transfxn(E[s])[k,kk] - MW
                rts = np.roots([p3,p2,p1,p0])
                print('Resonance polynomial roots:')
                print(rts)
                for kkk in range(len(rts)):
                    if np.isreal(rts[kkk]):
                        print('Root '+str(kkk)+' is real!')
                        Bres_temp = B[s]+rts[kkk]*(B[s+1]-B[s])
                        if (Bres_temp<B[s+1]) and (Bres_temp>B[s]):
                            print('...and sensible! (Bres = '
                                  + str(Bres_temp)+'mT) is within ('
                                  +str(B[s])+','+str(B[s+1])+')')
                            Bres.append(np.real(Bres_temp))
                        else:
                            print('...but non-sensible! (Bres = '
                                  + str(Bres_temp)
                                  +'mT) is NOT within ('+str(B[s])
                                  +','+str(B[s+1])+')')
```

```
            print('\nDone!\n')
        else:
            print('\nSegment␣'+str(s)+'␣is␣definitely␣non-resonant␣:)')

    print('\n␣HAPPY␣LANDING!!!\n\n')
    return (Bres,Si,Sf)
```

The *spin* script

```
import numpy as np

def sop(S,comp):
    Sq = np.zeros([int(2*S+1),int(2*S+1)],'complex')
    if comp == 'z':
        for k in range(int(2*S+1)):
                M = S - k
                Sq[k,k] = M
    elif comp == 'x' or comp == 'y':
        Sp = np.zeros([int(2*S+1),int(2*S+1)])
        Sm = np.zeros([int(2*S+1),int(2*S+1)])
        for k in range(int(2*S+1)):
            M1 = S - k
            M2 = M1 + 1
            if M2 <= S:
                Sp[k-1,k] = np.sqrt(S*(S+1)-M1*M2)

        for k in range(int(2*S+1)):
            M1 = S - k
            M2 = M1 - 1
            if M2 >= -S:
                Sm[k+1,k] = np.sqrt(S*(S+1)-M1*M2)

    if comp == 'x':
        Sq = (1/2)*(Sp+Sm)
    if comp == 'y':
        Sq = (1/2j)*(Sp-Sm)
    return Sq
```

Appendix D

The D_{2h} character table

The most relevant group theoretical character table for this thesis is the one for the D_{2h} point group given below:

	E	C_{2z}	C_{2y}	C_{2x}	i	σ_{xy}	σ_{xz}	σ_{yz}	linear, rotations	quadratic
A_g	+1	+1	+1	+1	+1	+1	+1	+1	–	x^2, y^2, z^2
B_{1g}	+1	+1	−1	−1	+1	+1	−1	−1	R_z	xy
B_{2g}	+1	−1	+1	−1	+1	−1	+1	−1	R_y	xz
B_{3g}	+1	−1	−1	+1	+1	−1	−1	+1	R_x	yz
A_u	+1	+1	+1	+1	−1	−1	−1	−1	–	
B_{1u}	+1	+1	−1	−1	−1	−1	+1	+1	z	
B_{2u}	+1	−1	+1	−1	−1	+1	−1	+1	y	
B_{3u}	+1	−1	−1	+1	−1	+1	+1	−1	x	

For the ^{3}**Fb**, ^{3}**Zn**, and ^{3}**Pd** systems investigated in Chapter 4, the z axis is taken to be perpendicular to the porphyrin plane, and the y-axis to be aligned with the aryl side chains. This definition is also the reason why the terms 'Cartesian frame' and 'molecular frame' are used interchangeably; it is because we are working in the frame implied by the above character table.

The direct product table for this point group can be constructed according to the following rules:

$$g \times g = u \times u = g$$
$$g \times u = u \times g = u$$
$$i \times i = 1$$
$$i \times j = j \times i = |\epsilon_{ijk}|k$$
$$A \times B = B$$

where $i, j, k \in \{1, 2, 3\}$, and ϵ_{ijk} is the Levi-Cevita symbol.

Appendix E

Selected ORCA input and output files

E.1 Chapter 2

Below is the ORCA input file used to generate the spin density in figure 2.5. The calculation was repeated using the EPR-II basis set. The latter basis set was also used for the longer oligoporphyrins.

```
!B3LYP def2-SVP GridX5 NoFinalGrid

%pal nprocs 16 end

*xyz 1 2
  Zn      -0.001005       0.000001      -0.000027
  N       -0.038893      -1.469463      -1.454428
  N        0.037658       1.469468      -1.454397
  N       -0.038889       1.469457       1.454384
  N        0.037651      -1.469467       1.454354
  C        0.022672      -1.268964      -2.804341
  C       -0.000447       0.000023      -3.452219
  C       -0.023559       1.269004      -2.804326
  C       -0.118191       2.528785      -3.495781
  C       -0.125325       3.499380      -2.534643
  C       -0.016145       2.828277      -1.258943
  C       -0.000365       3.487953       0.000002
  C        0.015328       2.828254       1.258938
  C        0.124902       3.499315       2.534628
  C        0.117739       2.528709       3.495751
  C        0.022677       1.268959       2.804298
  C       -0.000444      -0.000025       3.452179
  C       -0.023565      -1.269002       2.804284
  C       -0.118203      -2.528782       3.495741
  C       -0.125320      -3.499379       2.534607
  C       -0.016172      -2.828275       1.258904
  C       -0.000397      -3.487955      -0.000038
  C        0.015311      -2.828260      -1.258977
  C        0.124914      -3.499320      -2.534665
  C        0.117733      -2.528716      -3.495791
  H       -0.186225       2.646992      -4.573742
  H       -0.212600       4.572558      -2.674203
```

```
  H       0.212527       4.572462       2.674184
  H       0.186081       2.646880       4.573696
  H      -0.186234      -2.646987       4.573703
  H      -0.212584      -4.572558       2.674171
  H       0.212550      -4.572466      -2.674217
  H       0.186076      -2.646890      -4.573736
  C       0.000002      -4.977527      -0.000023
  C       0.000012       4.977527       0.000016
  C       1.046554      -5.694344       0.614272
  C      -1.046180      -5.694937      -0.614261
  C      -1.046180       5.694907       0.614271
  C       1.046573       5.694376      -0.614226
  C       1.049822      -7.090608       0.604984
  C      -1.048700      -7.091203      -0.604894
  C      -1.048706       7.091173       0.604965
  C       1.049836       7.090639      -0.604877
  C       0.000748      -7.791177       0.000065
  C       0.000748       7.791178       0.000054
  H       1.870913      -5.150329       1.081626
  H      -1.870827      -5.151392      -1.081653
  H      -1.870830       5.151339       1.081633
  H       1.870949       5.150384      -1.081579
  H       1.875958      -7.633222       1.071525
  H      -1.874547      -7.634288      -1.071401
  H      -1.874562       7.634235       1.071485
  H       1.875980       7.633277      -1.071377
  H       0.001047      -8.882967       0.000089
  H       0.001045       8.882968       0.000082
  C      -0.000109       0.000038      -4.874911
  C       0.000180       0.000051      -6.091693
  C      -0.000094      -0.000038       4.874871
  C       0.000206      -0.000044       6.091652
  H       0.000433       0.000066      -7.167466
  H       0.000470      -0.000051       7.167426
*

%eprnmr Nuclei = all N { aiso }
Nuclei = 26, 27, 28, 29, 30, 31, 32, 33, 46, 47, 48, 49, 54, 55 { aiso }
end
```

E.2 Chapter 4

CASSCF states for ^{3}Fb

```
------------------------------------------------
CAS-SCF STATES FOR BLOCK  1 MULT= 3 NROOTS= 4
------------------------------------------------

ROOT   0:   E=    -1592.4384331781 Eh
      0.92693 [      0]: 2110
      0.01941 [      3]: 1210
```

```
       0.01838 [      4]: 1201
       0.01171 [     12]: 0112
       0.01094 [      8]: 1021
       0.01089 [      1]: 2101
ROOT   1:  E=   -1592.4156663994 Eh  0.620 eV   4996.7 cm**-1
       0.89592 [      3]: 1210
       0.05197 [      1]: 2101
       0.02701 [      0]: 2110
       0.01327 [      9]: 1012
       0.01144 [     11]: 0121
ROOT   2:  E=   -1592.3980206413 Eh  1.100 eV   8869.5 cm**-1
       0.89080 [      1]: 2101
       0.06724 [      3]: 1210
       0.01930 [      4]: 1201
       0.01115 [     11]: 0121
       0.00843 [      0]: 2110
       0.00260 [      9]: 1012
ROOT   3:  E=   -1592.3867634225 Eh  1.406 eV  11340.2 cm**-1
       0.92574 [      4]: 1201
       0.02406 [      8]: 1021
       0.02254 [      1]: 2101
       0.02171 [      0]: 2110
       0.00492 [     12]: 0112
```

CASSCF states for ^{3}Zn

```
-------------------------------------------
CAS-SCF STATES FOR BLOCK  1 MULT= 3 NROOTS= 4
-------------------------------------------

ROOT   0:  E=   -3369.1766866302 Eh
       0.96646 [      0]: 2110
       0.00990 [     12]: 0112
       0.00820 [      8]: 1021
       0.00787 [      4]: 1201
       0.00621 [      3]: 1210
ROOT   1:  E=   -3369.1625434177 Eh  0.385 eV   3104.1 cm**-1
       0.83370 [      3]: 1210
       0.12536 [      1]: 2101
       0.01701 [      9]: 1012
       0.01558 [     11]: 0121
       0.00684 [      0]: 2110
ROOT   2:  E=   -3369.1423584621 Eh  0.934 eV   7534.2 cm**-1
       0.84948 [      1]: 2101
       0.14026 [      3]: 1210
       0.00802 [     11]: 0121
ROOT   3:  E=   -3369.1292697248 Eh  1.290 eV  10406.8 cm**-1
       0.95791 [      4]: 1201
       0.02340 [      8]: 1021
       0.01249 [      0]: 2110
       0.00466 [     12]: 0112
```

CASSCF states for ^{3}Pd

```
-------------------------------------------
CAS-SCF STATES FOR BLOCK  1 MULT= 3 NROOTS= 4
-------------------------------------------

ROOT   0:  E=   -1718.3965866229 Eh
       0.96858 [      0]: 2110
       0.00983 [     12]: 0112
       0.00802 [      8]: 1021
       0.00782 [      4]: 1201
       0.00387 [      3]: 1210
ROOT   1:  E=   -1718.3824224499 Eh  0.385 eV   3108.7 cm**-1
       0.84184 [      3]: 1210
       0.12066 [      1]: 2101
       0.01650 [      9]: 1012
       0.01511 [     11]: 0121
       0.00505 [      0]: 2110
ROOT   2:  E=   -1718.3621817916 Eh  0.936 eV   7551.0 cm**-1
       0.85126 [      1]: 2101
       0.13442 [      3]: 1210
       0.00810 [     11]: 0121
       0.00404 [      4]: 1201
ROOT   3:  E=   -1718.3492135347 Eh  1.289 eV  10397.2 cm**-1
       0.95609 [      4]: 1201
       0.02267 [      8]: 1021
       0.01184 [      0]: 2110
       0.00457 [     12]: 0112
       0.00298 [      1]: 2101
```

Calculating the ISC rates

The input below was used for the calculation of the ISC rate in ^{3}**Fb**. The 'trootssl' selects the triplet sub-level. The calculation also requires the hessian files (*e.g.* 'fbpT.hess') for the initial singlet and final triplet state, as well as the adiabatic energy difference ('DELE'). The exact same parameters were used for the ^{3}**Zn** system, except of course for the geometry and hessian files.

```
!B3LYP def2-SVP def2-SVP/C def2/J RIJCOSX GridX5 RI-SOMF(1X) ESD(ISC)

%pal nprocs 16 end

%tddft
        nroots 1
        sroot 1
        troot 1
        trootssl 0
        dosoc true
end

%esd
        ISCISHESSIAN "fbpS.hess"
        ISCFSHESSIAN "fbpT.hess"
```

```
         USEJ TRUE
         DOHT TRUE
         TEMP 80
         DELE 7000
end

*xyz 0 1
  H    5.14312988851232      1.36256230447962     -0.00001944770834
  H   -5.14312987310227     -1.36256232983148      -0.00002156876976
  H    5.14312700023427     -1.36256306478112     -0.00002569446273
  H   -5.14312692477379      1.36256307494676      -0.00002870557881
  C    4.27911868669202      0.70063332084171     -0.00001322970003
  C   -4.27911867041727     -0.70063333047596      -0.00001370665522
  C    4.27911705488871     -0.70063240123265     -0.00001735613610
  C   -4.27911698571386      0.70063239401673      -0.00001831383662
  C    2.92984142232268      1.12640994630539     -0.00000284236879
  C   -2.92984142030371     -1.12640995213166      -0.00000124986672
  C    2.42364331553102      2.46153162018631      0.00000378420873
  C   -2.42364336459018     -2.46153164163823       0.00000492186764
  N    0.00000328241562      2.04958844506381      0.00000592632464
  N   -0.00000330702496     -2.04958840695920       0.00000675906429
  C    2.92983871746902     -1.12640614892651     -0.00000647816736
  C   -2.92983866776383      1.12640613353309      -0.00000529668516
  C    1.09224006544061      2.87528944568746      0.00000871879529
  C   -1.09224009399782     -2.87528940172251       0.00000880381217
  N    2.14861069595250      0.00000327683710      0.00000024294333
  N   -2.14861066954760     -0.00000329473471       0.00000343638872
  C    2.42363823036801     -2.46152626095170     -0.00000257368667
  C   -2.42363822909991      2.46152626053580      -0.00000144996459
  C   -1.09223542574755      2.87528694611600       0.00000632790356
  C    1.09223540469270     -2.87528689160106      0.00000558669421
  H    1.12957111432404      0.00000570965280      0.00001110005068
  H   -1.12957108666237     -0.00000577187273       0.00001649479086
  C    0.67836233935966      4.28220528581423      0.00001183891781
  C   -0.67836235579934     -4.28220525697672       0.00001205875825
  C   -0.67836045022858      4.28220364684038       0.00001112451854
  C    0.67836042611459     -4.28220360707903      0.00001085061674
  H    1.35269361954839      5.13875286479186      0.00001471690382
  H   -1.35269363346067     -5.13875283447796       0.00001526631638
  H   -1.35269417579024      5.13874929990505       0.00001243827665
  H    1.35269415185462     -5.13874925949164      0.00001193172469
  H    3.18263471469901     -3.24787371119410     -0.00000670185072
  H   -3.18263477132546      3.24787364835528      -0.00000591637506
  H    3.18263982790615      3.24787886015502      0.00000399652972
  H   -3.18263985297654     -3.24787891798547       0.00000420640598
*
```

Appendix F

Further experimental details and results

F.1 Chapter 2

^{1}H-ENDOR and DFT simulations for the entire *l1*-PN$^{+\cdot}$ series

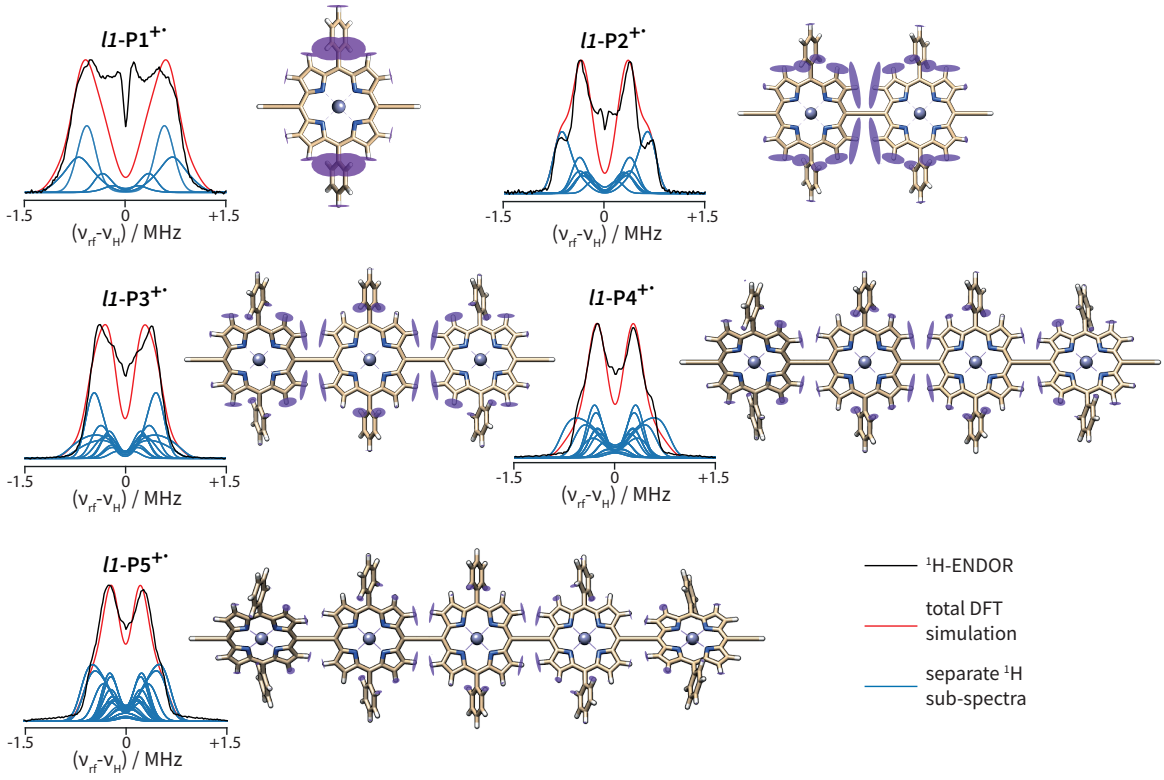


Figure F.1: Summary of Q-band ENDOR measurements for the radical cations of the linear ethyne linked oligoporphyrin systems. Within each panel the experimental data is shown in black, the total DFT simulation is shown in red, whereas the individual spectra of each proton are shown in blue. Adjacent to each ENDOR spectrum, the DFT computed hyperfine tensors are also plotted as ellipsoids superimposed onto the structure of the oligomer. The simulations were obtained using the function *saffron* from the EasySpin package [9] whereas the hyperfine tensors were computed using ORCA [45], as described in the main text.

F.2 Chapter 4

Additional experimental details

The samples were prepared to a concentration of ca. 200 μM using 2-methyltetrahydrofuran as a solvent for the X-band measurements and toluene for the W-band measurements. None of the EPR spectra of the palladium porphyrin oligomers change with either solvent (at X-band); likely a result of the fact that the Pd^{2+} does not admit an axial ligand when it is bound to the porphyrin macrocycle.

Unless stated otherwise, the trEPR spectra were taken at a temperature of 20 K on a Bruker Elexsys E680 spectrometer equipped with an MD4EN resonator. The excitation wavelength was 532 nm, unless MPS data was collected, in which case the wavelengths are reported in the corresponding data figures in Chapter 4. The laser light was delivered through the optical window of the cryostat in the X-band measurements and through an optical fibre (excitation from the top of the sample) for the W-band measurements.

Mims ENDOR measurements were carried by employing 16 ns microwave pulse lengths in combination with a 15 μs radiofrequency pulse. The τ value was set to 120, 180, and 240 ns and the resulting datasets were added in an attempt to minimise the effects of any potential blind spots.

Additional data and simulations

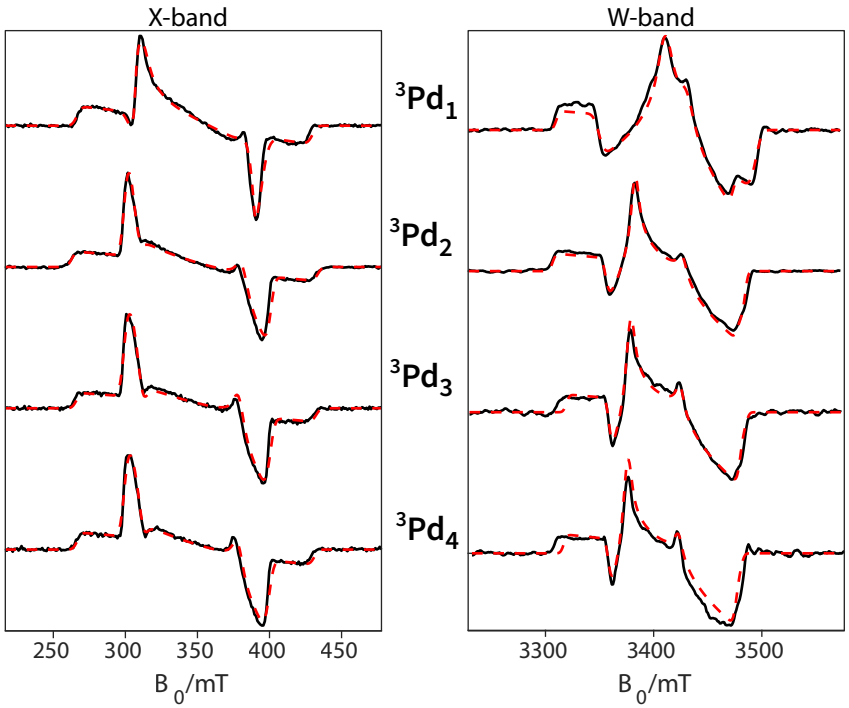


Figure F.2: Experimental (solid black lines) and simulated (dashed red lines) trEPR data for the ^{3}**Pd**$_{1-4}$ oligoporphyrins. The left and right panels represent data acquired at X- and W-band frequencies, respectively. The simulations are the result of a global fitting of both data sets. The fitting parameters are shown and discussed throughout Chapter 4, particularly in tables 4.1, 4.5, and 4.7. The most important conclusion from the data shown here is the pronounced asymmetry of the spectra relative to their barycenter. This is particularly obvious in the W-band data, and it is a clear signature of g-anisotropy.

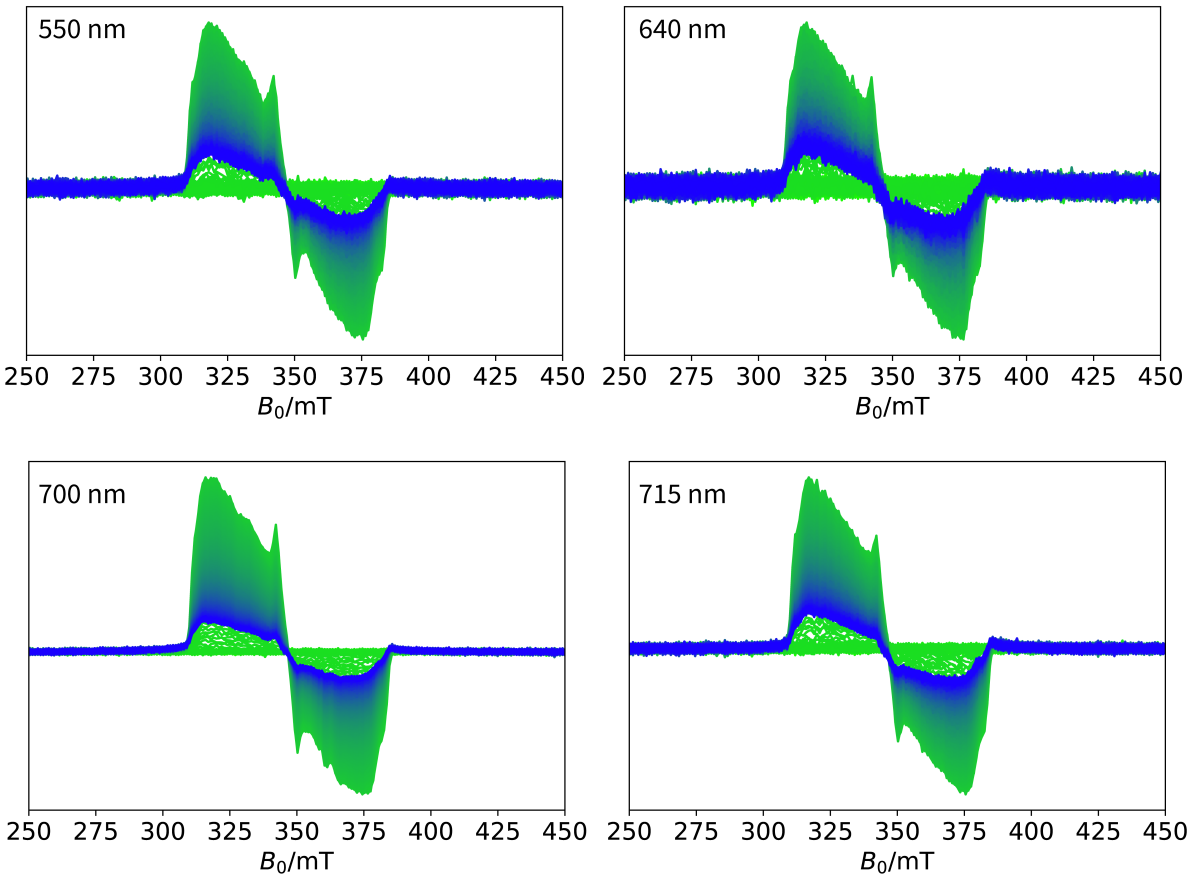


Figure F.3: Time evolution over a range of 8 μs of the trEPR spectra of the ^{3}**FbPd** system measured by excitation at the four indicated wavelengths. The laser pulse occurs at 1 μs after the spectrometer zero time (defined by an acquisition trigger). The colormap is such that at early times the lines are predominantly green and as time progresses the lines become predominantly blue. This figure illustrates that the overall shape of the EPR spectrum is conserved as a function of time regardless of excitation wavelength.

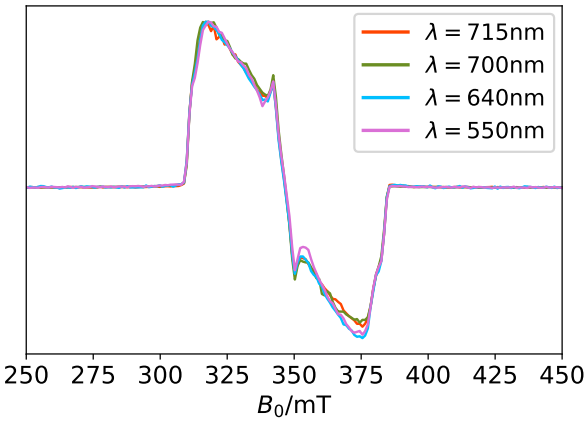


Figure F.4: Time averaged trEPR spectra of ^{3}**FbPd** obtained over a range of 800 ns after the maximum signal in time-domain (obtained from the data shown in figure F.3). These spectra illustrate that there is no change in the ZFS and spin polarisation parameters as a function of excitation wavelength. In other words, no matter which excitation wavelength is used, the final triplet state detected in the trEPR spectrum is the same.

F.3 Chapter 5

Multi-frequency ENDOR results

In order to deconvolute the ENDOR spectra of the acceptor porphyrin systems, it was necessary to perform multifrequency ENDOR measurements. These measurements were performed in collaboration with Mr. Ashley J. Redman and Dr. William K. Myers. The results are shown only for the **A_2-e** system in figure F.5. Measurements on the other systems were also attempted, however, due to the low signal-to-noise (at Q- and W-band), the analysis was less definitive. Nonetheless, the results shown for **A_2-e** are sufficient for the purposes of identifying the nuclei corresponding to the hyperfine peaks. The X-band ENDOR spectra of the other systems are sufficiently similar to **A_2-e** to allow us to assume, following the analysis in figure F.5, that their interpretation is analogous.

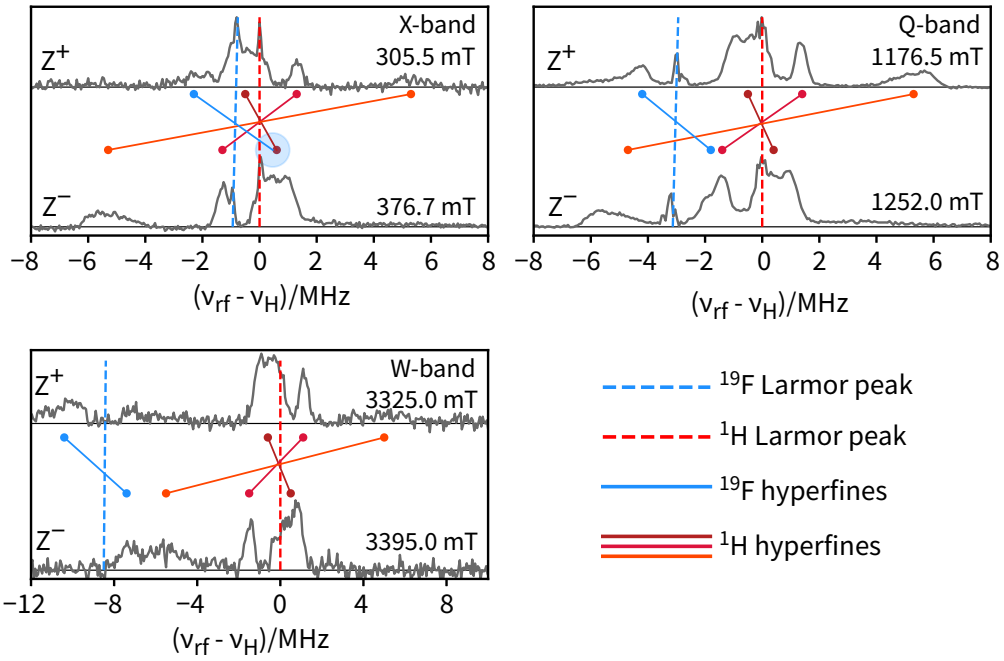


Figure F.5: Summary of multifrequency (X/Q/W-band) Mims-ENDOR results obtained for the **A_2-e** system. In each panel, the microwave frequency and the precise field value is indicated; in each case, the top spectrum corresponds to the Z^+ transition whereas the bottom spectrum corresponds to the Z^- field position. The reason for acquiring these spectra was to establish the identity of the nucleus to which the hyperfine peaks belong. As the microwave frequency increases, so does the field position of the $Z^{\pm}$ transitions. This means that the difference in Larmor frequency of the ^{1}H and ^{19}F nuclei increases (see the distance between the dashed vertical lines increasing from X- to Q- to W-band). In turn, this means that the 'swap-over point', *i.e.* the intersection of the dashed lines and the solid lines, of a given hyperfine peak will also be shifted to coincide with the new Larmor peak of the nucleus to which the coupling belongs. For example, we see in all of the panels above that the swap-over point of the ^{1}H hyperfines (red lines) shifts relative to the swap-over point of the ^{19}F hyperfines (blue line). The conclusion from these multifrequency ENDOR data is that there are some small non-zero fluorine hyperfine couplings (comprising the broad peak marked by the blue lines), however, the overall ENDOR spectrum is dominated by protons. This means that the degree to which the spin density delocalises onto the acceptor groups is likely to be very small.

F.4 Chapter 6

Echo-detected field swept spectra

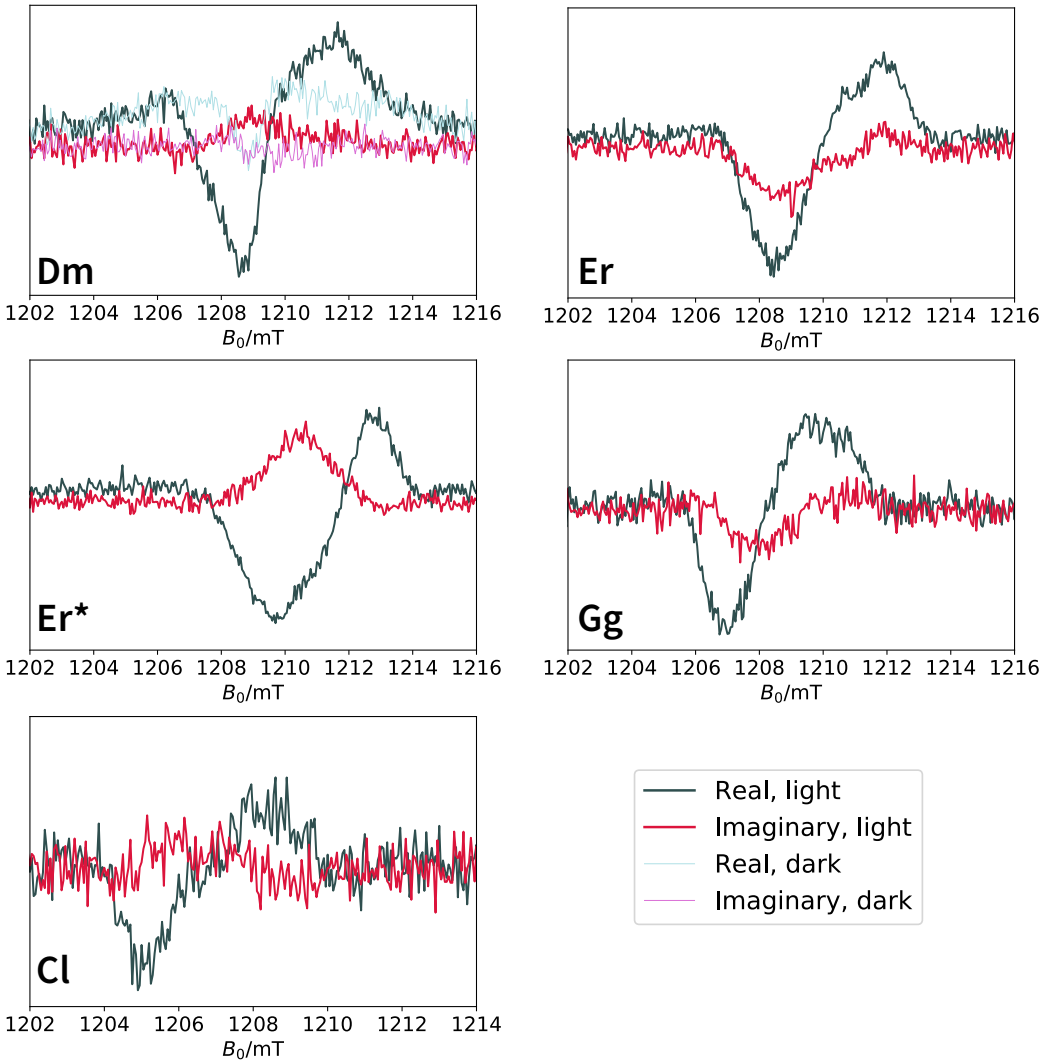


Figure F.6: Echo detected field swept EPR spectra for the five cryptochrome proteins. In each panel, the black and red lines correspond to the real and imaginary parts of the signal obtained with the laser switched on. The pulse sequence used here is the one described in section 6.3.2 with a τ value fixed to 200 ns. In the panel corresponding to the *Dm*Cry WT data, the spectra obtained by turning off the laser (dark scans) are also shown for reference. As can be seen, the laser pulse causes the appearance of a signal which has the emissive and absorptive features characteristic of SCRPs. The spectra with the laser off show some residual features due to the stable, dark-state radical which have not been entirely eliminated by the pre-saturation pulse. All spectra show a clear, non-zero imaginary component with a maximum which corresponds (approximately) with the zero-crossing of the real signal. The signal-to-noise ratio is not particularly favourable in some of these spectra; they are acquired only as 'setup' scans and they provide a consistency check, before the oopESEEM data is averaged over a longer period of time. It is not desirable to bleach a precious cryptochrome sample purely for the purpose of acquiring a high-quality echo-detected field-swept spectrum (which is not useful beyond the initial set-up experiments). Nonetheless, these spectra are useful as a reference point for the discussion in section 6.3.2.

Assignment of the flavin and tryptophan hyperfine couplings

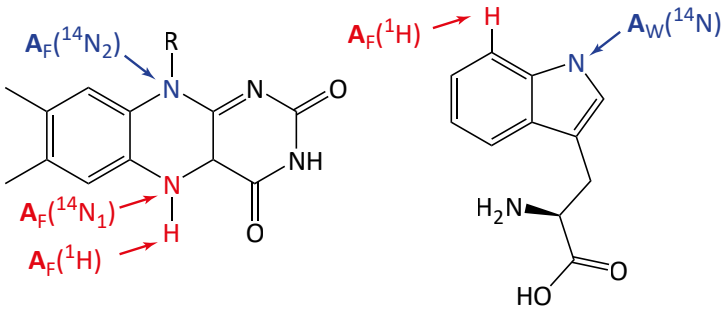


Figure F.7: (Left) Skeletal structure of the flavin radical and the assignment of the hyperfine couplings in table 6.3 used in the simulation of the trEPR spectra in figure 6.5. The assignment of these hyperfine couplings was done by comparison with the values reported in references [115, 130] for both free and cryptochrome bound flavin radicals. (Right) Skeletal structure of the tryptophan residue and the assignment of the hyperfine couplings used in the spectral simulation. The assignment in this case was done by comparison with the simulations and data in references [115, 131–133]. Note that, as far as the protons are concerned, it is unlikely that only the protons indicated in this figure have non-zero hyperfine couplings. In order to avoid adding more parameters to the fitting of these trEPR spectra, it was found that simplifying the spin system to only one proton coupling per radical was a suitable compromise. Similar approximations have been made in previous cryptochrome trEPR studies [115]. Due to this simplification, the values for $A_F(^1H)$ and $A_W(^1H)$ reported in table 6.3 should only be regarded as an average proton hyperfine coupling and the assignment of these parameters given in this figure is only tentative. Nonetheless, the assignment of the nitrogen hyperfine couplings is less ambiguous because these parameters are larger in magnitude and significantly anisotropic.

Appendix G

TrEPR simulation scripts for SCRPs

G.1 The *cockatiel* script

```
%%%%%%%%%%%%%%%%%%%%%%%%%%%%%%%%%%%%
%%%%%%%%%%%%%%%%%%%%%%%%%%%%%%%%%%%%
%%% TrEPR simulation of SCRPs %%%%%%
% Nickname: Cockatiel
% Capability:
%   - 2 electron spins
%   - Aribtrary nuclear spins
%   - anisotropic g-tensors + J + D
%   - anisotropic hyperfines
%   - powder average by integration
%   - Isotropic Gaussian broadening
%   - Boltzmann population
%   - Singlet-born polarisation
%   - Almost exact
% Requirements: EasySpin toolbox
% and Parallel computing
%%%%%%%%%%%%%%%%%%%%%%%%%%%%%%%%%%%%
% Authors: Gabriel Moise &  %%%%%%%%
%%%%%%%%%% Tommy L. Pitcher %%%%%%%%%
%%%%%%%%%%%%%%%%%%%%%%%%%%%%%%%%%%%%
%%%%%%%%%%%%%%%%%%%%%%%%%%%%%%%%%%%%
%%%%%%%%%%%%%%%%%%%%%%%%%%%%%%%%%%%%
clear all; close all; clc;
% % % % % % % % % % % % % % % % % % % % % % % % % % % % % % % % % % %
% % % % % % % % % % % % % % % % % % % % % % % % % % % % % % % % % % % %
% % % % % % % % % % INPUT DEFINITION  % % % % % % % % % %
% % % % % % % % % % % % % % % % % % % % % % % % % % % % % % % % % % % %
% % % % % % % % % % % % % % % % % % % % % % % % % % % % % % % % % % % %
% Current settings give Case 4 in figure 6.4 of Chapter 6 %
% % % % % % % % % % % % % % % % % % % % % % % % % % % % % % % % % % % %
% SECTION 1: The spin system
sys.S = [0.5 0.5];
sys.g = [2.00 2.003 2.003;
         2.00 2.003 2.003];
sys.gFrame = [0 0 0; 0 0 0]*pi/180;
```

```
J = mt2mhz(2*(0.5)/10); % this is twice the value given in 'fawns'
                        % (converted to MHz from Gauss)
D = -mt2mhz(2*(4)/10); % same as for J
Dframe = [0 0 0]*pi/180;
sys.ee = [J 0 0; 0 J 0; 0 0 J]...
            -erot(Dframe)*[-D/3 0 0; 0 -D/3 0; 0 0 2*D/3]*erot(Dframe).';
sys.Nucs = '14N';
sys.A = [2 2 20, 0 0 0];
sys.AFrame = [0 0 0, 0 0 0]*pi/180;
lw = 0.1; % Gaussian linewidth

% SECTION 2 : experimental parameters
Exp.mwFreq = 9.50;
Exp.Range = [337.5 342];
npoints = 1000;
knots = 33;

% SECTION 3: options
plt = true; % plotting?
pol = true; % spin polarisation? (alternative is Boltzmann)
lod = true; % load spectrum from 'fwrp'

% % % % % % % % % % % % % % % % % % % % % % % % % % % % % % % % % % % % % %
% % % % % % % % % % % % % % % % % % % % % % % % % % % % % % % % % % % % % %
% % % %  CALCULATION OF POWDER SPECTRUM % % % % % % % % % % % % % % % % % %
% % % % % % % % % % % % % % % % % % % % % % % % % % % % % % % % % % % % % %
% % % % % % % % % % % % % % % % % % % % % % % % % % % % % % % % % % % % % %

% MACRO-STEP 0: Setup
ntheta = 32;
nphi = 64;
n_ori = ntheta.*nphi; % orientational grid
B01 = linspace(Exp.Range(1),Exp.Range(2),npoints); % field axis
[Sx1,Sy1,Sz1] = sop(spinvec(sys),'x1','y1','z1');
[Sx2,Sy2,Sz2] = sop(spinvec(sys),'x2','y2','z2');
S_sqr_op = (Sx1+Sx2)^2+(Sy1+Sy2)^2+(Sz1+Sz2)^2;
[Sevecs,Sevals] = eig(S_sqr_op);
Sevals = diag(Sevals);
j = 0;
for k = 1:hsdim(sys)
    if Sevals(k) == 0
        j = j+1;
        S(j,:) = Sevecs(:,k); % Generating the electronic singlet
                              % state vectors
    end
end
n_nuc_states = j; % number of nuclear states

% MACRO-STEP 1: Find resonance fields (b) and total intensity (I) for
% every orientation on the grid
tic
b = cell(ntheta,nphi);
I = cell(ntheta,nphi);
```

```
parfor ORIt = 1:ntheta
    theta = (ORIt-1)*pi/ntheta;
    vb = cell(1,nphi);
    vI = cell(1,nphi);
    for ORIp = 1:nphi
        idx = nphi.*(ORIt-1)+ORIp;
        phi = (ORIp-1)*2*pi/nphi;
        Exp1 = Exp;
        Exp1.CrystalOrientation = [phi theta];

        [vb{ORIp},QI,~,lev] = resfields(sys,Exp1);

        % STEP 1: Determining the polarisation of the transition at the
        % resonance fields (contained in b)
        switch pol
            case true
                P = zeros([length(vb{ORIp}),1]);
                for k = 1:length(vb{ORIp})
                    % MINI-STEP 1: Spin Hamiltonian formation
                    H = sham(sys,(erot([phi theta 0]).'*...
                        [0 0 vb{ORIp}(k)]')');

                    % MINI-STEP 2: Eigenvalues and eigenvectors of
                    % Hamiltonian: H |n> = En |n>:
                    % NOTE: The eigenvectors are in the uncoupled basis for
                    % all spins (electronic or nuclear)
                    [n,En] = eig(H);

                    % MINI-STEP 3: Level |n> is populated by an amount
                    % given by its singlet character. Perform the dot
                    % product between |S> and |n>. The Singlet character of
                    % level |n> is given by |<S|n>|^2.
                    pop = zeros(1,hsdim(sys));
                    for qq = 1:hsdim(sys)
                        for j = 1:n_nuc_states
                            pop(qq) = pop(qq) + abs((S(j,:)*n(:,qq)))^2;
                        end
                    end

                    % MINI-STEP 4: Calculate polarisation of the transition
                    % at the resonance fields
                    P(k) = real(pop(lev(k,1))-pop(lev(k,2)));
                end

            % STEP 2: Determine final transition intensity for res. fields

                vI{ORIp} = real(QI.*P);
            otherwise
            vI{ORIp} = real(QI);
        end
    end
    b(ORIt,:) = vb;
```

```
    I(ORIt,:) = vI;
end
b = b';
I = I';
b = reshape(b,1,[]);
I = reshape(I,1,[]);
toc

% MACRO-STEP 3: Generate the sub-spectra over the orientation grid and
% integrate
tic
sub_spec = zeros(n_ori,length(B01));
spec = zeros(1,length(B01));
for ORIt = 1:ntheta
    for ORIp = 1:nphi
        idx = nphi.*(ORIt-1)+ORIp;
        for k = 1:length(b{idx})
            sub_spec(idx,:) = sub_spec(idx,:) +...
                gaussian(B01,b{idx}(k),lw)*I{idx}(k)...
                *sin((ORIt-1)*pi/ntheta);
        end
        spec = spec + sub_spec(idx,:);
    end
end
toc

% MACRO-STEP 5: Plot the spectrum
if plt
    figure(1); clf;
    hold on;
    axis tight;
    plot(B01*10,spec./max(abs(spec)),'b','linewidth',1)
    if lod
        load fawnsGM_J0p5_D4_ganiso3_9pt5GHz.mat
        plot(b_axis,spectrum,'r--','linewidth',1)
        legend('Cockatiel','FWRP')
    end
    if pol
        ylim([-1 1])
    else
        ylim([0 1])
    end
    xlabel('field / G')
    ylabel('Norm. Intensity')
    title('EPR spectrum')
    hold off;
end

disp('HAPPY LANDING!!!')
```

G.2 The *fawns* script

```
%%%%%%%%%%%%%%%%%%%%%%%%%%%%%%%%%%%%%%%%
%%%%%%%%%%%%%%%% FAWNS %%%%%%%%%%%%%%%%
%%%%%% TrEPR simulation of SCRPs %%%%
%%%%%%% Authors: Tommy Pitcher %%%%%%
%%%%%%%%% and Gabriel Moise %%%%%%%%%
% Current input gives same spectrum %
% as Case 4 in figure 6.4 %%%%%%%%%%%
%%%%% of Chapter 6 %%%%%%%%%%%%%%%%%%
clear all; close all; clc;

%%%%%%%%%%%% INPUT %%%%%%%%%%%%

%%%% sys input - Electrons %%%%
sys.gf = [2.00 2.003 2.003];              % Flavin e-
sys.gw = [2.00 2.003 2.003];              % Trp e-
sys.eul_w = deg2rad([0 0 0]);             % Euler angles of trp e-
sys.iso1 = 0;                             % Flavin 1H (all in G)
sys.iso2 = 0;                             % Trp 1H
sys.ax1 = mhz2mt(2).*10;                  % Flavin 14N(1) perp
sys.ax2 = 0;                              % Flavin 14N(2) perp
sys.ax3 = 0;                              % Trp 14N perp
sys.par1 = mhz2mt(20).*10;                % Flavin 14N(1) par
sys.par2 = 0;                             % Flavin 14N(2) par
sys.par3 = 0;                             % Trp 14N par
af_0 = [sys.ax1 sys.ax1 sys.par1;         % Matrix of Flavin hfcs
        sys.ax2 sys.ax2 sys.par2;
        sys.iso1 sys.iso1 sys.iso1;
        0 0 0];
aw_0 = [sys.ax3 sys.ax3 sys.par3;       % Matrix of Trp hfcs
        sys.iso2 sys.iso2 sys.iso2;
        0 0 0];
sys.eul_af = zeros(4,3);              % Flavin hyp Euler angles
                                      % All 0 as aligned with gf
eul_aw = [sys.eul_w;
          sys.eul_w;                  % Trp hfc Euler angles
          sys.eul_w];                 % All aligned with gw
sys.I_f = [1 0 0 0];             % Spin qtm no. of nuclei to flavin
sys.I_w = [0 0 0];               % Spin qtm no. of nuclei to trp

%%%% sys input - Coupling (electrons) %%%%
sys.J = 0.5;
sys.d = -4;
sys.eul_d = deg2rad([0 0 0]);      % Angles of dfw vector (3rd=0)

sys.linewidth = 1;           % Gaussian linewidth

%%%% Experimental input %%%%
exp.npoints = 1000;                  % No. of data points
exp.Band = 'X';                      % Freq. band (X,Q,W)
exp.temp = 10;                       % T /K (for thermal eqm spectra)
```

```
if exp.Band == 'X'
    exp.freq = 9.5;
    exp.Range = [3375 3420];
elseif exp.Band == 'Q'
    exp.freq = 35;
    exp.Range = [12440 12530];
elseif exp.Band == 'W'
    exp.freq = 90;
    exp.Range = [32040 32160];
end

% options input %
if length(sys.linewidth) == 2          % Can use to get out
    opt.split = true;                  % spectra for individual
else                                   % radicals
    opt.split = false;
end
opt.pol = true;                        % spin polarized
opt.ntheta = 32;                       % no. of theta
opt.nphi = 64;                         % no. of phi
tic
B0 = linspace(exp.Range(1),exp.Range(2),exp.npoints);
nf_nuc = nnz(sys.I_f);                 % no. of nuclei coupled to flavin
nw_nuc = nnz(sys.I_w);                 % no. of nuclei coupled to trp

%%%%%%%%% SIMULATION %%%%%%%%%

% Initial direction cosines (all aligned)
% Order = f_x/y/z, w_x/y/z, Dfw %
dir_cos = [1 0 0; 0 1 0; 0 0 1; 1 0 0; 0 1 0; 0 0 1; 0 0 1];
dirgf = orth(dir_cos(1:3,:));      % orthogonalized gf
dirgw = orth(dir_cos(4:6,:));      % orthogonalized gw
dirdfw = dir_cos(7,:);             % direction cosines of dfw vector

% Rotating gw by Euler Angles away from gf principal axes %
dirgw = (erot(sys.eul_w(1),sys.eul_w(2),sys.eul_w(3))).'*dirgw;

% Rotating dfw by Euler Angles away from gf principal axis (z-axis) %
Rp = erot(sys.eul_d(1),sys.eul_d(2),sys.eul_d(3));
dirdfw = (Rp.'*dirdfw')';

% Rotating hyperfine tensors by Euler angles %
af_axes = zeros(3,3,nf_nuc);
af_rotd = zeros(3,3,nf_nuc);
for aa = 1:nf_nuc        %Generate then rotate hfc axes
    af_axes(:,:,aa) = [af_0(aa,1) 0 0; 0 af_0(aa,2) 0; 0 0 af_0(aa,3)];
    af_rotd(:,:,aa) = (erot(sys.eul_af(aa,1),sys.eul_af(aa,2)...
        ,sys.eul_af(aa,3))).'*af_axes(:,:,aa);
end
aw_axes = zeros(3,3,nw_nuc);
aw_rotd = zeros(3,3,nw_nuc);
for bb = 1:nw_nuc
    aw_axes(:,:,bb) = [aw_0(bb,1) 0 0; 0 aw_0(bb,2) 0; 0 0 aw_0(bb,3)];
```

```
    aw_rotd(:,:,bb) = (erot(eul_aw(bb,1),eul_aw(bb,2),...
        eul_aw(bb,3))).'*aw_axes(:,:,bb);
end

multif = 2*sys.I_f + 1;      % Multiplicity of nuclei at flavin (2I+1)
multiw = 2*sys.I_w + 1;      % Multiplicity of nuclei at trp (2I+1)
multi = [multif multiw];
con = planck*10^13/bmagn*exp.freq;          % g_i values to B0_i (G)
akt = exp.temp*1.381*714.5*.5/6.626e-2;
% occurs as reciprocal in height for thermal spectrum

cph = zeros(1,opt.nphi);
sph = zeros(1,opt.nphi);
cth = zeros(1,opt.ntheta);
sth = zeros(1,opt.ntheta);
b0 = zeros(1,3);
spectrum1 = zeros(1,exp.npoints);
spectrum2 = zeros(1,exp.npoints);
spectrum = zeros(1,exp.npoints);
cosf = zeros(1,3);
cosw = zeros(1,3);

for k = 1:opt.nphi
    phi = (k-1)*2*pi/(opt.nphi-1);
    sph(k) = sin(phi);
    cph(k) = cos(phi);
end
for j = 1:opt.ntheta
    theta = (j-1)*pi/(opt.ntheta-1);
    sth(j) = sin(theta);
    cth(j) = cos(theta);
end

for j = 1:opt.ntheta          % theta/phi loop %
    for k = 1:opt.nphi
        field = zeros(4*multif(1),multif(2),multif(3));     % for total
        height = zeros(4*multif(1),multif(2),multif(3));    % spectrum
        field1 = zeros(2*multif(1),multif(2),multif(3));
        height1 = zeros(2*multif(1),multif(2),multif(3));   % for split
        field2 = zeros(2*multif(1),multif(2),multif(3));    % spectrum
        height2 = zeros(2*multif(1),multif(2),multif(3));
        b0(1) = sth(j)*cph(k);    % B0_x
        b0(2) = sth(j)*sph(k);    % B0_y
        b0(3) = cth(j);           % B0_z

        % cos angles between field and g components %
        cosf(1) = dot(b0,dirgf(:,1))/(norm(b0)*norm(dirgf(:,1)));
        cosf(2) = dot(b0,dirgf(:,2))/(norm(b0)*norm(dirgf(:,2)));
        cosf(3) = dot(b0,dirgf(:,3))/(norm(b0)*norm(dirgf(:,3)));
        gf_eff = sqrt((sys.gf(1)*cosf(1))^2 + ...
            (sys.gf(2)*cosf(2))^2 + (sys.gf(3)*cosf(3))^2);

        cosw(1) = dot(b0,dirgw(:,1))/(norm(b0)*norm(dirgw(:,1)));
```

```
cosw(2) = dot(b0,dirgw(:,2))/(norm(b0)*norm(dirgw(:,2)));
cosw(3) = dot(b0,dirgw(:,3))/(norm(b0)*norm(dirgw(:,3)));
gw_eff = sqrt((sys.gw(1)*cosw(1))^2 + ...
    (sys.gw(2)*cosw(2))^2 + (sys.gw(3)*cosw(3))^2);

% cos angle between field and dfw vector %
cosdfw = dot(b0,dirdfw)/(norm(b0)*norm(dirdfw));

% Calculating effective fields (convert g_i to B0_i) %
dzz = sys.d*(cosdfw^2 - 1/3);  % anisotropic mag dip coupling
b0w = con/gw_eff;              % resonant field for effective g_w
b0f = con/gf_eff;              % resonant field for effective p_f

% zeros %
b0f_hyp = zeros(multif);
b0w_hyp = zeros(multiw);
b0dif = zeros(multi);
b0sum = zeros(multi);
omega = zeros(multi);
sin2t = zeros(multi);
cos2t = zeros(multi);
af_eff = zeros(1,4);
aw_eff = zeros(1,3);
dotABf = zeros(nf_nuc,3);
dotABw = zeros(nw_nuc,3);

% Projection of hfc axes onto B to yield eff. hyps %
for cc = 1:nf_nuc
    for dd = 1:3
        dotABf(cc,dd) = dot(af_rotd(:,dd,cc),b0);
        af_eff(cc) = sqrt(sum(dotABf(cc,:).^2));
    end
end
for ee = 1:nw_nuc
    for ff = 1:3
        dotABw(ee,ff) = dot(aw_rotd(:,ff,ee),b0);
        aw_eff(ee) = sqrt(sum(dotABw(ee,:).^2));
    end
end

% loop over each hyperfine (4xflavin and 3xtrp) %
for gg = 1:multiw(3)          % Calc. all components needed for
for hh = 1:multiw(2)          % field and height for each m_i
for ll = 1:multiw(1)          % for each nuclei. Taking the
for mm = 1:multif(4)          % four-stick spectrum and keep
for nn = 1:multif(3)          % splitting by hfcs
for oo = 1:multif(2)          % 'Sticks' collected in multi-
for pp = 1:multif(1)          % dimensional matrices

    b0f_hyp(pp,oo,nn,mm) = b0f + af_eff(1)*(pp-1-sys.I_f...
        (1)) + af_eff(2)*(oo-1-sys.I_f(2)) + af_eff(3)*...
        (nn-1-sys.I_f(3)) + af_eff(4)*(mm-1-sys.I_f(4));
```

```
b0w_hyp(ll,hh,gg) = b0w + aw_eff(1)*(ll-1-sys.I_w(1))...
    + aw_eff(2)*(hh-1-sys.I_w(2)) + ...
    aw_eff(3)*(gg-1-sys.I_w(3));

b0dif(pp,oo,nn,mm,ll,hh,gg) = (b0w_hyp(ll,hh,gg) - ...
    b0f_hyp(pp,oo,nn,mm))/2;

b0sum(pp,oo,nn,mm,ll,hh,gg) = (b0w_hyp(ll,hh,gg) + ...
    b0f_hyp(pp,oo,nn,mm))/2;

omega(pp,oo,nn,mm,ll,hh,gg) = sqrt((sys.J + dzz/2)^2 + ...
    b0dif(pp,oo,nn,mm,ll,hh,gg)^2);

sin2t(pp,oo,nn,mm,ll,hh,gg) = b0dif(pp,oo,nn,mm,ll,...
    hh,gg)/omega(pp,oo,nn,mm,ll,hh,gg);
cos2t(pp,oo,nn,mm,ll,hh,gg) = (sys.J+dzz/2)/omega...
    (pp,oo,nn,mm,ll,hh,gg);

field(4*(pp-1)+1,oo,nn,mm,ll,hh,gg) = b0sum(pp,oo,nn,mm...
    ,ll,hh,gg) + dzz - sys.J -omega(pp,oo,nn,mm,ll,hh,gg);

field(4*(pp-1)+2,oo,nn,mm,ll,hh,gg) = b0sum(pp,oo,nn,mm...
    ,ll,hh,gg) + dzz - sys.J +omega(pp,oo,nn,mm,ll,hh,gg);

field(4*(pp-1)+3,oo,nn,mm,ll,hh,gg) = b0sum(pp,oo,nn,mm...
    ,ll,hh,gg) - dzz + sys.J +omega(pp,oo,nn,mm,ll,hh,gg);

field(4*(pp-1)+4,oo,nn,mm,ll,hh,gg) = b0sum(pp,oo,nn,mm...
    ,ll,hh,gg) - dzz + sys.J -omega(pp,oo,nn,mm,ll,hh,gg);

% Assign res fields to each radical %
if opt.split
    field1(2*(pp-1)+1,oo,nn,mm,ll,hh,gg) = field(4*...
        (pp-1)+1,oo,nn,mm,ll,hh,gg);
    field1(2*(pp-1)+2,oo,nn,mm,ll,hh,gg) = field(4*...
        (pp-1)+4,oo,nn,mm,ll,hh,gg);
    field2(2*(pp-1)+1,oo,nn,mm,ll,hh,gg) = field(4*...
        (pp-1)+2,oo,nn,mm,ll,hh,gg);
    field2(2*(pp-1)+2,oo,nn,mm,ll,hh,gg) = field(4*...
        (pp-1)+3,oo,nn,mm,ll,hh,gg);
end

switch opt.pol
    case true       % heights for polarized pop.
        h = .25*sin2t(pp,oo,nn,mm,ll,hh,gg)^2*sth(j);
        if (j==1) || (j==opt.ntheta)
            h = h/2;
        end
        if (k==1) || (k==opt.nphi)
            h = h/2;
        end
        height(4*(pp-1)+1,oo,nn,mm,ll,hh,gg) = h;
        height(4*(pp-1)+2,oo,nn,mm,ll,hh,gg) = h;
```

```
                height(4*(pp-1)+3,oo,nn,mm,ll,hh,gg) = -h;
                height(4*(pp-1)+4,oo,nn,mm,ll,hh,gg) = -h;

        otherwise           % heights for thermal pop.
            hin = (1+cos2t(pp,oo,nn,mm,ll,hh,gg))*sth(j)*...
                .25*b0sum(pp,oo,nn,mm,ll,hh,gg)/akt;
            hou = (1-cos2t(pp,oo,nn,mm,ll,hh,gg))*sth(j)*...
                .25*b0sum(pp,oo,nn,mm,ll,hh,gg)/akt;
            if (j==1) || (j==opt.ntheta)
                hin = hin/2;
                hou = hou/2;
            end
            if (k==1) || (k==opt.nphi)
                hin = hin/2;
                hou = hou/2;
            end
            height(4*(pp-1)+1,oo,nn,mm,ll,hh,gg) = hou;% Outer h
            height(4*(pp-1)+2,oo,nn,mm,ll,hh,gg) = hin;% Inner h
            height(4*(pp-1)+3,oo,nn,mm,ll,hh,gg) = hou;
            height(4*(pp-1)+4,oo,nn,mm,ll,hh,gg) = hin;
        end

        if opt.split        % Assign heights to each radical
            height1(2*(pp-1)+1,oo,nn,mm,ll,hh,gg) = height...
                (4*(pp-1)+1,oo,nn,mm,ll,hh,gg);
            height1(2*(pp-1)+2,oo,nn,mm,ll,hh,gg) = height...
                (4*(pp-1)+4,oo,nn,mm,ll,hh,gg);
            height2(2*(pp-1)+1,oo,nn,mm,ll,hh,gg) = height...
                (4*(pp-1)+2,oo,nn,mm,ll,hh,gg);
            height2(2*(pp-1)+2,oo,nn,mm,ll,hh,gg) = height...
                (4*(pp-1)+3,oo,nn,mm,ll,hh,gg);
        end
    end
    end
    end
    end
    end
    end
    end

    field = reshape(field,1,4*prod(multi));     % reshape matrices
    height = reshape(height,1,4*prod(multi));    % to vectors

    if opt.split
        field1 = reshape(field1,1,2*prod(multi));
        height1 = reshape(height1,1,2*prod(multi));
        field2 = reshape(field2,1,2*prod(multi));
        height2 = reshape(height2,1,2*prod(multi));
        sub_spec1 = zeros(1,exp.npoints);
        sub_spec2 = zeros(1,exp.npoints);

    % For each orientation build sub_spec of both radicals
        for ii = 1:2*prod(multi)
```

```
                sub_spec1 = sub_spec1 + height1(ii)*gaussian(B0...
                    ,field1(ii),sys.linewidth(1));
                sub_spec2 = sub_spec2 + height2(ii)*gaussian(B0...
                    ,field2(ii),sys.linewidth(2));
            end
        % Sum over all orientations
            spectrum1 = spectrum1 + sub_spec1;  % Spectrum of each
            spectrum2 = spectrum2 + sub_spec2;  % radical plus total
            spectrum = spectrum1 + spectrum2;   % spectrum
        else
            sub_spec = zeros(1,exp.npoints);
            for qq = 1:4*prod(multi)
                sub_spec = sub_spec + height(qq)*gaussian...
                    (B0,field(qq),sys.linewidth(1)); %lw in Gauss
            end
            spectrum = spectrum + sub_spec;
        end
    end
end
toc
b_axis = B0;
spectrum = spectrum./max(abs(spectrum));
plot(b_axis,spectrum)
```

Bibliography

[1] P. W. Atkins and R. S. Friedman. *Molecular Quantum Mechanics*. Oxford University Press, fifth edition, 2011.

[2] R. N. Zare. *Angular momentum*. John Wiley & Sons, Inc., 1987.

[3] R. Shankar. *Principles of quantum mechanics*. Plenum Press, New York, second edition, 1994.

[4] W. Pauli. Über den Zusammenhang des Abschlusses der Elektronengruppen im Atom mit der Komplexstruktur der Spektren. *Zeitschrift für Physik*, 31(1):765–783, 1925.

[5] A. Abragam and B. Bleaney. *Electron paramagnetic resonance of transition ions*. Oxford University Press, 2012.

[6] M. Reiher and A. Wolf. *Relativistic quantum chemistry: the fundamental theory of molecular science*. John Wiley & Sons, Inc., 2014.

[7] H. M. McConnell. Indirect hyperfine interactions in the paramagnetic resonance spectra of aromatic free radicals. *The Journal of Chemical Physics*, 24(4):764–766, 1956.

[8] G. R. Eaton, S. S. Eaton, D. P. Barr, and R.T. Weber. *Quantitative EPR*. Springer Science & Business Media, 2010.

[9] S. Stoll and A. Schweiger. EasySpin, a comprehensive software package for spectral simulation and analysis in EPR. *Journal of Magnetic Resonance*, 178(1):42–55, 2006.

[10] N. M. Atherton. *Principles of electron spin resonance*. Ellis Horwood and PTR Prentice Hall, 1993.

[11] G. van Veen. Simulation and analysis of EPR spectra of paramagnetic ions in powders. *Journal of Magnetic Resonance (1969)*, 30(1):91–109, 1978.

[12] R. Aasa and T. Vänngård. EPR signal intensity and powder shapes: A reexamination. *Journal of Magnetic Resonance*, 19(3):308–315, 1975.

[13] J. A. Weil. The analysis of large hyperfine splitting in paramagnetic resonance spectroscopy. *Journal of Magnetic Resonance*, 4(3):394–399, 1971.

[14] S. Stoll and A. Schweiger. An adaptive method for computing resonance fields for continuous-wave EPR spectra. *Chemical Physics Letters*, 380(3-4):464–470, 2003.

[15] G. Jeschke. Instrumentation and Experimental Setup. In *ESR Spectroscopy in Membrane Biophysics*, pages 17–47. Springer US, 2007.

[16] A. Schweiger and G. Jeschke. *Principles of pulsed electron paramagnetic resonance.* Oxford University Press, New York, 2001.

[17] P. J. Hore, J. A. Jones, and S. Wimperis. *NMR: The toolkit: How pulse sequences work.* Oxford University Press, 2015.

[18] J. Keeler. *Understanding NMR Spectroscopy.* John Wiley & Sons, 2011.

[19] F. Bloch. Nuclear induction. *Physical Review*, 70(7-8):460–474, 1946.

[20] E. L. Hahn. Nuclear induction due to free Larmor precession. *Physical Review*, 77(2):297–298, 1950.

[21] E. L. Hahn. Spin echoes. *Physical Review*, 80(4):580–594, 1950.

[22] W. B. Mims. Pulsed endor experiments. *Proceedings of the Royal Society of London. Series A. Mathematical and Physical Sciences*, 283(1395):452–457, 1965.

[23] C. Gemperle and A. Schweiger. Pulsed Electron-Nuclear Double Resonance Methodology. *Chemical Reviews*, 91:1481–1505, 1991.

[24] G. Moise, L. Tejerina, M. Rickhaus, H. L Anderson, and C. R Timmel. Spin Delocalization in the Radical Cations of Porphyrin Molecular Wires: A New Perspective on EPR Approaches. *The Journal of Physical Chemistry Letters*, 10:5708–5712, 2019.

[25] L. R. Milgrom and M. J. Warren. The colours of life: an introduction to the chemistry of porphyrins and related compounds. *The Journal of Chemical Education*, 75(4):420, 1997.

[26] Jr W. Buchler and D. Dolphin. The Porphyrins. *by D. Dolphin, Academic Press, New York*, 1:389, 1978.

[27] H. L. Anderson. Building molecular wires from the colours of life: conjugated porphyrin oligomers. *Chemical Communications*, (23):2323–2330, 1999.

[28] S. A. Wolf, D. D. Awschalom, R. A. Buhrman, J. M. Daughton, S. Von Molnar, M. L. Roukes, A. Y. Chtchelkanova, and D. M. Treger. Spintronics: a spin-based electronics vision for the future. *Science*, 294(5546):1488–1495, 2001.

[29] M. Ratner. A brief history of molecular electronics. *Nature Nanotechnology*, 8(6):378, 2013.

[30] A. A. Bakulin, A. Rao, V. G. Pavelyev, P. H. M. van Loosdrecht, M. S. Pshenichnikov, D. Niedzialek, J. Cornil, D. Beljonne, and R. H. Friend. The role of driving energy and delocalized states for charge separation in organic semiconductors. *Science*, 335(6074):1340–1344, 2012.

[31] Y. Bai, J.-H. Olivier, H. Yoo, N. F. Polizzi, J. Park, J. Rawson, and M. J. Therien. Molecular road map to tuning ground state absorption and excited state dynamics of long-wavelength absorbers. *Journal of the American Chemical Society*, 139(46):16946–16958, 2017.

[32] T. V. Duncan, K. Susumu, L.E. Sinks, and M. J. Therien. Exceptional near-infrared fluorescence quantum yields and excited-state absorptivity of highly conjugated porphyrin arrays. *Journal of the American Chemical Society*, 128(28):9000–9001, 2006.

[33] J. C. Ostrowski, K. Susumu, M. R. Robinson, M. J. Therien, and G. C. Bazan. Near-Infrared Electroluminescent Light-Emitting Devices Based on Ethyne-Bridged Porphyrin Fluorophores. *Advanced Materials*, 15(15):1296–1300, 2003.

[34] V. S. Lin, S. G. DiMagno, and M. J. Therien. Highly conjugated, acetylenyl bridged porphyrins: new models for light-harvesting antenna systems. *Science*, 264(5162):1105–1111, 1994.

[35] T. N. Singh-Rachford and F. N. Castellano. Photon upconversion based on sensitized triplet–triplet annihilation. *Coordination Chemistry Reviews*, 254(21-22):2560–2573, 2010.

[36] T. N. Singh-Rachford, A. Nayak, M. L. Muro-Small, S. Goeb, M. J. Therien, and F. N. Castellano. Supermolecular-chromophore-sensitized near-infrared-to-visible photon upconversion. *Journal of the American Chemical Society*, 132(40):14203–14211, 2010.

[37] V. S.-Y. Lin and M. J. Therien. The role of porphyrin-to-porphyrin linkage topology in the extensive modulation of the absorptive and emissive properties of a series of ethynyl-and butadiynyl-bridged bis-and tris (porphinato) zinc chromophores. *Chemistry–A European Journal*, 1(9):645–651, 1995.

[38] M. D. Peeks, P. Neuhaus, and H. L Anderson. Experimental and computational evaluation of the barrier to torsional rotation in a butadiyne-linked porphyrin dimer. *Physical Chemistry Chemical Physics*, 18(7):5264–5274, 2016.

[39] M. U. Winters, J. Kärnbratt, M. Eng, C. J. Wilson, H. L. Anderson, and B. Albinsson. Photophysics of a butadiyne-linked porphyrin dimer: Influence of conformational flexibility in the ground and first singlet excited state. *The Journal of Physical Chemistry C*, 111(19):7192–7199, 2007.

[40] L. Rintoul, S. R. Harper, and D. P. Arnold. A systematic theoretical study of the electronic structures of porphyrin dimers: DFT and TD-DFT calculations on diporphyrins linked by ethane, ethene, ethyne, imine, and azo bridges. *Physical Chemistry Chemical Physics*, 15(43):18951–18964, 2013.

[41] M. D. Peeks, C. E. Tait, P. Neuhaus, G. M. Fischer, M. Hoffmann, R. Haver, A. Cnossen, J. R. Harmer, C. R. Timmel, and H. L. Anderson. Electronic delocalization in the radical cations of porphyrin oligomer molecular wires. *Journal of the American Chemical Society*, 139(30):10461–10471, 2017.

[42] K. Susumu, P. R. Frail, P. J. Angiolillo, and M. J. Therien. Conjugated chromophore arrays with unusually large hole polaron delocalization lengths. *Journal of the American Chemical Society*, 128(26):8380–8381, 2006.

[43] J. Rawson, P. J. Angiolillo, and M. J. Therien. Extreme electron polaron spatial delocalization in pi-conjugated materials. *Proceedings of the National Academy of Sciences*, 112(45):13779–13783, 2015.

[44] J. R. Norris, R. A. Uphaus, H. L. Crespi, and J. J. Katz. Electron spin resonance of chlorophyll and the origin of signal I in photosynthesis. *Proceedings of the National Academy of Sciences*, 68(3):625–628, 1971.

[45] F. Neese. Software update: the ORCA program system, version 4.0. *WIREs Computational Molecular Science*, 8(1), jan 2018.

[46] C. D. Pun. *Recent Advances In Density Functional Methods, Part I.* World Scientific, 1995.

[47] M. Rickhaus, A. Vargas Jentzsch, L. Tejerina, I. Grübner, M. Jirasek, T. D. W. Claridge, and H. L. Anderson. Single-Acetylene Linked Porphyrin Nanorings. *Journal of the American Chemical Society*, 139(46):16502–16505, 2017.

[48] M. J. Frisch, G. W. Trucks, G. E. Schlegel, H. B. Scuseria, M. A. Robb, J. R. Cheeseman, G. Scalmani, V. Barone, G. A. Petersson, H. Nakatsuji, X. Li, M. Caricato, A. V. Marenich, J. Bloino, B. G. Janesko, R. Gomperts, B. Mennucci, H. P. Hratchian, J. V. Ortiz, A. F. Izmaylov, J. L. Sonnenberg, D. Williams-Young, F. Ding, F. Lipparini, F. Egidi, J. Goings, B. Peng, A. Petrone, T. Henderson, D. Ranasinghe, V. G. Zakrzewski, J. Gao, N. Rega, G. Zheng, W. Liang, M. Hada, M. Ehara, K. Toyota, R. Fukuda, J. Hasegawa, M. Ishida, T. Nakajima, Y. Honda, O. Kitao, H. Nakai, T. Vreven, K. Throssell, Jr. Montgomery, J. A., J. E. Peralta, F. Ogliaro, M. J. Bearpark, J. J. Heyd, E. N. Brothers, K. N. Kudin, V. N. Staroverov, T. A. Keith, R. Kobayashi, J. Normand, K. Raghavachari, A. P. Rendell, J. C. Burant, S. S. Iyengar, J. Tomasi, M. Cossi, J. M. Millam, M. Klene, C. Adamo, R. Cammi, J. W. Ochterski, R. L. Martin, K. Morokuma, O. Farkas, J. B. Foresman, and D. J. Fox. Gaussian 16, Revision C.01, 2016.

[49] C. E. Tait. *Electron Paramagnetic Resonance Studies of Artificial Supramolecular Structures and Biological Systems.* PhD thesis, University of Oxford, 2015.

[50] C. M. Marian. Spin-orbit coupling and intersystem crossing in molecules. *Wiley Interdisciplinary Reviews: Computational Molecular Science*, 2(2):187–203, 2012.

[51] D. G. Fedorov and M. S. Gordon. A study of the relative importance of one and two-electron contributions to spin-orbit coupling. *Journal of Chemical Physics*, 112(13):5611–5623, 2000.

[52] J. Tatchen, M. Kleinschmidt, and C. M. Marian. Calculating electron paramagnetic resonance g -matrices for triplet state molecules from multireference spin-orbit configuration interaction wave functions. *Journal of Chemical Physics*, 130(15):154106, 2009.

[53] O. Vahtras, M. Engström, and B. Schimmelpfennig. Electronic g-tensors obtained with the mean-field spin-orbit Hamiltonian. *Chemical Physics Letters*, 351(5-6):424–430, 2002.

[54] B. A. Hess, C. M. Marian, U. Wahlgren, and O. Gropen. A mean-field spin-orbit method applicable to correlated wavefunctions. *Chemical Physics Letters*, 251(5-6):365–371, 1996.

[55] F. Neese. Efficient and accurate approximations to the molecular spin-orbit coupling operator and their use in molecular g-tensor calculations. *Journal of Chemical Physics*, 122(3):034107, jan 2005.

[56] F. Neese and E. I. Solomon. Calculation of Zero-Field Splittings, g-Values, and the Relativistic Nephelauxetic Effect in Transition Metal Complexes. Application to High-Spin Ferric Complexes. *Inorganic Chemistry*, 37(26):6568–6582, 1998.

[57] S. Koseki, M. W. Schmidt, and M. S. Gordon. Effective nuclear charges for the first- through third-row transition metal elements in spin-orbit calculations. *Journal of Physical Chemistry A*, 102(50):10430–10435, 1998.

[58] S. Koseki, M. W. Schmidt, and M. S. Gordon. MCSCF/6-31G(d,p) calculations of one-electron spin-orbit coupling constants in diatomic molecules. *Journal of Physical Chemistry*, 96(26):10768–10772, 1992.

[59] S. G. Chiodo and N. Russo. One-electron spin-orbit contribution by effective nuclear charges. *Journal of Computational Chemistry*, 30(5):832–839, 2009.

[60] D. S. McClure. Spin-orbit interaction in aromatic molecules. *The Journal of Chemical Physics*, 20 (4):682–686, 1952.

[61] R. Mcweeny. On the origin of spin-Hamiltonian parameters. *The Journal of Chemical Physics*, 42 (5):1717–1725, 1965.

[62] S. L. Murov, C. Ian, and H. L. Gordon. *Handbook of photochemistry*. CRC Press, 1993.

[63] M. A. El-Sayed. Spin-orbit coupling and the radiationless processes in nitrogen heterocyclics. *The Journal of Chemical Physics*, 38(12):2834–2838, 1963.

[64] O. Vahtras, O. Loboda, B. Minaev, H. Ågren, and K. Ruud. Ab initio calculations of zero-field splitting parameters. *Chemical Physics*, 279(2-3):133–142, 2002.

[65] T. J. Penfold, E. Gindensperger, C. Daniel, and C. M. Marian. Spin-Vibronic Mechanism for Intersystem Crossing, 2018.

[66] B. R. Henry and W. Siebrand. Spin–Orbit Coupling in Aromatic Hydrocarbons. Analysis of Nonradiative Transitions between Singlet and Triplet States in Benzene and Naphthalene. *The Journal of Chemical Physics*, 54(3):1072–1085, 1971.

[67] A. Toniolo and M. Persico. Efficient calculation of Franck-Condon factors and vibronic couplings in polyatomics. *Journal of Computational Chemistry*, 22(9):968–975, jul 2001.

[68] J. L. Brédas, D. Beljonne, V. Coropceanu, and J. Cornil. Charge-transfer and energy-transfer processes in π-conjugated oligomers and polymers: A molecular picture. *Chemical Reviews*, 104 (11):4971–5003, 2004.

[69] M. Etinski, J. Tatchen, and C. M. Marian. Time-dependent approaches for the calculation of intersystem crossing rates. *Journal of Chemical Physics*, 134(15):154105, 2011.

[70] C. R. Timmel. *Magnetic field effects on radical pair reactions*. PhD thesis, The Queen's College, University of Oxford, 1998.

[71] S. Siegel and H. S. Judeikis. A magnetophotoselection study of the polarizations of the absorption bands of some structurally related hydrocarbons and heterocyclic molecules. *Journal of Physical Chemistry*, 70(7):2205–2211, 1966.

[72] M. C. Thurnauer and J. R. Norris. The ordering of the zero field triplet spin sublevels in the chlorophylls. A magnetophotoselection study. *Chemical Physics Letters*, 47(1):100–105, 1977.

[73] C. E. Tait, P. Neuhaus, H. L. Anderson, and C. R. Timmel. Triplet state delocalization in a conjugated porphyrin dimer probed by transient electron paramagnetic resonance techniques. *Journal of the American Chemical Society*, 137(20):6670–6679, 2015.

[74] P. K. Poddutoori, Y. E. Kandrashkin, C. O. Obondi, F. D'Souza, and A. Van Der Est. Triplet electron transfer and spin polarization in a palladium porphyrin-fullerene conjugate. *Physical Chemistry Chemical Physics*, 20(44):28223–28231, 2018.

[75] H. Levanon and J. R. Norris. The Photoexcited Triplet State and Photosynthesis. *Chemical Reviews*, 78(3):185–198, 1978.

[76] R. Clarke, D. Hobart, and W. Leenstra. The Triplet State Of The Chlorophyll Dimer. *Journal of the American Chemical Society*, 101(9):2416–2423, 1979.

[77] M. Huber, A. A. Doubinskii, C. W. M. Kay, and K. Mobius. ENDOR on the Triplet State of the Primary Electron Donor in the Photosynthetic Bacterium Rhodobacter sphaeroides-One Step Forward in a Still Unfinished Story. *Applied Magnetic Resonance*, 13:473–485, 1997.

[78] F. Lendzian, R. Bittl, and W. Lubitz. Pulsed ENDOR of the photoexcited triplet states of bacteriochlorophyll a and of the primary donor P865 in reaction centers of Rhodobacter sphaeroides R-26. *Photosynthesis Research*, 55(2-3):189–197, 1998.

[79] M. Bennati, K. Németh, P. R. Surján, and M. Mehring. Zero-field-splitting and π-electron spin densities in the lowest excited triplet state of oligothiophenes. *Journal of Chemical Physics*, 105 (11):4441–4447, 1996.

[80] C. E. Tait, P. Neuhaus, M. D. Peeks, H. L Anderson, and C. R Timmel. Transient EPR reveals triplet state delocalization in a series of cyclic and linear pi-conjugated porphyrin oligomers. *Journal of the American Chemical Society*, 137(25):8284–8293, 2015.

[81] C. E. Tait, P. Neuhaus, M. D. Peeks, H. L. Anderson, and C. R. Timmel. Excitation wavelength-dependent EPR study on the influence of the conformation of multiporphyrin arrays on triplet state delocalization. *Physical Chemistry Chemical Physics*, 18(7):5275–5280, 2016.

[82] C. E. Tait, P. Neuhaus, H. L Anderson, C. R. Timmel, D. Carbonera, and M. Di Valentin. HYSCORE on Photoexcited Triplet States. *Applied Magnetic Resonance*, 46:389–409, 2015.

[83] S. Richert, C. E. Tait, and C. R. Timmel. Delocalisation of photoexcited triplet states probed by transient EPR and hyperfine spectroscopy. *Journal of Magnetic Resonance*, 280:103–116, 2017.

[84] S. Richert, G. Bullard, J. Rawson, P. J. Angiolillo, M. J Therien, and C. R. Timmel. On the importance of electronic symmetry for triplet state delocalization. *Journal of the American Chemical Society*, 139(15):5301–5304, 2017.

[85] S. Richert, B. Limburg, H. L. Anderson, and C. R. Timmel. On the Influence of the Bridge on Triplet State Delocalization in Linear Porphyrin Oligomers. *Journal of the American Chemical Society*, 139(34):12003–12008, 2017.

[86] P. J. Angiolillo, H. T. Uyeda, T. V. Duncan, and M. J. Therien. Impact of electronic asymmetry on photoexcited triplet-state spin distributions in conjugated porphyrin oligomers probed via EPR spectroscopy. *Journal of Physical Chemistry B*, 108(32):11893–11903, 2004.

[87] P. J. Angiolillo, V. S-Y Lin, J. M. Vanderkooi, and M. J. Therien. EPR Spectroscopy and Photophysics of the Lowest Photoactivated Triplet State of a Series of Highly Conjugated (Porphinato)Zn Arrays. *Journal of the American Chemical Society*, 117:12514–12527, 1995.

[88] P. J. Angiolillo, K. Susumu, H. T. Uyeda, V. S. Y. Lin, R. Shediac, and M. J. Therien. Trends in triplet excitation delocalization in highly conjugated (porphinato)zinc(II) arrays probed by EPR spectroscopy. *Synthetic Metals*, 116(1-3):247–253, jan 2001. ISSN 03796779. doi: 10.1016/S0379-6779(00)00461-6.

[89] P. J. Angiolillo, J. Rawson, P. R. Frail, and M. J. Therien. The evolution of spin distribution in the photoexcited triplet state of ethyne-elaborated porphyrins. *Chemical Communications*, 49(84):9722–9724, 2013.

[90] F. Neese. Spin-Hamiltonian Parameters from First Principle Calculations: Theory and Application. pages 175–229. Springer, New York, NY, 2009.

[91] M. Gouterman, G. H. Wagniere, and L. C. Snyder. Spectra of porphyrins: Part II. Four orbital model. *Journal of Molecular Spectroscopy*, 11(1-6):108–127, 1963.

[92] A. Kerridge. A RASSCF study of free base, magnesium and zinc porphyrins: accuracy versus efficiency. *Physical Chemistry Chemical Physics*, 15(6):2197–2209, 2013.

[93] S. Perun, J. Tatchen, and C. M. Marian. Singlet and triplet excited states and intersystem crossing in free-base porphyrin: TDDFT and DFT/MRCI study. *ChemPhysChem*, 9(2):282–292, 2008.

[94] O. Loboda, I. Tunell, B. Minaev, and H. Ågren. Theoretical study of triplet state properties of free-base porphin. *Chemical Physics*, 312(1-3):299–309, 2005.

[95] B. Minaev and H. Ågren. Theoretical DFT study of phosphorescence from porphyrins. *Chemical Physics*, 315(3):215–239, 2005.

[96] F. Aquilante, J. Autschbach, R. K. Carlson, L. F. Chibotaru, M. G. Delcey, L. De Vico, I. Fdez. Galván, N. Ferré, L. M. Frutos, L. Gagliardi, M. Garavelli, A. Giussani, C. E. Hoyer, G. Li Manni, H. Lischka, D. Ma, P. Å. Malmqvist, T. Müller, A. Nenov, M. Olivucci, T. B. Pedersen, D. Peng, F. Plasser, B. Pritchard, M. Reiher, I. Rivalta, I. Schapiro, J. Segarra-Martí, M. Stenrup, D. G. Truhlar, L. Ungur, A. Valentini, S. Vancoillie, V. Veryazov, V. P. Vysotskiy, O. Weingart, F. Zapata, and R. Lindh. Molcas 8: New capabilities for multiconfigurational quantum chemical calculations across the periodic table. *Journal of Computational Chemistry*, 37(5):506–541, feb 2016.

[97] S. G. DiMagno, R. A. Williams, and M. J. Therien. Facile Synthesis of meso-Tetrakis(perfluoroalkyl)porphyrins: Spectroscopic Properties and X-ray Crystal Structure of Highly Electron-Deficient 5,10,15,20-Tetrakis(heptafluoropropyl)porphyrin. *Journal of Organic Chemistry*, 59(23):6943–6948, nov 1994.

[98] J. G. Goll, K. T. Moore, A. Ghosh, and M. J. Therien. Synthesis, structure, electronic spectroscopy, photophysics, electrochemistry, and X-ray photoelectron spectroscopy of highly-electron-deficient [5,10,15,20-tetrakis(perfluoroalkyl)porphinato]zinc(II) complexes and their free base derivatives. *Journal of the American Chemical Society*, 118(35):8344–8354, 1996.

[99] K. T. Moore, J. T. Fletcher, and M. J. Therien. Syntheses, NMR and EPR spectroscopy, electrochemical properties, and structural studies of [5,10,15,20- tetrakis(perfluoroalkyl)porphinato]iron(II) and -iron(III) complexes. *Journal of the American Chemical Society*, 121(22):5196–5209, jun 1999.

[100] J. T. Fletcher and M. J. Therien. Extreme electronic modulation of the cofacial porphyrin structural motif. *Journal of the American Chemical Society*, 124(16):4298–4311, 2002.

[101] K. Susumu and M. J. Therien. Decoupling optical and potentiometric band gaps in π-conjugated materials. *Journal of the American Chemical Society*, 124(29):8550–8552, 2002.

[102] H. Mouritsen. Long-distance navigation and magnetoreception in migratory animals. *Nature*, 558(7708):50–59, 2018.

[103] R. Wiltschko. *Magnetic orientation in animals*. Berlin: Springer-Verlag, 1995.

[104] H. Mouritsen. Magnetoreception in Birds and Its Use for Long-Distance Migration. In *Sturkie's Avian Physiology: Sixth Edition*, pages 113–133. Elsevier Inc., sep 2014.

[105] T. Fransson, S. Jakobsson, P. Johansson, C. Kullberg, J. Lind, and A. Vallin. Bird migration: Magnetic cues trigger extensive refuelling. *Nature*, 414(6859):35–36, 2001.

[106] K. Schulten, C. E. Swenberg, and A. Weller. A biomagnetic sensory mechanism based on magnetic field modulated coherent electron spin motion. *Z. Phys. Chem.*, 111:1–5, 1978.

[107] T. Ritz, S. Adem, and K. Schulten. A model for photoreceptor-based magnetoreception in birds. *Biophysical Journal*, 78(2):707–718, 2000.

[108] C. A. Dodson, P. J. Hore, and M. I. Wallace. A radical sense of direction: Signalling and mechanism in cryptochrome magnetoreception. *Trends in Biochemical Sciences*, 38(9):435–446, sep 2013.

[109] M. Liedvogel and H. Mouritsen. Cryptochromes - A potential magnetoreceptor: What do we know and what do we want to know? *Journal of the Royal Society Interface*, 7(SUPPL. 2), apr 2010.

[110] H. Mouritsen and P. J. Hore. The magnetic retina: Light-dependent and trigeminal magnetoreception in migratory birds. *Current Opinion in Neurobiology*, 22(2):343–352, 2012.

[111] K. Maeda, A. J. Robinson, K. B. Henbest, H. J. Hogben, T. Biskup, M. Ahmad, E. Schleicher, S. Weber, C. R. Timmel, and P. J. Hore. Magnetically sensitive light-induced reactions in cryptochrome are consistent with its proposed role as a magnetoreceptor. *Proceedings of the National Academy of Sciences of the United States of America*, 109(13):4774–4779, mar 2012.

[112] B. Giovani, M. Byrdin, M. Ahmad, and K. Brettel. Light-induced electron transfer in a cryptochrome blue-light photoreceptor. *Nature Structural Biology*, 10(6):489–490, 2003.

[113] P. J. Hore and H. Mouritsen. The Radical-Pair Mechanism of Magnetoreception. *Annual Review of Biophysics*, 45(1):299–344, 2016.

[114] W. Wiltschko and R. Wiltschko. The effect of yellow and blue light on magnetic compass orientation in European robins, Erithacus rubecula. *J Comp Physiol A*, 184:295–299, 1999.

[115] D. Nohr, S. Franz, R. Rodriguez, B. Paulus, L. O. Essen, S. Weber, and E. Schleicher. Extended Electron-Transfer in Animal Cryptochromes Mediated by a Tetrad of Aromatic Amino Acids. *Biophysical Journal*, 111(2):301–311, 2016.

[116] A. J. Hoff, P. Gast, S. A. Dzuba, C. R. Timmel, C. E. Fursman, and P. J. Hore. The nuts and bolts of distance determination and zero- and double-quantum coherence in photoinduced radical pairs. *Spectrochimica Acta - Part A: Molecular and Biomolecular Spectroscopy*, 54(14):2283–2293, 1998.

[117] G. Kothe, S. Weber, E. Ohmes, M. C. Thurnauer, and J. R. Norris. Transient EPR of light-induced spin-correlated radical pairs: Manifestation of zero quantum coherence. *Journal of Physical Chemistry*, 98(10):2706–2712, 1994.

[118] R. Bittl and S. Weber. Transient radical pairs studied by time-resolved EPR. *Biochimica et Biophysica Acta - Bioenergetics*, 1707(1 SPEC. ISS.):117–126, 2005.

[119] E. Schleicher and S. Weber. *Radicals in flavoproteins*, volume 321. Springer, Berlin, Heidelberg, 2012.

[120] T. Biskup. Time-resolved electron paramagnetic resonance of radical pair intermediates in cryptochromes. *Molecular Physics*, 111(24):3698–3703, 2013.

[121] T. Biskup, E. Schleicher, A. Okafuji, G. Link, K. Hitomi, E. D. Getzoff, and S. Weber. Direct observation of a photoinduced radical pair in a cryptochrome blue-light photoreceptor. *Angewandte Chemie - International Edition*, 48(2):404–407, jan 2009.

[122] C. Aubert, P. Mathis, A. P. M. Eker, and K. Brettel. Intraprotein electron transfer between tyrosine and tryptophan in DNA photolyase from Anacystis nidulans. *Proceedings of the National Academy of Sciences of the United States of America*, 96(10):5423–5427, may 1999.

[123] S. Weber, C. W. M. Kay, H. Mögling, K. Möbius, K. Hitomi, and T. Todo. Photoactivation of the flavin cofactor in Xenopus laevis (6-4) photolyase: Observation of a transient tyrosyl radical by time-resolved electron paramagnetic resonance. *Proceedings of the National Academy of Sciences of the United States of America*, 99(3):1319–1322, 2002.

[124] D. Nohr, B. Paulus, R. Rodriguez, A. Okafuji, R. Bittl, E. Schleicher, and S. Weber. Determination of Radical-Radical Distances in Light-Active Proteins and Their Implication for Biological Magnetoreception. *Angewandte Chemie International Edition*, 56(29):8550–8554, 2017.

[125] S. Weber, T. Biskup, A. Okafuji, A. R. Marino, T. Berthold, G. Link, K. Hitomi, E.D. Getzoff, E. Schleicher, and J. R. Norris. Origin of light-induced spin-correlated radical pairs in cryptochrome. *Journal of Physical Chemistry B*, 114(45):14745–14754, 2010.

[126] P. J. Hore, D. A. Hunter, C. D. McKie, and A. J. Hoff. Electron paramagnetic resonance of spin-correlated radical pairs in photosynthetic reactions. *Chemical Physics Letters*, 137(6):495–500, 1987.

[127] A. Günther, A. Einwich, E. Sjulstok, R. Feederle, P. Bolte, K. W. Koch, I. A. Solov'yov, and H. Mouritsen. Double-Cone Localization and Seasonal Expression Pattern Suggest a Role in Magnetoreception for European Robin Cryptochrome 4. *Current Biology*, 28(2):211–223.e4, jan 2018.

[128] R. M. Kowalczyk, E. Schleicher, R. Bittl, and S. Weber. The photoinduced triplet of flavins and its protonation states. *Journal of the American Chemical Society*, 126(36):11393–11399, sep 2004.

[129] T. L. Pitcher. *An Investigation of Spin-Correlated Radical Pairs in Cryptochromes by Electron Paramagnetic Resonance*. PhD thesis, Somerville College, University of Oxford, 2020.

[130] A. Okafuji, A. Schnegg, E. Schleicher, K. Möbius, and S. Weber. G-tensors of the flavin adenine dinucleotide radicals in glucose oxidase: A comparative multifrequency electron paramagnetic resonance and electron-nuclear double resonance. *Journal of Physical Chemistry B*, 112(11):3568–3574, 2008.

[131] F. Lendzian, M. Sahlin, F. MacMillan, R. Bittl, R. Fiege, St. Pötsch, B. M. Sjöberg, A. Gräslund, W. Lubitz, and G. Lassmann. Electronic structure of neutral tryptophan radicals in ribonucleotide reductase studied by EPR and ENDOR spectroscopy. *Journal of the American Chemical Society*, 118(34):8111–8120, 1996.

[132] S. Stoll, H. S. Shafaat, J. Krzystek, A. Ozarowski, M. J. Tauber, J. E. Kim, and R. D. Britt. Hydrogen bonding of tryptophan radicals revealed by EPR at 700 GHz. *Journal of the American Chemical Society*, 133(45):18098–18101, 2011.

[133] G. Bleifuss, M. Kolberg, S. Pötsch, W. Hofbauer, R. Bittl, W. Lubitz, A. Gräslund, G. Lassmann, and F. Lendzian. Tryptophan and tyrosine radicals in ribonucleotide reductase: A comparative high-field EPR study at 94 GHz. *Biochemistry*, 40(50):15362–15368, dec 2001.

[134] C. Levy, B. D. Zoltowski, A. R. Jones, A. T. Vaidya, D. Top, J. Widom, M. W. Young, N. S. Scrutton, B. R. Crane, and D. Leys. Updated structure of Drosophila cryptochrome. *Nature*, 495(7441): 396–399, 2013.

[135] K. M. Salikhov, Y. E. Kandrashkin, and A. K. Salikhov. Peculiarities of free induction and primary spin echo signals for spin-correlated radical pairs. *Applied Magnetic Resonance*, 3(1):199–216, 1992.

[136] J. Tang, M. C. Thurnauer, and J. R. Norris. Electron spin echo envelope modulation due to exchange and dipolar interactions in a spin-correlated radical pair. *Chemical Physics Letters*, 219 (3-4):283–290, mar 1994.

[137] D. L. Goodwin, W. K. Myers, C. R. Timmel, and I. Kuprov. Feedback control optimisation of ESR experiments. *Journal of Magnetic Resonance*, 297:9–16, 2018.

[138] S. A. Dzuba, M. K. Bosch, and A. J. Hoff. Electron spin echo detection of quantum beats and double-quantum coherence in spin-correlated radical pairs of protonated photosynthetic reaction centers. *Chemical Physics Letters*, 248(5-6):427–433, 1996.

[139] S. Santabarbara, I. Kuprov, W. V. Fairclough, S. Purton, P. J. Hore, P. Heathcote, and M. C. W. Evans. Bidirectional electron transfer in photosystem I: Determination of two distances between P700+ and A1- in spin-correlated radical pairs. *Biochemistry*, 44(6):2119–2128, 2005.

[140] S. G. Zech, R. Bittl, A. T. Gardiner, and W. Lubitz. Transient and pulsed EPR spectroscopy on the radical pair state P865QA to study light-induced changes in bacterial reaction centers. *Applied Magnetic Resonance*, 13(3-4):517–529, 1997.

[141] S. G. Zech, J. Kurreck, H-J Eckert, G. Renger, W. Lubitz, and R. Bittl. Pulsed EPR measurement of the distance between P680 and QA in photosystem II. *FEBS Letters*, 414(2):454–456, 1997.

[142] S. A. Dzuba, P. Gast, and A. J. Hoff. ESEEM study of spin-spin interactions in spin polarised PQA pairs in the photosynthetic purple bacterium Rhodobacter sphaeroides R26. *Chemical Physics Letters*, 236(6):595–602, 1995.

[143] C. E. Fursman and P. J. Hore. Distance determination in spin-correlated radical pairs in photosynthetic reaction centres by electron spin echo envelope modulation. *Chemical Physics Letters*, 303(5-6):593–600, 1999.